

Diss. ETH No. 25781

# **Unsteady Steam Turbine Optimization using High Fidelity CFD**

A thesis submitted to attain the degree of

Doctor of Sciences of ETH Zurich  
(Dr. sc. ETH Zurich)

presented by

**ILIAS PAPAGIANNIS**

Dipl. Mech.-Eng., Aristotle University of Thessaloniki  
Born on 1<sup>st</sup> of August 1989  
citizen of Greece

accepted on the recommendation of

Prof. Dr. Reza S. Abhari, examiner  
Prof. Dr. Mathioudakis Konstantinos, co-examiner  
Dr. Anestis I. Kalfas, co-examiner

2019





*“It gets easier...  
Everyday it gets a little easier...  
But you have to do it everyday -  
That’s the hard part.  
But it does get easier.”*



## Acknowledgments

The present doctoral thesis is the outcome of my research work of the last five years as a research assistant in the Laboratory for Energy Conversion of ETH Zurich. It is difficult to express with mere words the gratitude I owe to so many people that contributed in their own way in the completion of this work.

First I would like to thank Professor Dr. Reza S. Abhari for his guidance and for the challenging and goal-oriented inputs during the last five years. He has given me the opportunity to run a complex and multidisciplinary project in a very dynamic working environment, a great experience for which I am thankful.

Special thanks go to Professor Dr. Konstantinos Mathioudakis for accepting the role as co-examiner. I feel honored to have him as a co-examiner for this thesis.

I owe a debt of gratitude to my Professor from Aristotle University of Thessaloniki, Dr. Anestis Kalfas. I am deeply grateful for the trust he showed in me from the very beginning, his support and encouragement through all these years. I have learned so much under his guidance and I hope he will keep teaching me for the years to come.

I would also like to express my gratitude towards Dr. Shigeki Senoo. His valuable inputs all these years were crucial for understanding and explaining the results. The contribution of Mr. Kazuhiro Momma in technical issues is also gratefully acknowledged.

Special thanks go to my predecessor Dr. Altug Basol, from whom I have learnt many useful things during the first years of my work. He was always available whenever I needed him, always ready to support me and answer any questions I had. Thank you very much for everything.

I would like to thank all former and current colleagues at the laboratory for the stimulating discussions and other enjoyable moments during this period. Specifically, I would like to thank my office mate for many years Janis Vinklers, the experimental guys Rainer Schädler, Dominic Hänni and Carsten Degendorfer, and Asad Raheem from the CFD team. They have made my life as PhD student so much better, not only with our fruitful discussions but also with the lab outings. Thank you all.

I would like to thank my colleague and friend Vahid Iranidokht for all these years we worked together, for the countless discussions on interpreting the results and the many productive breaks outside of ETH. It was a real pleasure working with him and I am grateful for that.

Additionally, I would like to thank Dr. Ndaona Chokani for his support and guidance during the first years of my studies in the laboratory. Special thanks go to Marlene Hegner for the very competent and efficient management of all administrative issues and for all the smiles.

To my close friends Dr. Ilias Bosdas, Dr. Georgios Stefopoulos and especially Alexandros Chasoglou and my childhood friend Giannis Nendos, I would like to express my deepest and sincerest gratitude. They have been a much greater help to me than they could ever imagine and I am truly grateful for their support and friendship. I can only hope to be able to give it back to you some time. Thank you from the depths of my heart.

Finally, I could not finish this part any other way than to thank my family for their love and support. Ευχαριστώ τους γονείς μου Μάκη και Στέλλα, τον αδερφό μου Μιχάλη και τη θεία μου Βάσω για την αγάπη τους και την συμπαράστασή τους όλα αυτά τα χρόνια. Σας ευχαριστώ... A big part of who I am today, I owe it to them and I could never thank them enough for that.

Zurich, January 2019  
Ilias Papagiannis

## Abstract

Despite the rapidly increasing share of renewable energies on the electrical grid and power market, turbomachinery still remain the main source of power generation and the largest share of electricity production is currently held by steam turbines. Computational fluid dynamics have been a valuable tool for engineers for decades in the constant strive for better performance and efficient design of turbomachinery. The remarkable advances in computational power over that last couple of decades have allowed the introduction of optimization techniques being employed in the turbomachinery design. However, the research and knowledge in the field of turbomachinery is so advanced that it is getting more and more difficult to achieve improvements in their performance. Although there is an abundance of optimization studies in turbomachinery applications in the open literature, the vast majority of them are based on steady state solutions. State-of-the-art research is reaching a point where unsteady effects need to be taken into account during the design process if further improvements are to be achieved.

Steam turbines are the largest machines in turbomachinery. High capacity power plants use different sections of steam turbines, such as high-pressure steam turbine, intermediate-pressure turbine and low-pressure turbines. The flow mechanisms on each stage can differ considerably. Whether it is shock patterns interacting with upstream blade rows in the high aspect ratio blades of a transonic low-pressure steam turbine or leakage flow from cavity paths interacting with lower aspect ratio blades and the secondary flows in a high-pressure steam turbine, the common factor is the same: unsteadiness. This leads to the principal scope of the current research work, which is to provide suggestions for performance improvement of modern steam turbines, while taking into account the unsteady interaction present in the flow field. The objectives are achieved by performing time-accurate flow simulations using in-house developed solver, "MULTI3".

The first part of this doctoral thesis addresses the challenges of modern low-pressure steam turbines. Due to the increasing energy demand, the flow area of the last stages of low-pressure steam turbines is getting larger to achieve the necessary power augmentation, resulting in long blades that exceed 50 inches. As a

consequence, the rotor experiences supersonic relative inflow conditions, leading to a formation of a bow shock wave, which interacts with upstream blade rows and tip cavity path. In order to complement previously conducted time-accurate measurements in such a machine and to help understanding the complex flow mechanisms present in the flow field, unsteady simulations have been performed with equilibrium steam modeling using MULTI3. Results have shown that the bow shock wave interacts with the upstream stator and shows increased unsteadiness in the pressure field, as well as high variations on the flow yaw angles due to the sharp pressure gradients across the shock. It was also shown that the unsteady stator rotor interaction in the presence of the bow shock wave is mainly driven by the axial distance between stator trailing edge and rotor leading edge. Based on the analysis of the results, possible ways for improved performance are provided.

The second part is related to leakage and secondary flow management in a model, two-stage axial turbine, with geometry typical of a high-pressure steam turbine. Goal was to achieve an efficiency improvement by applying end wall contouring on the rotor hub end wall of the second stage. To achieve this, an optimization with a Genetic Algorithm coupled with an Artificial Neural Network was performed. Past research in the Laboratory for Energy Conversion has taught that leakage flows interact with the blade rows and secondary flows in an unsteady manner, which needed to be taken into account during optimization, if the objective was to be achieved. Therefore, it was decided to apply an optimization using time-accurate simulations, including real hub- and tip cavity paths, for highest accuracy in predictions and to ensure that the unsteady flow mechanisms are taken into consideration during the design process. For the rest of this thesis, this process will be referred to as an unsteady optimization.

An unsteady optimization is very expensive in terms computational resources. First, the necessary preparation steps before attempting an unsteady optimization is described in detail. Available computational resources were limited and only enough for one optimization run. To ensure success, certain work was performed to further reduce the computational cost and to minimize the required simulation time. The main idea was to remove the first stage from the two-stage configuration by applying unsteady inlet boundary conditions in a single-stage simulation. This approach reduced the

computational size to half, while still maintaining high accuracy in predictions and ensuring that multistage effects are taken into account.

Eventually, the unsteady optimization for end wall contouring was successfully performed achieving an increase in stage efficiency by  $\Delta\eta = 0.27\%$ . The profiled end wall worked beneficially in delaying the formation of the hub passage vortex, reduced its strength and kept it in lower span positions, while also improving the flow uniformity at rotor exit, which could act in a positive manner in the interaction with a downstream stage in a real configuration. The use of unsteady inlet boundary conditions for increased accuracy was confirmed by comparing numerical results with experimental measurements, where excellent agreement was found in both trends and absolute values.

The presence of cavity paths in the computational model and the time-accurate simulations increase considerably the mesh size and required computational resources. In order to address whether this is necessary, additional cases were studied to investigate the effect of cavities and unsteadiness in the flow physics and stage performance. Results have shown that the effect of cavities and the unsteady interaction with the main flow path is far from negligible plays an important role in strength and development of secondary flows. Therefore, it is concluded that in cases where the goal is performance improvements through secondary flow management, cavities should be included in the computational model and unsteadiness needs to be taken into account.

Eventually, the optimized rotor geometry was given for manufacturing and will be experimentally tested in the near future to validate the numerical predictions.

## Zusammenfassung

Trotz des rasant steigenden Anteils der erneuerbaren Energien im Stromnetz und am Strommarkt sind Turbomaschinen nach wie vor das Rückgrat der Stromerzeugung. Dabei decken Dampfturbinen den grössten Teil der Stromerzeugung ab. Die rechnergestützte Strömungsmechanik ist seit langem ein wertvolles Werkzeug für Ingenieure im ständigen Streben nach höheren Leistungen und effizienterem Design von Turbomaschinen. Durch die bemerkenswerte Zunahme der Rechenleistung über die letzten Jahrzehnte, wurde es möglich, numerische Optimierungstechniken in der Entwicklung von Turbomaschinen einzuführen. Die Forschung und das Wissen auf dem Gebiet der Turbomaschinen sind jedoch so weit fortgeschritten, dass es immer schwieriger wird Leistungsverbesserungen zu erzielen. Obwohl es in der offenen Literatur eine Fülle von Optimierungsstudien zu Turbomaschinenanwendungen gibt, basiert die überwiegende Mehrheit davon auf stationären Simulationen. Der Stand der Forschung erreicht einen Punkt, an dem instationäre Effekte bei der Auslegung berücksichtigt werden müssen, um weitere Verbesserungen zu erreichen.

Dampfturbinen sind die grössten Maschinen im Turbomaschinenbereich. Grosskraftwerke nutzen verschiedene Stufen wie Hochdruck-Dampfturbinen, Mitteldruckturbinen und Niederdruckturbinen. Die Strömungsmechanismen können in jeder Stufe sehr unterschiedlich sein. Seien es Stosswellen aus transsonischen Niederdruckturbinen mit hohem Seitenverhältnis, die mit stromaufwärts liegenden Schaufelreihen interagieren oder Leckagen-Strömung aus Radseitenräume und Dichtungen die mit den Sekundärströmungen in Hochdruckturbinen interagieren. Die darin liegende Gemeinsamkeit ist die Strömungsunstetigkeit. Dies führt zum Hauptbetrachtungspunkt der aktuellen Forschungsarbeit, der darin besteht, Vorschläge zur Leistungssteigerung moderner Dampfturbinen unter Berücksichtigung der instationären Wechselwirkung im Strömungsfeld zu liefern. Dazu werden zeitaufgelöste Simulationen mit dem intern entwickelten Strömungsrechner "MULTI3" durchgeführt.



Der erste Teil dieser Dissertation beschäftigt sich mit den Herausforderungen moderner Niederdruck-Dampfturbinen. Aufgrund des steigenden Energiebedarfs und um die erforderliche Leistungssteigerung zu erreichen, wird der Strömungsquerschnitt der letzten Stufen von Niederdruck-Dampfturbinen immer grösser und Schaufellängen über 50 Zoll werden erreicht. Infolgedessen kommt es im Einströmbereich der Rotoren zu Überschallströmungen im Rotor relativ System, was zur Bildung einer Bugstosswelle führt, die mit den stromaufwärts gelegenen Schaufelreihen und der Deckband-Kavität interagiert. Um zuvor durchgeführten zeitaufgelöste Messungen in einer solchen Maschine zu ergänzen und das Verständnis der komplexen Strömungsmechanismen im Strömungsfeld zu erhöhen, wurden instationäre Simulationen mit Gleichgewichtsdampfmodellierung mit MULTI3 durchgeführt. Die Ergebnisse haben gezeigt, dass die Bugstosswelle mit dem stromaufwärts liegenden Stator interagiert und eine erhöhte Instabilität im Druckfeld sowie hohe Schwankungen der Anströmungswinkel aufgrund des starken Druckgradienten über die Stosswelle aufweist. Es wurde auch gezeigt, dass die instationäre Stator-Rotor-Wechselwirkung in Gegenwart der Bugstosswelle überwiegend durch den axialen Abstand zwischen Statorhinterkante und Rotorvorderkante bestimmt wird. Basierend auf der Analyse der Ergebnisse werden mögliche Wege zur Leistungssteigerung aufgezeigt.

Der zweite Teil der Arbeit bezieht sich auf das Leckage- und Sekundärströmungsmanagement in einer zweistufigen Modellaxialturbine, mit einer für eine Hochdruck-Dampfturbine typischen Geometrie. Das Ziel war es, durch eine Rotorseitenwandkonturierung der zweiten Stufe eine Effizienzsteigerung zu erreichen. Zu diesem Zweck wurde eine Optimierung mit einem generischen Algorithmus in Verbindung mit einem künstlichen neuronalen Netzwerk durchgeführt. Frühere Arbeiten im Laboratory for Energy Conversion haben gezeigt, dass Leckagen mit den Schaufelreihen und Sekundärströmungen zeitabhängig interagieren, was zur Zielerreichung bei der Optimierung berücksichtigt werden musste. Infolgedessen wurde beschlossen, eine Optimierung mit Hilfe von zeitaufgelösten Simulationen, einschliesslich realer Naben- und Schaufelspitzenleckagepfaden durchzuführen. Dies, um bei der Vorhersage höchste Genauigkeit zu erreichen und sicherzustellen, dass die instationären Strömungsmechanismen während des

Auslegungsprozesses berücksichtigt werden. Für den Rest dieser Arbeit wird dieser Prozess als instationäre Optimierung bezeichnet.

Eine instationäre Optimierung ist in Bezug auf die Rechenleistung sehr teuer. Zunächst werden die notwendigen Vorbereitungsschritte vor dem Durchführen einer instationären Optimierung ausführlich beschrieben. Die verfügbaren Rechenressourcen waren begrenzt und reichten nur für einen Optimierungslauf. Um sicherzustellen, dass die Optimierung erfolgreich ist, wurden bestimmte Arbeiten durchgeführt um die Berechnungskosten weiter zu senken und die erforderliche Simulationszeit zu minimieren. Die Grundidee war, die erste Stufe aus der zweistufigen Konfiguration zu entfernen, indem zeitaufgelöste Eintritts-Randbedingungen in einer einstufigen Simulation verwendet wurden. Mit diesem Ansatz halbierte sich die Rechenzeit, während gleichzeitig die hohe Genauigkeit einer zeitaufgelösten Vorhersage beibehalten wurde.

Die instationäre Optimierung der Seitenwandkonturierung wurde erfolgreich durchgeführt und eine Steigerung des Stufenwirkungsgrades um 0.27% erreicht. Die profilierte Rotorseitenwand trug dazu bei, die Bildung des Passagenwirbels zu verzögern, seine Stärke zu reduzieren und ihn nahe der Seitenwand zu halten. Gleichzeitig wurde die Gleichmässigkeit der Strömung am Rotoraustritt verbesserte, die sich im Zusammenspiel mit einer nachgeschalteten Stufe in einer realen Konfiguration positiv auswirken könnte. Die Verwendung zeitaufgelöster Eintritts-Randbedingungen für eine höhere Genauigkeit wurde durch den Vergleich numerischer Ergebnisse mit experimentellen Messungen bestätigt, bei denen eine ausgezeichnete Übereinstimmung sowohl im Trend als auch in absoluten Werten gefunden wurde.

Das Vorhandensein von Sekundärströmungspfaden im Berechnungsmodell und die zeitaufgelöste Simulation erhöhen die numerische Modellgrösse und die erforderlichen Rechenressourcen erheblich. Um die Notwendigkeit dessen zu untersuchen, wurden zusätzliche Untersuchungen über den Einfluss von Kavitäten und zeitaufgelösten Strömungsphänomenen auf die Stufeneffizienz durchgeführt. Die Ergebnisse haben gezeigt, dass die Wirkung von Kavitäten und die instationäre Wechselwirkung mit dem Hauptströmungspfad bei weitem nicht unerheblich ist und eine wichtige Rolle bei der Stärke und Entwicklung von Sekundärströmungen spielen. Daher ist die Schlussfolgerung, dass

für gezielte Leistungssteigerungen durch verbessertes Sekundärströmungsmanagement, Kavitäten sowie zeitaufgelöste Strömungseffekte in das Berechnungsmodell miteinbezogen werden sollten.

Die optimierte Rotorgeometrie wurde zur Herstellung in Auftrag gegeben und wird in naher Zukunft experimentell getestet um die numerischen Vorhersagen zu bestätigen.



# List of Contents

<b>ACKNOWLEDGMENTS .....</b>	<b>V</b>
<b>ABSTRACT .....</b>	<b>VII</b>
<b>ZUSAMMENFASSUNG .....</b>	<b>X</b>
<b>LIST OF CONTENTS .....</b>	<b>XV</b>
<b>1 INTRODUCTION .....</b>	<b>1</b>
1.1 Motivation .....	1
1.2 Theoretical background on the operation of steam turbines ..	5
1.2.1 Inter-blade row interaction at the last stage under sonic and supersonic flow conditions .....	5
1.2.2 Secondary flow structures.....	8
1.2.3 Non-axisymmetric end wall contouring.....	11
1.2.4 Shrouded configurations and labyrinth seals .....	12
1.3 Optimization methods in turbomachinery .....	15
1.3.1 Definition of optimization.....	15
1.3.2 Artificial Neural Network.....	18
1.3.3 Genetic Algorithm.....	19
1.3.4 State-of-the-art optimization studies for turbomachinery	20
1.4 Research objectives.....	23
1.5 Thesis outline .....	25
<b>2 NUMERICAL METHODS .....</b>	<b>27</b>
2.1 Mesh generation .....	27
2.2 Compressible URANS solver “MULTI3” .....	30
2.2.1 Fourth order Runge Kutta scheme .....	31
2.2.2 Preconditioning .....	33
2.2.3 Adaptation of solver for equilibrium wet steam conditions 44	
2.2.4 Convergence assessment of unsteady simulations .....	47
2.2.5 GPU acceleration and parallelization approach.....	57
2.3 Optimization method.....	59
2.3.1 Endwall parametrization .....	61
2.3.2 Optimization algorithm.....	63
2.3.3 Database generation.....	64
2.3.4 The approximate model .....	65
<b>3 EXPERIMENTAL METHODS .....</b>	<b>69</b>
3.1 Steam turbine facility at MHPS .....	69
3.2 Axial turbine facility “LISA” .....	70

<b>4 UNSTEADY FLOW MECHANISMS IN A TRANSONIC LOW PRESSURE STEAM TURBINE.....</b>	<b>75</b>
4.1 Computational setup .....	75
4.1.1 Geometry and computational domain.....	75
4.1.2 Boundary conditions and simulation settings .....	78
4.1.3 Convergence monitoring .....	79
4.2 Results and discussion.....	81
4.2.1 Validation of numerical model .....	81
4.2.2 Unsteady bow shock wave interaction with stator.....	87
4.2.3 Effect of axial distance of L-0 rotor leading edge from upstream stator on the shock intensity .....	92
4.2.4 Unsteady bow shock wave interaction with L-0 rotor cavity path.....	94
4.2.5 Entropy generation in L-0 stage.....	98
4.3 Summary and conclusions.....	101
<b>5 TOWARDS UNSTEADY OPTIMIZATION FOR TURBOMACHINERY APPLICATIONS.....</b>	<b>105</b>
5.1 Computational setup .....	105
5.1.1 Geometry and computational domain.....	106
5.1.2 Boundary conditions and initial guess .....	108
5.1.3 Simulation settings.....	110
5.2 Automated, basic post-processing.....	110
5.3 Initial guess of simulation.....	111
5.4 Unsteady convergence monitoring.....	111
5.4.1 Global flow field.....	112
5.4.2 Local flow field .....	116
5.4.3 Convergence validation with experiments .....	119
5.5 Convergence acceleration of unsteady simulations.....	123
5.6 Summary and conclusions.....	126
<b>6 UNSTEADY OPTIMIZATION OF PROFILED ROTOR HUB ENDWALL .....</b>	<b>130</b>
6.1 Methodology.....	130
6.2 Computational Setup.....	132
6.2.1 Geometry and computational domain.....	132
6.2.2 Simulation settings.....	134
6.2.3 Boundary conditions .....	134
6.2.4 Optimization setup .....	136
6.3 Results and discussion.....	141
6.3.1 Validation of numerical model .....	141
6.3.2 Optimized end wall geometry .....	144
6.3.3 Upstream effects at S2 stator exit.....	146

6.3.4	Influence on cavity exit flow.....	148
6.3.5	Profiled hub end wall effects at R2 rotor exit.....	151
6.3.6	Rotor hub end wall effect on secondary flow evolution, blade loading and stage efficiency.....	157
6.3.7	Justification of choice for presence of cavities and unsteady simulations.....	162
6.4	Summary and conclusions .....	173
<b>7</b>	<b>SUMMARY AND CONCLUSIONS .....</b>	<b>176</b>
7.1	Summary.....	176
7.2	Concluding remarks.....	181
7.3	Suggestions for future work .....	183
<b>APPENDIX</b>	<b>.....</b>	<b>186</b>
	References .....	187
	Nomenclature .....	197
	List of Figures .....	200
	List of Tables.....	205
	List of Publications .....	207
	Curriculum Vitae .....	209





# 1 Introduction

## 1.1 Motivation

In the past decades the world population has grown at a fast pace alongside the global energetic needs. This is especially true for emerging economies such as the BRIC countries (Brazil, Russia, India and China). According to the International Energy Agency (IEA), the total world energy demand and economic growth are highly correlated and as a matter of fact, the actual and future needs in energy demand exhibit a positive rate. In the last two decades this is more prominent for China and India, since they have extended their energy demand, especially in transport and industry.

Primary energy consumption by fuel

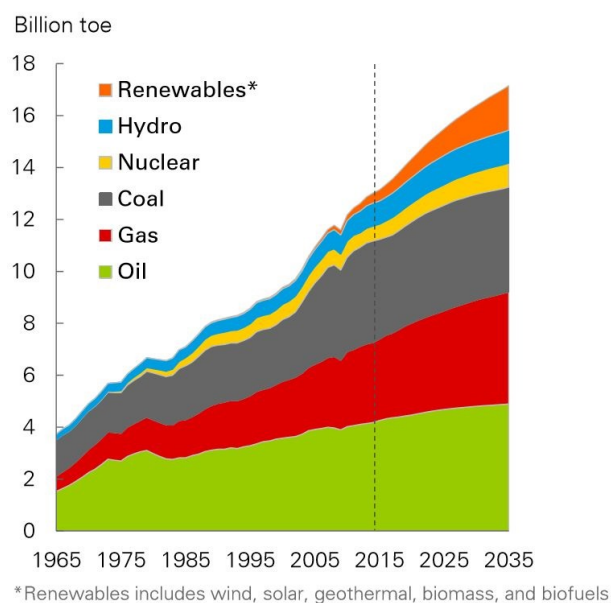


Figure 1–1: Energy by Fuel [1]

Energy consumption by region

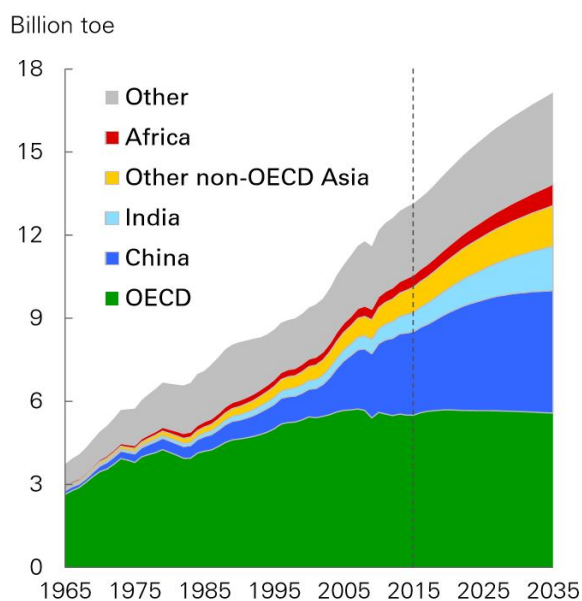


Figure 1–2: Energy by Region [1]

Turbomachinery is a major player in the crucial fields of industry and transportation. It is used in almost all power production processes (steam turbines, gas turbines, hydroplants, etc.) and its contribution to the transportation sector (aviation & marine) is also considerable.

Turbomachinery describes machines that are responsible for the energy transfer between a rotor and a fluid flow and includes both turbines and compressors. While turbines transform the energy of the fluid into useful work, a compressor transfers energy from a rotor to a fluid. In this research project the focus will be on turbines, more specifically in the study of the improvement of performance of axial steam turbines. In an axial turbine the working fluid flows inside an annular duct. The working fluid moves through several sets of blades, which are responsible to change its angular momentum. The blades are grouped in two different categories according to their ability to rotate or not around the central axis. If the blades rotate around the central axis they are denominated as rotor, if the blades are not able to rotate around the central axis they are called stators. Groups of stators and rotors are known as stages. The first element of the stage is the stator and it accelerates the flow. After the flow leaves the stator it encounters the rotor, which redirects and reduces the angular momentum of the working fluid, extracting work from the fluid. The temperature and static pressure of the fluid is reduced over the stator and rotor, with some exceptions (e.g. impulse turbines).

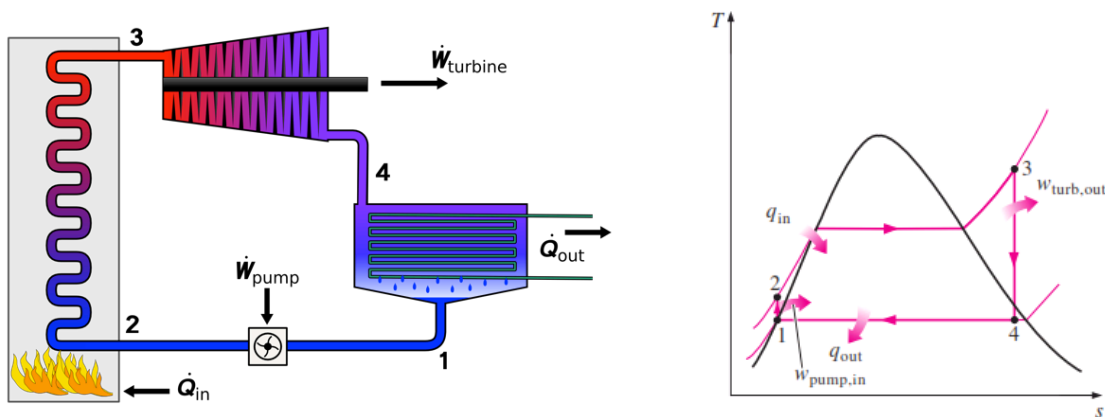


Figure 1-3: Schematic of Rankine cycle (left) with the respective temperature (T)-entropy (s) diagram of a steam turbine (right) [2]

Turbomachinery operation is based on the Rankine cycle, as shown in Figure 1-3. Rankine cycle converts heat into work. Steam is generated in the boiler (2-3) by providing energy to water, which is then enters the high pressure turbine section (3-4) and expands generating work on a rotating shaft. As the steam expands in the

turbine, it loses energy and changes its phase back to water status in the condenser (4-1).

Steam turbines currently hold the largest share in the energy market, which highlights the importance of having robust and efficient machines. Unlike gas turbines, which rely mainly on fossil fuels, steam turbines can operate with a flow of steam, regardless how the steam is produced. This is the reason that they are also used in nuclear power plants, in geothermal power and concentrated solar power applications.

High capacity power plants use different stages of steam turbines, such as high-pressure turbine, intermediate-pressure turbine and low-pressure turbine, as it is shown in Figure 1–5.

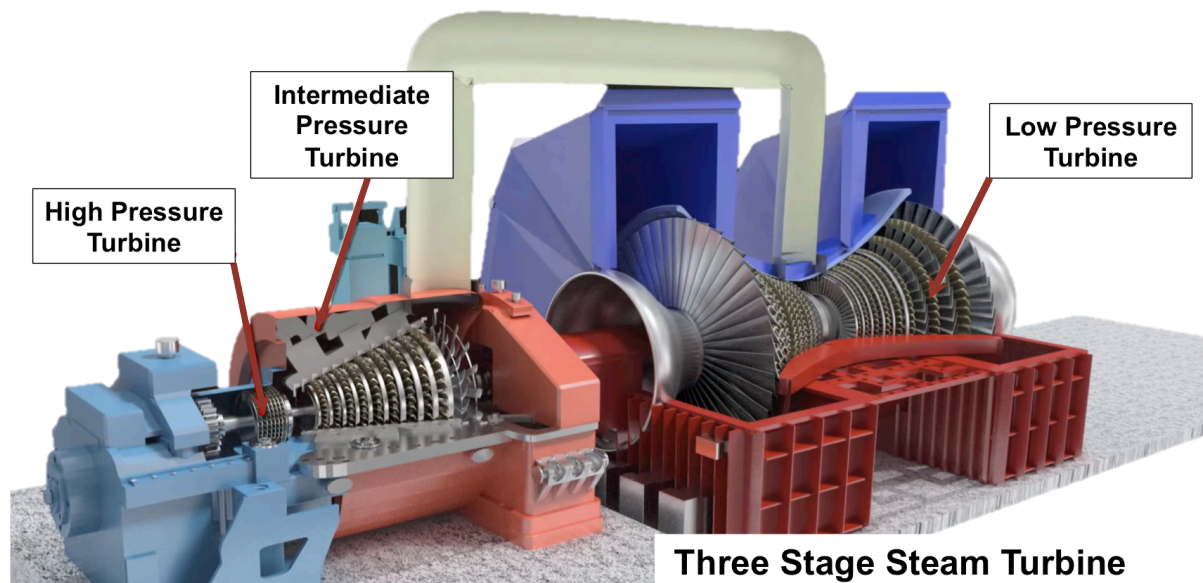


Figure 1–4: Different stages of a steam turbine [3]

The design of each stage and the underlying flow mechanisms are drastically different. On one hand, first stages of the turbine have low aspect ratio blades and large cavities, therefore secondary flows and leakage losses are of interest. The penetration of renewable energies in the market requires modern steam turbines to have operational flexibility. In order to accommodate for the thermal expansion of the machine under a wide range of thermal loads, steam turbines are equipped with large cavity paths, which increase the effect of leakage flows on performance. On the other hand, in the last stages of the low-pressure steam turbine, blades have very

high aspect ratio and secondary losses are of lower significance compared to profile and shock losses.

Recent advancements in steam turbines technology have led to increased area in the last stages of the turbines, with blade lengths reaching even 60 inches [4], in order to satisfy the need for higher power output. However, the design is quite challenging due to the fact that inlet flow conditions close to tip are supersonic in relative frame of reference. This leads to a generation of a bow shock wave upstream of the rotor's leading edge [5] that, if not given sufficient space to decay, will interact with the upstream stator blade row, causing high flow unsteadiness or even potential boundary layer separation on the stator and increased kinetic energy losses [6].

Taking all these into consideration, the importance for more efficient machines is highlighted. Nowadays, the performance improvement of turbomachinery through traditional methods has reached a plateau, so the state-of-the-art optimization methods make use of computational capabilities available in the present days. Computational Fluid Dynamics (CFD) makes use of the most advanced numerical methods in order to solve and analyze fluid flow problems. As described by Holmes et al [7], CFD is used: (1) to provide *absolute* performance predictions; (2) to provide *relative* performance predictions when comparing design iterations; and (3) to provide designers with a microscope to examine—and thus understand—the flow field with a resolution, and at a cost, not available in an experimental test. However, the knowledge in the field of turbomachinery is so advanced that it is much harder to achieve performance improvements, especially taking into account the uncertainty associated with measurement techniques. Therefore, efforts in research of turbomachinery also need to focus on improvements of accuracy and fidelity of modern numerical tools used during the design process.

## 1.2 Theoretical background on the operation of steam turbines

The research fields related to the current work are briefly reviewed and a number of relevant references are provided for the interested reader.

### 1.2.1 Inter-blade row interaction at the last stage under sonic and supersonic flow conditions

With increasing energy demand on one hand and the large penetration of renewable power in the energy market in the other, steam turbines require a power augmentation. This is achieved by increasing the annulus area of the last stage of the low-pressure steam turbine, leading to higher power output and efficiency. Additionally, the flow is expanded and its practically useless kinetic energy at the exit of the machine is reduced. Steam turbines are already the largest machines of turbomachinery and there is a trend to get even bigger. As a consequence, the rotor blades of the last stage become very long and large pressure gradients appear between hub and tip, due to the large blade height. Figure 1–5 shows the typical profiles of static pressure and Mach number at the inlet and exit of the last rotor. For radial equilibrium to be satisfied, the absolute Mach number at the stator exit decreases progressively from hub towards the tip region, as indicated in Figure 1–5 with  $Ma_1$ . As can be seen, relative Mach number  $Ma_{rel,1}$  close to the tip and absolute Mach number  $Ma_1$  close to the hub are greater than 1, implying supersonic flow conditions. Therefore, it is very difficult to avoid shock waves at these two locations within the last stage.

As explained by Havakechian and Denton in [8], the high Mach number close to the hub is associated with high loading, low degree of reaction and negative exit swirl, which results in strong trailing edge shocks and increased losses. Close to the tip, on the other hand, the high relative Mach number creates supersonic inflow conditions at the rotor inlet and a bow shock wave is formed, which is attached to the rotor leading edge.

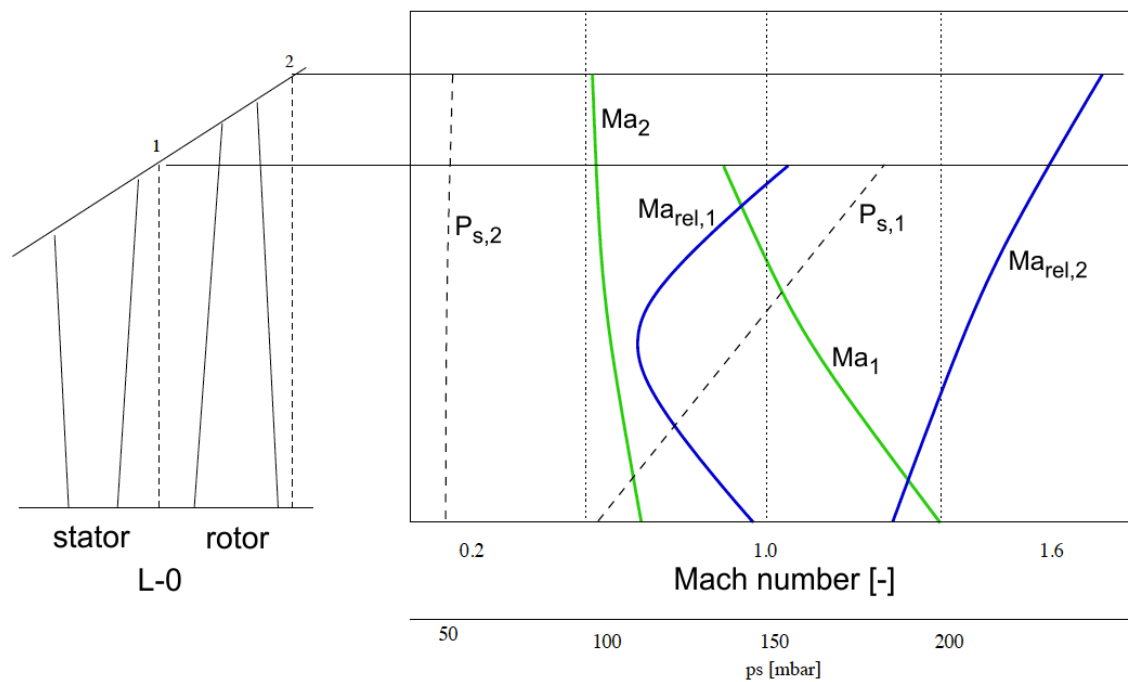


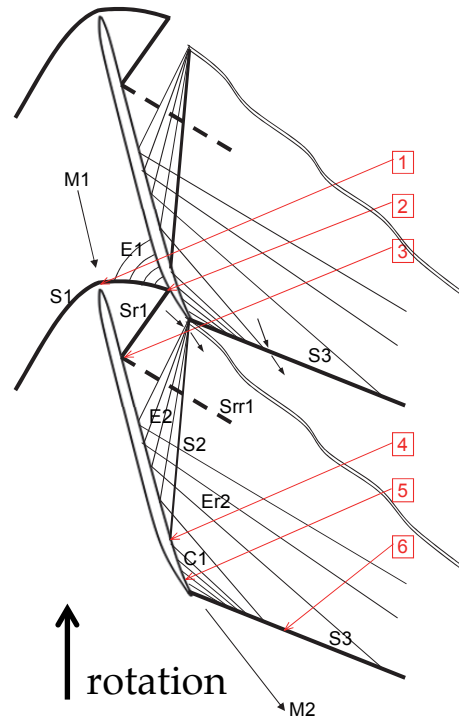
Figure 1-5: Sketch of Mach number and static pressure radial distribution in the last stage of a low-pressure steam turbine [9]

Depending on the rotational speed of the machine, there are cases where both relative inlet and outlet flow of the rotor are supersonic. These supersonic flow conditions lead to generation of strong shock waves, which are associated with high loading and aerodynamic losses. There are mainly six loss mechanisms related to shock waves at the last stage rotor with relative supersonic inlet flow conditions. These were described by Senoo [6] and are presented in Figure 1-6.

Due to blade blockage, the upstream shock wave S1 appears and generates total pressure losses. This shock wave S1 interacts with the boundary layer on the pressure of the following blade and generates the second loss source, labeled with number 2 in Figure 1-6. As the shock wave Sr1 is reflected on the pressure side, it interacts with the suction side of the blade and generates source number 3. Looking at the trailing edge, there are two shock waves, S2 and S3. Shock wave S2 is interacting with the boundary layer on the suction side of the neighbor blade and creates loss source number 4. The fifth loss is caused by the adverse pressure gradient due to the compression waves C1 originated from the concave suction surface. The last mechanism is the total pressure loss of the trailing edge shock wave S3, indicated by number 6 in Figure 1-6,



which is caused by the suction surface flow turning. The largest contribution to losses among all six sources is the sixth one, because the Mach number upstream of shock wave S3 is the highest.



- 1: Attached bow shock at leading edge (S1)
- 2: First shock wave reflection (Sr1) on pressure side
- 3: Second shock wave reflection (Srr1) on suction side
- 4: Trailing edge shock (S2) and reflection on suction side
- 5: Compression waves (C1) due to adverse pressure gradient on the concave suction side
- 6: Trailing edge (S3) shock wave on the suction surface

Figure 1–6: Losses associated to shock waves at the tip region of a supersonic rotor blade profile [6]

An interesting numerical analysis for the design of the last stage with supersonic blade profiles was presented by Stürer et al. in [9]. The modulation of the shock wave at the stator trailing edge at the hub, as well as at the rotor leading edge at tip, was investigated. The interaction of the shock wave with the boundary layers was explained using unsteady CFD results. Regarding the shock at the trailing edge in the hub region, results have shown extremely high unsteady interactions. The suction side branch of the trailing edge shock meets the suction surface of the rotating blade and multiple reflections interact with both boundary layers, suction and pressure side of the rotor passage, causing peak-to-peak fluctuations in the range of 30% of the mean value. On the other hand, their study on

the attached bow shock at the rotor leading edge at the blade tip region, showed reduced levels of unsteadiness. They state that the rotating bow shock is very steady and even weakens to become negligible before it interacts with the upstream stator.

Regarding the last finding, which is also related to the results of the current work, it has to be mentioned that the stator profile is swept forward, as shown in Figure 1–7, in order to increase the axial gap between the stator trailing and the rotor leading edge. It is possible that the weak interaction of the bow shock with the upstream stator is a result of this large axial gap.

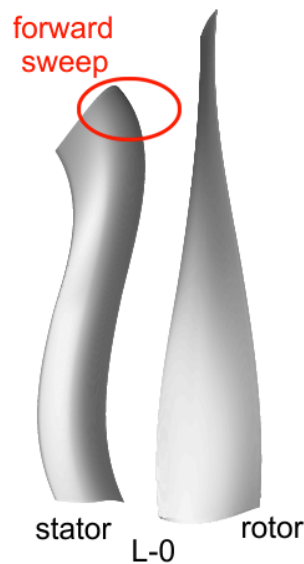


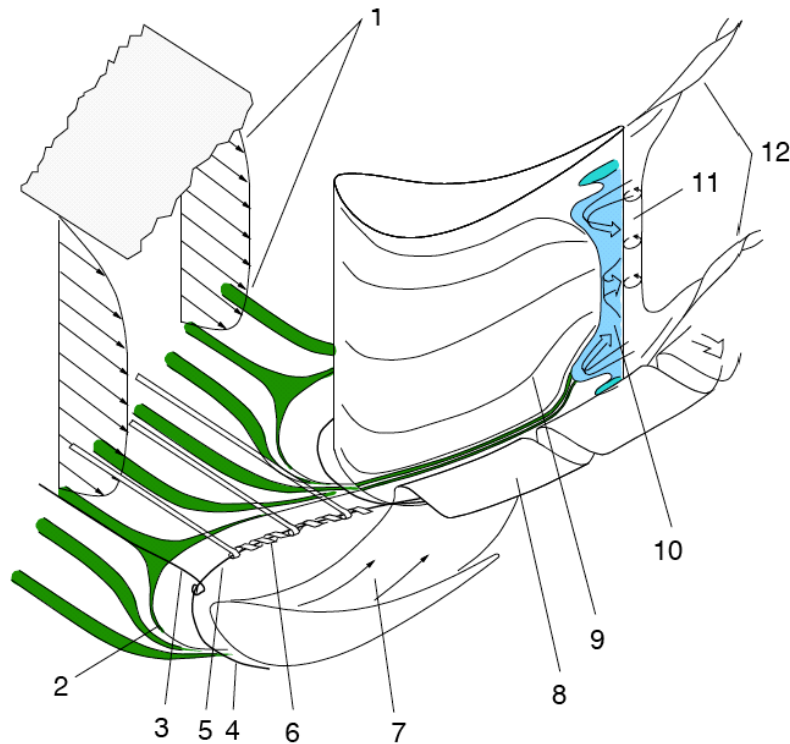
Figure 1–7: Side view of a forward swept stator blade at tip region from the last stage simulated by Stürer et al. [9]

### 1.2.2 Secondary flow structures

Secondary flows are present in all types of turbomachines. These secondary flow features are highly three-dimensional and do not follow the quasi two-dimensional turbine primary flow. They are generated by the redistribution of low momentum fluid within a blade passage. The redistribution occurs due to the pressure field of a turbine blade passage, which causes low momentum fluid to turn on a smaller radius than the main flow, also known as flow underturning. The low momentum fluid is a result of viscous effects during the boundary layer development on the endwalls. Although the appearance of the secondary flows depends on the individual



design of the turbine profiles, some of the features that are typically observed in every turbomachine are summarized in the secondary flow model of Vogt and Zippel [10], as shown in Figure 1–8. There are a few other interesting secondary flow models available in literature, such as the one by Langston [11], Sharma and Butler [12], Goldstein and Spores [13], and Wang et al [14].



- |  |  |
|--|--|
| 1: Inlet boundary layer                        | 7: Cross flow in the passage                 |
| 2: Separation line of the inlet boundary layer | 8: Passage vortex                            |
| 3: Horseshoe vortex, inlet flow                | 9: Motion of the suction side boundary layer |
| 4: Horseshoe vortex (suction side leg)         | 10: Separation with backflow                 |
| 5: Horseshoe vortex (pressure side leg)        | 11: Eddying in the wake                      |
| 6: Rolling up of the inlet boundary layer      | 12: Trailing edge vortices                   |

Figure 1–8: Secondary flow model described in [10]

*Passage vortices:* The profiles of a turbine blade row cause a turning of the incoming flow and generate a pressure gradient across the passage. Under the influence of this pressure gradient, the endwall boundary layer of the inlet flow turns on a smaller radius than the main flow, due to its low momentum. As a consequence, within the passage, an endwall cross-passage flow from the pressure to the suction side of the blade is generated and subsequently rolls up into a passage vortex.

*Horseshoe vortices:* The endwall boundary layer of the incoming flow can be considered to be a layer of tangential vorticity. At the leading edge of a blade profile this boundary layer rolls up into a system of two counter-rotating vortices that pass along each side of the blade leading edge. The pressure side leg of the horseshoe vortex has the same direction of rotation as the passage vortex, whereas the suction side leg of the horseshoe vortex has the counter rotation of the passage vortex. In the pressure side, both vortices merge within the passage and appear as one enhanced vortex downstream of the blade. The suction side leg of the horseshoe vortex stays close to the blade and then travels up the suction surface.

*Corner (Counter) Vortices:* A new highly skewed boundary layer is formed on the endwall downstream of the separation line caused by the pressure side leg of the horseshoe vortex. This strong crossflow impinges on the adjacent blade in the suction side corner of the blade profile and forms a new vortex that rotates counter to the passage vortex. The vortex is located right at the endwall suction side corner and its presence reduces the overturning near the endwalls.

The size and strength of the secondary flows depend on the blade turning, the pitch to chord ratio, the aspect ratio and the inlet vorticity. The importance of the secondary flow structures can be seen in their direct negative impact on the performance of a turbine. Endwall vortex flow is responsible for a loss of lift on a profile and increases the aerodynamic losses. According to Sharma and Butler [12], the aerodynamic loss attributed to secondary flows can be as high as 30-50% of the total aerodynamic losses of a certain blade row. The convection of secondary flow with flow angles that deviate substantially from the design may cause additional losses in downstream blade rows as well. The high impact of secondary flows on the loss generation in a turbine has led to three-dimensional blade designs, in order to minimize these flow structures. The principal design approaches are the blade sweep, blade twist and blade lean angles that alter these secondary flows, as well as the blade loading.

### 1.2.3 Non-axisymmetric end wall contouring

Apart from the three-dimensional blade stacking techniques mentioned above, profiled end-wall contouring has also been successfully applied for secondary flow management and performance improvement. A lot of experience on end wall contouring has been acquired over the past years in Laboratory for Energy Conversion through experimental measurement campaigns in the axial turbine research facility LISA.

Schüpbach [15] experimentally tested an axisymmetric baseline geometry and two different profiled end wall designs in an unshrouded 1.5-stage turbine, typical of a high work turbine. He reported a considerable increase in stage efficiency with end wall contouring for both cases, by 1% and 0.3%, respectively. Additionally, he investigated the effect of purge flow on performance in the presence of end wall contouring. He reported a sensitivity of efficiency to the amount of purge flow and it was found that the two designs have a drop in efficiency by -1.2%/ % and -0.7%/ % per injected massflow percent of purge flow.

Jenny [16] also experimentally investigated two different profiled end wall designs for a shrouded, low pressure turbine with three different purge flow injection rates. The profiled end wall was extended up to the leading edge of the rotor platform, giving it an interesting wavy shape. Both end wall designs lead to an increase of stage efficiency by 0.75% and 1.05%, respectively. Additionally, the end wall designs showed a 30% reduction in sensitivity of efficiency to purge flow. Finally, one of the end wall designs was shown to influence positively the unsteady size and shape of the separation bubble present in the pressure side.

Finally, Regina [17] experimentally quantified the sensitivity of the performance of a 1.5-stage high pressure gas turbine to the amount of purge flow injected, as well as to stage loading. As he reported, end wall contouring increased sensitivity of efficiency to purge flow injection rate but offers improved sensitivity to the variations of stage loading

An interesting case was presented by Torre et al [18] for a low pressure turbine. Traditionally, end wall contouring focused on

controlling the transverse pressure gradient in the blade passage as the key parameter affecting secondary flows. Torre on the contrary, applied endwall contouring with the goal to enhance the suction side leg of the horseshoe vortex. On one hand, more fluid from the inlet endwall boundary layer is contained in the suction side leg, reducing the strength of the pressure side leg. On the other hand, the suction side leg keeps the passage vortex away from the blade suction surface, delaying its development. Experimental data showed a 72% reduction of SKEH and a 20% of the mixed-out endwall losses.

There are numerous other studies on end wall contouring in open literature. A number of publications are given for the interested reader [19]–[28].

#### **1.2.4 Shrouded configurations and labyrinth seals**

Parts of turbomachinery are split in stationary and rotating, therefore a gap is inevitably required between them. Rotor blades can be either unshrouded, having a tip gap from the casing, or be shrouded, creating a labyrinth seal. Goal of these labyrinth seals is to minimize leakage flow and their associated losses. Leakage flow is one of the main sources of aerodynamic losses. For effective sealing, the minimum gap possible is desired between stationary and rotating parts. However, mechanical concerns and thermal expansion of materials set certain limits on minimum feasible gap. Typically, it is about 1% of the blade height.

It is well known that shrouded configurations have better sealing and higher efficiency compared to unshrouded. However, the extra weight and the centrifugal forces on the blade can become critical and limit the life expectancy of the components. For this reason, their use is limited mainly for power generation, such as in steam turbines, since weight is not a critical issue and temperature and rotational speeds are much lower compared to gas turbines in a jet engine. Figure 1-9 depicts a shrouded and an unshrouded turbine blade.

Cavities allow the relative motion between stationary and rotating parts of the machines. There are several different designs of a

labyrinth seal but they all have an inlet cavity, an outlet cavity and some closed cavities in between.

Due the extreme thermal loads that steam turbines undertake from cold state to operating conditions, these cavities need to be large enough to allow the thermal expansion of the machine. Indicatively, the gap of inlet or exit cavity can be more than 40% of the blade's axial chord. Figure 1-10 shows examples of different cavity configurations.

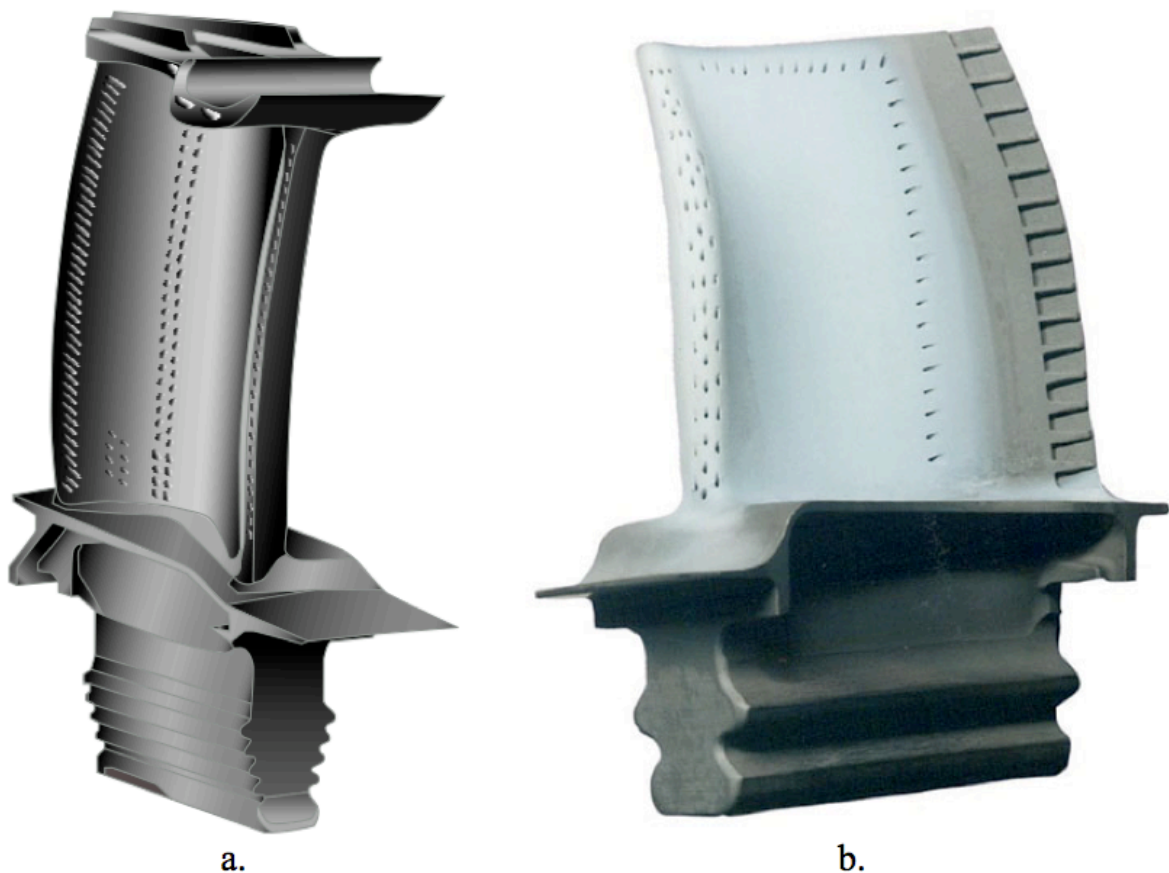


Figure 1-9: (a) Shrouded and (b) unshrouded turbine blade [29]

Although labyrinth seals are an effective way to reduce leakage losses, the mass flow by-passing the rotor and entering the cavities means less work production on the rotor. It is therefore important, not only to quantify the amount of the leakage mass flow, but also find ways to reduce it. It is very interesting to mention that this has been under investigation even from the early stages of turbomachinery and was studied by Egli [30] already in 1935 and Traupel [31] in 1966. Egli and Traupel presented a theoretical and

experimental approach, respectively, attempting to quantify leakage mass flow through cavities. Barmpalias [29] experimentally tested a large number of different rotor inlet cavity designs and reported increase in efficiency of up to 1.6%.

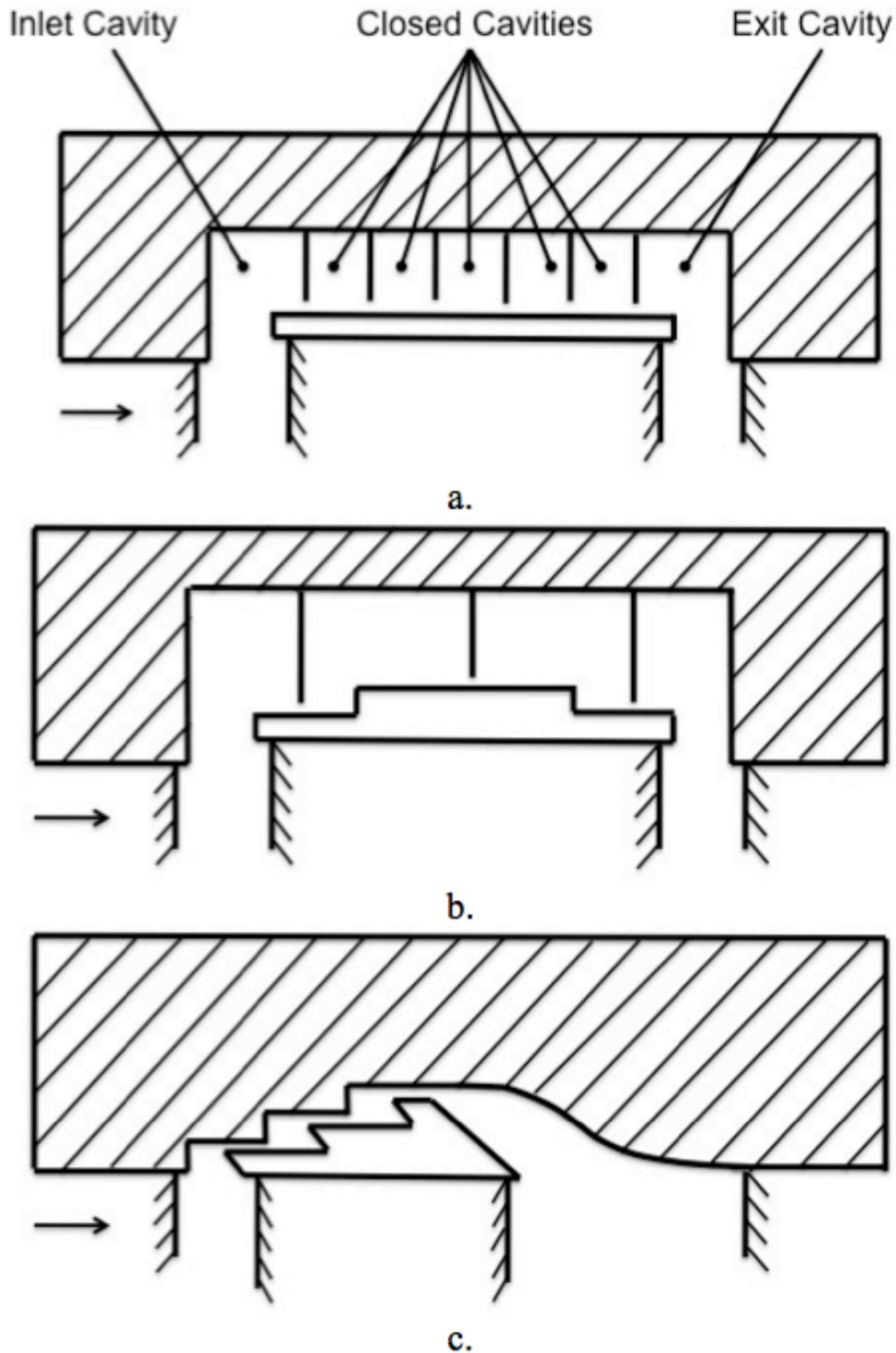


Figure 1-10: Examples of labyrinth seal configurations; look through (a), stepped labyrinth (b), and gas turbine (c) [29]

## 1.3 Optimization methods in turbomachinery

### 1.3.1 Definition of optimization

Optimization is defined by Rao [32] as the act of obtaining the best result under given circumstances. In an optimization process, the goal is to minimize the required efforts or to maximize a desired benefit. These can be described as a function of different decision variables [32]. Therefore, an optimization process can be defined as the process to find the minimum or maximum of a certain function. During a design process, certain requirements and restrictions need to be satisfied. These are called design constraints and limit the freedom of the optimization, in which an optimum solution can be found. These constraints are of mechanical, aerodynamic or manufacturing nature. Usually, there is more than one design that respects the constraints but their solution may not have the same quality. In order to measure the quality of the different solutions, the concept of an objective function is used. The objective of the optimization process is to find the values of a set of variables, which minimize the objective function, while remaining within the allowable design space defined by the constraints. The objective function and the constraints of the problem can be either linear or non-linear, which may require different optimization methods for solving it.

Figure 1-11 presents a schematic classification of the different design methods applied in turbomachinery. All the different approaches can be distinguished between inverse design methods and direct design methods. Inverse design methods can offer good designs with low computational cost and, therefore, have been used often in turbomachinery design problems [33]–[37]. However, this approach requires the specification of a target flow field, which highly depends on the designer's experience.

Direct methods are further classified in gradient-based methods and stochastic methods. Gradient-based methods require the derivatives of the objective function with respect to each design variable and are mainly split in finite-difference [38] and adjoint methods. The most time-consuming part in these approaches is the calculation of derivatives, something that the adjoint method can provide with low cost, independently of the number of design parameters. This is the reason why it is one of the most popular

methods in turbomachinery applications [39]–[48] , despite their increased complexity.

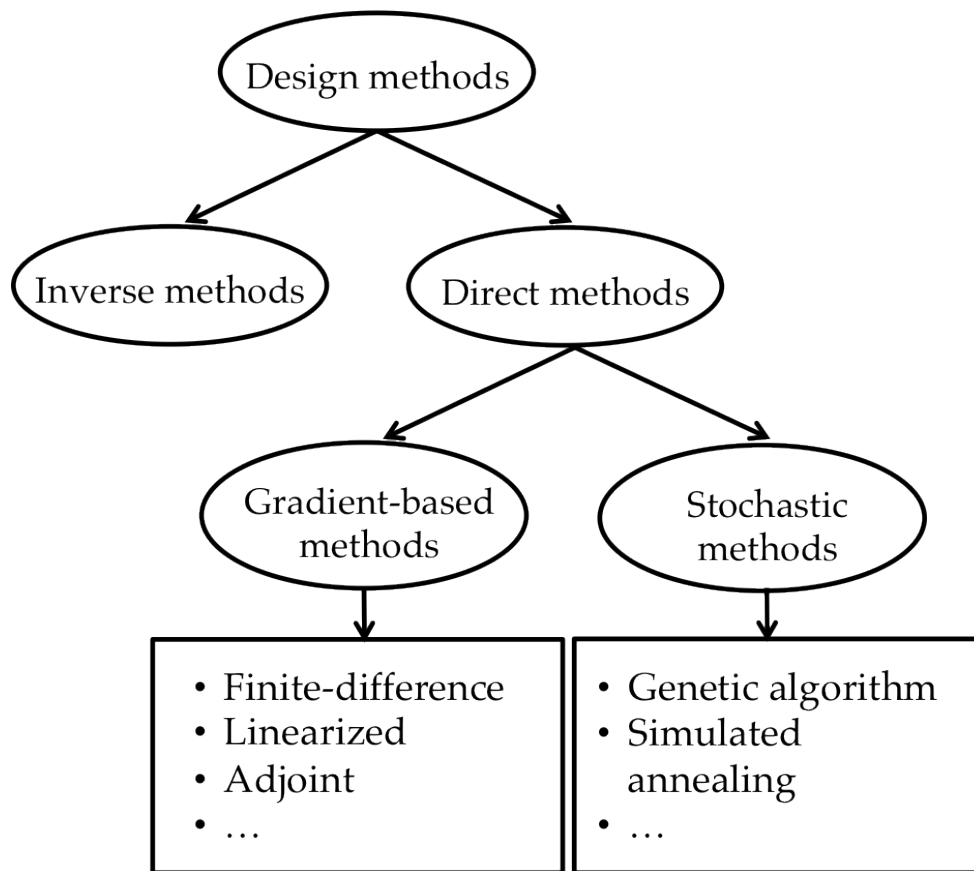


Figure 1-11: Classification of design methods

The major disadvantage of gradient-based methods is that they highly depend on the initial starting point. In cases where the problem is non-linear and multimodal, i.e. they may have several local minima and maxima, they can easily be trapped in a local minimum. On the other hand, stochastic methods do not depend on derivatives but rather need only the values of an objective function. This allows them to find the global optimum but comes with a very high computational cost. Such methods are the genetic algorithm and the simulated annealing and may require large number of function evaluations during the optimization process. Function evaluations for turbomachinery applications mean CFD calculations, which makes their use in routine designs prohibitively expensive. In the past several years, stochastic methods have been coupled with approximate models for fast function evaluations to reduce their computational cost, which has increased their popularity in industrial applications. Numeca's turbomachinery



design software Design3D combines the genetic algorithm with an artificial neural network to reduce the required number of function evaluations and allow to benefit from the advantages of a stochastic method but in a time-efficient manner. There are several publications in the open literature that utilize it for a wide range of turbomachinery applications, such as blade optimization [49]–[53], end wall contouring [54]–[59] and other cases [60]–[69], confirming its validity as a valuable turbomachinery design tool.

In an optimization problem, the objective function, as well as the constraints, can be non-linear and often there is no analytical formulation of the objective function with respect to the design variables. Therefore, the concept of a penalty term is introduced to solve the optimization problem. The objective function of the optimization problem is transformed from a non-linear, constrained function to a linear, unconstrained function using penalty terms. The penalty terms increase whenever a constraint is not respected and they are constructed in the following way:

$$P = W \cdot \left( \frac{|Q_{imp} - Q|}{Q_{ref}} \right)^k \quad \text{Eq. 1-1}$$

where  $Q_{imp}$  is the value of the imposed quantity,  $Q$  is the computed quantity and  $Q_{ref}$  is a reference value used to non-dimensionalize the penalty term. The term  $k$  is the penalty term exponent and usually it has the value 2. The variable  $W$  is the weight factor, which has the objective of scaling up or down the influence of a penalty term in the global objective function [70]. Finally, the objective function can be described as:

$$\text{Objective Function} = \sum P \quad \text{Eq. 1-2}$$

It is possible to set different types of penalties:

- **Minimum Allowable Value** penalizes geometries that lead to objective function values lower than the imposed one
- **Maximum Allowable Value** penalizes geometries that lead to objective function values higher than the imposed one
- **Equality Value** penalizes geometries that lead to objective function values different than the imposed one

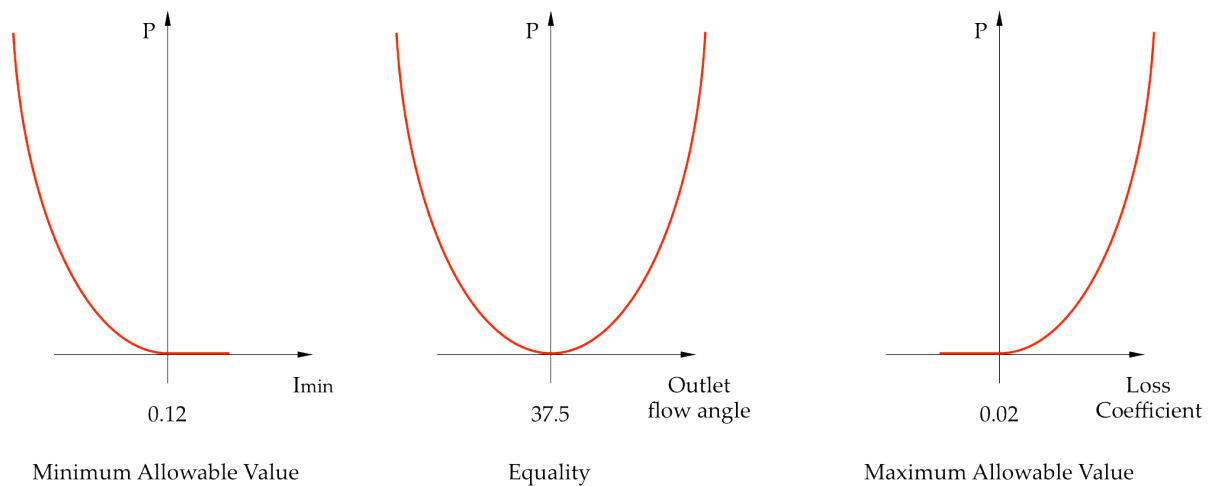


Figure 1-12: Penalty types [70]

The two main components of the presented methodology, the genetic algorithm and the artificial neural networks, are described in more detail in following sections.

### 1.3.2 Artificial Neural Network

Artificial Neural Networks are computing systems inspired by the functioning of biological neural networks. ANN are non-linear models, which can be used to map a function between different inputs and outputs. As it is very nicely described by Demeulenaere [51], ANN can be thought as a powerful interpolator. Nodes are the elementary processing units that constitute an ANN and they are connected between the different layers with different factors, called connection weights. Typically an ANN is constituted by several layers; a first input layer, one or more hidden layers and a final layer of output nodes [71]. Figure 1-13 shows an example of an ANN architecture. In turbomachinery applications, the input variables can be for example geometrical or flow parameters and the output could be performance or flow angles. Once the ANN is trained, it is able to predict the output values for a new input set.

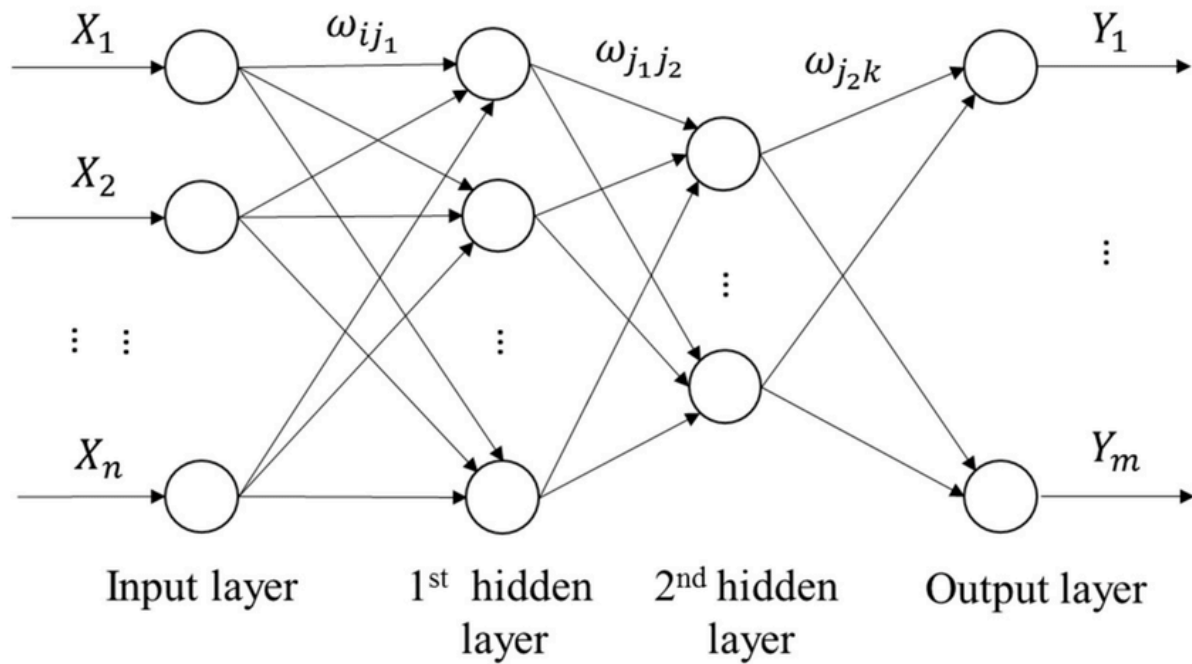


Figure 1-13: Architecture of an ANN [72]

### 1.3.3 Genetic Algorithm

The Genetic Algorithms were invented in the 1960s by John Holland and developed at the University of Michigan by Holland, his students and colleagues [73]. The GA is a metaheuristic procedure based on the biological concept of natural selection. The algorithm reproduces the natural selection behavior in order to achieve the best solution to the problem it is trying to optimize. In the following paragraph a brief description of how the GAs work will be presented.

The first step in the optimization through the use of GA is to randomly generate an initial population in the entire design space. From this initial database, pairs of individuals are selected based on their performance (objective function value). The individuals with the best performance (fittest individuals) have a longer life span and will reproduce while individuals, which have worst performances will die before reproducing. The fittest pairs of individuals undergo a reproduction cycle in order to generate the new population. The new individuals are called children and they will replace their parents. As the procedure goes on, the stronger individuals will combine with other fit individuals and their traits

will continue to pass between the new generations resulting in children who will have a better performance [70], [73], [74].

### 1.3.4 State-of-the-art optimization studies for turbomachinery

Among all studies of optimization problems in turbomachinery, there are a few that stand out for their novelty or for the important lessons that can be derived and will be presented briefly in this section.

The need for power augmentation of steam turbines leads to increased flow area and very long blades in the last stage of the low-pressure turbine and research is currently focused on optimizing such blades, both in terms of aerodynamic and mechanical performance. Li et al [75] presented an optimization system for multidisciplinary and multi-objective optimization of long blades. Goal was the optimization of the blades for maximum efficiency and minimization of maximum Von Mises stresses in the blade and three different designs were successfully identified. Similarly, Yin et al [76] recently presented an aerodynamic optimization of the last stage long blades using a Differential Evolution optimization algorithm and achieved an increase in efficiency by 1.35%. The optimization algorithm was previously developed and presented by Song et al [77] and was applied in a transonic turbine stage. All these studies are based on steady state solutions. It is very interesting to mention that Song [77] recognizes the great influence of unsteady stator-rotor interaction on the turbine stage performance. Nevertheless, at that time, he describes an optimization based on unsteady approach as unrealistic, due to the high computational cost. However, modern steam turbines have such long blades that create supersonic relative inflow conditions close to the rotor tip [4], [78]. The unsteady interaction of the bow shock wave with the upstream stator can only be described and optimized through time-accurate computations.

High-pressure turbines on the other hand have blades with much smaller aspect ratio and secondary flows and tip leakages have a higher contribution on loss generation. Due to the extreme thermal expansion of the rotor shaft from cold state to operating conditions, large cavity paths are required, with axial gaps that can reach up to 40% of stator axial chord. Rim seal cavity flows in gas turbines have

a similar interaction with secondary losses and various studies have focused on managing leakage flows with endwall contouring.

Shuzhen Hu et al [79] investigated the effect of rim seal cavities on total pressure losses by optimizing the rotor hub end wall. When the end wall was optimized without rim seal cavities, a reduction of 10% in total pressure losses was achieved. However, the benefit was reduced by more than 5 times, to only 1.63%, when rim seal cavity was included in the model. Including the cavity and re-contouring the end wall reduced the losses again by 9.8% compared to baseline case.

In a continuation of the previous study, Tang et al [80] applied end wall contouring on a high-pressure turbine and concluded that the rim seal flow is the main source of the hub passage vortex and can change the secondary flow structures considerably, therefore cavities should be included in the computational model.

In a different study, Lott et al [81] optimized the rotor hub end wall of a high pressure turbine for increased performance and rim seal effectiveness. The results of the steady state optimization, including rim seal cavities, were verified with an unsteady simulation. While steady results predicted 0.53% increase in efficiency, unsteady simulations showed a decrease of 0.04%. This was attributed to unsteady flow features observed in the main flow.

Finally, Shahpar et al [82] presented an automatic optimization of non-axisymmetric end walls for a high pressure turbine stage of a modern large civil aero-engine. It was shown that the end wall contouring significantly affected the path in which the leakage flow vortex enters the main passage.

Summarizing these studies, it can be concluded that for higher improvements to be achieved, higher-fidelity computational models are of paramount importance. It is encouraging for the advance in technology that more and more studies start including cavity paths in the numerical models to account for leakage flows. However, unsteadiness is still neglected due to the increased computational cost. Only very recently, some attempts on an unsteady optimization have been published but they are all based on adjoint method and are only for isolated, two-dimensional airfoils [43], [44],

[47] or, at best, for 2D multi-stage turbomachinery [44]. As good as they are, they are still only simplified cases and far from a real configuration. The work of the current doctoral thesis will try to fill this gap found in literature, which leads to the research objectives presented in the next section.

## 1.4 Research objectives

The field of turbomachinery has been a subject of research for many decades. While new techniques, both experimental and numerical, are continuously developed and employed to assist in research, the goal has always been the same: pushing the limits for higher efficiency and improved performance. For many decades, advances in turbomachinery were achieved solely through experimental work, trial and error, and experience of the designers, all building into knowledge and understanding of the flow phenomena present into turbomachines. With the advances in computer science, CFD and optimization methods have become a valuable toolset for designers to achieve more efficient machines. However, the research in the field is already so highly developed and advanced that is getting more and more difficult to achieve higher efficiencies, to the point where gains of even less than 0.1% are still an accomplishment and is welcomed by the turbomachinery community. Yet, efficiency gains of that order are often difficult to measure considering the involved measurement uncertainty, without even mentioning the cost of measurement campaigns. Therefore, higher fidelity of numerical models and increased accuracy of predictions are of paramount importance.

Through the conducted literature review, it has been seen that in the majority of available studies, it was necessary to make some simplifications in the numerical model to reduce drastically the required computational cost involved in the optimization. The reason for that is of course because optimizations using genetic algorithms are still a computationally expensive process, even when coupled with an ANN for reduced number of function evaluations. It was observed that these simplifications could be grouped and described as following:

- **Single-passage:** Many of the studies are performed on single-row configurations. Unfortunately, the predicted gains are reduced [57] or even lead to decreased performance [59] when the full stage environment was considered.
- **Absence of cavities:** Geometrical features such as rim seal cavities with purge flow in gas turbines or large labyrinth cavities in steam turbines, are excluded from the computational model, due to their highly complex geometries, the increase in mesh size and finally in computational cost. However, these

leakage flows and their interaction with the secondary flows, can have a great impact on the stage performance [83], [84].

- **Steady state:** Results are based on steady state solutions. However, predictions based on steady state optimizations can not always be verified when assessed with an unsteady simulation [48], [81].

Eventually, they all converge to one common factor and that is unsteadiness. Whether it is shock wave patterns in transonic rotors or cavity leakage flow interacting with the blades and secondary flows, they are all inherent unsteady phenomena present in the flow field and they need to be taken into account during the optimization processes, if better machines are to be achieved.

Considering all points discussed above, the research objective of the current doctoral thesis is to propose a design methodology for performance improvement of modern steam turbines through geometrical modifications using high fidelity unsteady CFD, while taking into consideration the unsteady flow mechanisms and their impact on loss generation and efficiency. More specifically:

- Suggest improvements for a modern transonic low-pressure steam turbine with supersonic airfoils near the tip region.
- Provide a detailed explanation of the unsteady stator-rotor interaction in the presence of a bow shock wave and its interaction with the rotor tip cavity, while taking into account multistage effects and tip leakage flows, in wet steam flow conditions.
- Perform an unsteady optimization of a typical geometry of a high-pressure steam turbine for improved stage efficiency. Goal is to optimize a non-axisymmetric end wall geometry of the rotor hub end wall, while including real tip and hub cavity geometries. Additionally, unsteady inflow boundary conditions are used at stage inlet to account for multistage effects, while effectively reducing computational cost.
- Assess possibilities and limitations of state-of-the-art numerical models and optimization methods by manufacturing and testing the resulting optimized geometry to validate numerical predictions
- Suggest ways to expand the proposed optimization methodology to be applicable to the whole range of turbomachinery.



## 1.5 Thesis outline

**Chapter 1** has presented an introduction for this work and the motivation behind it, a short literature review related to the field of low- and high-pressure steam turbines and has revealed topics that are not yet well described, thus leading to the research objectives of the current work.

**Chapter 2** describes the numerical tools that were used during the course of this numerical study. More specifically, it introduces the in-house developed unsteady RANS solver “MULTI3”, which was used for all numerical simulations. Following, a description of the numerical models that were implemented before and during the course of this work for the successful achievement of the research objectives is provided. Finally, optimization methodology and the used commercial software are presented, including a mesh generator, a tool for turbomachinery geometry parameterization and the optimization package.

**Chapter 3** gives a brief description of the two axial turbine facilities, on which measurement have been conducted for the low- and high-pressure steam turbine cases, respectively. The probes that were used during measurements are also introduced.

**Chapter 4** addresses the unsteady flow mechanisms in the last stage of a transonic low-pressure steam turbine, with supersonic airfoils near the tip of the rotor blade. Multistage effects and tip leakage flows in the last stage of the turbine are investigated and insight on the unsteady stator-rotor flow interaction in the presence of a bow-shock wave is provided. Numerical results are extensively compared and validated with available experimental data.

**Chapter 5** describes the preparation that was necessary for successfully performing an expensive unsteady optimization by reducing required computational cost. The numerical schemes that were implemented are described and some guidelines are provided as a future reference before a similar optimization case is initiated.

**Chapter 6** presents the resulting non-axisymmetric end wall geometry of a fully three-dimensional unsteady optimization, in the presence of hub and tip cavity leakage flows. The effect of end wall

contouring on stage performance and loss generation is discussed in detail. Numerical results for the baseline case with unsteady inflow boundary conditions are extensively compared and validated with experimental data. Additionally, an explanation of the efficiency gain given by the optimization is provided. Finally, the effect of cavities and flow unsteadiness in performance predictions is investigated.

**Chapter 7** summarizes and concludes the main outcomes of the current research work. Additionally, suggestions for future work and potential benefits of the suggested methodology are presented, for successful application in a wide range of turbomachinery configurations.

## 2 Numerical Methods

In this numerical work, a set of in-house developed and commercial tools has been used. LEC's CFD toolset consists of the following tools:

- Commercial toolset by NUMECA including:
  - Mesh generator tools "AutoGrid5" and "IGG".
  - Geometry parametric modeler "Autoblade"
  - Design optimization tool "FINE/Design3d".
- Compressible URANS solver "MULTI3".
- Commercial post-processing tools such as "Tecplot".

### 2.1 Mesh generation

The grid generation procedure was performed using AutoGrid and IGG from Numeca International. AutoGrid is a fully automatic grid generator for turbomachinery applications. Due to its features, AutoGrid allows the grid generation for a large array of rotating machinery (e.g Turbines, Compressors, Axial or Centrifugal turbomachinery, single or multistage turbomachinery), including easy meshing of cavity flow paths and sealings. IGG is also a meshing software from Numeca International which has the ability to create 2D and 3D shapes, as well as multi-block structured grids on 2D and 3D geometries [70].

The original grid for each case is created in AutoGrid by meshing the blade passages and their cavity flow paths separately using a multi-block strategy. Then, the mesh is slightly adjusted to fit the requirements of the in-house pre-processing tools and the solver. The final mesh needs to have fully matching interfaces, both between the blocks and row interfaces, in order to eliminate interpolation errors, which may lead to considerable loss of accuracy at the regions where highly unsteady phenomena take place. These adjustments are performed on IGG and include changing the block orientation, splitting and/or merging blocks in the flow domain. But the most important change to the original mesh is related to high node clustering and their propagation inside the main flow domain, when cavity flow paths are included in the computational model.

Figure 2-1 shows such an example of a single turbine stage with stator hub cavity and rotor tip cavity. As it is shown, an artificial shock is created in the cavity exit close to the hub. This is purely numerical and completely unphysical. The result of this is higher temperature and lower efficiency; hence the accuracy of the computation is severely deteriorated. The reason behind it is that smaller cells need more subiterations for the flow to develop properly compared to bigger cells. That small region defines the minimum number of subiterations needed for each physical timestep of the unsteady simulation. The issue can be resolved by increasing the number of subiterations for each timestep. However, this creates a bottleneck that can increase the computational cost by several times. Instead, the way to solve this is to simply relax this high clustering of those nodes as can be seen in Figure 2-2.

Both AutoGrid and IGG have an enormous advantage for the optimization process since they provide the user with the option of working with meshing templates and scripts, i.e. define mesh properties such as grid distribution and apply them to other configurations. Since in the optimization procedure a new geometry modification will be performed in each iteration, the use of templates and meshing scripts becomes extremely useful. Both options fundamentally require that the reference and modified geometries keep the same topology. This means that the reference and the modified geometries have the same surfaces, organized in the same way, but with different shapes. This assumption is completely justified in a design concept, where the shape of the geometry should be modified to optimize some flow features [70].

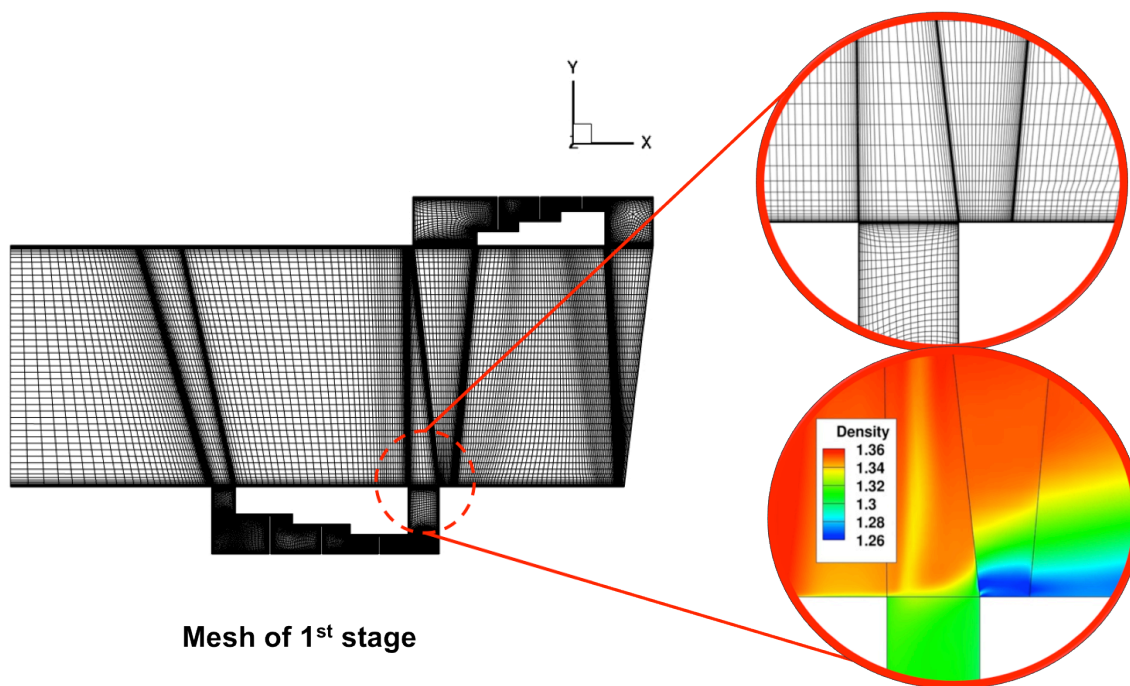


Figure 2-1: High clustering of the cavities is propagated inside main flow path and lead to numerical errors

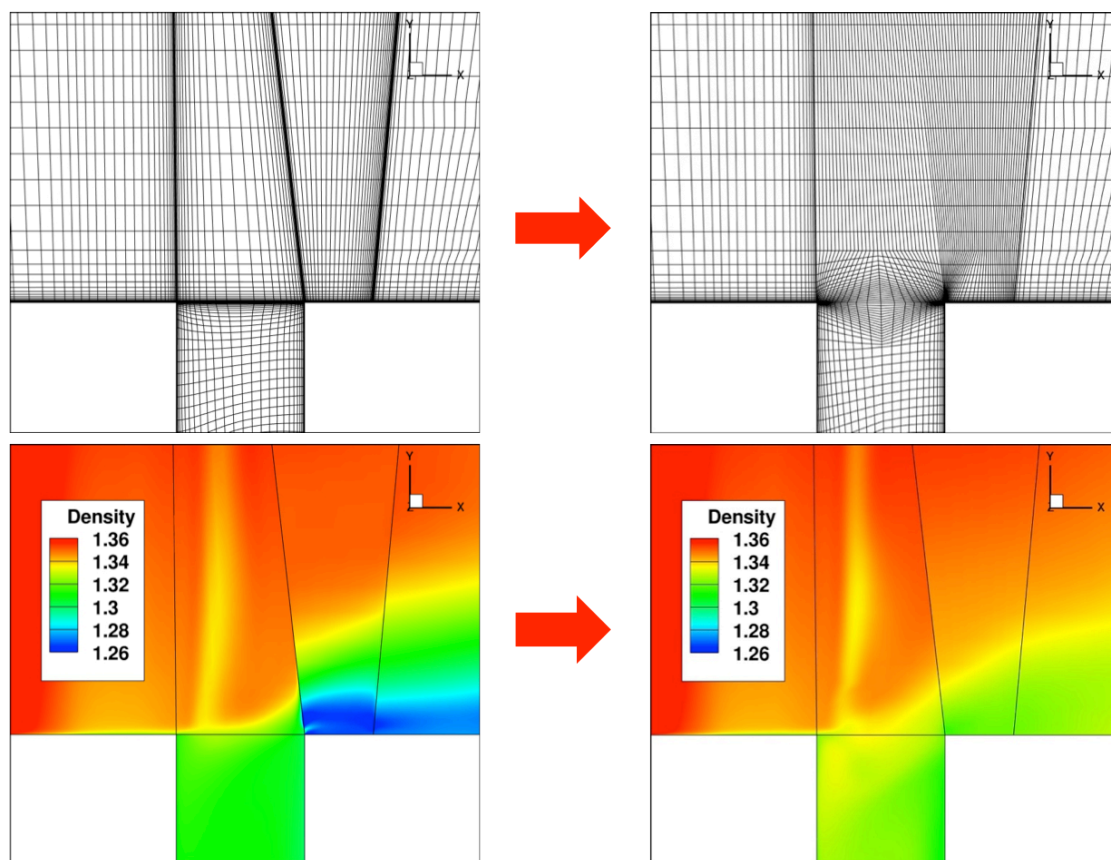


Figure 2-2: Mesh relaxation removes the numerical error and leads to a reasonable solution

## 2.2 Compressible URANS solver “MULTI3”

In this numerical study, the in-house developed solver “MULTI3” has been used. MULTI3 solves the unsteady compressible Reynolds averaged Navier-Stokes (RANS) equations. The numerical algorithm employs a Ni-Lax-Wendroff [85] approach in the context of the Finite-volume method, which is 2<sup>nd</sup> order accurate in both time and space. To prevent high frequency oscillations and capture shock waves, a JST [86] type scalar, anisotropic artificial dissipation algorithm is implemented, which is based on a blending of the second- and fourth order dissipation. The adaptive scaling of the smoothing coefficients accounts for the discrepancy in local CFL numbers in different cell dimensions at the high aspect ratio cells used at the wall. The modeled eddy viscosity is also taken into account in the scaling of the smoothing coefficients. The scheme has been developed by Basol [87] to reduce the artificial dissipation especially in the high aspect ratio cells and within the regions of high modeled eddy viscosity. For modeling the turbulence the Wilcox [88] k-omega turbulence model is used. For a robust implementation of the turbulence model equations, the source terms are modified according to Kato & Launder [89] and the non-oscillatory, Sweby [90] flux limiters are implemented. For time resolved simulations Jameson’s [91] dual time stepping scheme is utilized. Solver was also further developed for simulating the equilibrium wet steam conditions in steam turbines. The thermodynamic properties of steam are interpolated from a discretized version of IAWPS-IF97 steam table. The solver is explained in more detail in Basol [87].

During the preparation studies before the optimization cycle, a need for even faster completion of the simulations arose. The Lax-Wendroff scheme is suitable for compressible flows and turbomachinery applications but the presence of the cavities in the computational domain can lead to delays on convergence and longer simulation times. This, in addition to the mesh problems discussed previously and the increased mesh size due to the cavities, lead to the implementation of a multistage time integration and a preconditioning scheme [92] for convergence acceleration.

### 2.2.1 Fourth order Runge Kutta scheme

Multistage time integration methods are widely used for the solution of steady state, as well as unsteady problems. They allow to significantly increase the CFL number, which provides larger time steps per iteration. Increasing the time step means that fewer iterations need to be evaluated in order to reach the same convergence level. It is noted that the utilization of a multistage scheme implies an increase in computational time per iteration because of the repeated evaluation of the discretized equations. By taking these aspects into account, the fourth order Runge Kutta scheme constitutes a method that provides a considerable increase of the CFL number, while the increase in computational time per iteration remains moderately low.

The time integration of the Lax-Wendroff scheme can be summarized in simple terms by the explicit Euler method:

$$\mathbf{Q}^{n+1} = \mathbf{Q}^n + \delta\mathbf{Q} \quad \text{Eq. 2-1}$$

where  $n$  represents the physical time level and  $\delta\mathbf{Q}$  the overall residual. It is important to note that  $\delta\mathbf{Q}$  already includes the time step  $\Delta t$ .

In contrast, the explicit fourth order Runge Kutta scheme is given by:

$$\begin{aligned} \mathbf{Q}^{n+1,1} &= \mathbf{Q}^n + a_1 \cdot \delta\mathbf{Q}^0 \\ \mathbf{Q}^{n+1,2} &= \mathbf{Q}^n + a_2 \cdot \delta\mathbf{Q}^1 \\ \mathbf{Q}^{n+1,3} &= \mathbf{Q}^n + a_3 \cdot \delta\mathbf{Q}^2 \\ \mathbf{Q}^{n+1,4} &= \mathbf{Q}^n + a_4 \cdot (\delta\mathbf{Q}^0 + 2\delta\mathbf{Q}^1 + 2\delta\mathbf{Q}^2 + \delta\mathbf{Q}^3) \\ \mathbf{Q}^{n+1} &= \mathbf{Q}^{n+1,4} \end{aligned} \quad \text{Eq. 2-2}$$

where  $\delta\mathbf{Q}^k$  represents again the overall residual evaluated at stage  $k$ ,  $n$  is the physical time level and  $\alpha_i$ 's are the coefficients of the algorithm with values:  $\alpha_1 = 0.5$ ,  $\alpha_2 = 0.5$ ,  $\alpha_3 = 1$  and  $\alpha_4 = 0.1667$ . The benefit of the explicit fourth order Runge Kutta scheme can be visualized by comparing its eigenvalue stability region against the one of the time integration approach of the Lax-Wendroff scheme as seen in Figure 2-3.

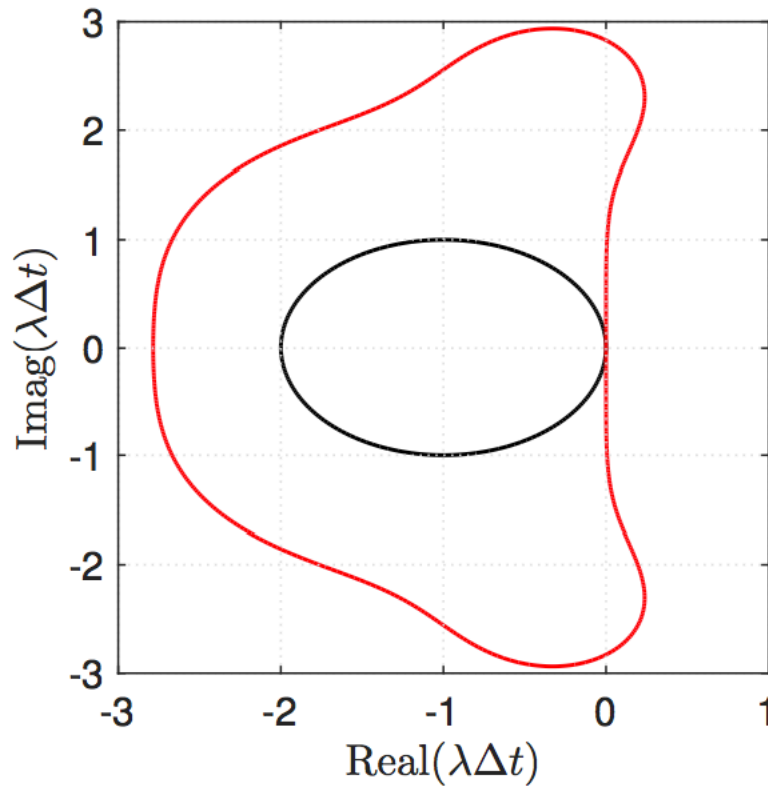


Figure 2-3: Comparison of stability regions: Explicit Euler method (black curve) vs. explicit fourth order Runge Kutta method (red curve)

The wider stability region of the fourth order Runge Kutta method translates into larger time steps  $\Delta t$  for unchanged eigenvalues  $\lambda$  and cell sizes of the mesh. With regard to the CFL, the theoretical limit of 1 can be raised to  $2\sqrt{2}$  by the utilization of the fourth order Runge Kutta method.

$$CFL \leq 2\sqrt{2} \quad \text{Eq. 2-3}$$

The basic implementation of the Runge Kutta scheme in MULTI3 is well described by Eq. 2-2. Before passing the residual of the discretized RANS-equations to the dual time stepping scheme, the four stages of the scheme are executed. The dual time stepping then receives an updated residual  $\delta Q^*$ , which equals the residual of the final step of the method:

$$\delta Q^* = a_4 \cdot (\delta Q^0 + 2\delta Q^1 + 2\delta Q^2 + \delta Q^3) \quad \text{Eq. 2-4}$$



The evaluation of each single term of the residual  $\delta\mathbf{Q}^*$  for every stage is computationally expensive. Therefore, the contributions of the turbulent state equations and the artificial dissipation terms are only evaluated once for the first stage. Nevertheless these contributions are added to the overall residual of each stage.

## 2.2.2 Preconditioning

It is well known that most compressible CFD codes will not converge to an acceptable solution when local Mach numbers within the flow field are very low. Preconditioning approaches adapt a numerical algorithm to allow convergence for compressible flows at very low Mach numbers. These methods adjust the eigenvalues of the system of equations in order to reduce - at low Mach numbers - the large discrepancy between the acoustic and convective wave speeds. Hence, the stiffness of the system of equations and further the limitations on time steps given by the CFL condition of explicit schemes are reduced [93].

Time-marching schemes, such as the dual time-stepping approach provide good stability and convergence characteristics when solving compressible flows at transonic and supersonic Mach numbers. However, at low flow speeds, system stiffness (i.e. large condition numbers  $\kappa$ ) causes convergence rates to be downgraded.

$$\kappa = \frac{|\lambda_{max}|}{|\lambda_{min}|} = \frac{|v| + c}{|v|} \gg 1 \quad \text{Eq. 2-5}$$

Preconditioning methods bring the values of acoustic and convective speeds closer to each other in order to obtain a more optimal condition number for the governing equations ( $\kappa \sim 1$ , see Figure 2-4). In addition, it is expected that the time step of a preconditioned solver is restricted by the convective speed rather than acoustic waves.

Because time-derivative preconditioning spoils the time accuracy of the governing equations, the solution of unsteady problem is only possible if a dual time-stepping procedure is employed. Employing dual time-stepping yields the benefit of treating a temporary solution as a steady state problem. The preconditioning of the

stage-wise residuals of the time-stepping scheme results in higher convergence rates and does not affect the accuracy in time. In this way the size of the physical time step is not affected by the stiffness of the system, whereas convergence of the iterations in pseudo-time is improved by preconditioning [93].

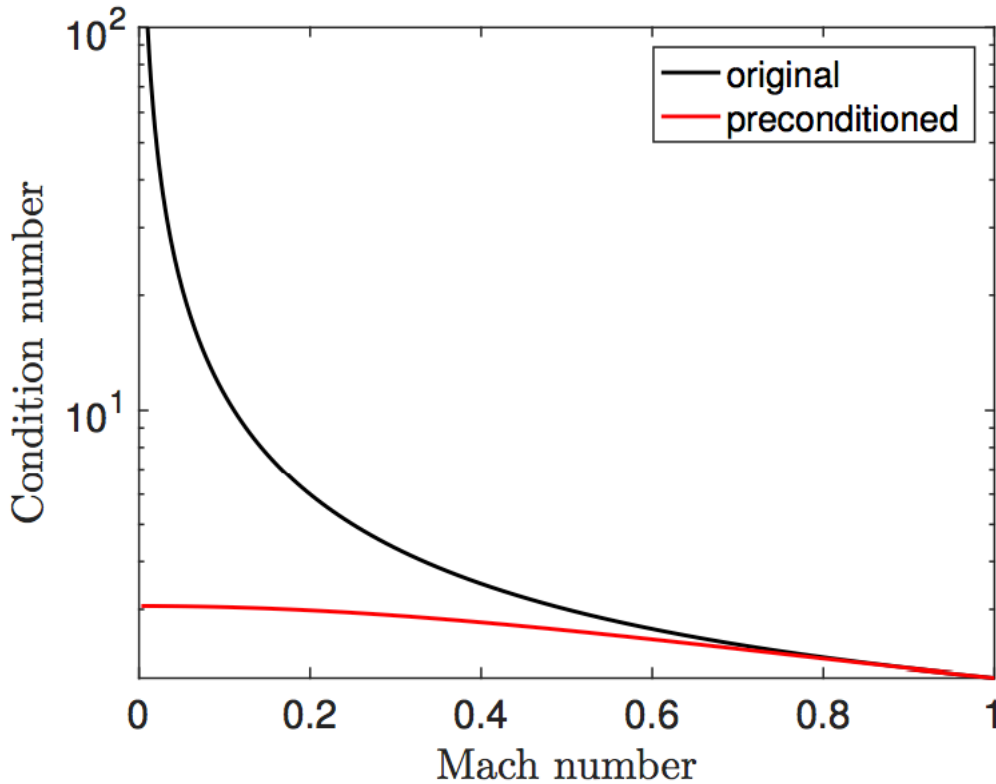


Figure 2-4: Improved stiffness at wider Mach number range due to preconditioning

### 2.2.2.1 Preconditioning derivation

The governing equations, as well as a detailed description of the numerical schemes applied for the discretization of the Navier-Stokes equations in MULTI3 can be found here [87]. For the derivation of the preconditioning matrix of Weiss and Smith [93] for compressible, viscous flows, the Navier Stokes equations are used. The system of equations is cast in integral, Cartesian form for an arbitrary control volume  $V$  with differential surface  $dA$ :

$$\frac{\partial}{\partial t} \iiint \mathbf{Q} dV + \iint [\mathbf{F}_{inv} - \mathbf{F}_{vis}] dA = 0 \quad \text{Eq. 2-6}$$

where

$$\mathbf{Q} = \begin{pmatrix} \rho \\ \rho v_x \\ \rho v_y \\ \rho v_z \\ \rho E \end{pmatrix}, \mathbf{F}_{inv} = \begin{pmatrix} \rho \mathbf{v} \\ \rho \mathbf{v} v_x \\ \rho \mathbf{v} v_y \\ \rho \mathbf{v} v_z \\ \rho \mathbf{v} E + p \mathbf{v} \end{pmatrix}, \mathbf{F}_{vis} = \begin{pmatrix} 0 \\ \tau_{xi} \\ \tau_{yi} \\ \tau_{zi} \\ \tau_{ij} v_j + \mathbf{q} \end{pmatrix}$$

Total energy is related to total enthalpy  $h_0$  by  $E = h_0 - p/\rho$ , where  $h_0 = h + |\mathbf{v}|^2/2$  and  $h = c_p T$ . The derivation of the preconditioning matrix begins by transforming the dependent variables in Eq. 2-6 from conserved quantities  $\mathbf{Q}$  to primitive variables  $\mathbf{W}$  as follows:

$$\frac{\partial \mathbf{Q}}{\partial \mathbf{W}} \frac{\partial}{\partial t} \iiint \mathbf{W} dV + \iint [\mathbf{F}_{inv} - \mathbf{F}_{vis}] dA = 0 \quad \text{Eq. 2-7}$$

where  $\mathbf{W} = (p, v_x, v_y, v_z, T)T$  and the Jacobian  $\partial \mathbf{Q} / \partial \mathbf{W}$  is given by:

$$\frac{\partial \mathbf{Q}}{\partial \mathbf{W}} = \begin{pmatrix} \rho_p & 0 & 0 & 0 & \rho_T \\ \rho_p v_x & \rho & 0 & 0 & \rho_T v_x \\ \rho_p v_y & 0 & \rho & 0 & \rho_T v_y \\ \rho_p v_z & 0 & 0 & \rho & \rho_T v_z \\ \rho_p h - 1 & \rho v_x & \rho v_y & \rho v_z & \rho_T h + \rho c_p \end{pmatrix}$$

with

$$\rho_p = \left. \frac{\partial \rho}{\partial p} \right|_T, \rho_T = \left. \frac{\partial \rho}{\partial T} \right|_p$$

The choice of the primitive variables  $\mathbf{W}$  is desirable for a couple of reasons. First, it is a natural choice when solving incompressible flows and second, the choice of pressure as dependent variable allows the propagation of acoustic waves in the system to be singled out [94]. This becomes clear when we transform Eq. 2-7 to non-conservative form by multiplying the equation by the transformation matrix  $K$ :

$$\left( K \frac{\partial \mathbf{Q}}{\partial \mathbf{W}} \right) \frac{\partial}{\partial t} \iiint \mathbf{W} dV + K \iint [\mathbf{F}_{inv} - \mathbf{F}_{vis}] dA = 0 \quad \text{Eq. 2-8}$$

where

$$K = \begin{pmatrix} 1 & 0 & 0 & 0 & 0 \\ -v_x & 1 & 0 & 0 & 0 \\ -v_y & 0 & 1 & 0 & 0 \\ -v_z & 0 & 0 & 1 & 0 \\ -(H - |\mathbf{v}|^2) & -v_x & -v_y & -v_z & 1 \end{pmatrix}$$

and the matrix pre-multiplying the time derivative in Eq. 2-8 is given by:

$$K \frac{\partial Q}{\partial W} = \begin{bmatrix} \rho_p & 0 & 0 & 0 & \rho_T \\ 0 & \rho & 0 & 0 & 0 \\ 0 & 0 & \rho & 0 & 0 \\ 0 & 0 & 0 & \rho & 0 \\ -1 & 0 & 0 & 0 & \rho c_p \end{bmatrix} \quad \text{Eq. 2-9}$$

Inspecting Eq. 2-9, it is noticed that the term  $\rho_p$  that multiplies the time derivative of pressure in the continuity equation controls the speed of propagation of acoustic waves in the system. It is interesting to note that, for an ideal gas,  $\rho_p = 1/RT = \gamma/c^2$ , where  $c$  is the speed of sound and  $\gamma = c_p/c_v$ , whereas for constant density flows is  $\rho_p = 0$ , consistent with the notion of infinite pressure wave speeds in an incompressible fluid. Thus, if this term is replaced with one proportional to the inverse of the local velocity squared, we can control the eigenvalues of the system such that they are all of the same order. We precondition the matrix given in Eq. 2-9 with the preconditioning matrix  $\Gamma_{nc}$ :

$$\Gamma_{nc} = \begin{bmatrix} \Theta & 0 & 0 & 0 & \rho_T \\ 0 & \rho & 0 & 0 & 0 \\ 0 & 0 & \rho & 0 & 0 \\ 0 & 0 & 0 & \rho & 0 \\ -1 & 0 & 0 & 0 & \rho c_p \end{bmatrix} \quad \text{Eq. 2-10}$$

where the subscript  $nc$  refers to the non-conservative formulation, and  $\Theta$  is given by

$$\theta = \left( \frac{1}{U_r^2} - \frac{\rho_T}{\rho c_p} \right) \quad \text{Eq. 2-11}$$

Here  $U_r$  is a reference velocity that is defined as:

$$U_r = \begin{cases} \epsilon c & \text{if } |\mathbf{v}| < \epsilon c \\ |\mathbf{v}| & \text{if } \epsilon c < |\mathbf{v}| < c \\ c & \text{if } |\mathbf{v}| > c \end{cases} \quad \text{Eq. 2-12}$$

where  $\epsilon$  is a small number ( $\sim 10^{-5}$ ) in order to prevent singularities at stagnation points. The form of Eq. 2-11 ensures that for an ideal gas, as  $U_r \rightarrow c$ ,  $\theta$  reduces to  $\gamma/c^2$ , consistent with the original Eq. 2-9. For viscous flows  $U_r$  is further limited such that it does not become smaller than the local diffusion velocity for example in boundary layer flows. Therefore, we pose an additional restriction on  $U_r$ :

$$U_r = \max \left( U_r, \frac{v}{\Delta h} \right) \quad \text{Eq. 2-13}$$

where  $\Delta h$  is the inter-cell length scale over which the diffusion occurs. Limiting  $U_r$  in this way is necessary in regions where diffusion effects dominate and grid spacing is small (boundary and shear layers).

The preconditioning system in conservation form is obtained by substitution of Eq. 2-10 for Eq. 2-9 in Eq. 2-8 and pre-multiplying the result by  $K^{-1}$ :

$$\Gamma \frac{\partial}{\partial t} \iiint \mathbf{W} dV + K \iint [\mathbf{F}_{inv} - \mathbf{F}_{vis}] dA = 0 \quad \text{Eq. 2-14}$$

where  $\Gamma = (K^{-1} \Gamma_{nc})$

$$\Gamma = \begin{pmatrix} \Theta & 0 & 0 & 0 & \rho_T \\ \Theta v_x & \rho & 0 & 0 & \rho_T v_x \\ \Theta v_y & 0 & \rho & 0 & \rho_T v_y \\ \Theta v_z & 0 & 0 & \rho & \rho_T v_z \\ \Theta H - 1 & \rho v_x & \rho v_y & \rho v_z & \rho_T H + \rho c_p \end{pmatrix}$$

The governing equations are in conservative form for steady state solutions, but not for time-dependent flows. This is not a problem, however, since the preconditioning has already destroyed the time accuracy of the equations, and we will not employ them in this form for unsteady calculations. One can show that with the described preconditioning of the equations, the eigenvalues of the system remain well conditioned at all speeds [93].

#### 2.2.2.2 Choice of preconditioning parameter

There are different choices for the preconditioning velocity  $U_r$ . The restriction given in Eq. 2-13 showed to be not very effective and has a large dependency on the mesh. For this work the following restrictions on the reference velocity were implemented in order to yield a robust approach:

$$U_r = \min(\max(\epsilon c, |\mathbf{v}|, \beta \cdot M_{inf}), c) \quad \text{Eq. 2-15}$$

where  $M_{inf}$  stands for the free stream Mach number at the domain inlet and is a case dependent parameter (usually  $\beta = [0,4]$ ). This term prevents the reference velocity to vanish in stagnation points and in boundary layers. Choosing a very small value for  $\beta$ , means very effective preconditioning specifically in low Mach number regions. However, if the value gets too small the robustness of the solver is greatly reduced. Therefore, a trade-off between fast convergence and stability of a simulation has to be met.  $\beta$  can be specified by the user in the simulation setup.

#### 2.2.2.3 Preconditioning for time-accurate computations

The incorporation of preconditioning improves the convergence and accuracy in the low Mach number range, but introduces inconsistency in the time behavior due to the precondition matrix. To provide for efficient, time-accurate solutions of the preconditioned equations a dual time-stepping approach can be employed. For this purpose a dual time-derivative term that is multiplied by the preconditioning matrix is introduced to the governing equations [93]:

$$\Gamma \frac{\partial}{\partial \tau} \iiint \mathbf{W} dV + \frac{\partial}{\partial t} \iiint \mathbf{Q} dV + \iint [\mathbf{F}_{inv} - \mathbf{F}_{vis}] dA = 0 \quad \text{Eq. 2-16}$$

where  $t$  denotes again physical time and  $\tau$  the pseudo-time in the time-marching procedure. To solve the preconditioning equations, first the viscous and inviscid fluxes are computed using the basic scheme (here Ni's Lax-Wendroff scheme). In addition artificial smoothing terms are added to ensure numerical stability. Rewriting Eq. 2-16 in discretized form and multiplying the whole equation with  $\Gamma^{-1}$ :

$$\mathbf{W}^{n+1,k+1} = \mathbf{W}^{n+1,k} - \Delta\tau\Gamma^{-1} \left( \frac{1}{2\Delta t} (3\mathbf{Q}^{n+1,k} - 4\mathbf{Q}^n + \mathbf{Q}^{n-1}) + \delta\mathbf{Q}^{n+1,k} \right) \quad \text{Eq. 2-17}$$

After the primitive state vector  $W$  is updated from pseudo-time level  $k$  to  $k + 1$ , the conserved state vector at the new time level can be calculated by:

$$\mathbf{Q}^{n+1,k+1} = \frac{\partial \mathbf{Q}}{\partial \mathbf{W}} \mathbf{W}^{n+1,k+1}$$

In this context, again  $k$  is the pseudo-time level counter and  $n$  represents any physical time level. Throughout the iterations in pseudo-time,  $\mathbf{Q}^n$  and  $\mathbf{Q}^{n-1}$  are held constant while  $\mathbf{Q}^{n+1,k}$  is computed from  $\mathbf{W}^{n+1,k}$ . As  $\tau \rightarrow \infty$ , the solution at the next time level  $\mathbf{Q}^{n+1}$  is given by  $\mathbf{Q}(\mathbf{W}^{n+1,m})$ , where  $m$  is the number of iterations completed in pseudo-time. The preconditioning matrix can be inverted analytically and evaluated in a point-wise fashion. The analytical expression for  $\Gamma$  and  $\Gamma^{-1}$  are given as:

$$\Gamma = \begin{pmatrix} \Theta & 0 & 0 & 0 & -\frac{\rho}{T} \\ \Theta u & \rho & 0 & 0 & -\frac{\rho u}{T} \\ \Theta v & 0 & \rho & 0 & -\frac{\rho v}{T} \\ \Theta w & 0 & 0 & \rho & -\frac{\rho w}{T} \\ \Theta h_0 - 1 & \rho u & \rho v & \rho w & -\frac{\rho E_{kin}}{T} \end{pmatrix} \quad \text{Eq. 2-18}$$

$$\Gamma^{-1} = \begin{pmatrix} a_2 \left[ \frac{c^2}{\gamma-1} - (h_0 - 2E_{kin}) \right] & -a_2 u & -a_2 v & -a_2 w & a_2 \\ -\frac{u}{\rho} & \frac{1}{\rho} & 0 & 0 & 0 \\ -\frac{v}{\rho} & 0 & \frac{1}{\rho} & 0 & 0 \\ -\frac{w}{\rho} & 0 & 0 & \frac{1}{\rho} & 0 \\ a_3 [1 - \Theta (h_0 - 2E_{kin})] & -\Theta a_3 u & -\Theta a_3 v & -\Theta a_3 w & \Theta a_3 \end{pmatrix} \quad \text{Eq. 2-19}$$

with the abbreviations

$$\alpha_2 = (\gamma - 1)\phi, \alpha_3 = \frac{\alpha_2 T}{\rho}, \phi = \frac{1}{\Theta c - (\gamma - 1)}$$

where  $\Theta$  for a perfect gas is:

$$\Theta = \frac{1}{U_r} - \frac{(\gamma - 1)}{c^2} \quad \text{Eq. 2-20}$$

The Jacobian matrix  $\frac{\partial \mathbf{Q}}{\partial \mathbf{W}}$  and its inverse  $\frac{\partial \mathbf{Q}^{-1}}{\partial \mathbf{W}}$  for perfect gases are defined as:

$$\frac{\partial \mathbf{Q}}{\partial \mathbf{W}} = \begin{pmatrix} \frac{\rho}{p} & 0 & 0 & 0 & -\frac{\rho}{T} \\ \frac{\rho u}{p} & \rho & 0 & 0 & -\frac{\rho u}{T} \\ \frac{\rho v}{p} & 0 & \rho & 0 & -\frac{\rho v}{T} \\ \frac{\rho w}{p} & 0 & 0 & \rho & -\frac{\rho w}{T} \\ \frac{\rho E}{p} & \rho u & \rho v & \rho w & -\frac{\rho E_{kin}}{T} \end{pmatrix} \quad \text{Eq. 2-21}$$

$$\frac{\partial \mathbf{Q}^{-1}}{\partial \mathbf{W}} = \begin{pmatrix} (\gamma - 1) E_{kin} & (1 - \gamma)u & (1 - \gamma)v & (1 - \gamma)w & \gamma - 1 \\ -\frac{u}{\rho} & \frac{1}{\rho} & 0 & 0 & 0 \\ -\frac{v}{\rho} & 0 & \frac{1}{\rho} & 0 & 0 \\ -\frac{w}{\rho} & 0 & 0 & \frac{1}{\rho} & 0 \\ \frac{1}{\rho} \left[ \frac{\gamma E_{kin}}{c_p} - T \right] & -\frac{\gamma u}{c_p \rho} & -\frac{\gamma v}{c_p \rho} & -\frac{\gamma w}{c_p \rho} & \frac{\gamma}{c_p \rho} \end{pmatrix} \quad \text{Eq. 2-22}$$

### *Implications on time step*

The pseudo-time step  $\Delta \tau$  is updated every iteration and for each cell separately based on the CFL condition. Since preconditioning alters the eigenvalues of the governing equations, the maximum



allowable time step of the scheme will be affected. In theory, the resultant convective eigenvalues of the preconditioned system are [93]:

$$\lambda \left( \Gamma^{-1} \frac{\partial \mathbf{F}_{inv}}{\partial \mathbf{W}} \right) = u, u, u, u' + c', u' - c' \quad \text{Eq. 2-23}$$

where in this context

$$\begin{aligned} u &= \mathbf{v} \cdot \mathbf{n} \\ u' &= u(1 - \alpha) \\ c' &= \sqrt{\alpha^2 u^2 + U_r^w} \\ \alpha &= (1 - \beta U_r^2) / 2 \\ \beta &= \left( \rho_p + \frac{\rho_T}{\rho c_p} \right) \end{aligned}$$

For an ideal gas  $\beta = 1/c^2$ . At the sonic limit ( $U_r = c$ ),  $\alpha = 0$  and the eigenvalues of the preconditioned system take their traditional form  $u \pm c$ . On the other hand, at low speeds all eigenvalues become of the same order as  $u$ . This means that the eigenvalues of the preconditioned system stay well conditioned at all speeds.

### *Turbulence modeling*

The application of preconditioning for the turbulence model equations is not necessary since the wave speeds are already equalized within the preconditioned RANS- equations [95].

### *Artificial dissipation model*

Additionally to poor convergence behavior, compressible CFD solvers often fail to calculate accurate solutions in low Mach number flow regions. Jafari [96] demonstrates this fact by analyzing the order of the different terms of the Euler equations for low Mach number flows. It is shown that the artificial dissipation terms do not scale properly in the low Mach number regime. Introducing a low Mach number preconditioning matrix eliminates this problem by scaling the artificial dissipation terms back to the order of the

convective fluxes. In order to do so, the eigenvalues of the artificial dissipation model need to be altered according to the modifications discussed in section 2.2.2.3 to improve the accuracy while maintaining stability. However, Basol's [87] anisotropic artificial dissipation approach already aims for optimal smoothing levels by scaling the fourth order dissipation dependent on a local CFL number. Therefore, the implementation with the original eigenvalues without the modifications due to preconditioning was tested first together with preconditioning. The test runs with this configuration could not be completed either because of the high occurrence of artificial oscillations within the flow field or solver crashes. The alteration of the eigenvalues due to preconditioning was thus included in the implementation.

During the testing of the preconditioning implementation it was observed that the alteration of the eigenvalues drastically reduced the overall amount of smoothing added to the equations. This did not cause simulation crashes but artificial high frequency oscillations originated at a few locations inside the flow field. In order to get rid of these artifacts, the smoothing approach of Basol was slightly modified. First, the deactivation of the smoothing for local CFL numbers bigger than 0.7 was adapted to the maximum CFL number stated in the input file. On one hand this was necessary since we obtained oscillations in regions where the local CFL numbers were rather high and also for the reason that the combination of the multistage time integration scheme with preconditioning yields even higher local CFL numbers, which reduces the amount of smoothing even more. The second adaptation affects the fourth order smoothing parameter  $\epsilon^{(4)}$ . In the original implementation of Basol this parameter depends only on the local CFL number. Several test runs with preconditioning showed that the combination of Basol's approach and the modifications due to preconditioning result in too low levels for  $\epsilon^{(4)}$ . Therefore, a lower limit on  $\epsilon^{(4)}$  is imposed that can be specified in the input file. The modifications can be summarized by Eq. 2-24.

$$\epsilon^{(2)} = \epsilon^{(2)}$$

$$\epsilon^{(4)} = \begin{cases} 0 & \text{if } CFL_{loc} \geq 0,7 \\ f(CFL_{loc}) & \text{if } 0,7 > CFL_{loc} \geq 0,02 \\ g(CFL_{loc}) & \text{if } 0,02 > CFL_{loc} \end{cases} \quad \text{Eq. 2-24}$$

$$\epsilon^{(4)} = \max(\epsilon^{(4)}, \epsilon_{min}^{(4)})$$

The labeling of  $\epsilon^{(2)}$  and  $\epsilon_{min}^{(4)}$  in the input file are *sig2* and *sig4* respectively. It can be laborious to select a combination of the right amount of smoothing and optimal convergence levels for each grid node that leads in the end to a flow field that is well converged and is not affected by excessive artificial smoothing. Reducing  $\beta$  means that  $\epsilon_{min}^{(4)}$  will need to be increased to retain the same amount of smoothing in low Mach number regions. To illustrate this we use the following simplified description of the smoothing as a function of the maximum local inviscid eigenvalue and  $\epsilon_{min}^{(4)}$ :

$$\delta Q_{smo} = \lambda_{max}^{inv}(\beta) \cdot \epsilon_{min}^{(4)} \cdot f(CFL_{loc}, \dots) \quad \text{Eq. 2-25}$$

where  $\delta Q_{smo}$  refers to the amount of smoothing added to the residual and  $f(CFL_{loc}, \dots)$  describes the dependency of the local CFL number and other variables. In a very low Mach number region the maximum eigenvalue  $\lambda_{max}^{inv}$  will be restricted to a lower limit imposed by  $\beta$ . Lowering  $\beta$  simultaneously lowers  $\lambda_{max}^{inv}$ . Assuming that the same CFL number is used for two different simulation setups (A and B) for  $\beta$ ,  $\epsilon_{min}^{(4)}$  can be estimated by taking the ratio of the smoothing residuals  $\delta Q_{smo}$ . If the same smoothing level wants to be reached in low Mach number flow regions, this ratio has to be approximately equal to one:

$$\frac{\delta Q_{smo}^A}{\delta Q_{smo}^B} \approx 1 = \frac{\lambda_{max}^{inv}(\beta^A)}{\lambda_{max}^{inv}(\beta^B)} \cdot \frac{\epsilon_{min}^{(4),A}}{\epsilon_{min}^{(4),B}} \cdot 1 \quad \text{Eq. 2-26}$$

By rearranging the terms, one can figure out what the ratios of the eigenvalues and the lower limits on the smoothing would need to be.

### 2.2.3 Adaptation of solver for equilibrium wet steam conditions

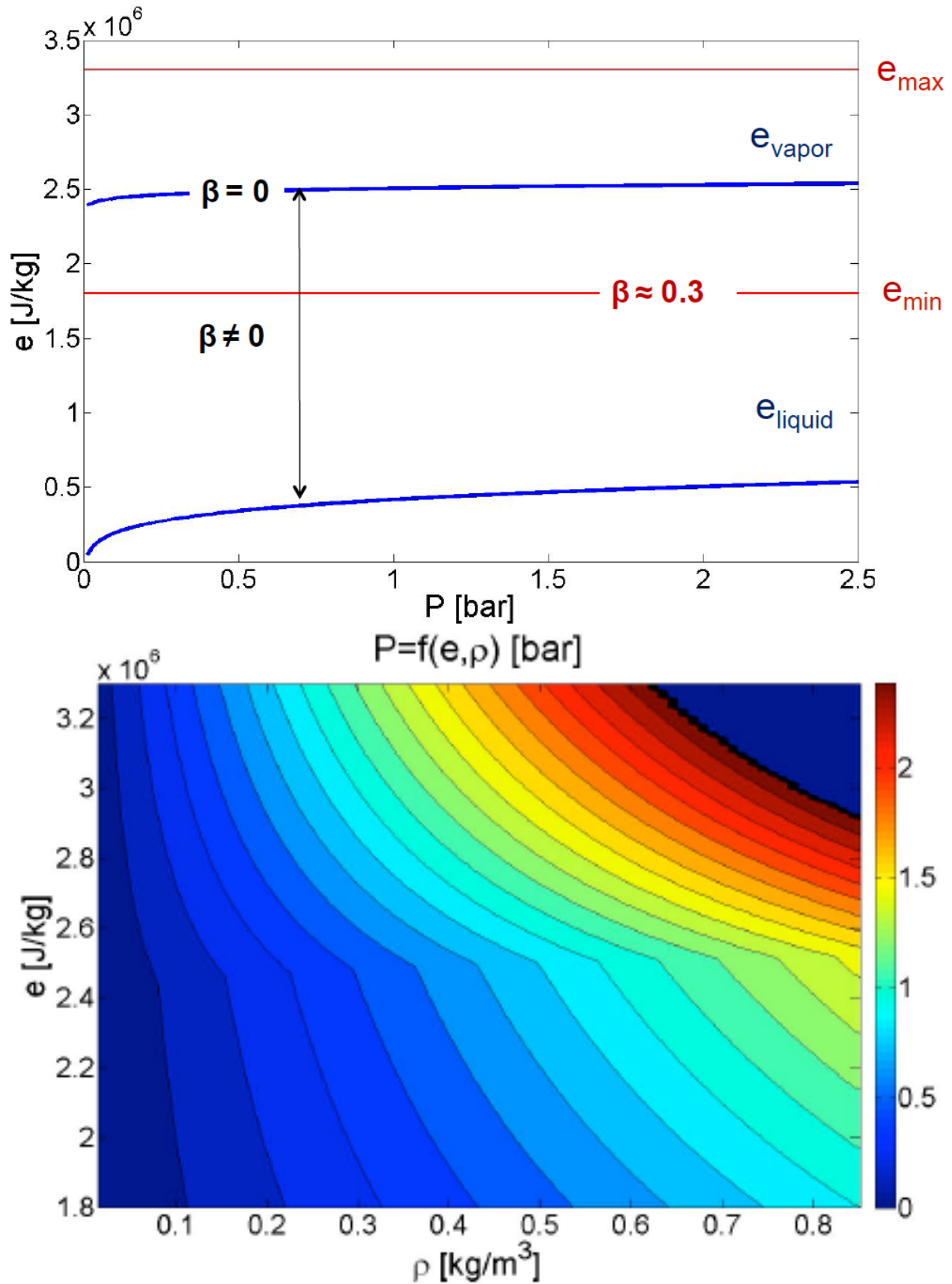


Figure 2-5: Steam table range in terms of pressure and internal energy generated table for pressure  $P=f(e,\rho)$  derived from IAPWS-IF97

A discrete version of steam table is derived from the IAPWS-IF97 standard formulation. The tables are generated using Matlab library XSteam [97] and cover both the superheated and the saturated steam regions up to a wetness mass fraction of  $\beta=0.3$  as shown in Figure 2-5. The state of condensed steam including temperature, pressure, enthalpy, entropy, wetness mass fraction  $\beta$  is read from the tables using a second order accurate bi-linear interpolation scheme. As suggested by Senoo [98], internal energy and density are used as independent variables in the tables.

A major modification is required for adapting the existing Giles' characteristic boundary conditions [99] for wet-steam conditions. In the implementation of Giles, boundary conditions are imposed in terms of total enthalpy, entropy and flow angles. The flow field at the inlet and outlet are updated such that the imposed level of enthalpy and the entropy hold. The implementation requires partial derivatives, which can be analytically derived for the ideal gas law. However, for the wet-steam implementation they all have to be read from the tables. List of the required partial derivatives are given as following:

$$\left. \frac{\partial h}{\partial \rho} \right|_p, \left. \frac{\partial h}{\partial p} \right|_\rho, \left. \frac{\partial S}{\partial \rho} \right|_p, \left. \frac{\partial S}{\partial p} \right|_\rho, \left. \frac{\partial e}{\partial \rho} \right|_p, \left. \frac{\partial e}{\partial p} \right|_\rho \quad \text{Eq. 2-27}$$

Partial derivatives with respect to pressure have to be derived from partial derivatives with respect to internal energy and density since the generated tables have these two independent variables. The partial derivatives of enthalpy with respect to pressure at constant density can be expressed as follows.

$$\left. \frac{\partial h}{\partial p} \right|_\rho = \left. \frac{\partial h}{\partial e} \right|_\rho / \left. \frac{\partial p}{\partial e} \right|_\rho \quad \text{Eq. 2-28}$$

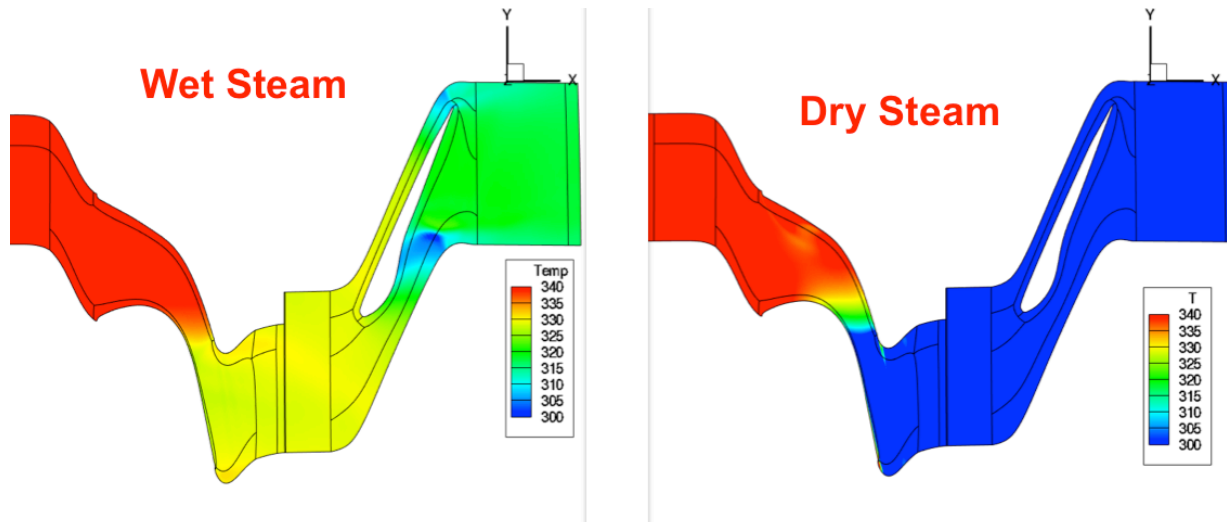


Figure 2-6: Temperature for wet steam and ideal, dry steam

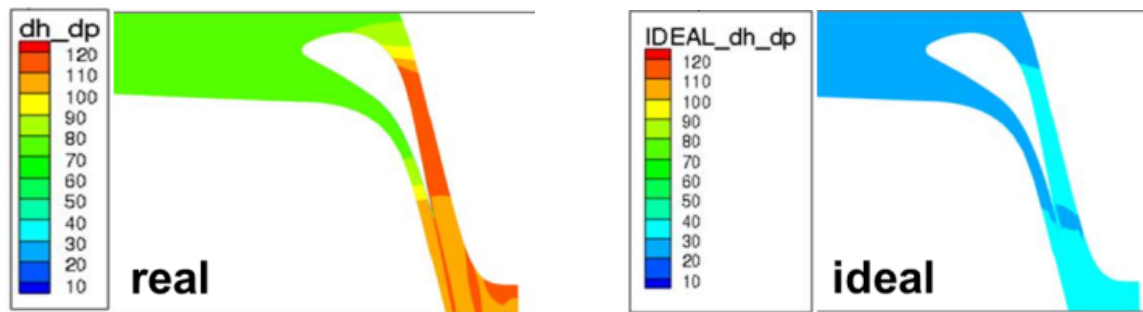


Figure 2-7: Partial derivatives of enthalpy with respect to pressure at constant density for wet-steam and ideal, dry steam conditions.

As shown in Figure 2-6, the temperature is considerably different for the wet-steam than it is for the dry, ideal steam. Similar is for the partial derivative of enthalpy with respect to pressure, shown in Figure 2-7. This highlights the importance of steam modeling for the accuracy of the numerical solution.

Speed of sound  $c$  has to be derived differently for wet-steam simulations. The formulation used for the calculation is given below [98]:

$$c^2 = \left. \frac{\partial p}{\partial \rho} \right|_e + \left. \frac{\partial p}{\partial e} \right|_\rho \frac{p}{\rho^2} \quad \text{Eq. 2-29}$$

Speed of sound is about 10 % lower for the wet-steam conditions compared to dry steam conditions under current operating conditions.

#### 2.2.4 Convergence assessment of unsteady simulations

Convergence of a steady state CFD-simulation is typically achieved when the root mean square of a predefined error norm of the numerical residuals falls below a predefined limit. In case of unsteady simulations the specification of a converged solution is not always that clear. If the objective of a CFD-study is to obtain a time-resolved solution of an unsteady flow field, one has to take into account - in addition to the numerical error - physical constraints on the flow field that must be fulfilled. If these constraints can be satisfied the next step is then to identify an iteration point when the results obtained start repeating themselves quantitatively in a periodic manner over time. Convergence assessment of both time-mean and time-resolved flow field variables is important.

Two very practical methods to characterize the periodicity of unsteady flows, are the Discrete Fourier Transform (DFT) and cross-correlation. DFT gives the possibility to determine the dominant frequencies appearing for example due to vane-blade interactions, as well as to access the whole frequency content of a signal. This is a very effective criterion in cases where the blade passing frequency (BPF) or other physical frequencies is known beforehand. If neither the amplitudes nor the phase angles of the Fourier components of the expected frequencies calculated by the DFT change between two consecutive periods, this convergence criterion is considered fulfilled. Cross-correlation allows to characterize the inherent periodicity existing in an unsteady flow field as follows: By looking at the magnitude of the cross-correlation coefficient at zero lag of a time-resolved signal specified over one period correlated with the same signal calculated over the next period, one obtains a direct measure of how alike the signal is over the expected periodic intervals. If the computed magnitude is clearly lower than one, either the number of lags is inconsistent with the expected periodic interval or the flow is truly non-periodic. Both of these facts indicate that significant unsteadiness has to exist in the flow field. In most cases of CFD simulations for turbomachinery applications, the period of the most considerable

unsteady fluctuations is anticipated from the circumferential interval modeled and the rotational speed of the machine [100].

Convergence criteria can be categorized into two groups: The ones that are evaluated on the boundaries of the domain or at row interfaces, whereas others are evaluated at local nodes or cells. The first category analyzes global parameters such as the mass balance across a given boundary or the temperature at a specific interface [101]. In the following subsections several simulation and flow parameters are discussed with respect to their relevance for the convergence level of a solution. Further, the convergence criteria together with the signal processing methods applied for a specific quantity are described. Finally, necessary convergence criteria are defined which have to be respected when conducting an unsteady simulation.

#### 2.2.4.1 Signal processing

Here, some signal processing methods are introduced in a simple and concise form, used for convergence assessment based on work of Clark et al [100].

##### *Time-average*

$$\bar{q} = \frac{1}{N} \sum_{j=1}^N q_j \quad \text{Eq. 2-30}$$

##### *Discrete Fourier Transformation (DFT)*

The DFT (Fourier coefficients  $Q_{k+1}$ ) of a discrete realization of quantity  $q$  is defined as:

$$Q_{k+1} = \sum_{j=0}^{N-1} q_{j+1} \exp\left(-i \frac{2\pi k j}{N}\right) \quad \text{Eq. 2-31}$$

where  $i = \sqrt{-1}$ ,  $k$  is the wavenumber and  $N$  is the total number of realizations or samples. Further we can decompose a specific Fourier coefficient as:



$$Q_{k+1} = Re + i IM \quad \text{Eq. 2-32}$$

A reconstruction of the corresponding time-periodic signal can then be given as:

$$q(t) = Re[Aexp(i(\omega t + \phi))] = A \cos(\omega t + \phi) \quad \text{Eq. 2-33}$$

where  $\omega$  is the circular frequency corresponding to an integer multiple of the frequency spacing ( $\Delta f_{k+1} = f_{sampling}^{k+1}$ ),  $A$  is the normalized DFT and  $\phi$  is the phase angle:

$$\omega = 2\pi\Delta f_{k+1} \quad \text{Eq. 2-34}$$

$$A = \frac{2}{N}(Re^2 + Im^2)^{\frac{1}{2}} \quad \text{Eq. 2-35}$$

$$\phi = \tan^{-1}\left(\frac{Im}{Re}\right) \quad \text{Eq. 2-36}$$

### ***Cross-correlation***

The fluctuation of quantity  $q$  at sample  $j$  can be written as:

$$q'_j = q_j - \bar{q} \quad \text{Eq. 2-37}$$

The cross-correlation coefficient (CC<sub>q</sub>) at lag  $L$  is given by:

$$CC_q(L) = \frac{\frac{1}{N} \sum_{j=1}^N q'_{j+L} q'_{j+N}}{\frac{1}{N} \left[ \sum_{j=1}^N q_j'^2 \sum_{j=1}^N q_{j+N}'^2 \right]^{\frac{1}{2}}} \quad \text{Eq. 2-38}$$

The calculation is accomplished by multiplying the time-lag-shifted fluctuations of the signal ( $q'_{j+L}$ ) over the first interval by the

fluctuations of the signal for the second periodic time interval ( $q'_{j+N}$ ). Summing up the result of this multiplication and dividing by the number of samples per period gives the numerator. This result is then normalized by the root-mean-square of the product of the variances of the two signals.

#### 2.2.4.2 Numerical residuals

The *DQ rms* refers to the root-mean-square of the numerical residual computed over the whole domain in MULTI3. Just as for steady state simulations, it is important for unsteady flow field predictions that the numerical error drops below a given limit before a viable solution can be achieved. From this quantity only the change from simulated period to period and the effective value of the time average are needed for the convergence assessment. Typically this criterion is fulfilled before any other criterion reaches a high level of convergence. Mathematically, this can be formulated in the following way:

$$C_{mean,DQ}^n = 1 - \left| 1 - \frac{\bar{q}_{DQ}^n}{\bar{q}_{DQ}^{n-1}} \right| \quad \text{Eq. 2-39}$$

where the superscript index  $n=2,3,4,\dots$  refers to the number of cycles, and:

$$\bar{q}_{DQ}^n \leq \alpha_{DQ} \quad \text{Eq. 2-40}$$

where  $\alpha_{DQ}$  specifies limit that the time average needs to fall below for convergence. This limit is for every simulated case different but from several applications of MULTI3,  $\alpha_{DQ}$  can be estimated to be roughly  $10^{-4}$ . However, the more stringent requirement is that  $C_{mean,DQ}^n$  is close to one, which implies that the residuals have stabilized at a certain level.

### 2.2.4.3 Local monitoring points

MULTI3 allows monitoring of static pressure, static temperature as well as turbulent kinetic energy and dissipation of selected grid points inside the computational domain. This offers the possibility to examine the local flow field. Furthermore this information can be used to compare the convergence status of different locations inside the domain. Clark and Grover already observed, that the unsteadiness in a static pressure field is driven by potential field effects or shock interactions, and that viscous disturbances propagate much slower than pressure waves. This has a remarkable impact on the convergence rate of flow variables that depend on the propagation of such disturbances. In chapter 5 the convergence rates of all quantities of interest are discussed.

The locally monitored flow quantities are expected to show up unsteady variations and therefore the whole arsenal of introduced signal processing methods is used to assess the convergence level. The convergence levels for each flow quantity respectively is then given by the set of separate convergence criteria:

$$C_{mean,q,mon}^n = 1 - \left| 1 - \frac{\bar{q}_{mon}^n}{\bar{q}_{mon}^{n-1}} \right| \quad \text{Eq. 2-41}$$

$$C_{A,q,mon}^n = 1 - \left| 1 - \frac{A_{q,mon}^n}{A_{q,mon}^{n-1}} \right| \quad \text{Eq. 2-42}$$

$$C_{\phi,q,mon}^n = 1 - \left| \frac{\phi_{q,mon}^n - \phi_{q,mon}^{n-1}}{\pi} \right| \quad \text{Eq. 2-43}$$

$$C_{CC,q,mon}^n = |CC_{q,mon}^n(L=0)| \quad \text{Eq. 2-44}$$

The criteria compare the calculated informations from the signal processing routines from period  $n$  against the ones from the previous period  $(n-1)$ .  $C_{mean,q,mon}^n$  refers to the change of the time average of monitored quantity  $q$  from one periodic interval to the previous interval. A value of  $C_{mean,q,mon}^n$  close to 1, indicates a constant average from period to period. Eq. 2-42 to Eq. 2-44 evaluate the level of convergence in terms of the normalized DFT-

amplitude  $A$ , the calculated phase angle  $\phi$  and the cross-correlation coefficient at zero lag  $CC(L = 0)$  in a similar manner. Again, if the values calculated by these equations are close to one, a high level of convergence is achieved.

The actual convergence level is then given by the minimum value of the whole set of criteria:

$$C_{q,mon}^n = \min \{ C_{mean,q,mon}^n, C_{A,q,mon}^n, C_{\phi,q,mon}^n, C_{CC,q,mon}^n \} \quad \text{Eq. 2-45}$$

#### 2.2.4.4 Mass flow at row interfaces

The mass flow rate in a turbine is a direct indicator for the output and the loading of the machine. The temporal evolution of the mass flows at each spatial interface between stationary and rotating frames of reference shows up marginal oscillations around a certain mean value due to vane/blade interactions. The known flow rate at the inlet of the computational domain sets the mean values of these oscillations. Accordingly, the requirement for convergence for the mass flow at each interface is that the difference of the time average between the inlet plane of the domain and a certain interface needs to converge to zero.

Since the unsteady fluctuations of the computed mass flows are usually only very small in magnitude compared to the mean, DFT and cross-correlation are not necessary to assess this criterion. The major requirement for mass flow convergence can be mathematically formulated as follows:

$$C_{mean,\dot{m}_f}^n = 1 - \max_j \left\{ \left| 1 - \frac{\bar{\dot{m}}_{f,j}^n}{\bar{\dot{m}}_{f,inlet}^n} \right| \right\} \quad \text{Eq. 2-46}$$

where the superscript  $n$  refers again to the period number ( $n = 1, 2, 3, \dots$ ) and the subscript index  $j$  a specific interface ( $j = 1, 2, 3, \dots, N_{interfaces}$ ).

### 2.2.4.5 Design objectives and further parameters

Variables such as efficiency and loss generation are very important from a designer's point of view. Apart from them, there is a whole set of typical design parameters that are desired to be tracked during a simulation. This allows not only to assess the convergence level of a design parameter, but also to evaluate them without large post processing efforts, which is crucial for an already expensive optimization cycle. A set of parameters that are in general considered during design optimization studies [38], [102]–[104] have been identified and implemented within the solver. The parameters that have been added are defined by equations Eq. 2-47 to Eq. 2-61.

Figure 2-8 displays the interfaces, which are relevant for the calculation of these parameters. Interface 1 represents the stator inlet, interface 2 the stator outlet and therefore also the rotor inlet and interface 3 the outlet of the rotor. The parameters are calculated between inlet and outlet of a row or even over a complete turbine stage (depending on the type of quantity). The indicated interfaces refer to the stator-rotor interfaces present in the mesh.

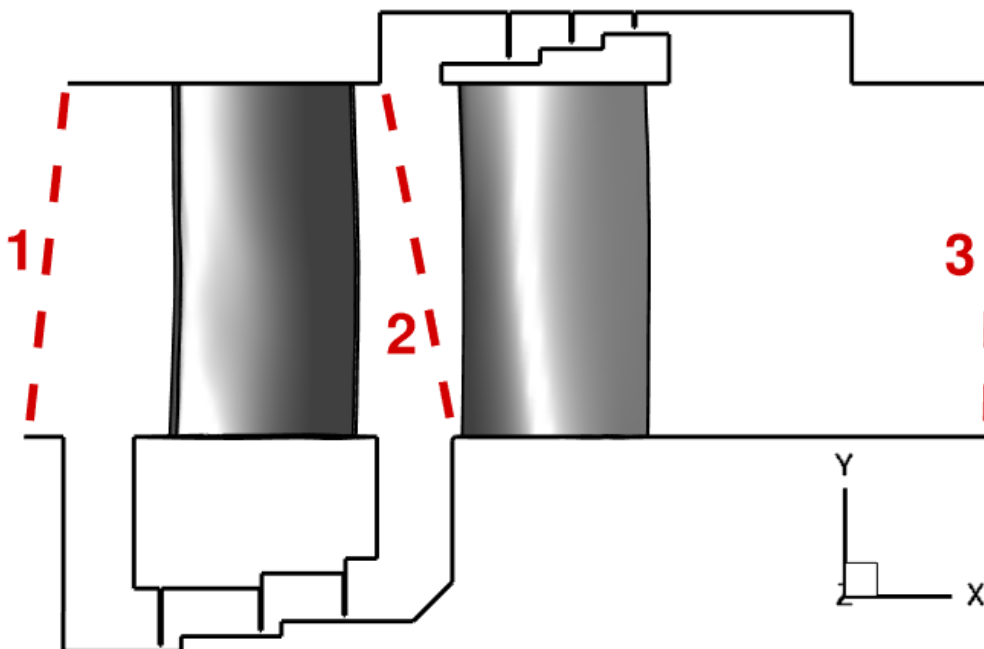


Figure 2-8: Single stage turbine schematic visualizing the selected interface numbering for the calculation of design variables

The parameters are in a first sense mass averaged in circumferential direction to get a spanwise distribution and in addition mass averaged along the span to get a mean value over the whole interface. A detailed description of the implemented code and the files into which the stated information is written out, can be found in Kleinheinz [105]. Alongside with the design parameters, other flow variables are accessible along the span as well as mass averaged over the row interfaces. Table 1 lists all variables that are calculated. All the quantities displayed in Table 1 characterize the main flow field and are therefore very useful for the determination of the convergence level of a solution.

Table 1: List of all quantities that are calculated or assessed at row interfaces distributed along the span, as well as mass averaged over the whole interface

<b>Flow variable/ parameter</b>
Static pressure
Total pressure
Static temperature
Total enthalpy
Mach-number
Entropy
Axial velocity
Relative yaw angle
Absolute yaw angle
Secondary kinetic energy
Polytropic efficiency (total-to-total)
Isentropic efficiency (total-to-total)
Isentropic efficiency (total-to-static)
Total pressure ratio
Total pressure loss
Relative total pressure loss
Entropy generation
Loading coefficient
Flow coefficient
Degree of reaction

Most of the parameters in Table 1 are expected to show up unsteady variations, hence they are examined in terms of

convergence with all the signal processing methods introduced in subsection 2.2.4.1. In this sense, equations Eq. 2-41 to Eq. 2-46 can be used in the same manner to identify the convergence level for these parameters. The user can specify which quantities or parameters are of interest and should be quantitatively evaluated in terms of convergence.

***Polytropic efficiency (turbine)***

$$\eta_P = \frac{\gamma}{\gamma - 1} \ln \left( \frac{T_1}{T_3} \right) / \ln \left( \frac{p_1}{p_3} \right) \quad \text{Eq. 2-47}$$

***Isentropic efficiency (total-to-total) (turbine)***

$$\eta_{is,t-t} = \frac{h_{0,1} - h_{0,3}}{h_{0,1} - h_{is,0,3}} \quad \text{Eq. 2-48}$$

***Isentropic efficiency (total-to-static) (turbine)***

$$\eta_{is,t-t} = \frac{h_{0,1} - h_{0,3}}{h_{0,1} - h_{is,3}} \quad \text{Eq. 2-49}$$

$$h_{is,3} = \frac{\gamma}{\gamma - 1} RT_1 \left( \frac{p_3}{p_1} \right)^{\frac{\gamma}{\gamma - 1}} \quad \text{Eq. 2-50}$$

***Degree of reaction (turbine)***

$$DR = \frac{h_2 - h_3}{h_1 - h_3} \quad \text{Eq. 2-51}$$

***Total pressure ratio***

$$\Pi_t = \frac{p_{0,3}}{p_{0,1}} \quad \text{Eq. 2-52}$$

*Total pressure loss (stationary frame of reference)*

$$\xi_0 = \frac{p_{0,1} - p_{0,2}}{p_{0,1}} \quad \text{Eq. 2-53}$$

*Total pressure loss (relative/ rotating frame of reference)*

$$\xi_{0,rel} = \frac{p_{0,rel,2} - p_{0,rel,3}}{p_{0,rel,2}} \quad \text{Eq. 2-54}$$

*Entropy generation function*

$$\Gamma_{1-2} = \exp\left(\frac{s_2 - s_1}{R}\right), \quad \Gamma_{2-3} = \exp\left(\frac{s_3 - s_2}{R}\right) \quad \text{Eq. 2-55}$$

*Secondary kinetic energy*

The secondary kinetic energy is calculated at each row interface, therefore the indices are dropped for simplicity. Secondary kinetic energy is often used to quantify secondary losses, and can be defined by the pitch-wise averaged velocity profiles method described by Reising et al [55]. A cylindrical coordinate system is used for the derivation (coordinates:  $r, \phi, x$ ). The normalized primary flow field (along the span) is defined as:

$$\vec{v}_{prim}(r) = \frac{1}{\sqrt{v_r(r)^2 + v_\phi^2 + v_x(r)^2}} \begin{bmatrix} v_r(r) \\ v_\phi(r) \\ v_x(r) \end{bmatrix} \quad \text{Eq. 2-56}$$

And the local primary flow field at a x-constant position along the span:



$$\vec{v}_{prim}(r, \varphi) = [\vec{v}_{prim} \cdot \vec{v}(r, \varphi)] \vec{v}_{prim}(r) \quad \text{Eq. 2-57}$$

The local secondary flow field is defined as the difference between the local velocity vector and the primary velocity field:

$$\vec{v}_{sec}(r, \varphi) = \vec{v}(r, \varphi) - \vec{v}_{prim}(r, \varphi) \quad \text{Eq. 2-58}$$

The secondary kinetic energy is then defined as:

$$SKE = \frac{1}{2} |\vec{v}_{sec}(r, \varphi)|^2 \quad \text{Eq. 2-59}$$

*Loading coefficient*

$$\Psi = \frac{h_{0,2} - h_{0,3}}{U^2} \quad \text{Eq. 2-60}$$

*Flow coefficient*

$$\Phi = \frac{v_x}{U} \quad \text{Eq. 2-61}$$

## 2.2.5 GPU acceleration and parallelization approach

MULTI3 is also GPU accelerated using "PGI's Accelerator" [106] programming model, initially started by Huber [107] and finalized by Basol [87]. GPU acceleration offers considerable speed-up of the computations, enabling the performance of unsteady, multi-stage simulations in a matter of hours. However, the main limitation is the GPU on-board memory, which is related to the mesh size that can fit and be simulated on each GPU. MULTI3 requires about 1 GByte of memory per million nodes. Modern GPUs have an on-board memory between 6-16 GB [108], allowing a mesh size of 6-16 million nodes. Multistage simulations that include cavity paths in the computational model can easily exceed mesh sizes of 30-50 million nodes.

To enable simulations of larger mesh size in reasonable time frame, the solver is parallelized on multiple GPU's [109], where each GPU solves a particular domain of the problem and the data at the interface between the different domains is exchanged using the functions of the MPI library. The implementation has been validated on the multiple scenarios including complex, 3D, unsteady turbomachinery simulations.

For problems of bigger size than they would fit into a single graphic card the domain is decomposed in the grid generation stage and distributed into separate graphic cards. The communication between the GPU's is handled using MPI. Subdomain size is adjusted to fit the GPU memory available. Typically 6 million mesh nodes for 6GB or 16 million mesh nodes for 16GB of GPU onboard memory is considered for NVIDIA Tesla K20X and Tesla P100 type graphics cards, respectively.

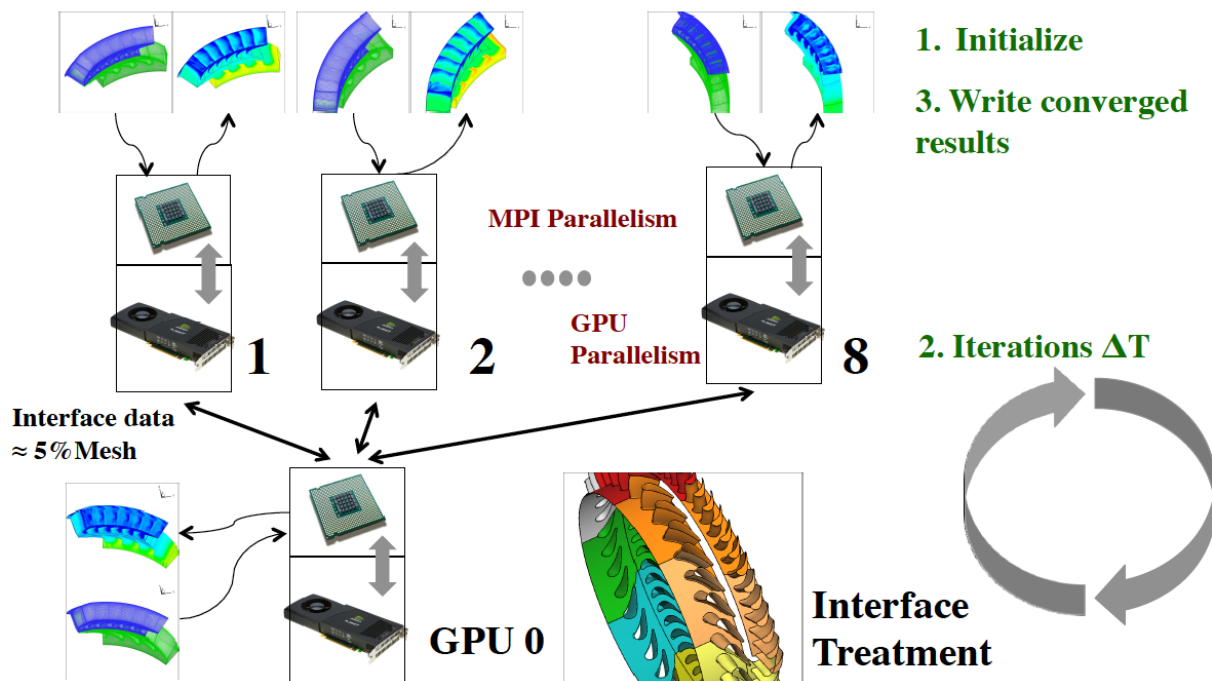


Figure 2-9: Multi-GPU parallelization architecture. A CPU-GPU pair is responsible for sub-domain computations independently, except sub-domain boundaries are computed at "GPU 0" master node

Each GPU is paired with one CPU core. In the pre-processing stage, each subdomain is stored in a separate grid and flow file. MULTI3 framework is initialized with MPI parallel threads equal to number of sub-domains, and associates one GPU with each thread (CPU

core). Each CPU-GPU pair reads sub-domain grid and flow files independently, and all of computational data is transferred to GPU memory. A CPU-GPU pair performs computations on allocated sub-domain independently, except operations on domain boundaries and interfaces. Two types of interfaces need to be treated for every time step during the simulation. Periodic interfaces are between the blade passages in circumferential direction that are within the same blade row. On the other hand, row interfaces are between the adjacent blade rows. Interface data is first transferred from GPU to CPU memory for each sub-domain and assembled at Master node "GPU 0" via MPI synchronous calls as shown in Figure 2-9. The master node is responsible for the treatment of periodic interfaces of the respective row and of row-interface of the adjacent row. Interface treatment is then performed at master node GPU, and results are communicated back to each sub-domain CPU-GPU pair.

## 2.3 Optimization method

Goal of this work regarding the HP turbine is to increase efficiency by applying non-axisymmetric shape on the rotor hub endwall, which will be the result of an optimization cycle. The case with the modified endwall will be experimentally tested in LEC's axial turbine research facility "LISA".

The method used to obtain the optimum non-axisymmetric end wall shape uses the idea of taking the information obtained from previous designs and using it in order to obtain a better behaved shape. The optimization will be performed using the commercial software FINE/Design3D. In this optimization process, the chosen optimization algorithm is a Genetic Algorithm (GA) since it can enhance the capability of reaching the global minimum but with a drawback of needing thousands of iterations to do so. Artificial Neural Networks (ANN) can be used to approximate the CFD computations since it would be too costly to perform a CFD computation for every geometry generated by the optimization algorithm. A database constituted by the design examples feeds the artificial neural network in what is known as the training of the ANN. As new design shapes are generated they are added to the database, updating it. After the update of the database, the ANN is subjected to a new learning step. This process follows until the

predictions of the ANN are closer to what the actual CFD solution would be. The steps for the optimization process are the following:

- Creation of a meshing template for the grid generator using AutoGrid5 and IGG
- Parameterization of the geometry using Autoblade
- Definition of the free and fixed geometrical parameters, generation of the initial database based on CFD simulations of arbitrary geometric samples using FINE /Design3D
- Definition of the optimization goals, run the optimization by means of the ANN, based on self-learning algorithm and performance check to compare the current sample with regard to the optimization goals using FINE /Design3D
- Analyze the CFD results, convergence and selection of the best non-axisymmetric end wall shape

A flow chart of the optimization process is presented in Figure 2-10.

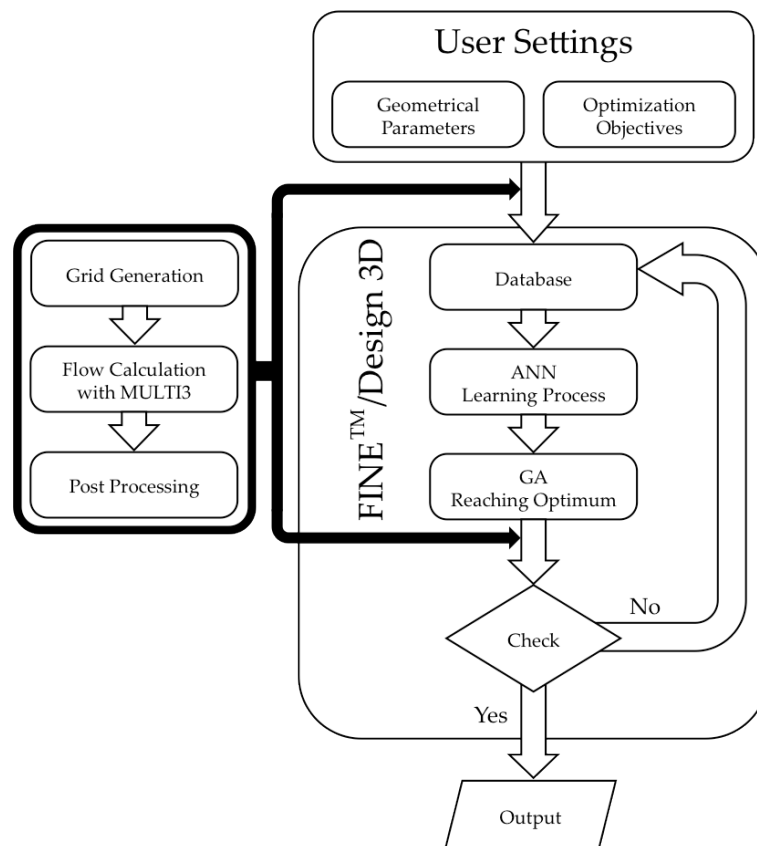


Figure 2-10: Flow chart of the optimization process [70]

### 2.3.1 Endwall parametrization

In any method of geometry optimization, the parameterization of the geometry is a very important step that should be done in a way where it would use as few design variables as possible, while still being able to create physically realistic geometries. The geometry parameterization was done with Autoblade software. Autoblade is a three-dimensional parametric blade modeler, specifically developed for turbomachinery applications, with an advanced fitting module to start designs either from scratch or from an existing geometry. It stacks two-dimensional blade sections along the blade span in order to obtain a three-dimensional blade geometry.

Regarding the endwall parameterization, there are several ways to develop a parameterization of an end wall but it is important to use an approach that does not create unnecessary restrictions. For example, some methods consider the use of sinusoidal curves as shape functions [110]–[114] and although they help to conserve the cross passage area, they also restrict the design space since it has an assumed shape of how the resulting design should be [74].

Instead of assuming a shape function, a parametric-based technique provided by Autoblade is used for the end wall parameterization. Autoblade allows the use of three different types of curves for the parameterization, such as Bezier, B-spline or C-spline curves. In the framework of this work the default Bezier type curves were used. The space of definition of our parameterization is defined as an area built in the  $(m', \theta)$  plane. The mean line of the main blade at hub/shroud section is computed in the first place. This creates the first side limit of the domain inside the blade channel; the second limit to be created is the vertical translation of the first side limit of value  $(\Delta\theta = -2\pi/NB)$  as it is seen in Figure 2-11. The extension of the domain is limited at the inlet and outlet, as well by the mean line of the main blade and its translated repetition. The inlet and outlet are built from either a smooth Bezier curve ending horizontally at the opposite end or from a line segment tangent to the mean line of the blade at the edge point. The advantage of defining the domain in this way is that the perturbation can occur

over a space covering the entire hub surface once repeated, since a  $2\pi$  extent is travelled in the  $\theta$  direction [70].

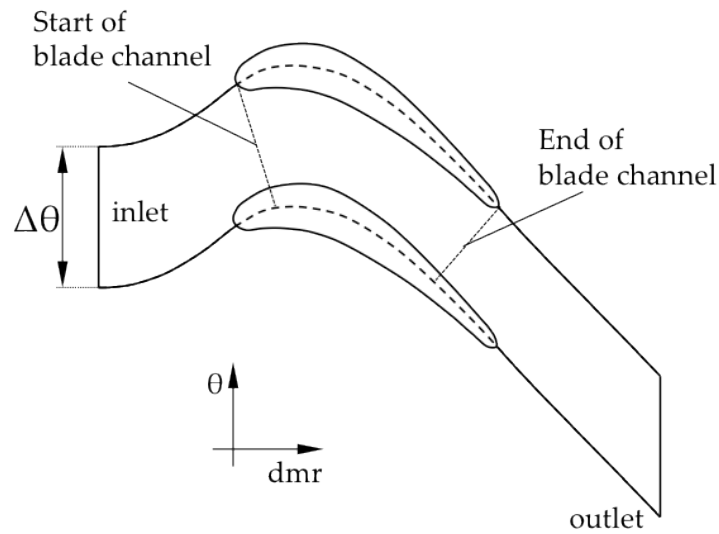


Figure 2-11: “Across method” of endwall parametrization [70]

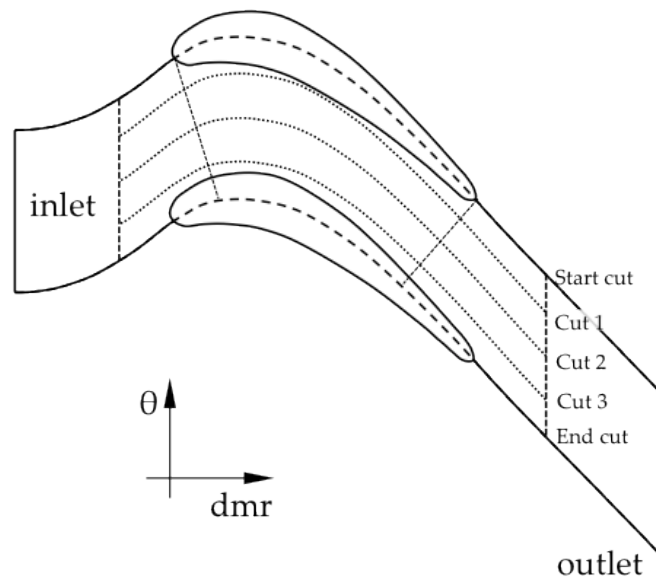


Figure 2-12: “Along method” of endwall parametrization [70]

Although both “Across-” and “Along” method can be used for the endwall optimization, the “Across” method is not recommended for blades with high turning, as the resulting cuts will be clustered towards the suction side and relaxed on the pressure side. The “Across” method is more suitable for compressors or supersonic airfoils. For turbine applications, the “Along” method is

recommended and is the one chosen for the current work. This method creates cuts along virtual streamlines, as seen in Figure 2-12, which are aligned with the blade camber curve. The cuts can extend outside the blade channel but the start and end channel must be identical in order to maintain continuity between periodics.

In the circumferential direction the perturbation law is controlled by height parameters and continuity is automatically ensured using an algorithm, which the user cannot modify. If Bezier curves are used the algorithm will automatically freeze two additional heights. Finally, the resulting parameterization surface is a loft surface passing through each of the cuts.

### 2.3.2 Optimization algorithm

The optimization procedure is done through the software FINE/Design3D from Numeca International. FINE/Design3D is a powerful optimization software specifically developed for turbomachinery applications.

The optimization has the objective of finding the minimum of the objective function through the use of analysis models. In the case of a single objective optimization, FINE/Design3D offers the possibility of using four different types of optimization (Random Walk, Gradient method, Genetic Algorithm and Simulated Annealing). The chosen optimization method was the Genetic Algorithm (GA) due to the fact that in this optimization many local minima may exist in the design space, therefore a global optimization method is necessary.

The sequence of steps used by FINE/Design3D in order to perform an optimization procedure (Figure 2-13) is the following:

**CFD Loop:** The CFD loop starts with the parameterization of the geometry (Autoblade) and is followed by the mesh generation (AutoGrid and IGG). Instead of the CFD flow solver included in the FINE/Turbo package, the in-house developed solver MULTI3 is coupled externally with Design3D. Final step is the post-processing procedure (Tecplot and Matlab). This simulation task starts with a vector of input variables (Design Variables (D)) and provides a vector of output variables (System Responses (R)) [70]

**Optimization:** The optimization loop has the objective of optimizing the System Responses (R) (Geometrical and CFD results) produced by the CFD loop by modifying the Design Variables (D) (Geometrical Parameters) [70]

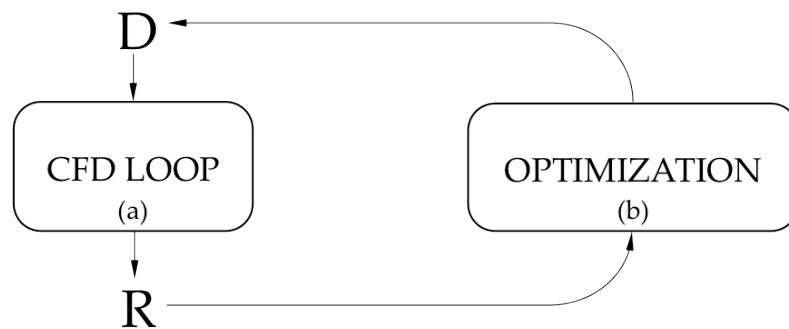


Figure 2-13: Optimization procedure [70]

### 2.3.3 Database generation

Before the optimization process starts it is necessary that a database containing the blade/non-axisymmetric end wall geometries and their associated CFD computations is generated. FINE/Design3D includes an automatic database generation tool that allows the user to create the initial database required for the optimization procedure. The database generation takes a significant part of the total computational resources needed by the global optimization process.

In order to generate the initial database some physical and numerical conditions must be chosen. It is important that these conditions are chosen carefully since they remain the same for the entire optimization procedure. These conditions are:

**Parameterization (Autoblade):** The number of free parameters that will be modified during the optimization process must be as low as possible, while still being able to generate accurate physical results but without over-constraining the design space. If too many parameters are chosen, the computational time will be too high and it is possible that it creates several local minima in the objective function resulting in a very complex optimization process.



**Mesh Template:** The mesh template file is created through the meshing of the baseline geometry. The mesh of the baseline case is created manually by the user. Then, with the help of templates and scripts, the new grids of the database and optimization cycles are created automatically. The mesh must satisfy certain quality criteria, such as cell aspect ratio or minimum cell skewness, to avoid numerical errors and/or solver crashes.

**Post-Processing Macros:** The desired design parameters that will be modified are declared with macros and are the result of the numerical simulations. The macro selection process is very important and they must be carefully selected since the macros used for the database generation will be the ones available during the optimization runs.

The initial database is constituted by several samples and their associated geometries and CFD results. The number of samples that forms the database should be two to three times the number of free parameters chosen by the user [70]. For the current work, it was chosen to have a database with a number of samples of 3 times the number of free parameters. The samples are generated by perturbing all the free parameters within the lower and upper bounds previously selected. FINE/Design3D offers a range of 10 different methods for the database generation and they are based on the Design of Experiments (DOE) concept. Design of Experiments refers to planning, conducting, analyzing and interpreting a number of controlled tests to evaluate the factors that control the value of a parameter or group of parameters. In this work, the chosen method is the default method of Design3D, called Latin Hypercube method [70].

#### 2.3.4 The approximate model

Once the initial database is generated the optimization procedure can be initiated. The optimization is done with the FINE/Design3D software, whose optimization technique is based on the concept of function approximation. The basic principle is to create an approximate model of the original analysis problem so it can be used during the optimization runs instead of the original model, i.e. CFD simulations. By using the approximate model it is expected to have a fast model to predict the aerodynamic performance. Since no

CFD simulations are needed for the approximate model it has less computational cost, so the performance evaluation process must be as fast and accurate as possible in order to correctly emulate the accurate model.

The database samples are used to construct the approximate model and as the number of the database samples increase, with every optimization iteration, it will result in an approximate model with a higher accuracy and capable of generating more efficient geometries.

The optimization process can be either single or multi-objective optimization. In this work, a single objective optimization is performed.

The main objective of a single objective optimization is to find the best solution, which may correspond to the maximum or the minimum value of an objective function. The optimization algorithm has the task of computing the best solution of the approximate model and once the best solution is found by the algorithm, then a CFD computation is performed for this individual for comparison of the prediction. Following the CFD, the database gets updated and this new individual, as well its CFD results, are stored in the database.

On the other hand, in a multiobjective optimization there is no such thing as a single optimal solution. Due to the existence of different objectives, a set of solutions also known as Pareto-optimal is computed.

There are a large number of techniques capable of generating the approximate model, such as the polynomial response surface method, the Kriging model and the support vector machine [115]. In this case, the Artificial Neural Network (ANN) method is the one used by FINE/Design3D and its architecture can be found in the user manual [70].

Typically an ANN is constituted by several layers; a first input layer, one or more hidden layers and a final layer of output nodes. The first layer of the ANN is called the input layer and it connects all the given inputs (i.e endwall geometry and constraints) to each

node of this layer through a connection weight. Every node proceeds to make a summation of the value of the weighted inputs and of an additional bias value resulting in a scalar output. The output is then submitted to a sigmoidal transfer function  $F$  and it is given by:

$$a_n(i) = F\left[\sum_{j=1}^{S(n-1)} W_{ij}a_{n-1}(j) + b(i)\right] = F[i_n(i)] \tag{Eq. 2-62}$$

where:  $F$  is the transfer (or activation) function  
 $W_{ij}$  are the weights  
 $a_i$  is the ANN value for the output  $i$   
 $b$  is the bias value

The purpose of the transfer function is to bound the value of the nodes in order to prevent the ANN from getting paralyzed by divergent nodes and also to introduce non-linearity to the ANN [71]. In Figure 2-14, an example of the commonly used sigmoidal function is shown, given by:

$$F(u) = \frac{1}{1 + \exp(-u)} \tag{Eq. 2-63}$$

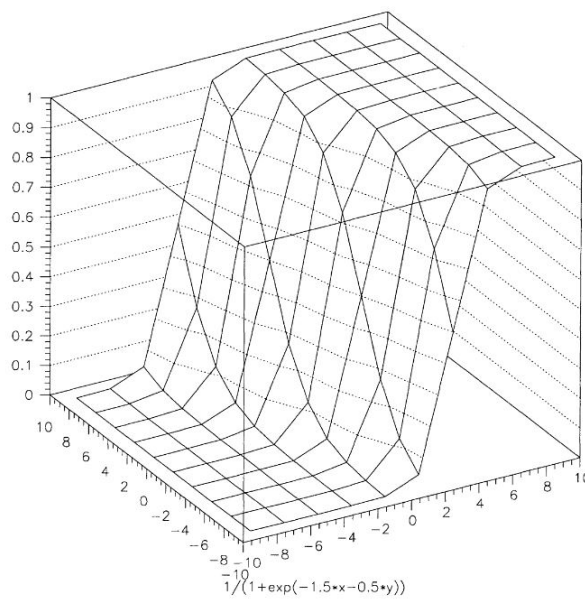


Figure 2-14: Example of sigmoidal function with two nodes [71]

The training of the ANN is done through submitting the network to an initial set of inputs called a training set (database). Since the outputs of the samples in the database are known then the aim of the training will be minimizing an error function [71]. The minimization is done by finding the weights and bias in order to make the actual output vector coincide with the prescribed output vector [70].

The method used for the training is the back-propagation method, also known as "Learning by back-propagation of the errors". This is an iterative method, which calculates the gradient of the loss function with respect to the weights. Once this gradient is calculated it is then fed into an optimization algorithm (e.g gradient descend algorithm), which uses it to update the value of the weights. The value alteration of the weights and bias are done in an iterative way with the purpose of eliminating the error. The error function is given by:

$$Erms(l) = \frac{\sum_t [d(l) - a(l)]^2}{N_t} \quad \text{Eq. 2-64}$$

where:  $Erms(l)$  is error for the output node  $L$  over all the training samples  
 $L$  is the output node index  
 $a$  is the neural network predicted output  
 $d$  is the desired output

The global training error is given by:

$$Erms = \sqrt{\frac{\sum_o (Erms(l))^2}{N_o}} \quad \text{Eq. 2-65}$$

where:  $Erms$  is the global neural network error based on the training database  
 $N_o$  is the number of neural network outputs

### 3 Experimental methods

During the course of this numerical work, a set of experimental data was used for inlet boundary conditions, as well as for validation of the predictions of the numerical model. The experimental measurements have been conducted in two different test facilities. The first one is a research steam turbine test facility from Mitsubishi Hitachi Power Systems, Ltd. The second is the axial turbine research facility “LISA” at ETH Zurich.

#### 3.1 Steam turbine facility at MHPS

The results of the following chapter are from a 10MW research steam turbine test facility in MHPS in Hitachi, Japan. Figure 3-1 shows the four-stage low-pressure steam turbine (L-3 to L-0) rig. The rig is a downscaled model with a 1/3 ratio of a turbine with actual 50in steam turbine blades in the rotor of the last stage, which enable supersonic flow conditions in the relative frame close to the tip region [78].

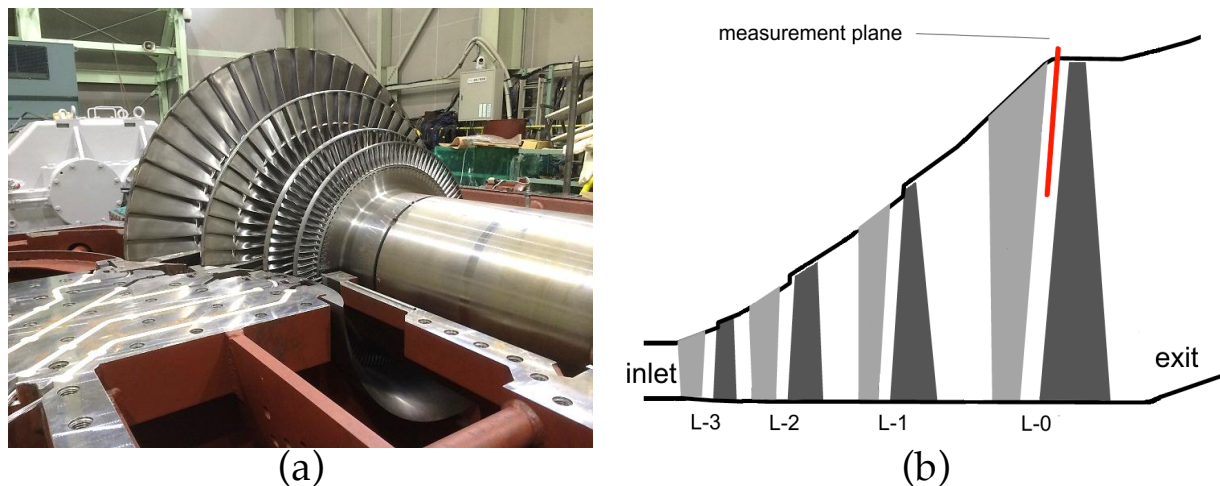


Figure 3-1: MHPS' low-pressure steam turbine test facility where FRAP-HTH and FRAP-OB measurements were conducted (a). Schematic of test facility, the measurement plane of the probe is marked in red (b). [116]

The steam is generated in the boiler and directed in the inlet of the turbine. A condenser at the exit of the last stage, which also controls the exit static pressure, collects the condensed water and directs it back to the boiler. Different operating conditions and loads can be

achieved by varying the controlled inlet temperature and pressure. Additionally, during low load tests, the turbine shaft can be driven by an inverter motor. The turbine's generated power is absorbed by the inverter motor generator and a water brake dynamometer. The measurements were conducted at a rated speed of 10,800rpm, which is converted to 60Hz through a gearbox and is typical for power plants in USA, Korea and Japan.

Steady measurements have been conducted by MHPS at the exit of each stage with a pneumatic 5-hole probe, as well as unsteady flow measurements conducted by Bosdas [116] with a FRAP-HTH probe. The sampling rate of data acquisition for the FRAP-HTH probe is equal to 200kHz over a period of 2s. As seen in Figure 3-1b, the plane covered only the last 30% of the blade span, for one single stator pitch. The measurement grid consisted of 21 radial traverses, with each traverse measuring 19 points in the radial direction.

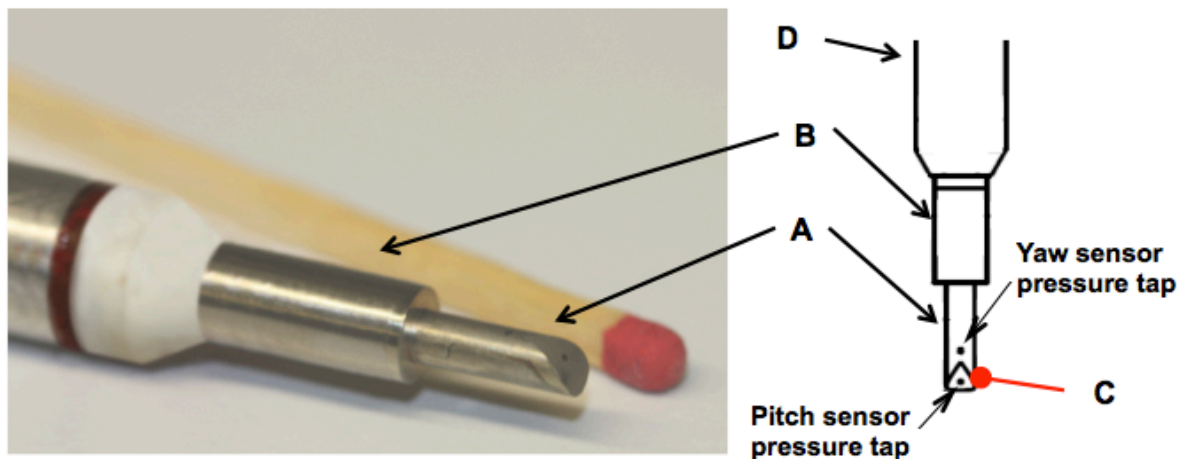


Figure 3-2: FRAP-HTH probe tip schematic. A: Probe tip ( $D_p=2.5\text{mm}$ ), B: Heating elements ( $D_{\text{Heating-Spot}}=4.7\text{mm}$ ), C: Tip temperature monitoring ( $T_{\text{tip}}$ ), D: 8mm shaft. [116]

### 3.2 Axial turbine facility "LISA"

Numerical results of the last two chapters were validated with measurements conducted in the axial research turbine facility named "LISA" of the Laboratory for Energy Conversion at ETH Zurich.



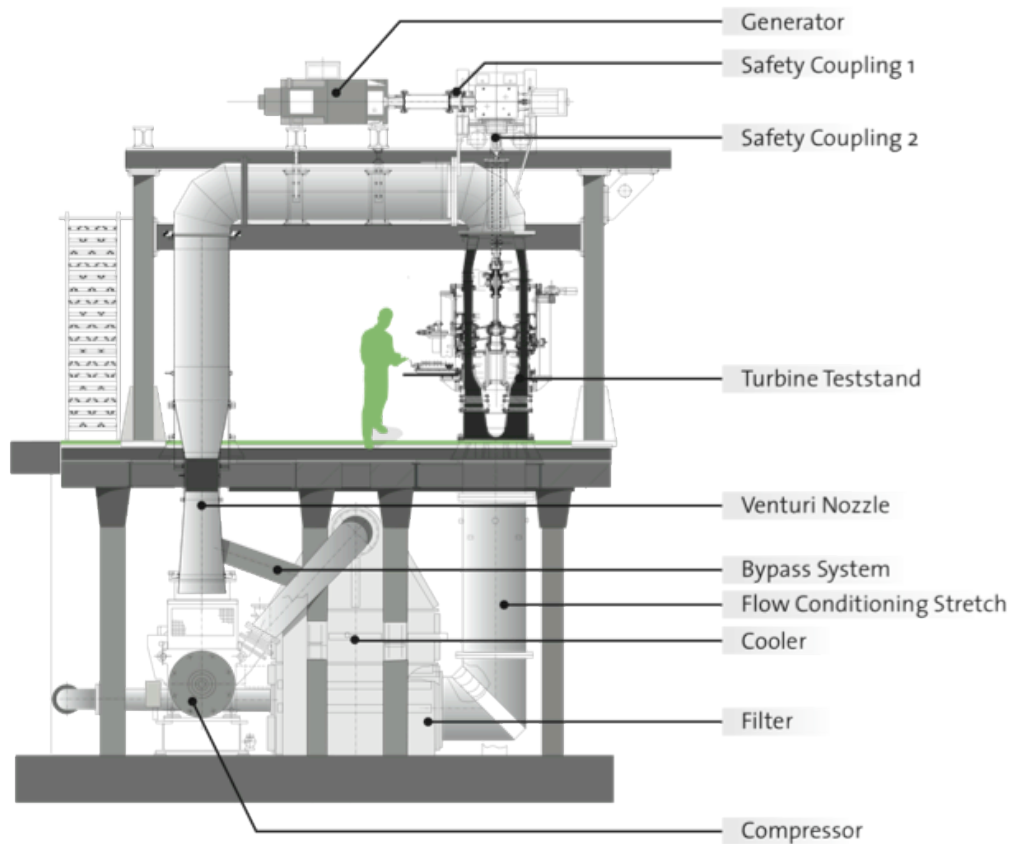
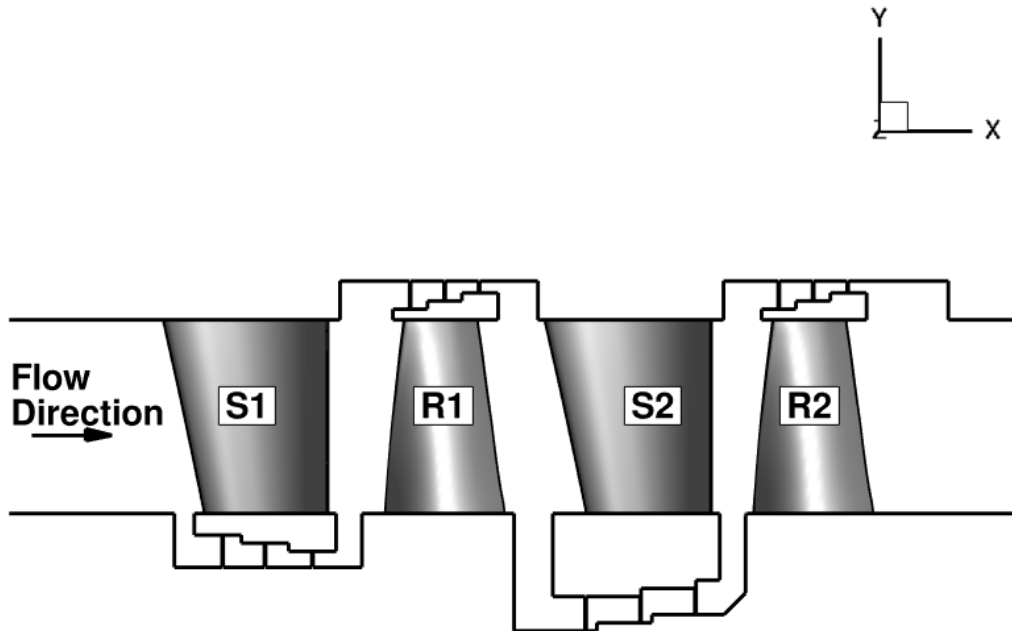


Figure 3-3: Schematic of LISA turbine test facility

The facility extends to 3 stores and a schematic is presented in Figure 3-3. The working fluid is air, which is supplied by a 750kW radial compressor with a maximum pressure ratio of 1.5 and a maximum massflow of 13 kg/s. The exact operating conditions of the compressor are controlled by adjustable inlet guide vanes. The compressed air from the compressor passes through a filter, a two-stage water-to-air heat exchanger and a 3m flow conditioning stretch before it is lead to the axial, vertically positioned turbine to expand. The exit of the turbine is opened to atmospheric pressure. The turbine power is absorbed by a DC generator, which is connected with an angular gearbox to the turbine and halves the rotational speed. Then, an electrical power converter feeds the current back to the grid. High accuracy is achieved in controlling massflow, turbine inlet temperature and rotational speed. Massflow is measured by a calibrated ventouri nozzle upstream of the compressor. Total turbine inlet temperature is regulated by the heat exchanger for a

constant value with an accuracy of  $\pm 0.3\%$ . Finally, the rotational speed is controlled by the generator with an accuracy of  $\pm 0.1$  RPM. The current two-stage configuration is derived from the turbine design extensively presented by Porreca [117].

a)



b)

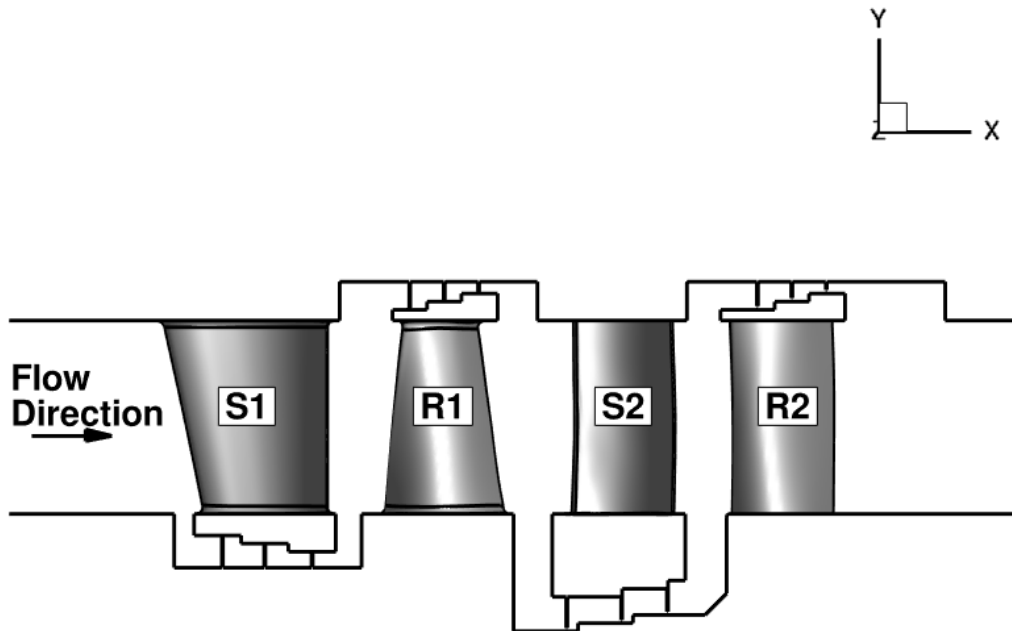


Figure 3-4: Schematic of LISA-H1 (a) and LISA-H2 (b) turbine cases

In this study two two-stage turbine geometries of the "LISA-H" case turbine are considered, mentioned as H1- and H2-case from



here on. The shrouded turbine geometries are representative of high-pressure steam turbines. The two geometries differ in the second stage of the configuration, while the first stage is identical for both cases. Schematics of the cases are presented in Figure 3-4. These two cases have been investigated experimentally and the resulting measurement data have been used during the course of this computational study.

One of the goals of this work was to apply and optimize endwall contouring on the hub endwall of the second rotor blade row of LISA-H2 case. LISA-H1 has been used for validation during the early stages of the development and preparation for the endwall optimization cycle. The operating conditions of the facility for the turbine geometries are given in Table 2.

Time-averaged flow field measurements have been conducted for both cases at second stage inlet and outlet, as well as at second stator outlet, with a miniature cobra-head 5 hole-probe (5HP) [118] with a probe tip diameter as small as 0.9mm. Additionally, the unsteady flow field is measured in the same planes with a FRAP probe. The probe technology has been under development for the past two decades at the Laboratory for Energy Conversion [119], [120]. The two-sensor FRAP design has been accomplished by Schlienger [121] and has a miniaturized tip diameter of 1.8mm for minimum intrusion and blockage effects. The probes are presented in Figure 3-5.

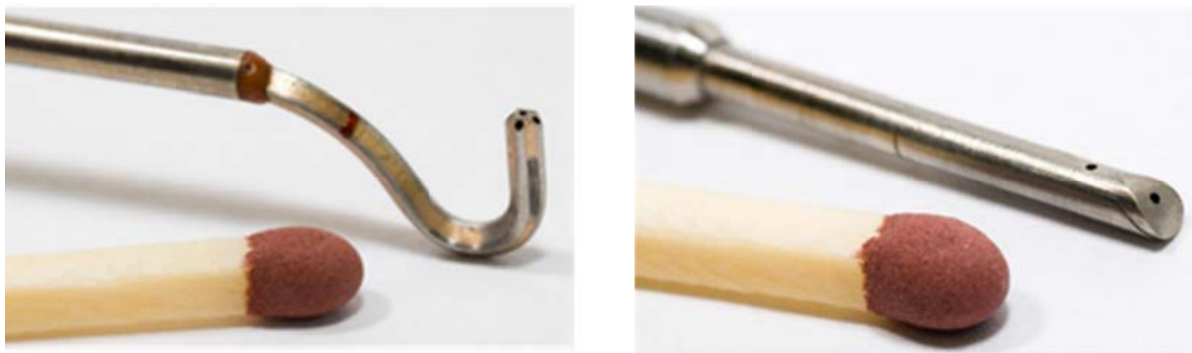


Figure 3-5: 5HP pneumatic probe on the left, FRAP probe on the right (with match for scale comparison)

Table 2: Operating conditions of the turbine

	<b>Variable</b>	<b>Value</b>	<b>Unit</b>
<b>Turbine</b>	Rotor speed ( $\Omega$ )	2700	rpm
	Pressure ratio (2 stages, total-to static)	1.35	-
	Total inlet pressure	129997	Pa
	Total inlet temperature	40	$^{\circ}\text{C}$
	Hub / Tip diameter	660. / 800.	mm
<b>H1 case</b>			
	Mass flow	8.62	kg/s
	Blade count (S1-R1-S2-R2)	50-52-50-52	
<b>1<sup>st</sup> stage</b>	Pressure ratio	0.870	
	Degree of reaction	0.451	
	Stage loading coefficient $\Psi = \Delta h_0 / (r\Omega)^2$	1.216	
	Flow coefficient $\phi = V_x / (r\Omega)^2$	0.329	
<b>2<sup>nd</sup> stage</b>	Pressure ratio	0.843	
	Degree of reaction	0.484	
	Stage loading coefficient $\Psi = \Delta h_0 / (r\Omega)^2$	1.432	
	Flow coefficient $\phi = V_x / (r\Omega)^2$	0.371	
<b>H2 case</b>			
	Mass flow	9.19	kg/s
	Blade count (S1-R1-S2-R2)	50-52-42-42	
<b>1<sup>st</sup> stage</b>	Pressure ratio	0.858	
	Degree of reaction	0.451	
	Stage loading coefficient $\Psi = \Delta h_0 / (r\Omega)^2$	1.337	
	Flow coefficient $\phi = V_x / (r\Omega)^2$	0.354	
<b>2<sup>nd</sup> stage</b>	Pressure ratio	0.854	
	Degree of reaction	0.468	
	Stage loading coefficient $\Psi = \Delta h_0 / (r\Omega)^2$	1.333	
	Flow coefficient $\phi = V_x / (r\Omega)^2$	0.396	

## 4 Unsteady flow mechanisms in a transonic low pressure steam turbine

In this chapter, an unsteady investigation of the last two stages of a low-pressure steam turbine with supersonic airfoils near the tip of the last stage's rotor blade is presented. The goal is to investigate multistage effects and tip-leakage flow in the last stage of the turbine and provide insight on the stator-rotor flow interaction in the presence of a bow-shock wave. The numerical results are combined with experimental data for code validation and comparison with a numerical simulation of the last two stages of a real steam turbine, including tip-cavity paths and seals and equilibrium steam modelling.

### 4.1 Computational setup

#### 4.1.1 Geometry and computational domain

In this study, the last two stages (L-1 and L-0) of MHPS's low-pressure (LP) steam turbine are considered, as it was presented in Chapter 3. The geometrical model was created with a modified blade count for L-0 stators to allow the simulation of only a sector of the full annular domain and it includes full span shrouds and tip-cavity paths and seals for both rotor blade rows. The reason for the modification of blade count was that the real blade count required a half-annular simulation with a prohibitively high computational cost. However, the total number of blades in full annular was increased by only two blades, therefore the change is considered small enough for the flow field to remain representative of the original. Geometry is scaled by 1/3 to match the size of test turbine facility by Haraguchi et al [78]. Geometry solid surfaces and mesh were generated with the geometry of tip-cavities and seals of L-1 and L-0 rotors, as provided by MHPS, using AutoGrid5 and IGG meshing tools by NUMECA.

The computational domain consists of four blade rows plus the diffuser and is presented in Figure 4-1. A multi-block structured, body fitted mesh is generated for each passage separately. In total, 156 radial nodes were used in spanwise direction with higher clustering towards the endwalls.

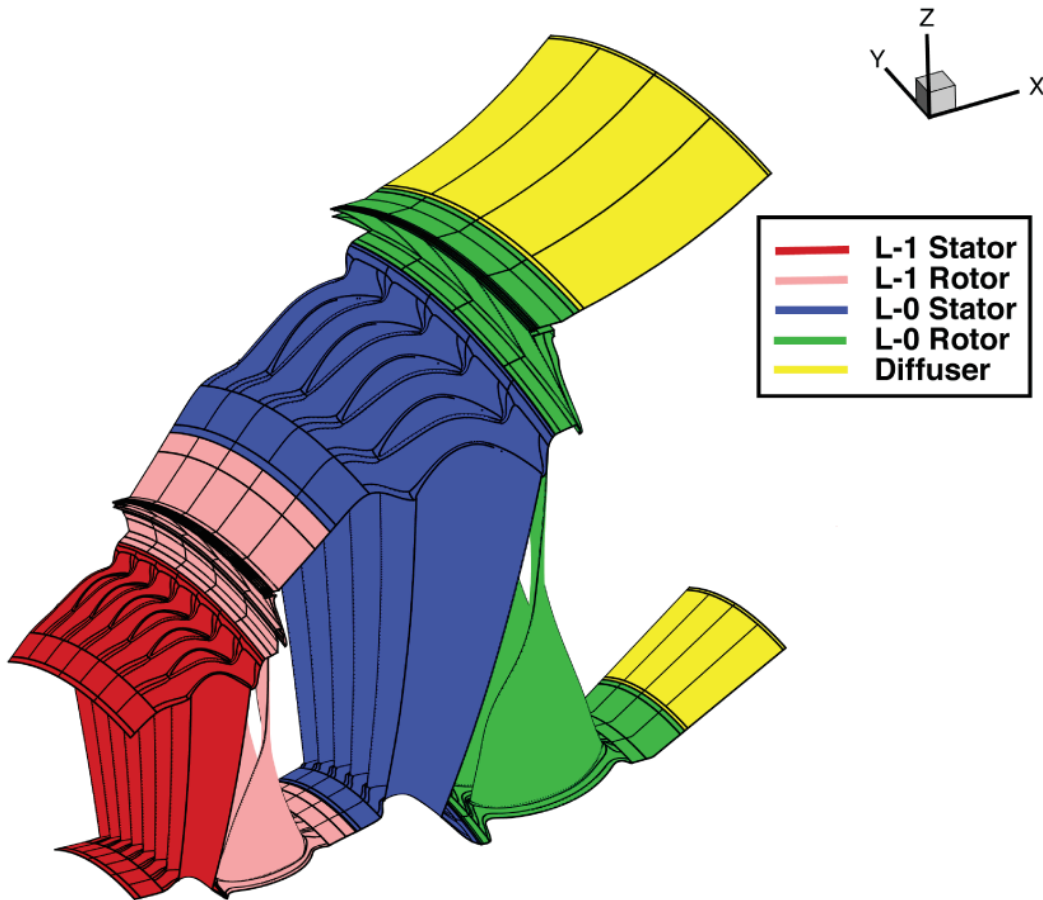


Figure 4-1: Solid surfaces of L-1 and L-0 domains plus diffuser

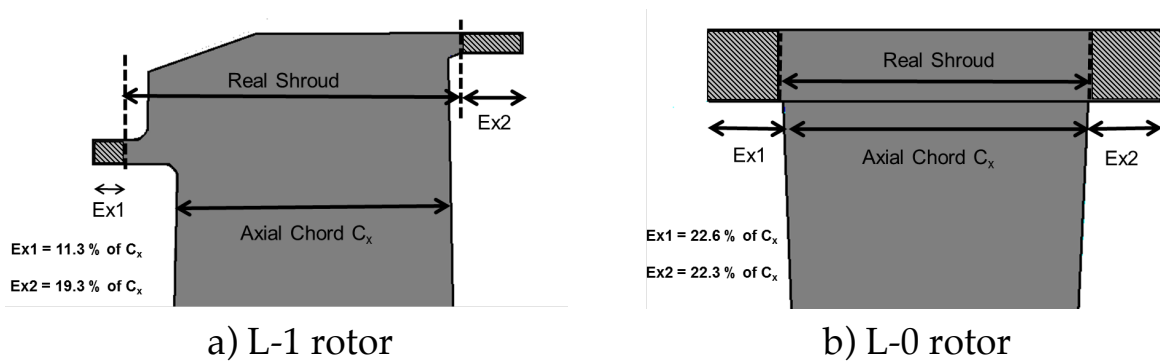


Figure 4-2: Shroud geometry of L-1 and L-0 rotor blades

A larger portion of these nodes was clustered close to the tip-cavity regions of the rotors in order to increase the accuracy of the numerical model at the interaction zones of the cavity and the main flow. However, in order to achieve matching interfaces in the domain with acceptable mesh quality, the tip shroud had to be extended in both stages.

Shroud of L-1 and L-0 rotors had to be extended, both at leading edge and trailing edge to achieve matching interface with the main flow domain.

Tip shroud geometry of L-1 rotor is extended by 11.3% and 19.3% of axial chord length at the leading and trailing edge, as shown in Figure 4-2a. Mesh in this region between tip-shroud and seals-casing is resolved with ~1.6 million mesh nodes for a single passage. Matching interface between all blocks of cavity region and main flow, as well as between nozzle and bucket domain interfaces, has been successfully achieved.

Similarly for L-0 stage bucket, tip shroud geometry of L-0 rotor is extended by 22.6% and 22.3% of axial chord length at the leading and trailing, as shown in Figure 4-2b. Mesh in this region between tip-shroud and seals-casing is resolved with ~ 1.8 million mesh nodes for a single passage. Mesh is resolved using 56 mesh nodes in radial span of the tip-cavity region.

In total, 21 blades were modeled resulting in a mesh of almost 57 million nodes, of which more than 20 million were used in the regions of L-1 and L-0 cavities to resolve the complex geometry and capture unsteady flow features. The  $y^+$  value is kept below 2.5 in the whole computational domain. More details about the mesh of each blade row and mesh quality are given in Table 3 and Table 4, respectively. Despite the presence of some skewed cells, especially in the region of tip cavity and seals of L-1 stage, the overall quality is considered well within acceptable range.

Table 3: Mesh size of the different flow domains

Domain	No. of Blades	GPUs	Mesh Size (millions)
L-1 Stator	7	3	9.2
L-1 Rotor	5	5	21.8
L-0 Stator	5	3	8.5
L-0 Rotor	4	4	14.6
Diffuser	-	2	2.6
<b>Total</b>	<b>21</b>	<b>17</b>	<b>56.7</b>

Table 4: Mesh quality report of whole domain

Minimum angle	Maximum aspect ratio	Maximum expansion ratio
4.6°	1752	5.21

The whole mesh was created with fully matching interfaces, both between blocks and row interfaces, in order to eliminate interpolation errors, which may lead to considerable loss of accuracy at the regions where highly unsteady phenomena take place.

Part-span connectors are not included in the numerical model, neither for L-1 nor for L-0 stage, due to the fact that including both them and the tip cavities and seals in the numerical model increase considerably the mesh generation complexity, as well as mesh size requirements. However, its effect is considered to not be significant, as the analysis focuses above 90% of the radial span.

The full computational domain was split in 17 sub-domains in such a way to allow them to fit on-board GPU memory of 6 GBs of “Nvidia K20X” GPUs of Piz Daint computing system. 17 graphic cards were used in total. Simulations have been performed using in-house developed CFD code “MULTI3” with equilibrium steam modelling. Computational study has been carried out using Piz Daint Cray XC30 hybrid computing system in Swiss National Supercomputing Centre CSCS in Lugano, Switzerland, under project ID s594.

#### 4.1.2 Boundary conditions and simulation settings

The inlet boundary conditions are taken from experimental measurements conducted by MHPS at the exit of L-2 stage. The measurements have been performed at the inlet of the turbine and the outlet of each stage separately using a 5-hole probe, resulting in time-averaged radial profiles of flow quantities. Using these experimental data, non-uniform, radial profiles of total pressure and total temperature, along with flow angles (yaw and pitch) distributions are imposed in the inlet of the computational domain.

Regarding outlet boundary conditions, representative value of static pressure, also extracted from experimental measurements, with radial equilibrium is imposed at the hub endwall in the diffuser outlet. Additionally, no-slip, adiabatic wall boundary conditions are set for all solid surfaces. The sliding interface approach is used at the interface between the rows.

Unsteady simulations have been performed, under these boundary conditions, using dual time stepping approach. 120 equal time steps have been used for each period, where a period is defined as the rotation of four rotor blades of L-0 stage. For each physical time step, 200 sub-iterations are simulated with CFL number of 0.7.

Due to the presence of very fine cells in the computational mesh, especially close to the cavity regions, a sufficient number of sub-iterations is needed in order to ensure proper propagation of information through the regions of very high node clustering, due to the fact that smaller cells need more sub-iterations for the flow to develop properly compared to bigger cells. Both the number of physical time steps and sub-iterations are a result of a separate study that was conducted during the course of the main investigation.

### **4.1.3 Convergence monitoring**

The simulation has covered more than three-full revolutions of the rotor domain. One full rotor revolution requires 4.5 days for completion. For the assessment of convergence of the unsteady simulation, two criteria have been set. On one hand, mass flow levels are monitored over time at the interface of each blade row, as well as the inlet and the outlet of the domain.

Results are presented in Figure 4-3 for the last two periods of the simulation, where the calculated mass flow at each row is normalized with the real mass flow as was measured and provided by MHPS. Location of interfaces is visible in top left schematic of Figure 4-3.

As observed in Figure 4-3, the mass flow rate at L-1 stator and L-1 rotor inlet is fairly constant, while some fluctuations are present in the downstream blade rows. This could be a result of the rotor blades rotation and some inflow and outflow from the periodic boundaries to adjacent domains. The calculated mass flow rate in

the inlet of the domain is predicted with good accuracy compared to the experimentally measured, with a difference below 0.4%. The mass imbalance observed between inlet and downstream interfaces could be due to interpolation at the sliding mesh interface. Nevertheless, the difference is kept at low levels.

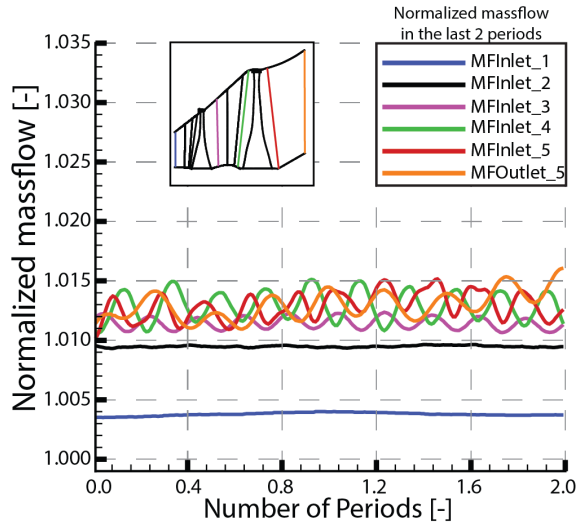


Figure 4-3: Convergence according to mass flow rate in the last 2 periods

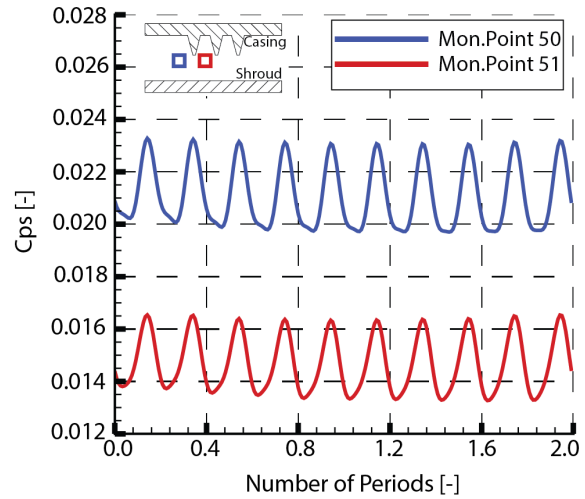


Figure 4-4: Static pressure variation over time at monitoring points 50 and 51

On the other hand, the pressure levels are monitored at different locations by setting monitoring points throughout the whole computational domain. In total, 55 points were used. To keep it concise, the static pressure coefficient  $Cps$  for only two monitoring points is presented indicatively in Figure 4-4 for the last two periods of the simulation. Static pressure coefficient is defined in Eq. 4-1. It is important to mention that the inlet refers to the conditions in the inlet of the machine, not the inlet of the computational domain. Exit refers to the conditions in the exit of the machine.

$$Cps = \frac{P_{s,CFD} - P_{s,exit}}{P_{t,inlet} - P_{s,exit}} \quad \text{Eq. 4-1}$$

The location of the presented monitoring points is in the tip-cavity path of L-0 rotor between casing and shroud, with one of them being located directly upstream of the first seal and the second directly downstream of the first seal. Schematic is shown on top left



of Figure 4-4. These monitoring points were specifically chosen to be presented because they are located in a region with very high mesh clustering and consist of the thinnest cells with the highest aspect ratio of the whole domain. As shown in Figure 4-4, the static pressure coefficient for both points shows a periodic modulation of amplitude levels over a constant mean value. It is, therefore, fairly safe to assume that if this region of the mesh shows a periodicity of the solution that is preserved over different periods, then regions with much larger cells will have already reached a satisfactory level of convergence. At this point, it is important to mention that the convergence monitoring, as well as the Runge Kutta and preconditioning scheme, discussed in Chapter 5, were not yet implemented on the code.

## **4.2 Results and discussion**

### **4.2.1 Validation of numerical model**

The validity of the numerical model has been extensively evaluated with available experimental measurements conducted in the test facility. More specifically, predictions of the CFD model have been compared with 5-hole probe (5HP) measurements conducted by MHPS at the outlet of L-1 and L-0 stages. More importantly, numerical results were additionally compared with time resolved and time averaged measurements at the stator exit of the last stage of MHPS's LP steam turbine that were conducted by Bosdas et al [116]. Measurements were conducted in MHPS's test facility in Japan using a novel fast response heated probe (FRAP-HTH) and was the first time that time resolved measurements in wet steam environment with supersonic relative flows at the rotor inlet had ever been reported. Details on FRAP measurement method and uncertainty are available in the original publication [116].

The locations of the experimental measurements that were used for comparison with the current numerical study are presented in Figure 4-5.

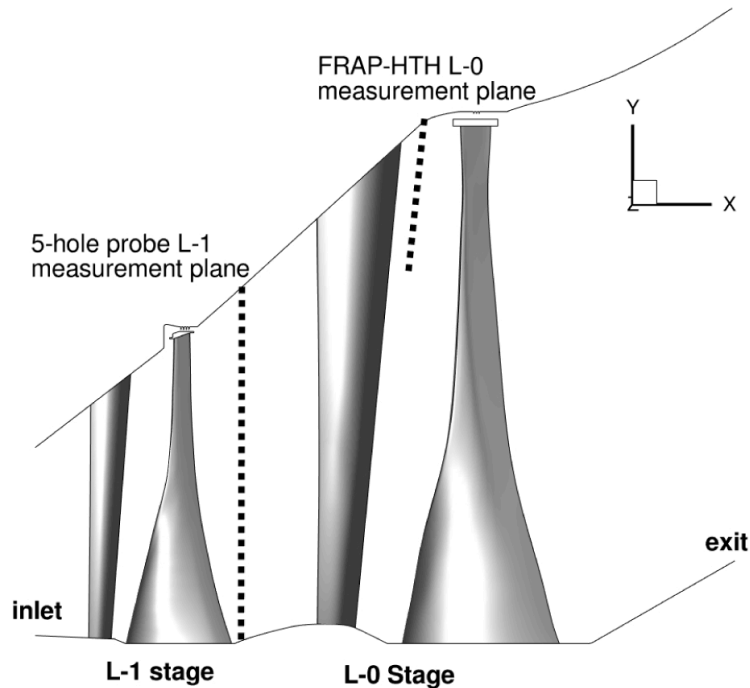


Figure 4-5: Schematic of steam turbine test facility with respective probe measurement locations

#### 4.2.1.1 Comparison of CFD with 5-hole probe at L-1 rotor exit

Figure 4-6a and b show comparison of CFD with 5HP experimental data for absolute yaw angle, as well as total temperature across the blade span at L-1 rotor exit, respectively.

CFD results are circumferentially averaged over five rotor pitches and time averaged over five rotor blade passing periods of L-1 rotor blades with 156 nodes in spanwise direction, while 5HP measurements were performed along a single radial traverse and averaged over 10 sample data measured at intervals of a second with 20 points in spanwise direction.

For absolute yaw angle, only grid resolution is shown, while total temperature has been normalized by dividing both numerical and experimental data with the mean of experimental values.

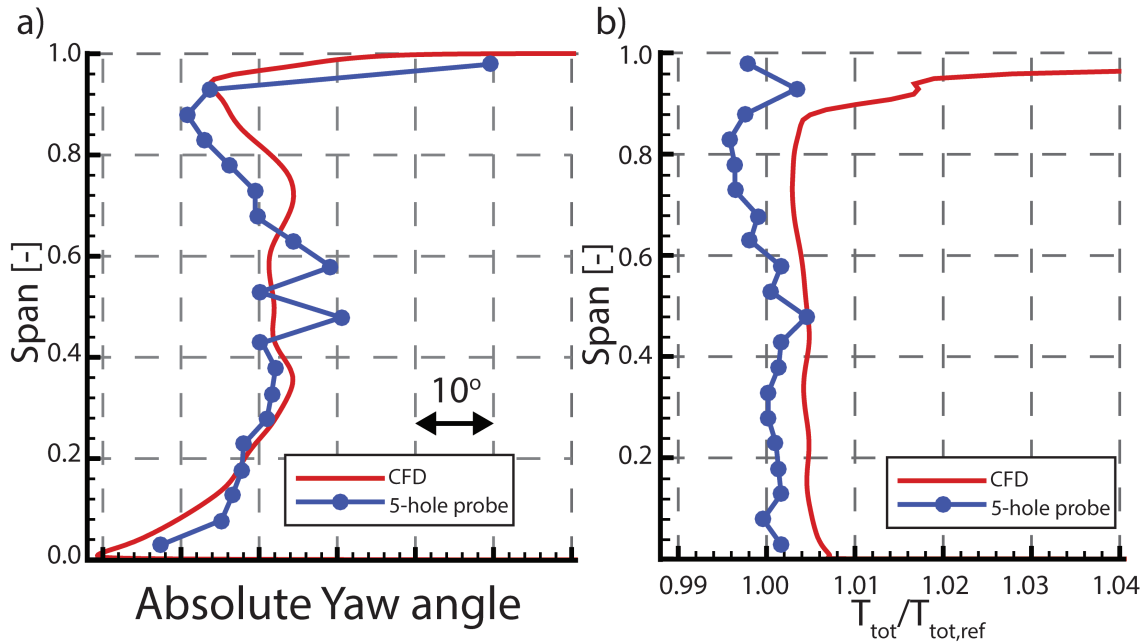


Figure 4-6: Comparison of CFD and 5HP for absolute yaw angle (a) and total temperature (b) at rotor exit of L-1 stage

As shown, a good agreement has been achieved between numerical results and experimental data, both in trends and absolute values across the span. The RMS deviation between them is  $3.8^\circ$  but the value is increased due to the very high gradient close to the tip. The mismatch in yaw angle between 40% and 60% of the span is due to the presence of the part-span connector (PSC), which causes an overturning of the flow at 58% and 48% span. Part-span connectors are not included in the numerical model. Separate in-house studies on the part-span connector showed that the changes are only local and the tip-region remains unaffected by its presence in the computational model [109].

Total temperature is well predicted by CFD, with RMS difference from experiments equal to 1.15%. The effect of PSC is also visible on total temperature that causes a slight increase in the exact same span locations.

It is worth noting here that total temperature is not calculated using isentropic relations of the ideal gas but is rather indexed directly from the steam tables.

#### 4.2.1.2 Comparison of CFD with time-averaged FRAP-HTH probe at L-0 stator exit

In this paragraph, CFD predictions are compared with time-averaged results of FRAP-HTH measurements at the outlet of L-0 stator. This area is of particular interest because the flow becomes supersonic in the relative frame of reference in the inlet of the last rotor, generating a shock wave upstream of the rotor leading edge [6]. Figure 4-7a and b show comparison of CFD with FRAP-HTH for delta flow yaw angle and relative Mach number, respectively.

In Figure 4-7a the absolute yaw angle is subtracted from the mean blade metal angle, representing essentially the deviation flow angle at the stator blade exit. Positive values indicate overturning of the flow, while negative values imply flow underturning. In Figure 4-7b, relative Mach number has been normalised by dividing both numerical and experimental data with the mean of experimental values.

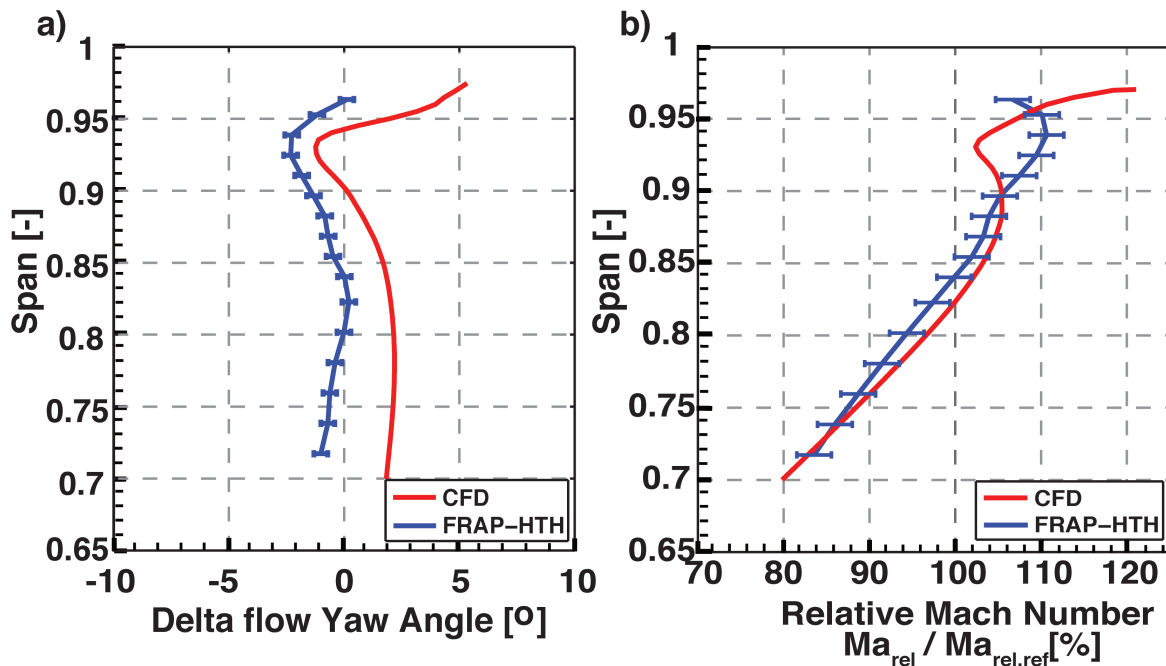


Figure 4-7: Comparison of CFD and time-averaged FRAP-HTH for delta flow yaw angle from the mean blade metal angle (a) and relative Mach number (b) at L-0 stator exit

CFD results in Figure 4-7 are circumferentially averaged over five L-0 stator pitches and time averaged over four rotor blade passing periods of L-0 rotor blades with 57 nodes in spanwise direction, while FRAP-HTH measurements are time averaged and circumferentially area averaged over one L-0 stator pitch with 16 points in spanwise direction.

Comparison shows that yaw angle is slightly over predicted by  $2.4^\circ$  on average compared to measurements but trend is captured accurately. The reason of the mismatch could rely on the fact that the computational model has a slightly modified blade count compared to the real, which was done in order to allow the simulation of only a sector of the full annulus. The offset could also be due to probe alignment error during installation.

Relative Mach number also matches well the measurements both in trend and in absolute values, with RMS deviation equal to 3.27%. The difference observed above 90% span could be due to the fact that measured values are very close to the probe's calibration range.

#### 4.2.1.3 *Comparison of CFD with time-resolved FRAP-HTH probe at L-0 stator exit*

Comparison of CFD predictions with time-averaged FRAP-HTH and 5-hole probe experimental data has shown good agreement. Finally, numerical prediction of static pressure coefficient,  $C_{ps}$ , at 90% span at the exit of L-0 stator is compared with time-resolved experimental data of FRAP-HTH and results are presented in Figure 4-8, for four time steps of one rotor blade passing period. Direction of rotation is from left to right and observer looks downstream in all figures.

As shown in Figure 4-8, there is a good agreement between CFD and experiments, both in trend and phase of the unsteady peak-to-peak fluctuations for all time steps. The difference in absolute values is probably due to the different spatial resolution of the two methods. Regarding the experimental results, the FRAP-HTH probe tip size enables a minimum spatial resolution of 2.5mm in the circumferential direction where the shock propagates. This poses limitations in spatially resolving the pressure step of the shock wave due to the greater tip size compared to the shock wave length

scale [122]. On the other hand, the greater spatial resolution obtained with the CFD results, with maximum cell distance of 0.95mm, result in higher peak-to-peak fluctuations of the static pressure coefficient and it is believed that this is the main reason for the difference in absolute values. The interaction of the shock wave with the probe requires further investigation.

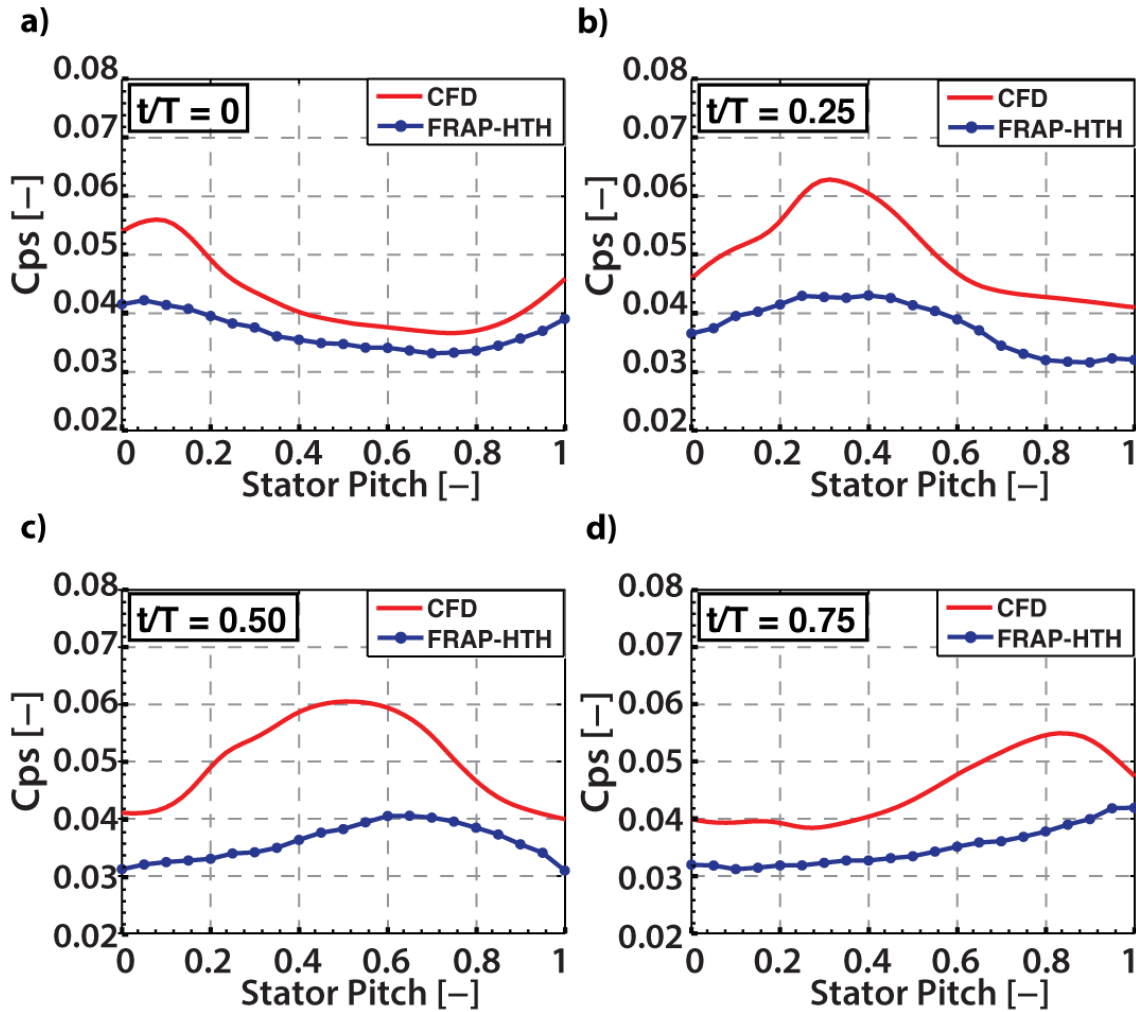


Figure 4-8: Comparison of CFD and time-resolved FRAP-HTH of Cps [-] at L-0 stator exit, 90% span – Unsteady comparison in four time steps of one rotor blade passing period

The results presented so far show that the modified solver with equilibrium steam modeling is able to provide reliable predictions of the flow field in the last two stages of the LP steam turbine. Being able to trust CFD predictions is crucial in understanding the complex, unsteady, three-dimensional flow features in wet steam

flows and in gaining insight of the flow in regions where measurements are infeasible.

#### 4.2.2 Unsteady bow shock wave interaction with stator

As it has been reported [116], the detached bow shock wave at the rotor leading edge of the last stage increases the flow unsteadiness compared to the subsonic region, both in pressure and flow angles. Supersonic airfoils require unique incidence in the inlet [6] and this increased unsteadiness can lead to higher losses. Key in identifying the cause of this is to understand the stator-rotor interaction and its effect on the flow field. For this reason, time resolved results are presented in this section.

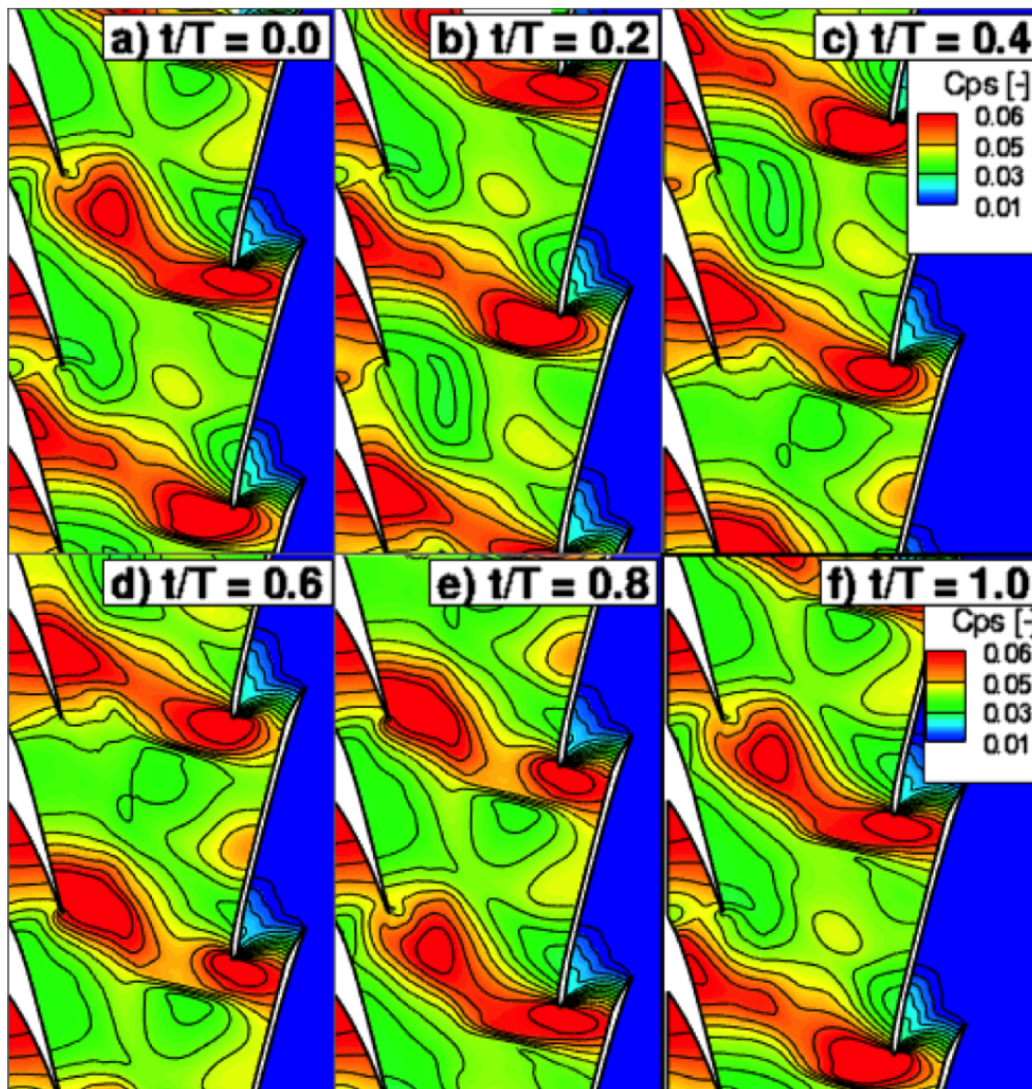


Figure 4-9: Static pressure coefficient  $C_{ps}$  [-] at 90% span - Bow shock formation and interaction with upstream stator for one rotor blade passing period



Figure 4-9 presents blade-to-blade contours of static pressure coefficient at 90% of the blade span, where the flow is supersonic relative to the rotor inlet, in six time steps of one rotor blade-passing period.

Direction of flow is from left to right and the rotor blades are moving from top to bottom. The bow shock wave can be identified by regions of sharp increase of static pressure or  $C_{ps}$  values. Analysis will focus on the trailing edge of the second stator blade looking from the top.

In the beginning of the period, the bow shock wave is not interacting with the suction side of the upstream stator, as seen in Figure 4-9a. As the rotor blades are moving, the bow shock wave impinges on the suction side of the upstream stator and starts moving along it (Figure 4-9b and Figure 4-9c). It is observed that the boundaries of high-pressure region caused by the bow shock wave are fairly straight, as shown by the black dashed lines in Figure 4-9c. However, as it is moving with the rotor blade, it starts interacting with the stator trailing edge and its shape deforms and bends backwards, opposite to the direction of rotation (Figure 4-9e). It has been seen before that an upstream metal blockage can result on a shock wave angle variation [123]. While it tries to overcome the trailing edge, it can be seen that static pressure is increasing also in the pressure side of the upstream stator. Finally, the shock detaches from the trailing edge of upstream stator and impinges on the suction side of the next upstream stator blade, Figure 4-9f. Such an interaction of the shock wave with the upstream row could not be captured by any mixing-plane or single blade row configuration.

In order to further analyze the effect of the bow shock wave interaction with the upstream stator, the unsteady flow field was investigated for a single stator pitch at two axial locations, at 92.5% and 107.5% of the blade's axial chord. The locations are visible in the schematic in the top of Figure 4-10 and side of Figure 4-12, respectively. The results are presented in Figure 4-10 to Figure 4-13 and the observer looks downstream in all figures.



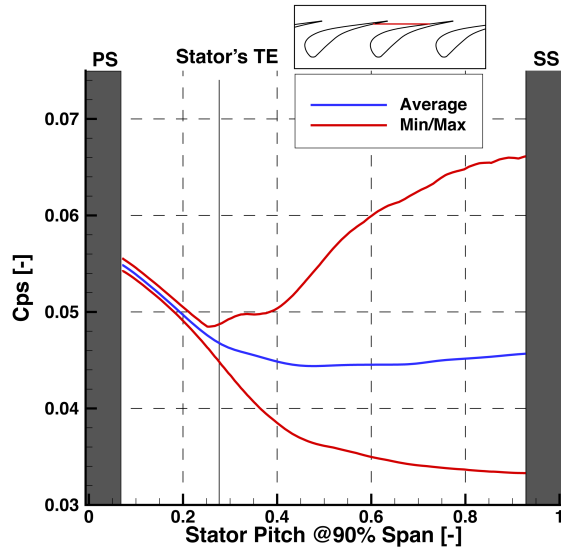


Figure 4-10: Circumferential distribution of  $C_{ps}$  [-] at 92.5% axial chord of L-0 stator blade

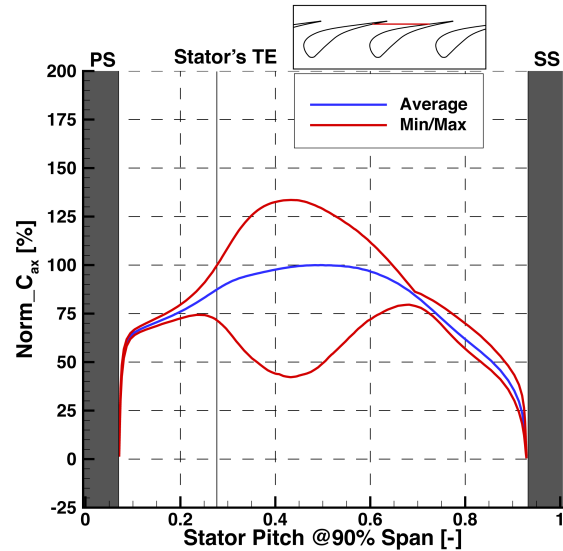


Figure 4-11: Circumferential distribution of normalized axial velocity  $C_{ax}$  [%] at 92.5% axial chord of L-0 stator blade

Figure 4-10 shows the circumferential distribution of static pressure coefficient at the passage between two blades at 90% span, located at 92.5% of stator's axial chord. The results are time averaged over four rotor blade passing periods and are presented with the solid blue line, for one stator pitch. The solid red lines represent the minimum and maximum values of all time steps, obtained from the unsteady data. Since the axial line cuts through the blades, approximately 7% from left and right in the plot represent the pressure side (PS) and suction side (SS), respectively, with the grey shaded area.

As shown in Figure 4-11, starting from the pressure side, the time averaged static pressure coefficient decreases from 0.055 to 0.045 at around 40% of stator pitch and remains constant along the stator pitch until the suction side. The peak-to-peak fluctuations are relatively low in the region close to the pressure side and increase almost 24 times close to the suction side, where they reach  $\pm 34.4\%$ . The interaction of the bow shock wave with the flow in the unguided region above 30% of the stator pitch is very clear by the high unsteadiness present, while the flow shows very low unsteadiness below 30% because it is protected from the influence of the shock wave by the downstream part of the solid blade.

For the calculation of the peak-to-peak fluctuations, Eq. 4-2 was used.

$$\frac{rms(\widetilde{Fq}_{max} - \widetilde{Fq}_{min})}{mean(\overline{Fq})} \times 100 [\%] \quad \text{Eq. 4-2}$$

It is additionally observed that the maximum Cps on the suction side is greater than the maximum Cps on the pressure side. This implies that there are moments in time when the blade is counter-loaded close to the trailing edge of the blade.

These high fluctuations on static pressure not only increase the unsteady loading in the blade but, in worst case could even lead to a boundary layer separation on the suction side of the blade, which would be detrimental for the efficiency. If there were a boundary layer separation, one would expect that the axial velocity would receive negative values due to flow recirculation. However, looking at the axial velocity in Figure 4-11, there is no such evidence of a boundary layer separation.

The axial velocity is reducing to zero close to the walls due to the no-slip boundary conditions. Both time averaged and min-max values have been normalised with the maximum velocity of the time averaged results, located in the centre of the passage. As seen in Figure 4-11, unsteadiness is fairly low close to the pressure side of the blade with  $\pm 4.5\%$  fluctuations, while it is more than double close to the suction side with  $\pm 10.4\%$  peak-to-peak variations. More importantly, the line of minimum  $C_{ax}$  is greater than zero at all time steps, implying there is no flow recirculation at any point in time due to the interaction with the travelling shock wave. This confirms previous findings by Bosdas et al [116], where no clear evidence of periodical wake widening could be experimentally measured.

To analyze the flow field downstream of stator, time-space diagrams for four-rotor blade passing periods are used for one stator pitch at 107.5% of axial chord and 90% span. Figure 4-12 and Figure 4-13 show the absolute flow yaw angle relative to the blade metal exit angle (deviation angle) and the static pressure coefficient Cps, respectively. Positive values of deviation angle indicate flow overturning while negative values imply flow

underturning. Location of the line is shown on schematic at left of the figures.

In both plots, features travelling with the downstream rotor appear as inclined parallel lines (i.e. bow shock wave), while features related to the stationary frame of reference are visible on vertical lines (i.e. stator wake). Observer looks downstream in both plots.

The time-averaged results of deviation angle have shown a constant underturning along the whole stator pitch of  $2.5^\circ$  on average, while the unsteadiness is  $\pm 3.1^\circ$  at 20% of the pitch. The high fluctuations observed in the middle of the passage between 30% and 70%, both in Figure 4-11 and Figure 4-12 are related to the modulation of the wake due to the interaction with the passing shock wave. Both axial locations of 92.5% and 107.5% happen to capture the upstream and downstream boundary, respectively, in which the modulation of the wake occurs.

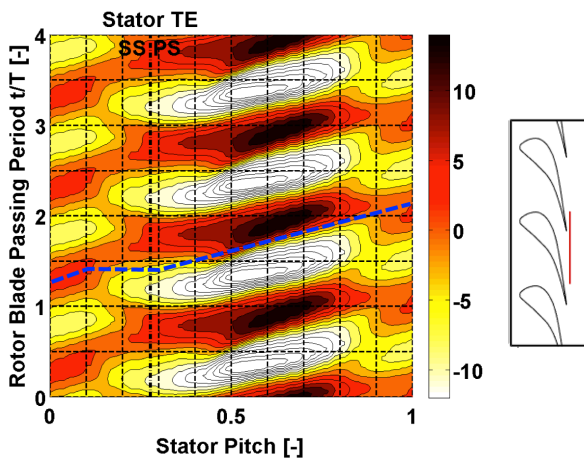


Figure 4-12: Circumferential distribution of deviation flow angle  $[\circ]$  at 107.5% axial chord of L-0 stator blade, 90% span

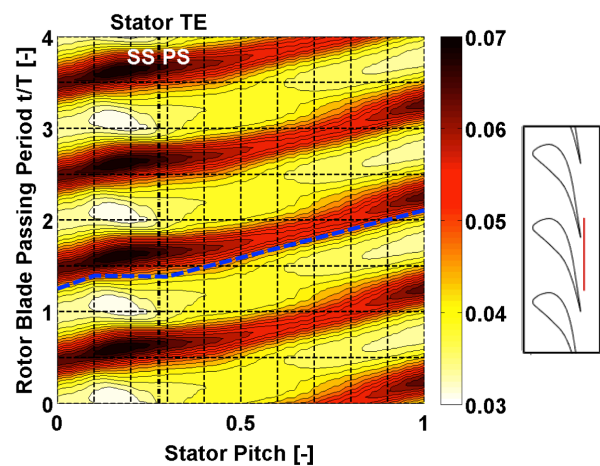


Figure 4-13: Circumferential distribution of  $C_{ps} [-]$  at 107.5% axial chord of L-0 stator blade, 90% span

As seen on Figure 4-12, the minimum and maximum values appear in constant position but also have a smeared shape. This is because, as the shock wave overpasses the trailing edge of the stator, it interacts with the incoming wake, overturning the flow. As the shock wave moves further, static pressure drops because the flow has enough space to expand, leading to an underturning in that region.

As observed in Figure 4-13 the shock wave has its highest intensity when located close to the stator trailing edge due to available area reduction, and is reduced again afterwards since it has more axial distance from upstream stator, which allows it to weaken slightly. It is also interesting to notice, that the inclined shape of the shock wave flattens at around 10% of the passage and is inclined again after 30%. This is because the shock wave is bending backwards and interacts with the trailing edge for longer time, as it has been explained on Figure 4-9e.

#### 4.2.3 Effect of axial distance of L-0 rotor leading edge from upstream stator on the shock intensity

It was shown previously in Figure 4-13 that the shock wave has its lowest intensity when it overpasses the upstream stator's trailing edge and has enough space to decay. In a previous computational study [9], the rotating shock wave weakens before it reaches the stator, showing a very steady behaviour. However, increasing the axial distance between stator and rotor in an existing machine would be a challenge due to limitations coming from bearing locations. Potential solution would be to apply forward sweep on the stator, close to the tip. This would not only increase the stator-rotor gap, but could also help with the reaction variation and the rotor work variation [8].

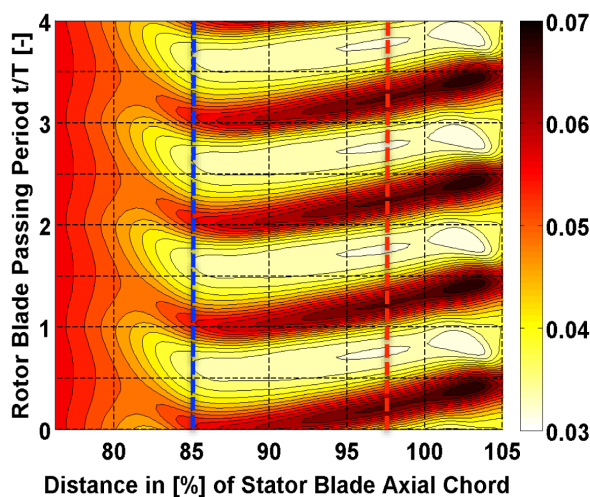


Figure 4-14: Cps [-] distribution along stator suction side between 76% and 105% of stator axial chord, at 90% span

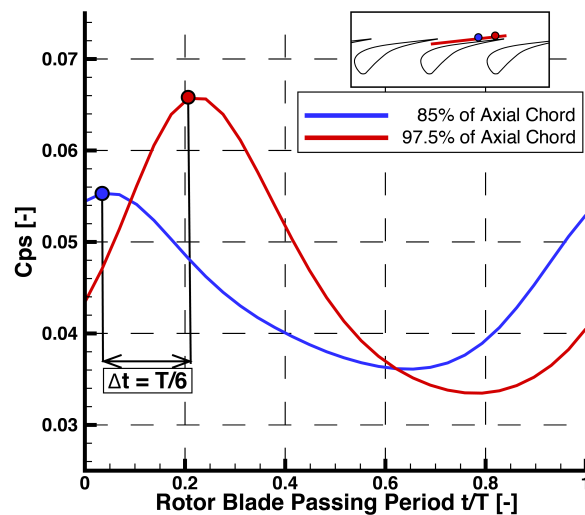


Figure 4-15: Time resolved Cps [-] distribution at 85% and 97.5% of stator axial chord, at 90% span

Since there was no geometry available with larger stator-rotor gap, in order to further investigate the effect of axial distance of the L-0 leading from the upstream stator, the unsteady flow was analyzed on a line along the suction side of the stator for four rotor blade passing periods, at 90% span, since the axial distance of the rotor leading edge from the suction side of the stator varies in time between 2.36 and 3 rotor blade axial chords, at 90% span.

Figure 4-14 shows the distribution of static pressure coefficient along the line close the suction side for four rotor blade passing periods, ranging from 77.5% until 105% of the stator's axial chord, where 100% is the trailing edge of the stator. The location of the line is shown on schematic of Figure 4-15.

As seen in Figure 4-14, the flow shows low unsteadiness in time up to approximately 80% of the axial chord. The flow further of 83% is unguided and the unsteadiness increases due to the interaction with the travelling shock wave. This axial location coincides with the throat of the passage.

It is also observed that the maximum Cps has a decreasing trend further from the trailing edge, implying that the intensity of the shock wave is weakening. However, the blade does not experience the maximum loading at each axial location at the same time step. In order to verify and analyze further, Cps at two axial locations, at 85% and 92.5% of axial chord, is shown in Figure 4-15 for one rotor blade passing period.

As seen in Figure 4-15, the maximum Cps decreases as the shock wave impinges further from the trailing edge, by 15.7%. It is clear that larger stator-rotor gaps are desirable in order to decrease the unsteadiness due to the stator-rotor interaction. What is more important is that the maximum at these two locations have a difference in phase equal to one-sixth of the rotor blade passing frequency. This is of high importance because these high fluctuations on the unsteady loading of the blade, along with the difference in phase between the axial distance, could potentially lead to high cycle fatigue or failure and needs to be taken into account during the design process.

Currently yet-unpublished work conducted in LEC, has indeed confirmed the gains from applying a forward sweep, close to the tip, showing reduction in flow unsteadiness and increased stage efficiency as a result of reduced stator-rotor interaction.

#### 4.2.4 Unsteady bow shock wave interaction with L-0 rotor cavity path

Analysis of the full flow field has shown that the bow shock wave upstream of the leading edge of the last stage's rotor is a highly three-dimensional feature. As the radius of the machine increases, so does the travelling speed of the blades, leading to an increase of relative inlet Mach number. It has been seen that the shock wave that is formed is impinging on the casing, interacting with the shroud of the blade and the inlet to the tip-cavity path. Shrouds in such long blades are crucial both to reduce the losses from tip leakage flows, as well as to ensure the mechanical integrity of the long blades. The leakage flow that goes through the cavity path does not produce any power on the rotor, therefore it is desirable to quantify this amount of flow. In this section, the flow field in the inlet of the tip cavity is analyzed in order to quantify the leakage flow and assess the interaction with travelling shock wave.

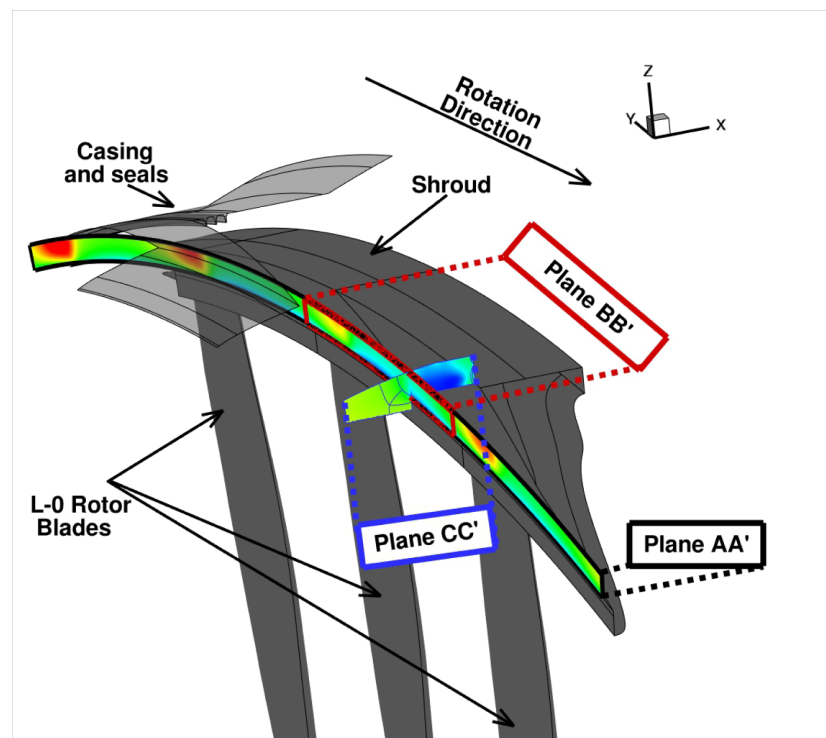


Figure 4-16: Extracted planes of cavity flow analysis - Contours of  $C_p$  [-]



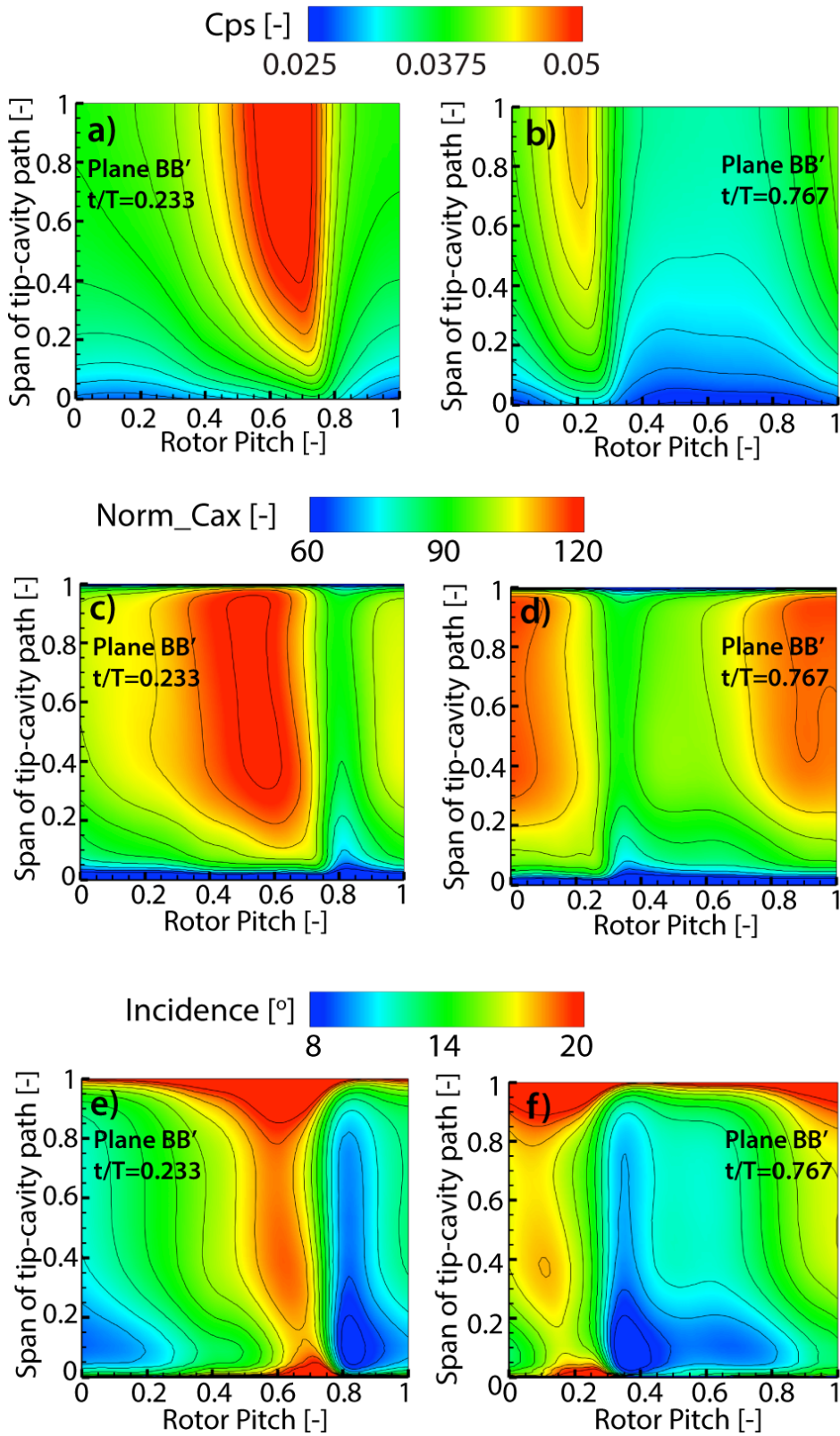


Figure 4-17: Plane BB' - Circumferential distribution of  $C_{ps}$  [-] (a-b), normalised axial velocity  $C_{ax}$  [-], (c-d), and incidence angle [°] (e-f) at time steps of maximum (left) and minimum (right) mass flow

Figure 4-16 shows the planes for a specific time step, on which the analysis has been conducted. First, Plane AA' was extracted along the full circumference of the sector (four rotor pitches). The plane is located exactly in the lip of the shroud. This location is selected because downstream there is an inlet separation bubble that is forming in the lip of the shroud and it would make it difficult to calculate accurately the mass flow without the amount being present inside the bubble. Additionally, plane BB' equal to a single rotor pitch was extracted, in order to analyze the effect of the shock wave on the flow field and the mass flow. Finally, plane CC' was extracted to gain insight of the flow field downstream of the inlet. All planes stay fixed in space and do not rotate with the rotor blades.

It was calculated that the mass flow through plane BB' amounts to roughly  $\frac{1}{4}$  of the total tip leakage mass flow on average through plane AA' and shows peak-to-peak fluctuations of  $\pm 5.25\%$ . These unsteady fluctuations are caused by the travelling shock wave, causing a mass flow redirection. The maximum amount was recorded on time step  $t/T = 0.233$ , while the minimum occurs on time step  $t/T = 0.787$ .

Figure 4-17 shows the flow quantities in plane BB' for the two time steps that the minimum (right column) and maximum (left column) mass flow is monitored. Observer looks downstream in all figures and direction of rotation is from left to right.

In Figure 4-17a, there is a region of increased static pressure that presents a blockage in the flow, causing a redirection of the flow, as seen in Figure 4-17e. Figure 4-17e shows the flow angle relative to the blade inlet angle of the rotor at 90% of blade span, essentially the incidence angle. Inside the region of increased static pressure, the relative Mach number decreases and the absolute Mach number increases. As the flow is redirected, the circumferential velocity decreases. Additionally, the downstream separation bubble, whose presence is desirable in that location to increase losses and reduce the leakage ingested in the cavity path, is suppressed in this time step as shown in Figure 4-18a.

On the contrary, in Figure 4-17b, it expands again causing additional blockage in the flow, as seen in plane CC' in Figure



4-18b. All these are leading to an axial acceleration of the flow in left time step and axial deceleration in the right time step, as presented in Figure 4-17c and Figure 4-17d. Therefore, the mass flow shows its maximum value on the left time step.

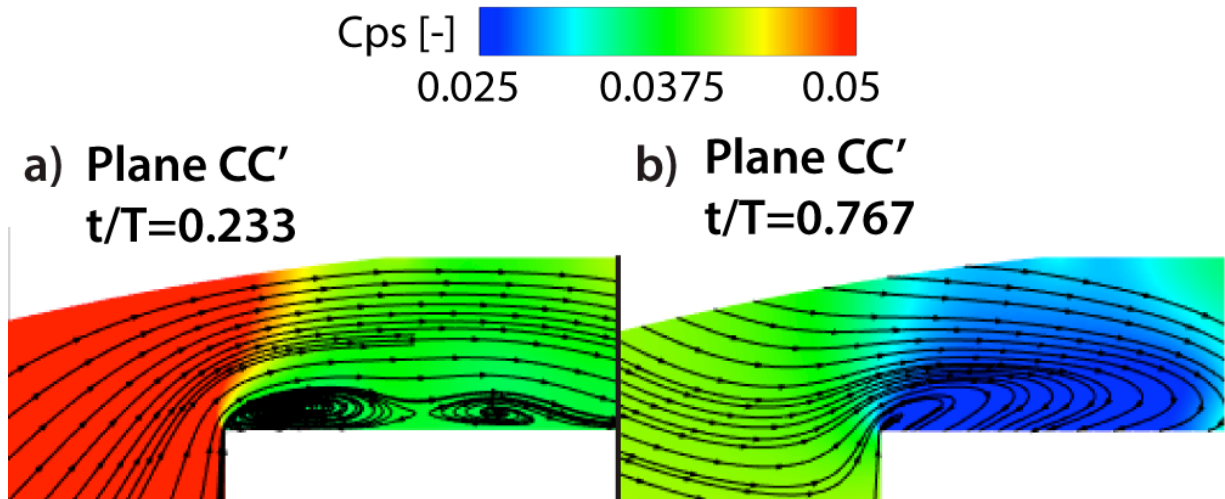


Figure 4-18: Plane CC' – Meridional view of Cps [-] at time steps of maximum (a) and minimum (b) mass flow

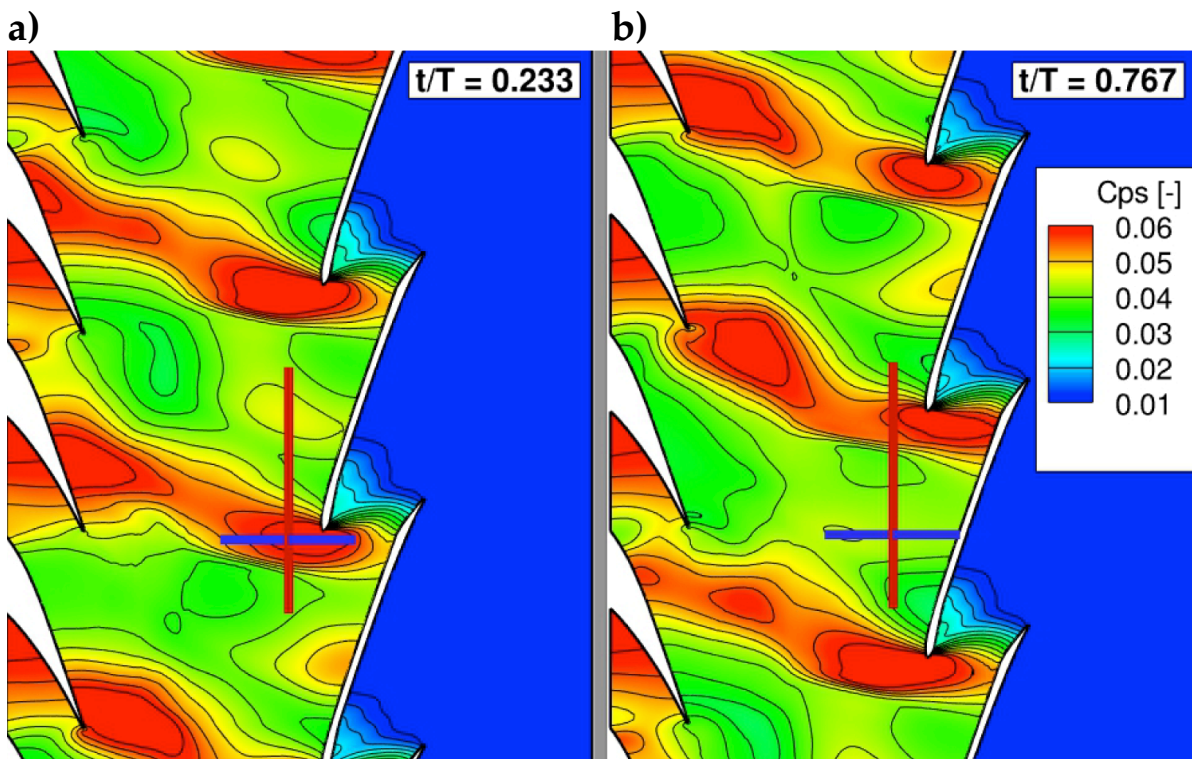


Figure 4-19: Formation of bow shock in time steps of max (a) and min (b) mass flow through plane BB'

It is interesting also to know the location of the shock wave relative to the upstream stator. This is presented in Figure 4-19, along with planes BB' and CC' as solid lines. It is observed that the maximum mass flow coincides with the time when the shock wave interacts with the suction side of the upstream stator when it reaches the trailing edge, while the minimum is recorded when it has overpassed it and high pressure region caused by the shock wave is located at throat of the upstream stator, looking in the third stator passage from the top.

Despite the flow redirection and unsteadiness in time induced by the passing high pressure region, the total tip leakage mass flow that passes through the plane AA' has been calculated to be 5% of the mass flow in the inlet of the L-0 stage and it is fairly steady with very low fluctuations at only  $\pm 0.2\%$ . The area of this plane amounts to 1.98% of the whole available area at the specific axial location. These results need to be treated with caution though because the calculations occur in "cold state". In reality, the high rotational speed along with the thermal load on the blade, definitely cause an expansion of the solid bodies, closing even further the available path and reducing the leakage flow.

#### 4.2.5 Entropy generation in L-0 stage

To conclude the present study, entropy generation in the last stage of the low-pressure steam turbine is investigated. For this reason entropy loss coefficient is calculated for L-0 stator and L-0 rotor, separately. Definition of entropy loss coefficient is given in Equation 4-3, where R is the individual gas constant for water vapour.

$$q = e^{\frac{-(S_{in}-S_{out})}{R}} \quad \text{Eq. 4-3}$$

Figure 4-20 shows the time-averaged entropy levels in meridional view in the inlet of L-0 stator. Close to the casing, the entropy is high due to tip-leakage flow coming from L-1 rotor. The effect of this feature would be either lost or smeared out in case estimated boundary conditions were used in the absence of L-1 stage in the computational domain. This shows the importance of multistage simulations over single stage or single row simulations.

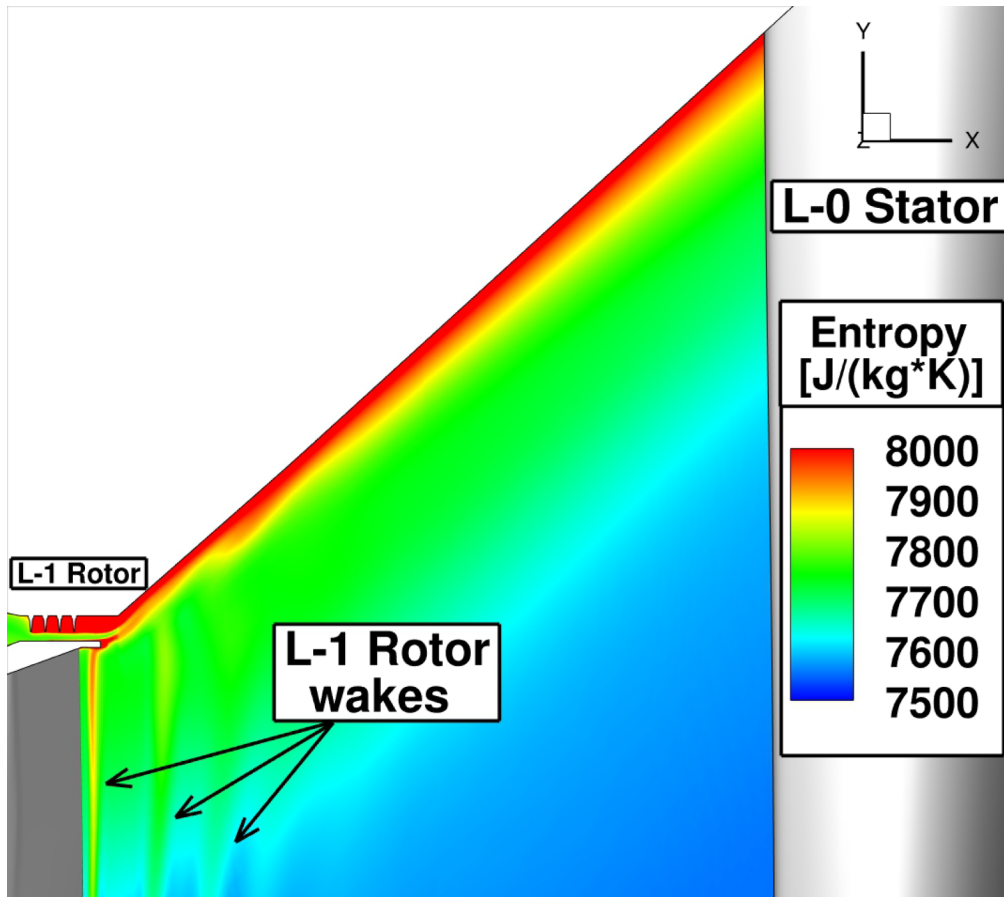


Figure 4-20: Meridional view and entropy levels in L-0 stage inlet

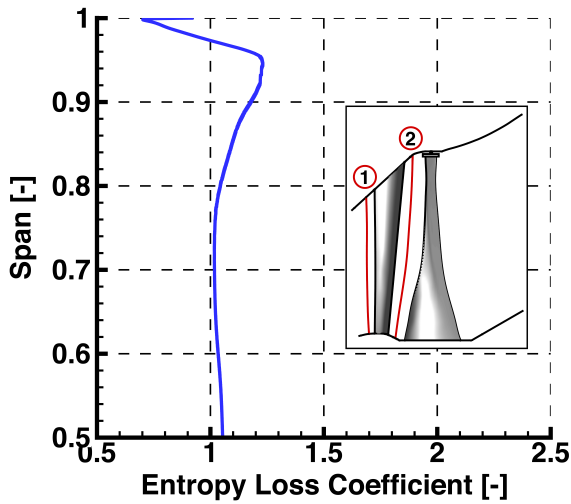


Figure 4-21: Entropy loss coefficient [-] for L-0 stator for top 50% of blade span

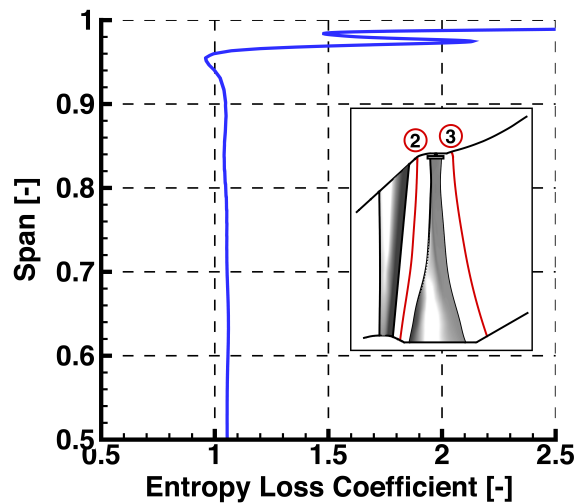


Figure 4-22: Entropy loss coefficient [-] for L-0 rotor for top 50% of blade span

The entropy loss coefficient for stator is presented in Figure 4-21. Results are circumferentially averaged for one stator pitch and time-averaged for four rotor blade passing periods. Values greater and lower than one imply entropy increase and decrease relative to inlet in the according span position, respectively. Obviously, values are slightly greater than one due to entropy rise along the blade row. The decrease observed in the last top 3% is due to radial migration of the tip-leakage flow coming from L-1, causing a local decrease of 23.4% at 99% span compare to mid-span. This loss transport is also contributing in the increase observed above 80% span, which is also induced by the travelling bow shock wave, causing a local maximum increase of 22.3% at 95% span compared to mid-span. Similar radial migration has been also observed in a transonic compressor rotor [123].

Similarly, Figure 4-22 presents entropy loss coefficient for L-0 rotor. Results are circumferentially averaged for one rotor pitch and time-averaged for four rotor blade passing periods. Slight decrease at 95% span also suggests radial transport of losses. The increase observed above 95% span is due to tip-leakage flow in L-0 cavity path. In that region, two peaks and a trough are present. The trough is in the middle of the leakage flow, while the peaks above and below it originate from the flow close to the solid boundaries of casing and blade span respectively. The local increase in the middle of the leakage flow, at 98% span, amounts to 42.3% higher compared to mid-span.

Apparently, the top 4% span of the full annulus is dominated by the effect of the tip-leakage flow, increasing entropy generation. However, it is important to mention again that the simulation was performed for “cold state” of the machine. In reality, the expansion due to rotational speed and thermal loads would close further the tip cavity path, limiting the entropy generation in a smaller percentage of the span.

### 4.3 Summary and conclusions

Multistage effects and tip leakage flows have been investigated in an unsteady manner for the last two stages of a low-pressure steam turbine with supersonic airfoils near the tip of the last stage's rotor blade.

This study is unique in a sense of combining experimental data for code validation and comparison with a numerical simulation of the last two stages of a real steam turbine, including tip-cavity paths and seals, steam modeling and experimental data used as inlet and outlet boundary conditions. Numerical results have been extensively validated with experimental data; time averaged 5-hole probe and FRAP-HTH, as well as time resolved FRAP-HTH. In general, the numerical predictions with equilibrium steam modeling show good agreement with measurements, even under these extreme flow conditions. Flow quantities are predicted with RMS difference below 3.8° for yaw angle, 3.27% for relative Mach number, and 1.15% for total temperature

Analysis of results shows high unsteadiness close to the tip of the last stage, due to the presence of a bow-shock wave upstream of the rotor blade leading edge and its interaction with the upstream stator blades. The shock wave causes locally an unsteadiness of  $\pm 34.4\%$  in static pressure and  $\pm 10.4\%$  in axial velocity, close to the suction side of the upstream stator, at 92.5% axial chord and 90% span.

The maximum fluctuation in time on suction side is greater than the maximum fluctuation in pressure side at the same axial location close to the trailing edge. This implies that there are moments in time where the blade is instantaneously counter-loaded locally in that location. However, despite the unsteadiness incurred by the periodic impingement of the shock wave on the suction side of the stator, there is no evidence of a boundary layer separation, even under these extreme flow conditions.

The intensity of the shock wave is weakest, when the axial distance of the rotor leading edge from the upstream stator trailing edge is largest, since it has more space available to weaken. The maximum  $C_p$ s recorded at 85% of stator axial chord is lower by 15.7% compared to 97.5% of stator axial chord. However, a phase shift

between the maximum values of static pressure along the suction side of the stator blade is identified, due to the shock wave moving with the rotor blades. The phase shift between the maximum values at these two locations is equal to  $T/6$  of the rotor blade passing period

Additionally, the bow-shock wave interacts with the blade shroud and the tip leakage flow. The mass flow passing through a domain equal to a rotor pitch in the inlet of the tip cavity of L-0 rotor shows an unsteadiness of  $\pm 5.25\%$ , due to shock wave interaction and suppression of the inlet separation bubble in the lip of the blade shroud. Despite the interaction with the incoming flow, the total tip leakage mass flow ingested in the tip-cavity shows a steady behavior with extremely low fluctuations in time.

The total tip leakage mass flow through the tip-cavity path was calculated to be 5% of the total mass flow, passing through 1.98% of the total available area in that axial location. However, results are derived for “cold state” of the machine, without taking into account the expansion occurred due to rotational speed and thermal load. Nevertheless, an estimation of ingested mass flow by the cavity path is crucial and can provide valuable information that needs to be taken into account from early steps of the turbine design.

Finally, traces of upstream stage’s leakage flow have been identified in the last stage, contributing to entropy generation in inlet and outlet of last stage’s stator blade, highlighting the importance of performing multistage simulations. Calculation of entropy loss coefficient for stator and rotor in the last stage reveals the effect of bow shock wave and tip-leakage flow on entropy generation, respectively. Regarding the stator, a decrease of 23.4% compared to mid-span is observed at 99% span due to radial migration of leakage flow coming from L-1 stage to lower span position. This loss transport, along with the effect of the bow shock wave, contributes to a local maximum increase of 22.3% compared to mid-span, at 95% span. The inevitable entropy generation due to tip-leakage flow in L-0 rotor amounts to 42.3% at 98% span and its presence affect the top 4% of the full annulus.

Currently yet-unpublished work completed in the laboratory [109] has confirmed that there are indeed ways to increase efficiency by

reducing the stator-rotor interaction, such as forward sweep or change of throat-to-pitch ratio of the stator blade rows. These changes rely so far only on the experience of the designer and the understanding of the flow field. However, an optimized solution can only be found by employing modern optimization techniques. Presented results highlight the importance of performing multistage-, as well as unsteady simulations, instead of steady state, due to the impact of these unsteady flow mechanisms on loss generation and stage efficiency.





## 5 Towards Unsteady Optimization for Turbomachinery Applications

In a typical design optimization cycle in turbomachinery, the largest bottleneck is the computational time required to reach a valid solution. An optimization of a fully three-dimensional computational model could require tens of simulations and days or even weeks to be completed, even if only the main flow paths are considered and are solved in a steady state. One can easily understand that the problem becomes much harder when the simulations become time-accurate and cavity flow paths are included in the computational model, simply due to the computational resources required. Therefore, it was deemed necessary to investigate and identify measures to accelerate the obtaining of a solution in a reasonable time frame before attempting an unsteady optimization. After consideration of the problem, four different ways were identified, related to:

- Automated, basic post-processing
- Initial guess of the solver
- Minimum convergence level assessment of solution and
- Numerical scheme of the simulation, i.e. multistage time integration and preconditioning

Each one is discussed in detail in this chapter. The results of development were also validated with experimental data [92], [105].

### 5.1 Computational setup

The development of this work was performed on a computational model of the H1 turbine case, details of which were discussed in section 3.2. The reason that H1 case was selected was because the blade count allows the sector simulation both stages. Additionally, experimental measurements had been already conducted in LEC's axial turbine facility "LISA", which were used for validation of numerical predictions. Measurements for H2 case were not yet available at the time.

### 5.1.1 Geometry and computational domain

The computational domain consists of a two-pitch, two-stage, annular configuration of an axial HP steam turbine. As seen in Figure 5-1, the geometry includes the cavity paths for both stators and rotors, at hub and tip, respectively. The geometrical model was created with a modified blade count for both rotors R1 and R2, which was reduced by two of the full annular domain. This, modified the blade count to 50-50-50-50, and allowed the simulation of only two pitches. In order to account for this change in blade number, the trailing edge of both R1 and R2 were tilted towards the suction side of the neighboring blade, in order to keep the same throat area and the operating point same to original, but with a change of the blade exit angle as a consequence.

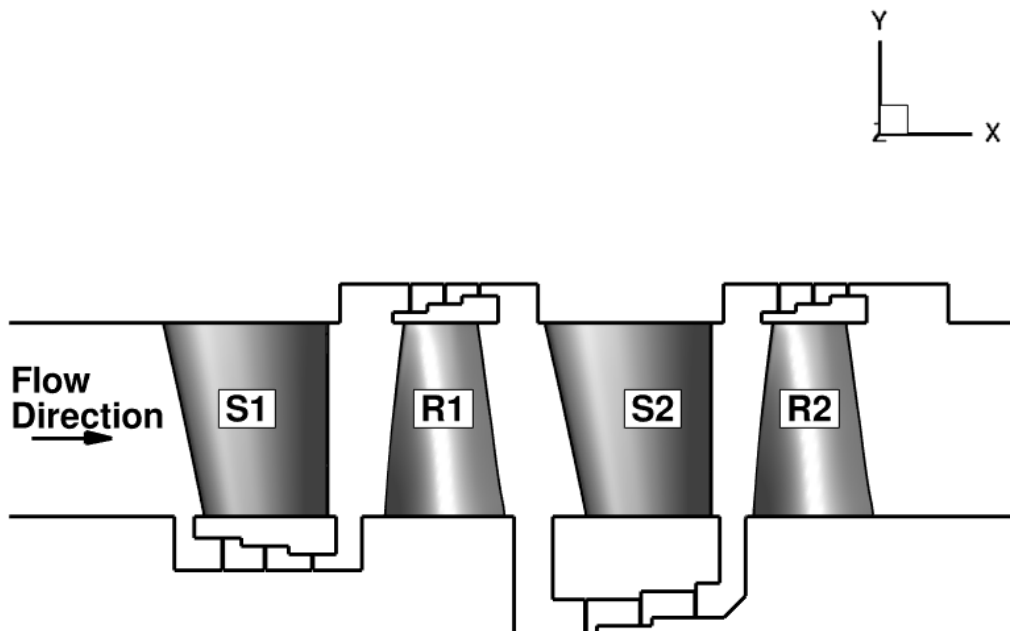


Figure 5-1: Solid surfaces of LISA-H1 turbine case

All simulations have been performed using in-house developed CFD solver MULTI3 in LEC's high-performance computing GPU cluster. The cluster consists of three nodes, two of which have 16 CPUs and 4 NVIDIA P100 GPUs with 16 GB of on-board memory each. The third node has 12 CPUs and 4 NVIDIA K40 GPUs with 12 GB on-board memory. A mesh of 15 and 11 million nodes can fit on each kind of GPU, respectively. The computational domain was split in 2 sub-domains of a one-pitch, two-stage configuration, to allow it to fit on both P100 and K40 GPUs.

A multi-block structured, body fitted mesh is generated for each passage separately. In spanwise direction, 72 radial nodes were used with higher clustering towards the endwalls. In total, 14 blades were modeled, resulting in a mesh of 16.6 million nodes, of which more than 7 millions were used in the cavities to resolve the complex geometry and capture unsteady flow features. The  $y^+$  value is kept below 5 in the whole domain. Mesh quality of the model was well within acceptable range. Details of mesh size for each row and final mesh quality are given in Table 5 and Table 6 for each GPU.

Table 5: Mesh size per GPU of the different flow domains, in millions

Domain	Mesh Size (main domain)	Mesh Size (cavities)	Total Mesh Size
S1 Stator	1	1	2
R1 Rotor	1.2	0.9	2.1
S2 Stator	1	1	2
R2 Rotor	1.4	0.8	2.2
<b>Total</b>	<b>4.6</b>	<b>3.7</b>	<b>8.3</b>

Table 6: Mesh quality report of whole domain

Minimum angle	Maximum aspect ratio	Maximum expansion ratio
4.6°	1752	5.21

The whole mesh was created with fully matching interfaces, both between blocks and row interfaces, in order to eliminate interpolation errors, which may lead to considerable loss of accuracy at the regions where highly unsteady phenomena take place. Number of radial nodes and total mesh size was a result of a separate, sensitivity study that was conducted during the course of the main investigation.

### 5.1.2 Boundary conditions and initial guess

Because of the almost uniform flow field at the inlet of the domain, only a radial flow profile is imposed there. The total pressure, total temperature, yaw and pitch angle, axial Mach number as well as the turbulence intensity and turbulent length scale at each radial position are required by the solver (see Table 7). Radial equilibrium is imposed at the outlet plane of the domain, so only the static pressure at the hub is needed, which is set to 0.95997 [bar]. The values for the inlet and outlet boundary conditions are taken from measurements conducted in LEC's axial turbine facility, "LISA".

Table 7: Inlet boundary conditions

	$p_t$ [bar]	$T_t$ [K]	Yaw angle [°]	Pitch angle [°]	$Ma_{ax}$ [-]	$Tu_{in}$ [%]	$Tu_{ls}$ [m]
Hub	...	...	...	...	...	...	...
	1.29997	313.5	0	0	0.05	5	0.0001
Tip	...	...	...	...	...	...	...

To specify the frame of reference of the solid walls inside the domain, flags are used to define whether a certain wall is rotating, counter-rotating or stationary. The rotation is always defined relative to the associated domain movement. The stator and rotor blades were set to stationary. In case of a stator row, the walls facing the rotor disc were set as rotating, whereas for the rotor rows the casing walls are counter-rotating. Figure 5-2 illustrates the different wall rotation. Besides the rotation, adiabatic and no slip boundary conditions were applied for all walls.

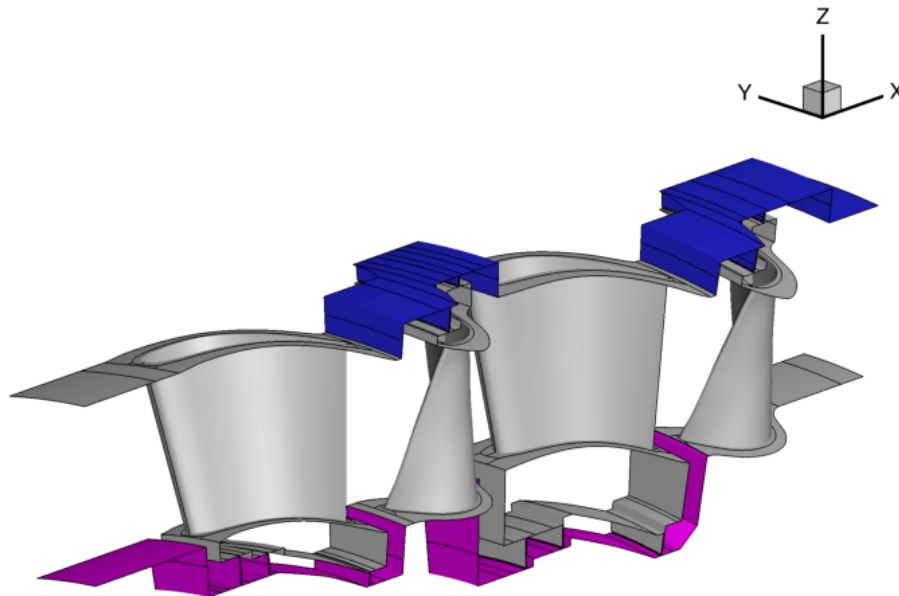


Figure 5-2: Stationary (grey), rotating (purple) and counter-rotating (blue) defined walls relative to the respective frame of reference

To initialize the computation, a simple flow field is deduced by using the boundary conditions at inlet and outlet of the domain. In addition, predefined yaw and pitch angles, as well as axial velocities are set at inlet and outlet of each row. The rest of the flow field is a simple linear interpolation of the interface quantities. The initial static pressure distribution is shown in Figure 5-3.

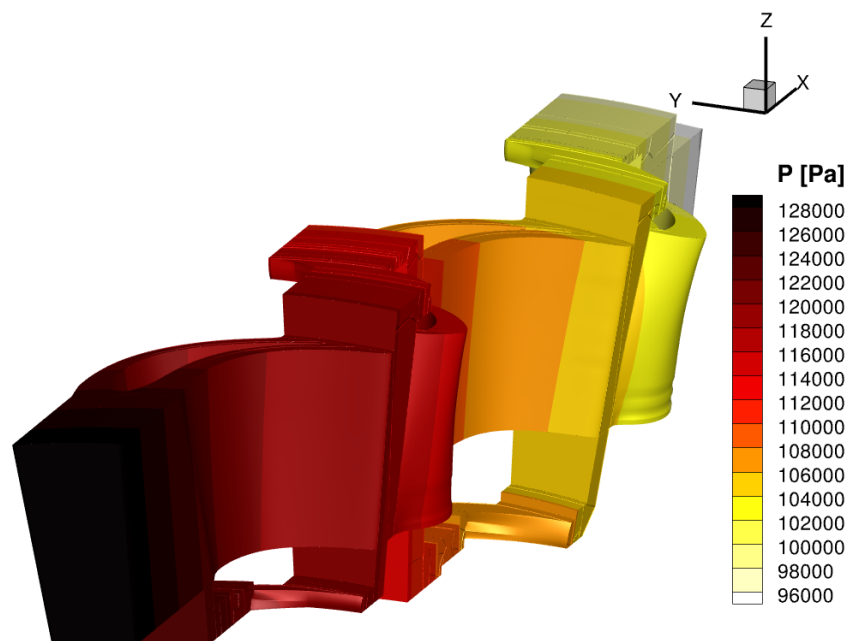


Figure 5-3: Static pressure distribution of the initial guess

### 5.1.3 Simulation settings

Unsteady simulations have been performed, under these boundary conditions, using dual time stepping approach. 60 equal time steps have been used for each period, where a period is defined as one sector rotation, which for the current case is two rotor blades of each stage. For each physical time step, 350 sub-iterations are simulated with CFL number of 0.8.

Due to the presence of very fine cells in the computational mesh, especially in the cavity regions, a sufficient number of sub-iterations is needed in order to ensure proper propagation of information through the regions of very high node clustering, due to the fact that smaller cells need more sub-iterations for the flow to develop properly compared to bigger cells, as it was already discussed in section 2.1. Both the number of physical time steps and sub-iterations are a result of a separate study that was conducted during the course of the main investigation.

## 5.2 Automated, basic post-processing

With tens or hundreds of simulation required during an optimization cycle, an automated post-processing is essential for saving time. For this reason, a basic post-processing was implemented to MULTI3 for calculation of typical parameters in turbomachinery design. Full list of these parameters were presented in section 2.2.4.5. These parameters are monitored and written by MULTI3 while the unsteady simulation is running. Evolution of these parameters over time, as well as time-averaged values are written at all interfaces of the domain in three formats:

- **0D values**, which are circumferentially- and radially mass-averaged at the interface
- **1D values**, which are the circumferentially, mass-averaged radial profiles along the span and
- **2D values**, which is the full flow field on the interface, in a plane with  $r$ - $\theta$  coordinates.

In this way, basic but important information for each case is readily available with eliminated post-processing efforts. Additionally, these serve also as an input for the convergence monitoring routine.

### 5.3 Initial guess of simulation

The second measure is quite simple and is related to the initial guess of the flow field provided to the solver. An optimization cycle starts with the calculation of the baseline case, while the rest of the cases are given a geometrical perturbation until an optimum is found.

Once the baseline reaches convergence and a solution is acquired, it can be used as an initial guess for the next case. Thanks to the data structure of MULTI3, the grid and flow information are stored in two separate files and are the basic input of the solver. Therefore, one can simply replace the old grid file with a new one, containing the new geometrical perturbation, while keeping the old flow file. The only restriction is that the new grid must have identical format to the old one, such as same number and orientation of blocks, same number of nodes etc. The only thing different would be the  $x$ -,  $y$ -, and  $z$ -coordinates of the mesh nodes close to the perturbation. In this way, the initial guess of the flow field for the new case is no longer just a simple linear distribution but a fully developed flow field. Then the new simulation starts and the flow adjusts itself according to the changes inflicted by the difference in geometry.

Grid templates and scripts supported by Autogrid enable the automatic generation of each new mesh, while respecting the requirements mentioned above. Just by applying this simple idea, can reduce the required simulation time of each new case to be reduced by a factor of almost 3x, compared to starting each time from a simplified initial guess.

### 5.4 Unsteady convergence monitoring

This section discusses the global and local flow field variables in two separate subsections. For the global variables convergence rates and interdependencies between the convergence levels of various variables are established. For this purpose, the residuals, the mass flow imbalances and the mass averaged interface quantities are

considered. The local flow field is analyzed with the static pressure, static temperature and the turbulence modeling variables of the monitoring points. Temperature and the turbulent variables are of particular interest, because of their dependency on the propagation rate of viscous effects inside the flow field. It is expected that the convergence rates of these variables will be smaller compared to the one of pressure, since the static pressure field depends on potential field effects.

### 5.4.1 Global flow field

The logarithm of root-mean-square of the residuals stabilizes after 10 simulation periods around  $-4.7$  (see Figure 5-4). The respective convergence criterion reaches a high value as soon as the change of the windowed average from period to period goes to zero (see Figure 5-5). A similar behavior can be observed for the turbulent residuals.

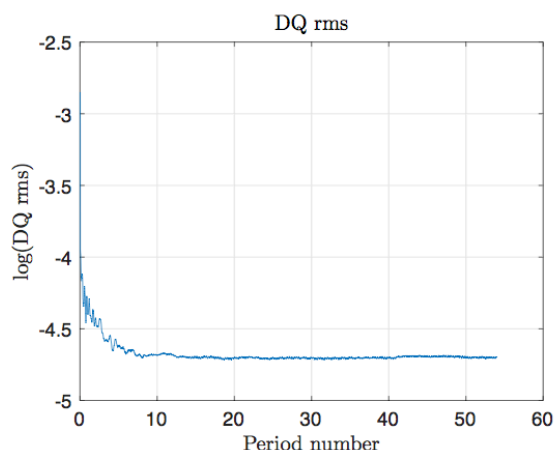


Figure 5-4: History of the root-mean-square of the numerical residuals [105]

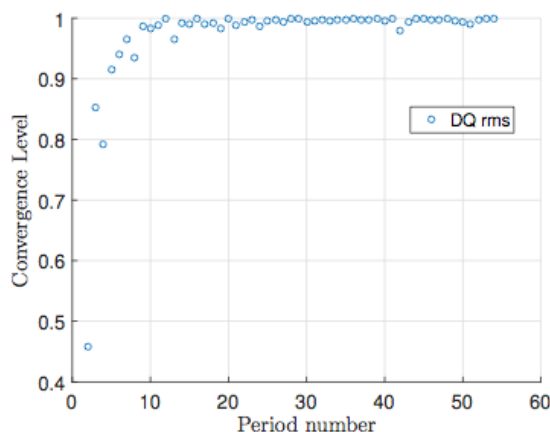


Figure 5-5: Convergence history of the root-mean-square of the numerical residuals [105]

The consequence of the achievement of a stable residual level has direct impact on the mass flow evolution and also on all other flow variables. Figure 5-6 displays all computed mass flows at all given row interfaces and Figure 5-7 shows the evolution of the convergence level for the mass flow imbalances. As soon as the numerical error has converged, the mass flow at the domain inlet converges to a constant mean. Due to the longer flow distances, the information at the inlet requires significantly more time to reach the



interfaces further downstream. This slows down the convergence, especially at the outlet of the domain. A convergence level of over 0.95 for the imbalances is achieved, after the residuals have stabilized. But, conservation of mass is a very important requirement for the physicality of the flow field and in fact a steady convergence level is achieved for the first time at the 30th periods. Looking only at the first stage of the geometry, the mass flow imbalances converge after 16 to 17 periods.

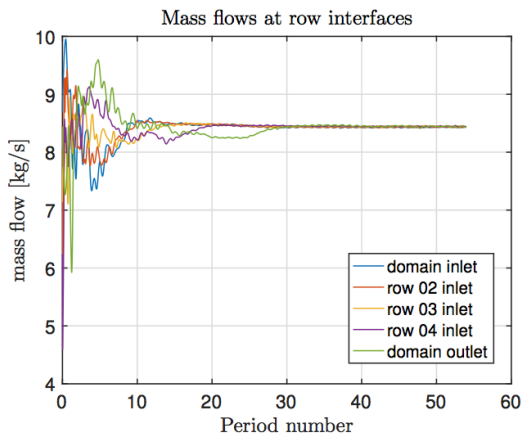


Figure 5-6: History of the mass flow at row interfaces [105]

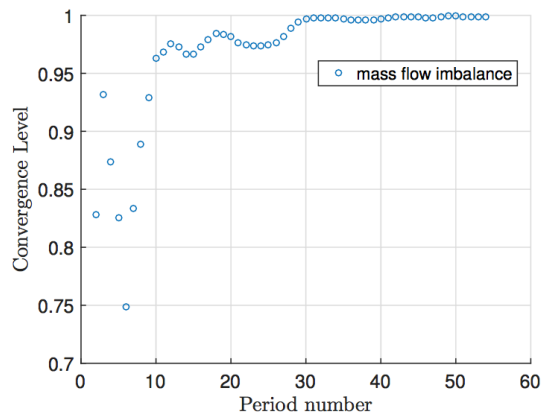


Figure 5-7: Convergence history of the mass flow at domain outlet

By examining the circumferentially and radially mass averaged values for total enthalpy and entropy generation at the outlet interfaces of the modeled stages, in Figure 5-8 and Figure 5-9 respectively, it is observed that these quantities converge to a steady level after the mass flow imbalance at the most downstream interface contained in a specific stage disappears.

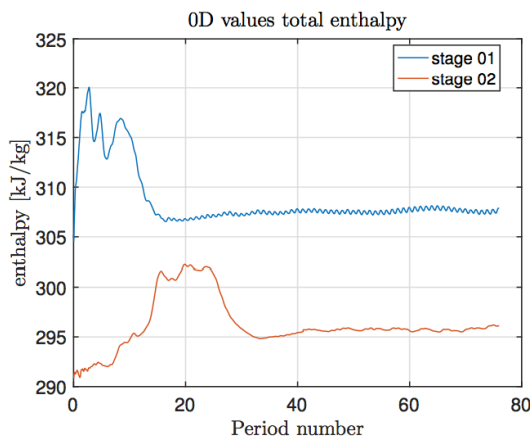


Figure 5-8: History of mass

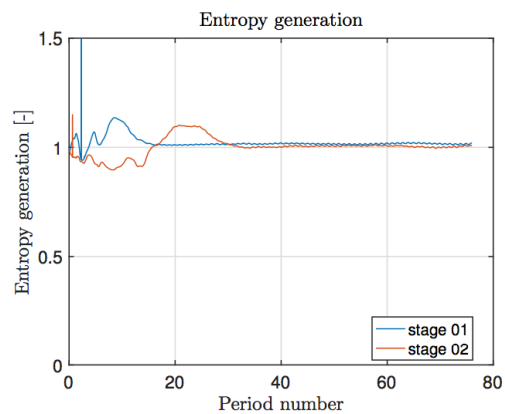


Figure 5-9: History of mass

averaged total enthalpy at stages outlet [105]

averaged, non-dimensionalized entropy generation at stages outlet [105]

So a relation between the convergence of the mass flow imbalances and other flow variables can be established. Further implications are the varying convergence rates depending on the location of interest inside the computational domain.

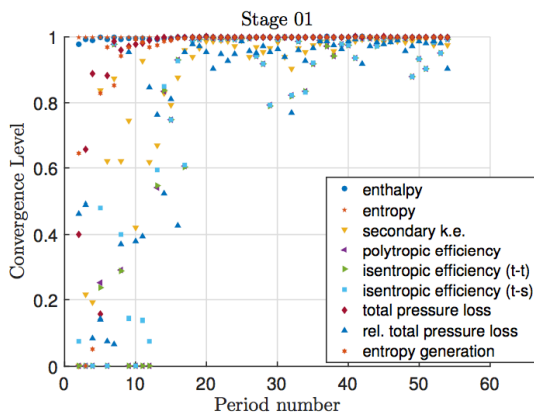


Figure 5-10: Convergence history of all investigated variables for the first stage [105]

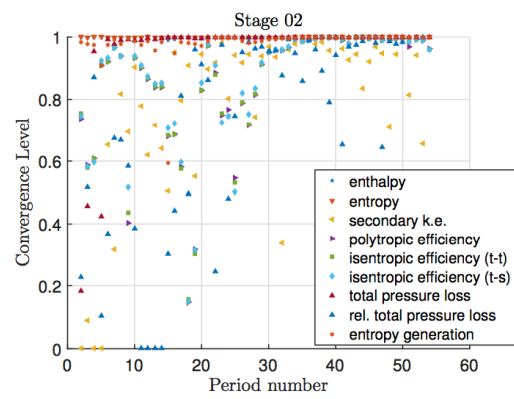


Figure 5-11: Convergence history of all investigated variables for the second stage [105]

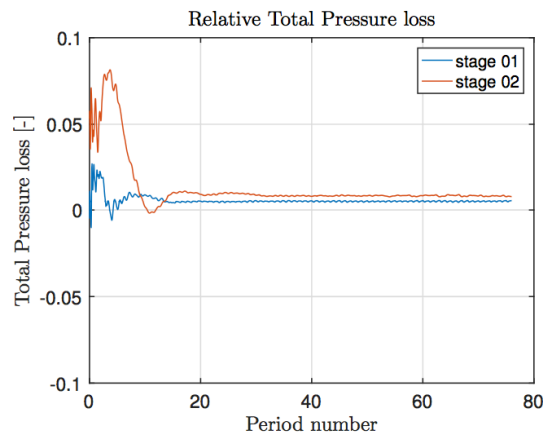


Figure 5-12: History of mass averaged total pressure loss values across rotor row in a relative frame of reference at stage outlets [105]

Figure 5-10 and Figure 5-11 display the convergence levels of all global variables that have been investigated for the two stages. Up to the 20th period a high level of convergence is achieved for almost

all variables from the first stage. The mass flow imbalance at the domain outlet settles around the 30th period. Most of the variables belonging to the second stage converge to a stable level after this period. The variables which have not converged are again the relative total pressure loss and in addition the secondary kinetic energy and efficiency values. The most fluctuating level is the one of the pressure loss in the rotating frame of reference, as shown in Figure 5-12. This comes from the correlation of very small oscillations around the constant mean. These oscillations are in fact negligible when considering the stable level of the mean value. In order to get rid of these disturbances in the convergence level, an if-statement was additionally implemented which only considers cross correlation or the DFT-analysis when the averaged deviation amplitudes are larger than one percent of the mean value. Other global quantities such as efficiency, entropy generation, pressure loss and secondary kinetic energy follow the same trend.

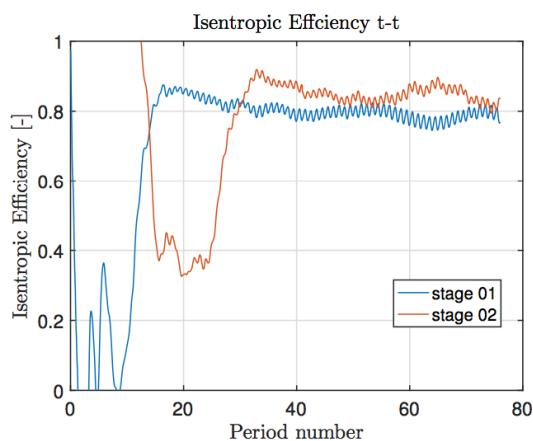


Figure 5-13: History of mass averaged total-to-total isentropic efficiency at stage outlets [105]

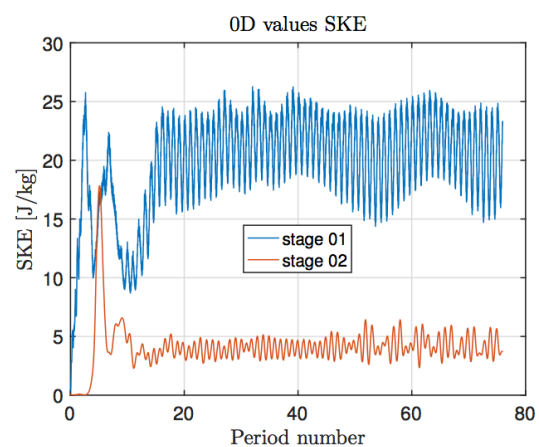


Figure 5-14: History of mass averaged secondary kinetic energy values at stage outlets [105]

The computed efficiencies need a few periods more, compared to other considered variables, until a more stable mean level is reached (see also the slight overshoot and the gradual decay between periods 17 and 30 in figure Figure 5-13). Nevertheless, the point in time when the mass flow imbalances settles, can also be detected for this variable. An additional indicator for the convergence of a solution is constant frequency oscillations of the variables (DFT-criterion). The polytropic efficiency as well as the total-to-static isentropic efficiency show a similar evolution over

time. The converged values for efficiencies are far lower than expected. SKE shows similar behavior in Figure 5-14.

The mass averaged quantities at the interfaces obtained from the simulation are shown for the very latest simulation results to get a feeling about the steadiness of the signals over time. This is very important regarding the convergence prediction in a design optimization cycle. One can observe that enthalpy, relative total pressure and entropy generation converge to a very steady level, while isentropic efficiency and secondary kinetic energy show variations throughout the whole simulation process. Since very high convergence levels - especially for efficiency - are required from a design optimization perspective, the obtained results are far from satisfying. The reason was due to a numerical problem of the solver dealing with a high clustering of very fine cells right after and inside the cavity, which caused a spurious density decrease at the rotor hub, as it was described in detail in section 2.1. This resulted in an unphysical, local temperature increase that gives not only lower efficiency than expected, but also creates oscillations over time. Unfortunately, the reason was detected only later and was resolved with mesh relaxation close to that region but the numerical experiments were not repeated after this.

#### 5.4.2 Local flow field

To analyze the convergence of the local flow field, six monitoring points are evaluated. Three of them are located in the main flow field (numbers 01, 03 and 05) while the others are inside cavities (numbers 02, 04 and 06). The pair 01 and 02 is inside the domain of the first stator, 03 and 04 are inside the domain of the first rotor and 05 and 06 are inside the domain of the second stator. From Figure 5-15, one can directly recognize the rather fast convergence of all pressure signals to a constant mean value. Since the fluctuations around the constant mean values after 9 periods are very small, a high level of convergence for all pressure signals is achieved already before the 10th period, as show in Figure 5-16.

The temperature signals (Figure 5-17) and also the turbulent variables (Figure 5-19 and Figure 5-21) show varying developments dependent on the location of the monitoring point. All the static

temperature signals that are recorded inside cavities gradually increase to a constant level after a very large number of periods. On the contrary, the local temperatures in the main annulus converge way faster, but essentially in point 03 and 05 still slower than the pressure signals.

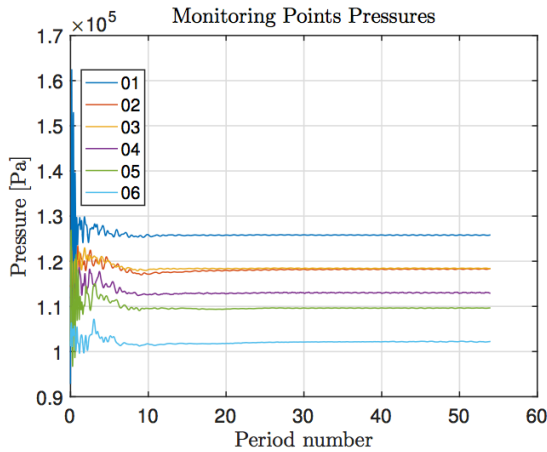


Figure 5-15: History of local pressure signals at specific locations inside the flow field [105]

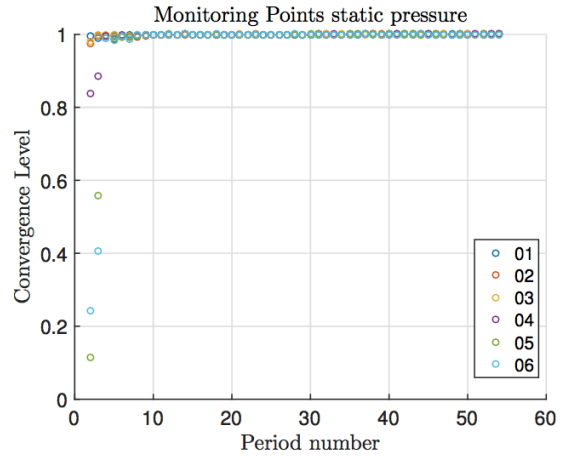


Figure 5-16: Convergence history of local pressure signals at specific locations inside the flow field [105]

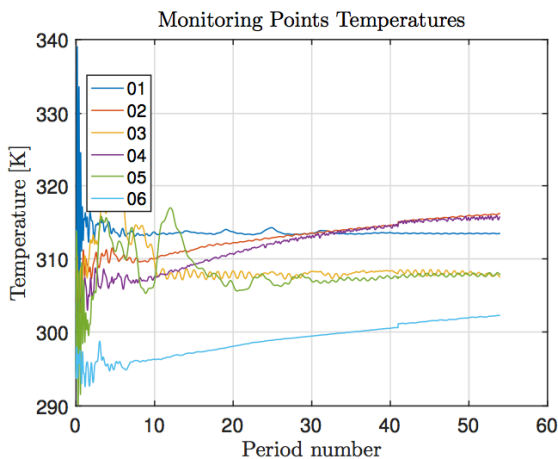


Figure 5-17: History of local temperature signals at specific locations inside the flow field [105]

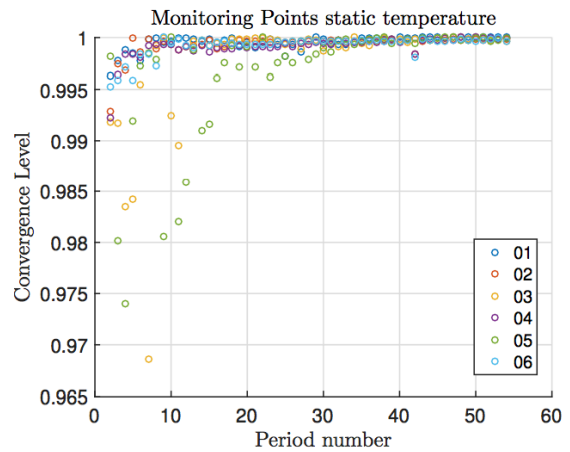


Figure 5-18: Convergence history of local temperature signals at specific locations inside the flow field

The gradual temperature increase inside the cavities is either due to turbulence dissipation into heat and a poor removal of the generated heat or - which is more likely - the same problem that

came up for the efficiency calculation: The very high clustering of very small grid cells as well as the low Mach-number flows inside the cavities present difficulties for the compressible CFD-solver and lead to spurious solutions, as was shown in Figure 2-1. In general, the temperature variations are so small, that the monitoring routine gives right away from the starting periods a very high convergence level, as it is noticed by the scale of the y-axis in Figure 5-18. Further the incremental temperature rise in the cavities cannot be identified by the routine and the level of convergence is also high for the temperatures in this regions.

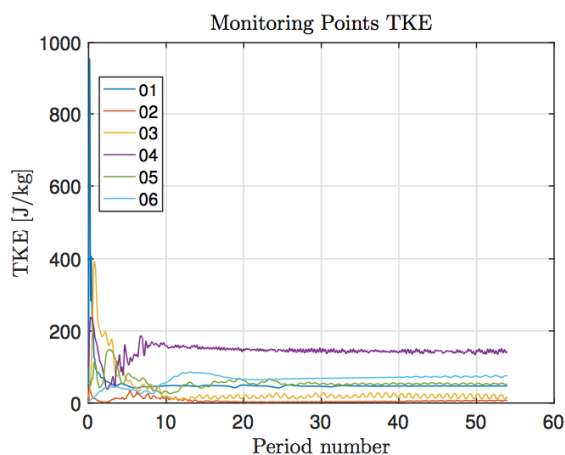


Figure 5-19: History of local TKE signals at specific locations inside the flow field [105]

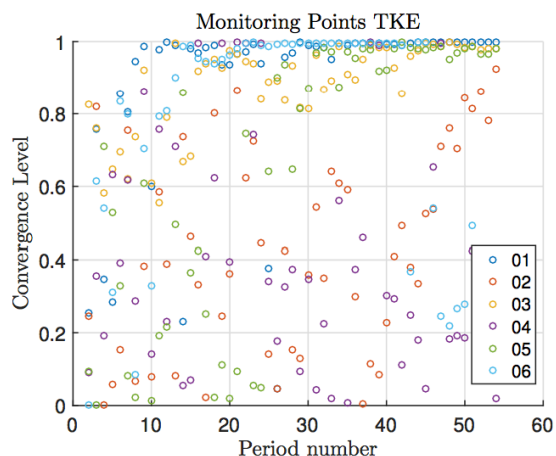


Figure 5-20: Convergence history of local TKE signals at specific locations inside the flow field [105]

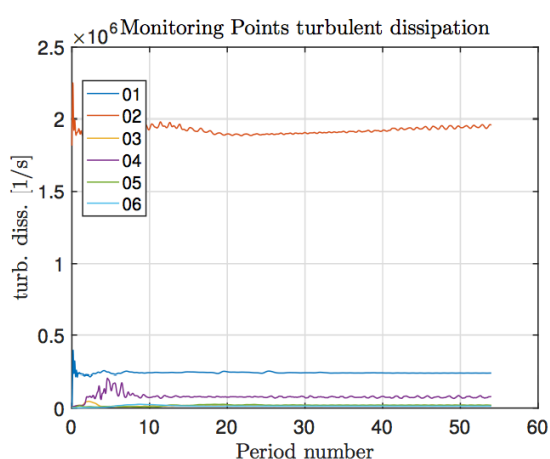


Figure 5-21: History of local turbulent dissipation signals at specific locations inside the flow field [105]

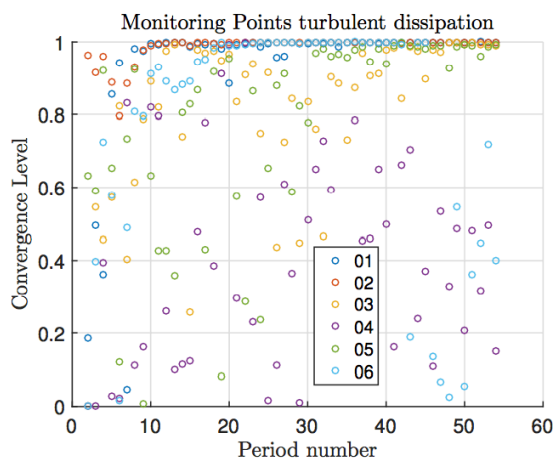


Figure 5-22: Convergence history of local turbulent dissipation signals inside the flow field [105]

The turbulence modeling variables converge to a constant mean while the fluctuations remain comparatively small. Nevertheless the fluctuations are very chaotic and produce in some cases very poor convergence levels.

### 5.4.3 Convergence validation with experiments

To validate the convergence predictions of the monitoring routine, but also the obtained CFD solutions, results are compared against experiments conducted in LEC's in-house axial turbine research facility "LISA". For this purpose two measurement planes were selected for comparisons between experimental and CFD-data. The measurement planes under consideration are displayed in Figure 5-23. The planes B and D are located behind the first and second rotor, respectively. Unsteady flow measurements have been conducted using a standard FRAP probe. In every plane, the parameters Mach number, yaw angle and total pressure coefficient are evaluated at different simulation periods (10, 25 and 41) to specify the convergence level. Finally, the converged solution is compared with time-averaged values of the experimental data.

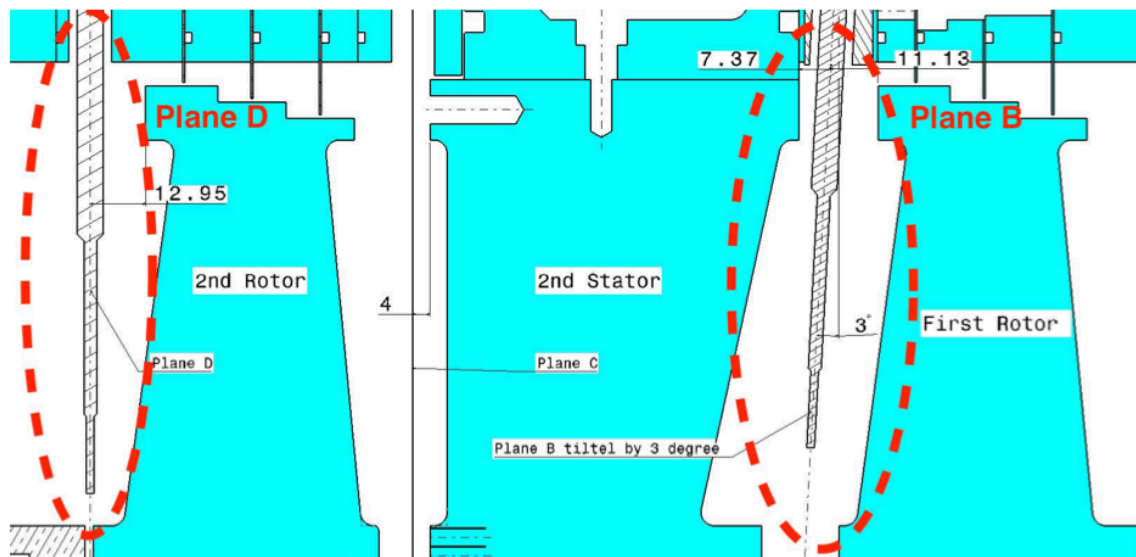


Figure 5-23: Measurement planes in LISA

#### 5.4.3.1 Measurement plane B



Measurement plane B was effectively utilized to validate the convergence predictions for the global flow variables and quantities of the first stage. The evolution of the Mach number distribution along the span (span over 1 means inside tip cavity, below 0 inside hub cavity) over the simulation periods 10, 15 and 41 is shown in the left plot of Figure 5-24. It is obvious that in between the solutions at period 25 and 41 there is no detectable difference apart from the small change inside the tip cavity. Since the distribution at 10 periods shows comparatively strong over- and undershoots, a well-converged solution can be stated to be obtained after 25 periods. Further the comparison between the solution at 41 periods with the experimental data shows that the trends can be reflected very accurately by the computation, even inside the cavities

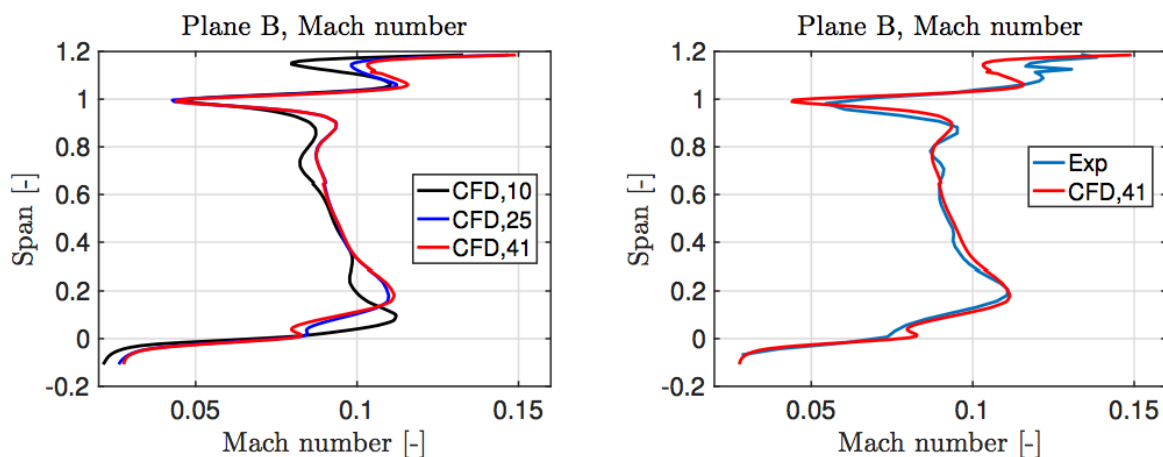


Figure 5-24: Plane B, Evolution of Mach number distribution along the span over time and comparison with experimental data

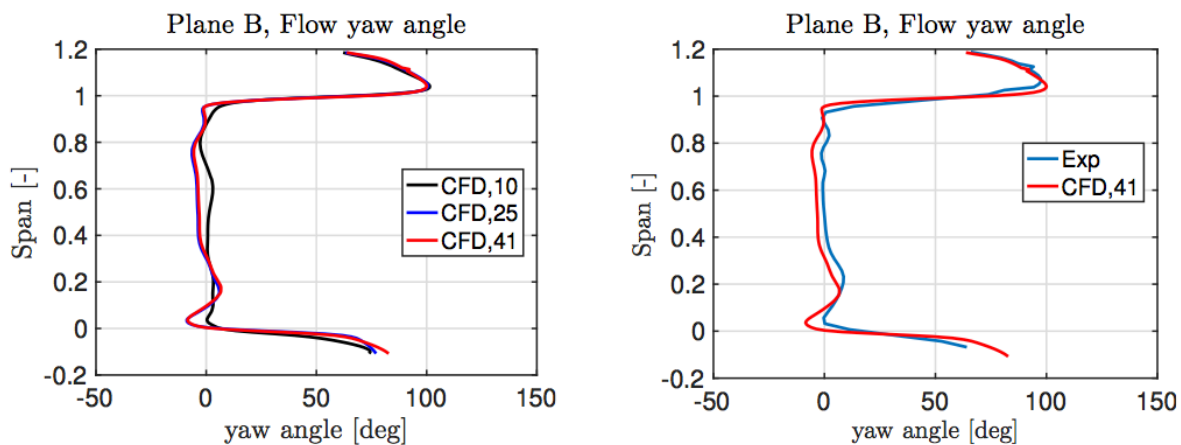


Figure 5-25: Plane B, Evolution of absolute yaw angle distribution along



the span over time and comparison with experimental data

These observations can also be made for the yaw angle Figure 5-25 and the total pressure coefficient. The trends of the experiments can be matched very well after 25 simulation periods. Trend of yaw angle is captured well all along the span but there is a mismatch in absolute values. Total pressure coefficient for the stage, on the other hand, is captured accurately both in trend and value, with a maximum error of  $-0.34\%$  under-prediction of CFD compared to experiments. The reason of this is related to the airfoil modification close to trailing edge to account for reducing the blade count from 52 to 50. This results in a penalty of flow yaw angle accuracy but the capacity of the turbine has remained the same as seen by Mach number and pressure coefficient plots.

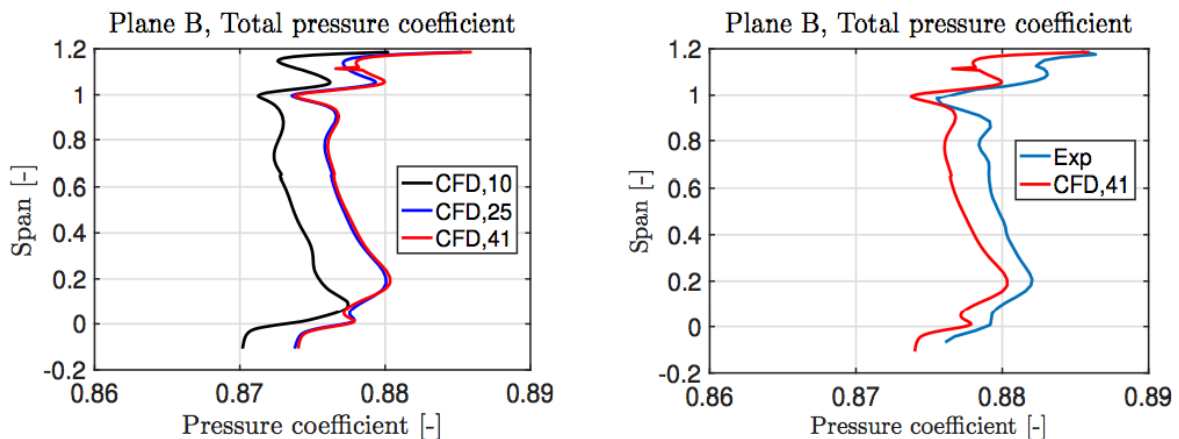


Figure 5-26: Plane B, Evolution of total pressure coefficient along the span over time and comparison with experimental data

#### 5.4.3.2 Measurement plane D

The experimental data of measurement plane D can be taken as a reference for the convergence predictions for the global flow variables and quantities of the second stage. As like for plane B, the solutions between periods 25 and 41 have a very similar trend, but the gradients and the curvatures of the solution at 41 periods seem to be slightly more distinct than for the previous periods, as seen in Figure 5-27 to Figure 5-29. In addition, the solutions at periods 10

and 25 show up sharp peaks in the tip cavity region, which are not visible at period 41. Therefore, the flow field inside the second stage is not completely converged after 25 periods.

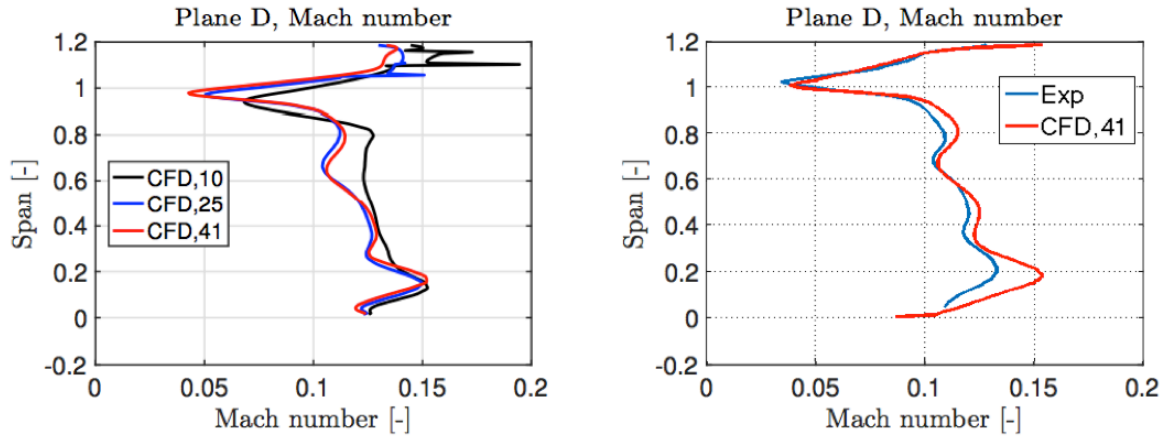


Figure 5-27: Plane D, Evolution of Mach number distribution along the span over time and comparison with experimental data

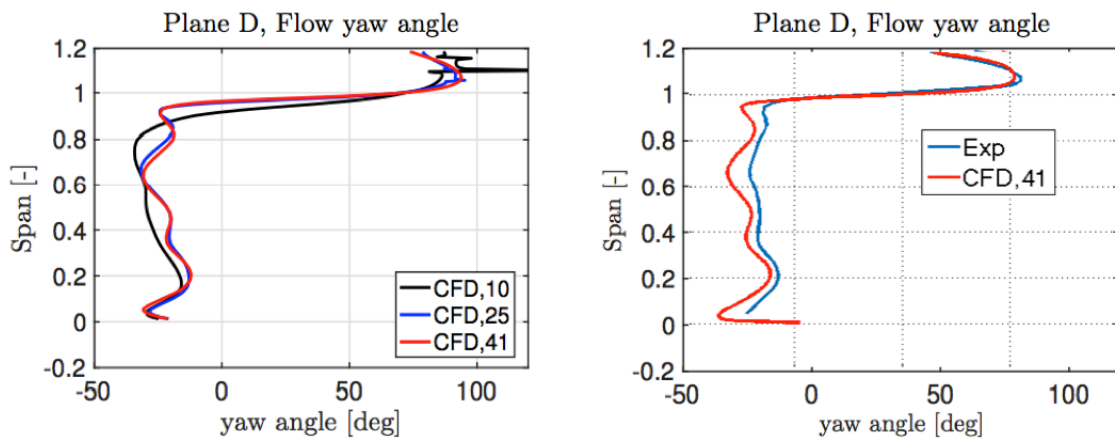


Figure 5-28: Plane D, Evolution of absolute yaw angle distribution along the span over time and comparison with experimental data

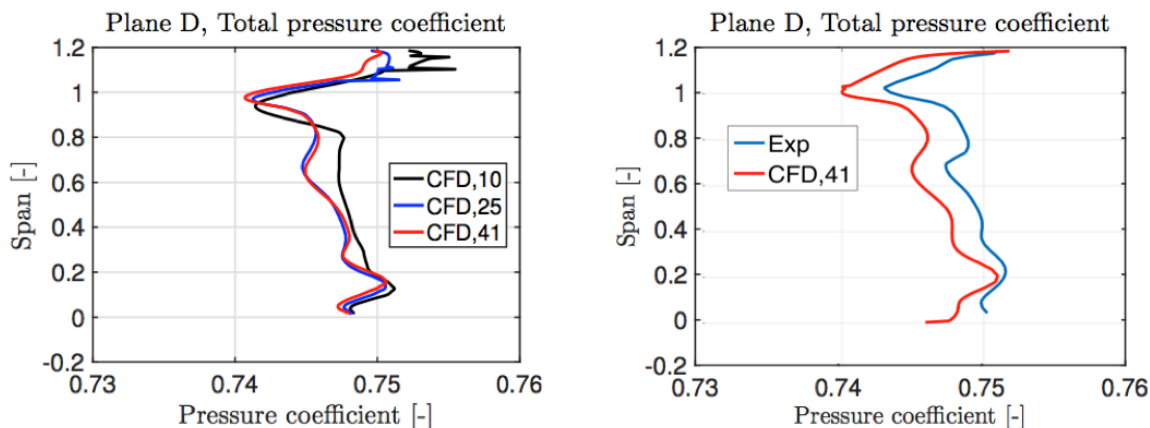


Figure 5-29: Plane D, Evolution of total pressure coefficient along the span over time and comparison with experimental data

As with Plane B, CFD capture very accurately the flow field in Plane D, both in trends and absolute values with one exception. As seen in Figure 5-27, at 20% span there is a sharp increase of Mach number, which is overpredicted by CFD compared to experiments. The reason was once again the spurious decrease of density in the rotor inlet due to poor mesh quality (section 2.1). As a result, temperature is artificially increased, which leads to higher local Mach number and local drop in efficiency. The problem was identified much later and was taken well into account for the later cases.

## 5.5 Convergence acceleration of unsteady simulations

Originally, MULTI3 was using the Lax-Wendroff scheme to solve the RANS equations, as it is a suitable and well-trusted model for compressible flows. The presence of cavities in the computational model and the low Mach number flow in them pose certain challenges for the model, i.e.:

- Increase the mesh size requirements considerably, in order to resolve the complex cavity geometry
- Increase the required number of subiterations per physical time step, due to very fine cells inside cavities and their propagation inside the main flow.
- Slow down convergence and

- Increase wall time required until completion of each simulation.

These matters had to be issued before an attempt of an expensive unsteady optimization cycle. In order to address these problems, multistage time integration and a preconditioning scheme were implemented in MULTI3. The implementation of preconditioning was carried out by Kleinheinz [92]. These extensions are very well suited for the problem in hand since the 4<sup>th</sup> order Runge Kutta scheme is more suitable for low Mach number flows and allows an increased CFL number. Additionally, there is a potential reduction of number of subiterations by application of preconditioning for whole computational domain, since for the test case under consideration Mach number is below 0.5 everywhere in the domain, as seen in Figure 2-4 and 5-30, respectively.

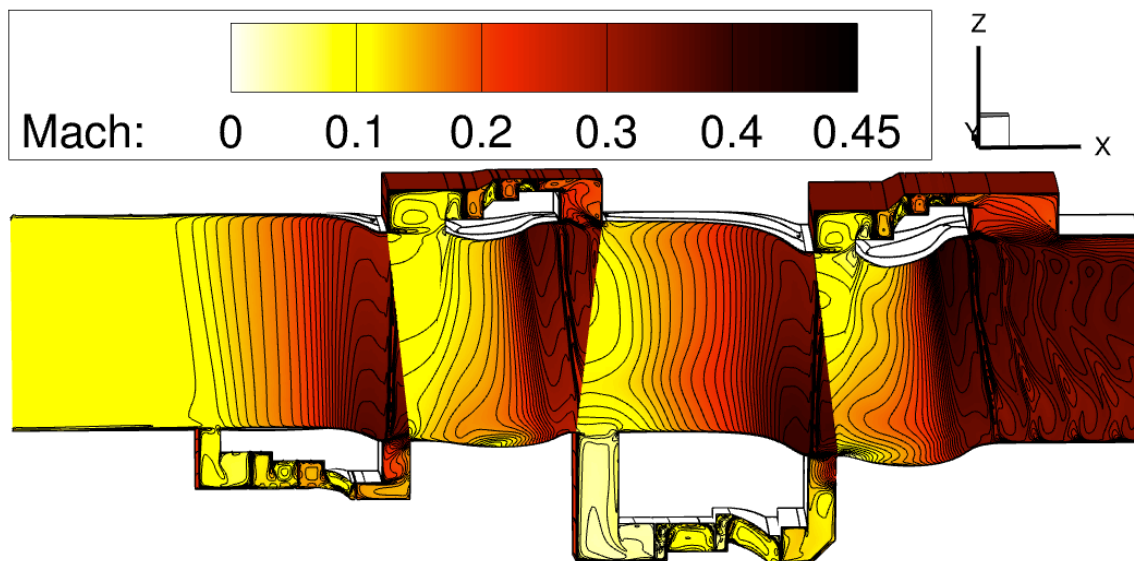


Figure 5-30: Mach number distribution along the domain

The testing of the solver extensions with respect to the speed-up of convergence and the credibility of the computational solutions obtained with the modified version of the solver were discussed in detail by Kleinheinz [92], where each method was separately compared and verified. For this purpose the solutions from simulations conducted with the modified code were verified against a reference solution obtained with the original solver. The reference solution was generated with the simulation setup

presented in section 5.1. In addition, all computational solutions were validated against experimental data from measurements conducted in “LISA”. Indicatively, only relative yaw angle at plane D is presented in Figure 5-31, compared between the reference solution with Lax-Wendroff scheme, the new solution with 4<sup>th</sup> order Runge Kutta scheme with preconditioning, and experiments from “LISA”. The differences between the schemes in terms of absolute values were accounted to the different numerical smoothing applied in each case [92], but the overall trend and main flow features are captured in both cases with improvements seen in the new simulation.

The new implementations give more options in the selection of the decisive simulation parameters like the CFL number, the number of sub-iterations and also the lower limit for the preconditioning parameter. Various parameter combinations were investigated and their solutions were judged, on one hand on their credibility by comparing them against a reference solution and experiments, and on the other hand by evaluating the speed-up they provide.

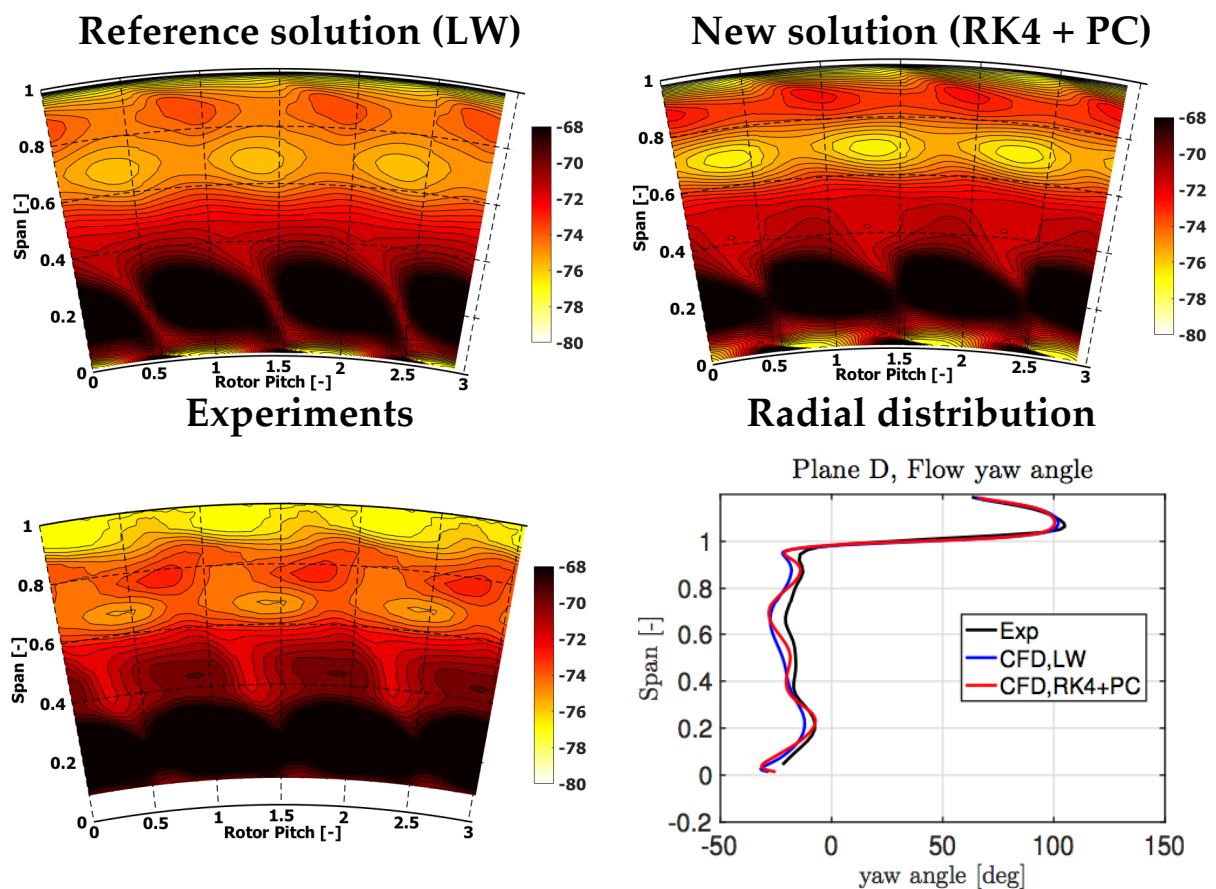


Figure 5-31: Time-averaged relative yaw angle [°] at plane D [104]

The combined benefits of the higher CFL number provided by the multistage time integration scheme and the faster convergence rates of preconditioning yield a speed-up of the solver, despite the considerable additional computational cost of the two new schemes. More specifically, due to the multiple evaluations of the residual in the multistage time integration and the preconditioning, the computational time per period of simulation was increased by 191%. However, the higher CFL number and the gains of preconditioning allowed decreasing the required number of subiterations per physical timestep from 350 to only 50. Eventually, the solution with RK4+PC could be obtained faster by a staggering factor of 3.65x compared to original solver. Additionally, the same speed-up was achieved regardless if the simulations were performed on the K40 or the P100 GPUs of LEC's high performance computing cluster, indicating true speed-up independent of card architecture. This speed-up was proven to be of paramount importance for the successful completion of an unsteady optimization design.

## 5.6 Summary and conclusions

As the available computational power of modern GPUs increased over the past few years, so did the complexity of computational models investigated with MULTI3, moving from single-row, single-pitch to multi-stage, multi-pitch unsteady simulations with cavities. Since the first GPU acceleration of MULTI3 in 2011, the computational power of the GPUs have increased more than nine-fold (from Fermi C2050 to Tesla P100 GPUs) [108]. But even this was not enough in order to perform an unsteady optimization in a reasonable time frame. Since both LEC's and CSCS's high performance computing clusters were equipped with the latest generation of GPUs, the Tesla P100, any additional speed-up of simulations could not come from hardware side, but instead different measures needed to be taken. This chapter summarized the main guidelines that are suggested for reducing the computational cost of an unsteady optimization.

An automated post-processing for calculation of typical parameters in turbomachinery design, as well as a developed/converged solution given as an initial guess to the solver can without a doubt reduce post-processing efforts and computational cost, although the actual advantage is case-dependent and difficult to quantify. Nevertheless, the advantage is easy to understand, if one thinks that most of the computational time in the early stages is spent to develop a proper flow field, especially the turbulent quantities.

Similarly, the monitoring of convergence of unsteady simulations can help identify the minimum level when a simulation can be stopped without having an impact on the accuracy of the solution. A speed-up factor cannot be quantified again but valuable guidelines concerning evaluation of convergence have been extracted.

Throughout the testing of the monitoring routine, several interrelations between the convergence levels of different flow variables could be established. The quantity that was found to represent the convergence level of the global flow field most suitably is mass flow. The mass flow rate at the row interfaces will fluctuate wildly and will not converge as long as the numerical residuals have not stabilized. Further the evaluation of the convergence criterion for the mass flow imbalances can be used to make statements regarding the convergence level of other global variables such as efficiency or entropy generation. This means that a lot of information can be gained by only considering a single parameter. Reasoning for that can be derived by the large dependency of the velocity triangles, which are representative for the velocity field inside the domain, on the mass flow rate.

In general a well-converged unsteady flow field is obtained if the maximum mass flow imbalance reaches a steady - preferably high - convergence level. From a design optimization cycles perspective however, where for example the only concerns are the convergence level of entropy generation, the user will need to simulate at least the same amount of periods it would take the mass flow imbalances to settle. Then, it further depends on how stable the level of convergence for the variable of interest needs to be.



Finally, convergence acceleration measures were identified and successfully implemented for unsteady CFD simulations as extensions to the solver MULTI3. The measures used include the fourth order Runge Kutta scheme and a low Mach number preconditioning method. The new implementations were verified against a reference solution computed with the original solver and validated with experimental data.

The fourth order Runge Kutta scheme provides a larger eigenvalue stability region, which allowed raising the stability limit based on the CFL condition. The less restrictive limit on the CFL number gave the possibility to take advantage of larger time steps per iteration.

Many compressible CFD codes do not converge to an acceptable solution within feasible computational time when local Mach numbers within the flow field are very low. Preconditioning approaches adapt numerical algorithms to provide improved convergence behavior for compressible flows at very low Mach numbers. These methods alter the eigenvalues of the RANS-equations in order to reduce the large discrepancy between the acoustic and convective wave speeds, therefore reducing the stiffness of the system of equations. During the testing of the chosen preconditioning method, a faster decay of the residuals was obtained; consequently fewer iterations were needed to reach similar convergence levels as in the reference computation.

By employing both of these methods, the total iteration count necessary to obtain a converged solution was reduced by 86% but came with an increased computational cost. The implementation of the preconditioning approach is highly GPU-accelerated and requires only 0.8% more computational time per iteration compared to the original implementation. The main contributor was the multi-stage time integration, which increased the computational time per iteration by 191%. Nevertheless, the combination of both resulted in an overall speed-up of the solver by a factor of 3.65 for the case under investigation. Numerical results were compared and validated with experimental data.

In conclusion, this preparatory work allowed the successful unsteady optimization of rotor hub endwall contouring for



efficiency increase, which is discussed in detail in the following chapter.

## 6 Unsteady Optimization of Profiled Rotor Hub Endwall

This chapter describes the optimization work performed to improve the performance of a high-pressure (HP) steam turbine using non-axisymmetric hub endwall profiling on the rotor blade passage. Endwall optimization is something already well established and has been used for years for performance improvement. Something that is neglected in the vast majority of studies available in literature is the effect of cavity leakage flows on secondary losses and efficiency. Similarly for gas turbines, rim seal cavities are excluded from the computational domain during the optimization cycle, due to the high computational cost they require. Additionally, this leakage flow is a strongly unsteady phenomenon, which is known that steady state solutions fail to capture accurately. To take into account this unsteady interaction, as well as unsteady blade row interactions, an unsteady optimization of endwall contouring is performed, including the cavity paths in the numerical model. To the author's best knowledge, this is the first time that an unsteady optimization is used for a real, three-dimensional case with cavities. First, the followed approach and the computational models are presented. Then, the results of the optimization and a comparison of the baseline and profiled case are presented. Numerical results of the baseline case have been compared extensively and validated with experimental data.

### 6.1 Methodology

The turbine geometry under investigation is the LISA-H2 turbine geometry, which is typical of high-pressure steam turbines. Goal of this work was to achieve an efficiency improvement of the second stage, while taking into account, during the whole optimization process, the unsteady flow mechanisms present in the flow field. The resulting geometry of the optimization is planned to be experimentally tested in LEC's axial turbine facility "LISA".

A typical optimization process requires dozens of simulations. In order to reduce the computational cost, while still maintaining a high accuracy, a novel approach is followed and is described in the schematic of Figure 6-1. First, an unsteady, two-stage simulation of

the baseline geometry is performed. Unsteady data are then extracted at the first stage outlet on the rotor-stator interface. This data are then imposed on a new single-stage simulation as unsteady inlet boundary conditions. Finally, the unsteady, single-stage simulation of the baseline is performed. At this point, numerical results were compared and validated with experimental measurements that had been conducted in LISA for the H2 case. Validation with experiments ensured that high accuracy on numerical predictions is maintained even without the first stage, since the full unsteady information is passed on successfully in the single-stage simulations.

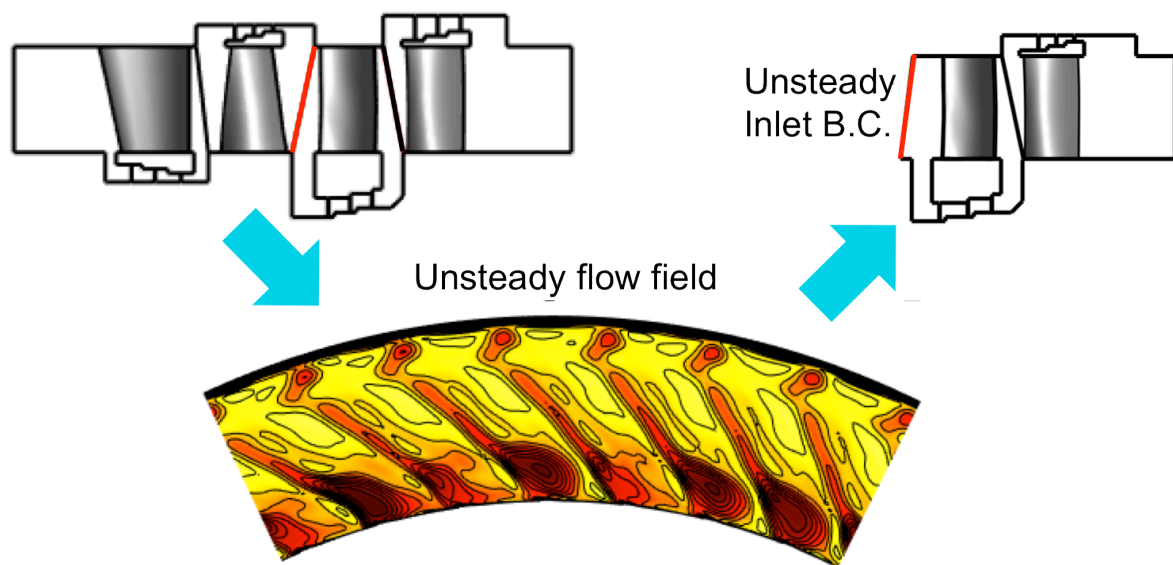


Figure 6-1: Approach to reduce computational cost of optimization, while maintaining high accuracy – Unsteady inflow

The optimization was performed using Numeca's FINE/Design3D software package with the application of a Genetic Algorithm. An Artificial Neural Network is used to approximate CFD computations during the optimization algorithm. The ANN has been trained by a Database, which consists of a set of cases with different endwall geometries that have been evaluated by unsteady CFD simulations and their performance has been quantified. All simulations of the database and the results of the optimization algorithm were single-stage simulations with imposed unsteady inlet boundary conditions. Computational and optimization setup is discussed in detail in the following section.

## 6.2 Computational Setup

The optimization was performed on a computational model of the H2 turbine case, details of which were discussed in section 3.2.

### 6.2.1 Geometry and computational domain

The computational domain consists of a two-stage configuration of an axial HP steam turbine. As seen in Figure 6-2, the geometry includes the cavity paths for both stators and rotors, at hub and tip, respectively.

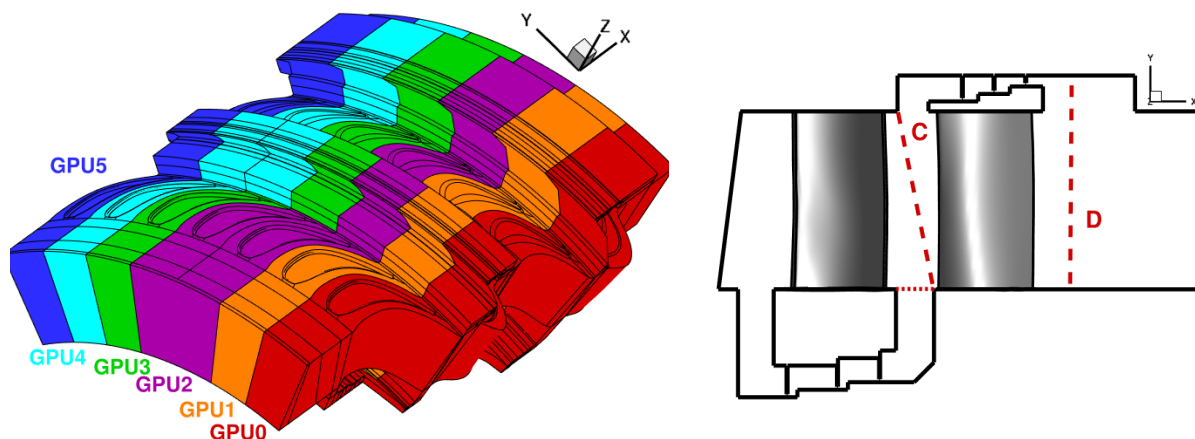


Figure 6-2: Computational domain of LISA-H2 turbine case for two-stage (left) and single-stage (right)

In order to allow the simulation of only a sector, the model was created with a modified blade count for the first stage's stator and rotor, which was reduced by 1 and 3 blades of the full annular domain, respectively. This, modified the blade count from 50-52-42-42 to 49-49-42-42, and allowed the simulation of a sector with a configuration of 7-7-6-6 (S1-R1-S2-R2) blades. In order to account for this change in blade number, the blade profiles of the first stage have been adjusted to maintain the same turbine capacity. For the optimization process, the first stage was removed from the model and only the second stage was kept, still in a 6-6 blade configuration. The domain remained the same to be able to use the unsteady inlet flow field as inlet boundary conditions.

Computational study has been carried out using in-house developed CFD solver MULTI3 on Piz-Daint Cray XC40/XC50 hybrid computing system in Swiss National Supercomputing Centre CSCS in Lugano, Switzerland, under projects ID sm01 and s822. Piz-Daint is equipped with latest NVIDIA P100 GPUs, with on-board memory of 16 GB. The computational domain was split in 6 sub-domains, as seen in Figure 6-2, for both the two- and single-stage simulations.

Table 8: Mesh size of the different flow domains per pitch, in millions

Domain	Mesh Size (main domain)	Mesh Size (cavities)	Total Mesh Size
S1 Stator	0.63	0.62	$(7 \times 1.25) = 8.75$
R1 Rotor	0.59	0.63	$(7 \times 1.22) = 8.54$
S2 Stator	0.63	0.85	$(6 \times 1.48) = 8.88$
R2 Rotor	0.76	0.79	$(6 \times 1.55) = 9.3$
<b>Total</b>	16.88	18.59	35.47

Table 9: Mesh quality report of whole domain

Minimum angle	Maximum aspect ratio	Maximum expansion ratio
6.2°	1353	7.2

A multi-block structured, body fitted mesh is generated for each passage separately. In spanwise direction, 72 radial nodes were used with higher clustering towards the endwalls. In total, 26 blades were modeled for the two-stage configuration, resulting in a mesh of 35.5 million nodes, of which more than 18.5 millions were used in the cavities to resolve the complex geometry and capture unsteady flow features. For the single-stage simulations, the mesh size was reduced to 18.2 million nodes, of which 9.8 millions were used inside the hub and tip cavity paths. The  $y^+$  value is kept below 5 in the whole domain. Mesh quality of the model was well within acceptable range. Details of mesh size for each row and final mesh quality are given in Table 8 and Table 9.

The whole mesh was created with fully matching interfaces, both between blocks and row interfaces, in order to eliminate

interpolation errors, which may lead to considerable loss of accuracy at the regions where highly unsteady phenomena take place. Number of radial nodes and total mesh size was a result of a separate, sensitivity study that was conducted during the course of the main investigation.

### 6.2.2 Simulation settings

Unsteady simulations have been performed using dual time stepping approach. Both for the two- and single-stage models, 210 equal time steps have been used for each period, where a period is defined as the rotation of 7 rotor blade passings of the first stage or 6 rotor blade passings of the second stage. For time integration the 4<sup>th</sup> order Runge-Kutta scheme was used combined with preconditioning, reducing the required computational cost significantly, as discussed in detail in chapter 5. The  $\beta$  parameter for preconditioning was chosen equal to 3.0 for increased solver stability during simulation.

Due to the presence of very fine cells in the computational mesh, especially in the cavity regions, a sufficient number of sub-iterations is needed in order to ensure proper propagation of information through the regions of very high node clustering, due to the fact that smaller cells need more sub-iterations for the flow to develop properly compared to bigger cells, as it was already discussed in section 2.1. For each physical time step, only 60 sub-iterations were sufficient with CFL number of 1.0. Both the number of physical time steps and sub-iterations are a result of a separate study that was conducted during the course of the main investigation.

### 6.2.3 Boundary conditions

Regarding the two-stage simulation, only a radial flow profile is imposed at inlet, because of the almost uniform flow field at the inlet of the domain. The total pressure, total temperature, yaw and pitch angle, axial Mach number as well as the turbulence intensity and turbulent length scale at each radial position are required by the solver (see Table 10). Radial equilibrium is imposed at the outlet plane of the domain, so only the static pressure at the hub is

needed, which is set to 0.95997 [bar]. The values for the inlet and outlet boundary conditions are taken from measurements conducted in LEC’s axial turbine facility, “LISA”.

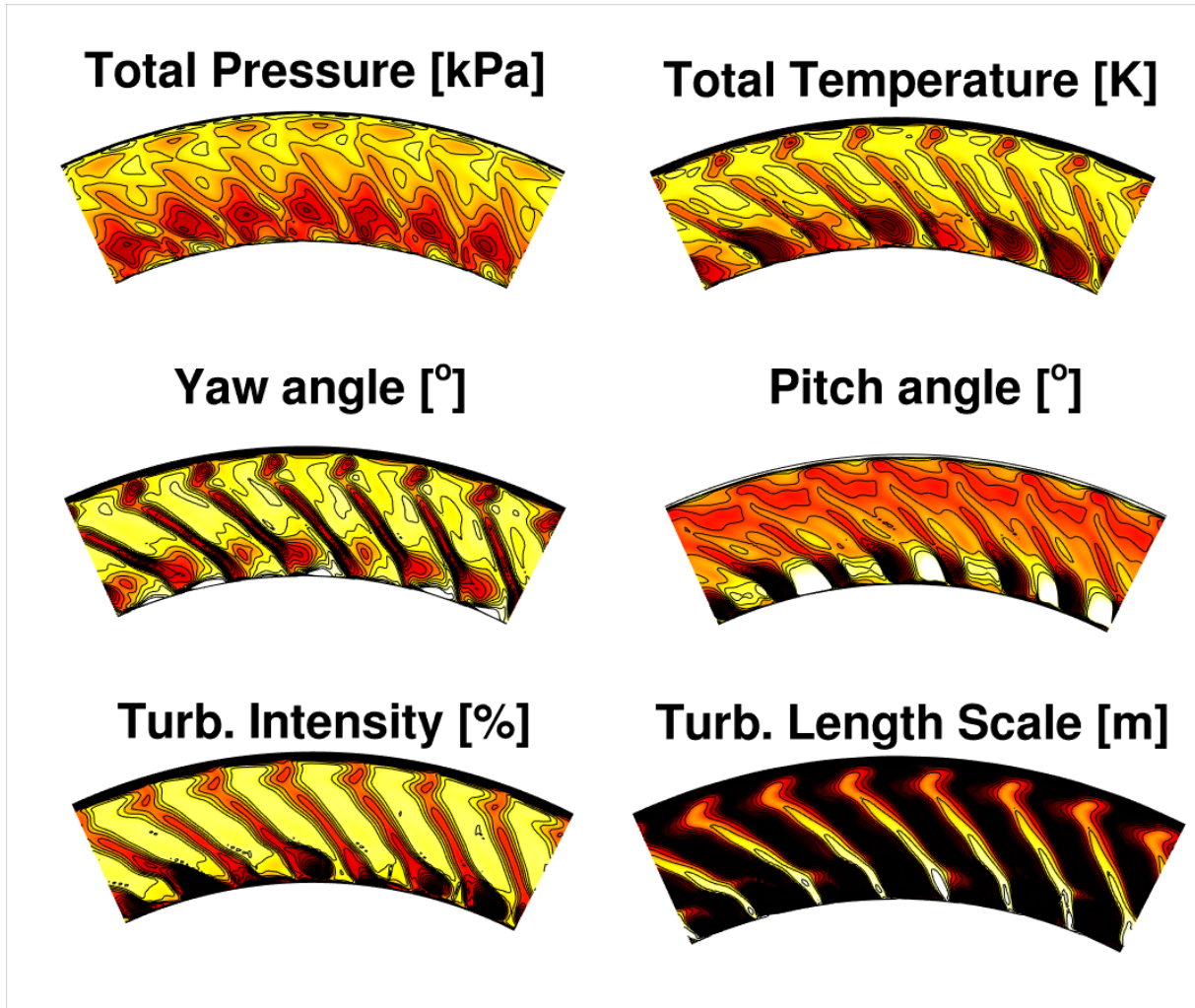


Figure 6-3: Boundary conditions at single-stage inlet at  $t/T=0$

Table 10: Inlet boundary conditions

	$p_t$ [bar]	$T_t$ [K]	Yaw angle [°]	Pitch angle [°]	$Ma_{ax}$ [-]	$Tu_{in}$ [%]	$Tu_{ls}$ [m]
Hub	...	...	...	...	...	...	...
	1.29997	313.5	0	0	0.05	5	0.0001
Tip	...	...	...	...	...	...	...

After successful completion of the two-stage, unsteady simulation, the full unsteady flow field was extracted at the first stage’s outlet,

for all 210 time steps. These were then imposed for all cases of the single-stage simulation. Figure 6-3 shows an example of the boundary conditions that were imposed on the first time step, where seven distinct flow features appear coming from the seven rotor blades of the first stage. In this way, the unsteady flow behind the first stage's rotor is passed on successfully to the second stage, having reduced the computational domain by almost half of its original size.

Regarding the rotating wall boundary conditions and initial guess, similar approach was followed as the one discussed in section 5.1.2, in Figure 5-2 and Figure 5-3. Besides the rotation, adiabatic and no slip boundary conditions were applied for all walls.

#### **6.2.4 Optimization setup**

Before the start of the optimization, the geometry needs to be parameterized and the free parameters, which will be available for modification during optimization, need to be decided. Next step is the database generation, which contains a set of differently perturbed cases that will be evaluated with unsteady CFD simulations with MULTI3 in terms of their performance. This database will be used to train the artificial neural network. Finally, the optimization with the genetic algorithm is initialized. GA uses the predictions of the ANN during each generation and finally gives the "optimum" solution, according to ANN's prediction. This solution is evaluated with an unsteady simulation and, during the first few design cycles, the predictions of CFD and ANN differ. This case is added to the database, the ANN is re-trained and a new design cycle begins. This process is continued until the predictions of CFD and ANN match and the optimum solution is found. The setup of each step is presented below.

##### *6.2.4.1 Geometry parameterization*

The parameterization is performed with Autoblade, where the hub and shroud lines, the end wall and the blade profile are described by a set of parameters. In the case of the turbine geometry under investigation, the target to be modified is the hub end wall of the rotor blade. Therefore, a high accuracy on the blade



parameterization is allowed to ensure that the parameterized geometry is as close as possible to the real geometry. For the blade, 11 radial cuts were used to define the profiles at different span locations. In total 473 parameters were used for the geometry parameterization. Of course, only those related the end wall surface were set as free. The rest were set to frozen for the whole optimization procedure. Needless to say that an optimization with almost 500 free parameters would be close to impossible to optimize and reach convergence.

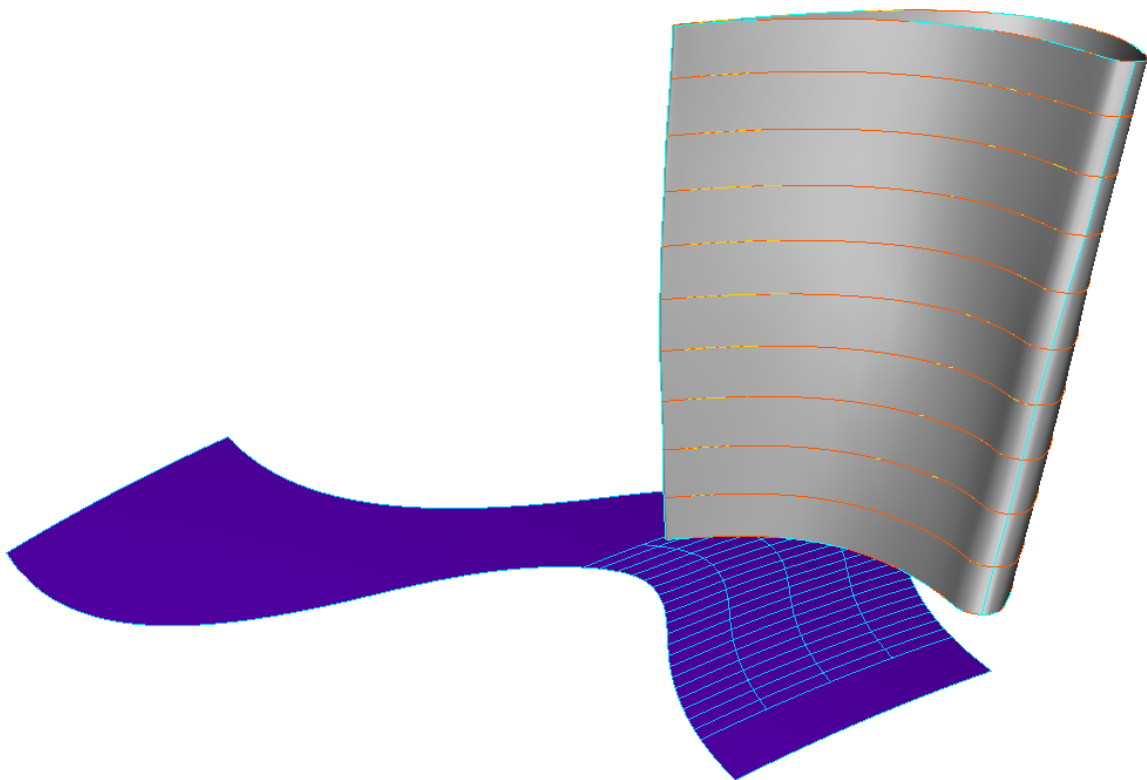


Figure 6-4: Geometry parameterization with Autoblade

The parameterization area of the endwall started upstream of the leading edge of the blade at the inlet interface while the end was at the trailing edge of the blade. The blade channel was divided into 5 equidistant Bezier cuts, each cut being constituted of an equidistant distribution of 6 parameters. Since the user-defined cuts extended outside of the blade channel it is necessary that the start and end cut are identical in order to ensure geometrical continuity. This geometrical continuity led to 24 free parameters for the optimization. The choice of the number of parameters comes from the balance between predicted aerodynamic benefit and the

computational cost of the optimization. Each one of the 24 free parameters is limited to a movement normal to the end wall, i.e. one-degree freedom. The contour shape can be received simply by the control point values as these values define the deformation displacements from the datum contour [74]. In the parameterization, all the free parameters were allowed to vary the same quantity. The allowed variation was of 6.75 mm, which corresponds to 7.5% of the blade span. The resulting geometry after parameterization is presented in Figure 6-4. The used setup is summarized in Table 11.

Table 11: End wall parameterization setup in Autoblade

<b>General settings</b>	
<b>Method</b>	Along
<b>Channel start</b>	Inlet
<b>Channel end</b>	Blade trailing edge
<b>Number of cuts</b>	5
<b>Cut locations (Relative)</b>	0, 0.25, 0.5, 0.75, 1
<b>Perturbations</b>	
<b>Curve type</b>	Bezier
<b>Number of free parameters</b>	6
<b>Variation range</b>	$\pm 7.5\%$ of blade span

#### 6.2.4.2 Database

The initial database is constituted by several samples and their associated geometries and CFD results. The number of samples that forms the database should be twice or three times the number of free parameters chosen by the user [70]. For this specific case, it was chosen to have a database with a number of samples of 3 times the number of free parameters, e.g 72 samples. The samples are generated by perturbing all the free parameters within the lower and upper bounds previously selected. FINE/Design3D offers a range of 10 different methods for the database generation and the chosen method was the default, the Latin hypercube method.

Database generation is the most expensive step of the optimization cycle, in terms of required computational time, due to the large

number of cases that need to be computed. However, these cases are independent of each other, so they can be performed in batches or even all in once, if computational resources are available. For this work, in order to speed up the convergence, first only the baseline was computed and the final solution was used as initial guess for the rest 71 cases. This was only allowed due to the structured mesh that is used, leading to a decrease of required time for a modified geometry by more than 66%. All remaining 71 cases of the database were performed simultaneously in CSCS, using 6 GPUs for each case, 426 GPUs in total, and were completed in less than 24 hours. The results were then given as an input to the artificial neural network for training. However, the main bottleneck is the optimization phase because the new cases are given in a serial manner, requiring about one full day for each optimization design cycle.

#### 6.2.4.3 Artificial Neural Network

The training and learning of the artificial neural network is done within the Design3D software. For this case, a network with 2 hidden layers has been used, which has been shown previously to achieve better training and representation of the problem [51]. The used setup is described in Table 12. After training completion, the optimization process was initiated. Every training process requires approximately 5-10 minutes for completion.

Table 12: Artificial neural network learning setup

<b>Neural network learning parameters</b>	
<b>Neural network</b>	<b>Backward mode</b>
<b>Number of iterations</b>	20000
<b>Learning rate coefficient</b>	0.5
<b>Momentum coefficient</b>	0.8
<b>Decay factor</b>	0.0
<b>Convergence level criteria</b>	0.0001

#### 6.2.4.4 Optimization Algorithm

Genetic Algorithm was chosen for the optimization, which is a global optimization technique that is far less likely to get stuck on

local minimum compared to more conventional, gradient optimization methods. The genetic algorithm starts with an initial population, randomly selected from the whole design space. From this population new generations with better elements are created. The performance of each individual is measured by its fitness (inverse of the objective function). There are different operations that are applied during the algorithm, such as elitism, combination and mutation, with the final goal being that the strongest individuals will spread their genes to create better children, while those with inferior traits will die out due to lack of reproduction. Setup is summarized in Table 13.

Table 13: Genetic algorithm optimization setup

<b>Genetic algorithm setup</b>	
<b>Population size</b>	50
<b>Number of reproduction cycles</b>	100
<b>Truncation rate</b>	20
<b>Elitism</b>	1
<b>Extrapolation range</b>	1
<b>Mutation probability</b>	0.03
<b>Mutation mu</b>	20

#### 6.2.4.5 Objective function

Goal of the optimization is to achieve an efficiency gain by applying end wall contouring. However, the geometrical changes could potentially be highly aggressive, leading to a significant reduction or increase of blockage. Therefore, in order to keep the turbine capacity the same, a restriction on mass flow is imposed, which is allowed to only vary within  $\pm 1\%$  of the baseline mass flow. The objective function can then be represented by Eq. 6-1:

$$OF = w_{\eta}P_{\eta} + w_{\dot{m}}P_{\dot{m}} \quad \text{Eq. 6-1}$$

where  $w$  are the weighting factors and  $P$  are the penalty terms defined by Eq. 6-2:

$$P = \left( \frac{|Q_{imp} - Q|}{Q_{ref}} \right)^k \quad \text{Eq. 6-2}$$

The desired value of efficiency is obviously 1, therefore there will always be a penalty term for efficiency. On the other hand, the mass flow can vary within an acceptable range, therefore its penalty term will be positive when mass flow exceeds allowed limits and zero for the rest of the cases. These are incorporated in the objective function by applying an equality penalty for efficiency and a min-max penalty for mass flow. The setup of the objective function is summarized in Table 14.

Table 14: Summary of objective function

	$\eta$ [%]	$\dot{m}_{min}$ [kg/s]	$\dot{m}_{max}$ [kg/s]
Penalty type	Equality	MIN	MAX
Imposed value ( $Q_{imp}$ )	1	0.99 $\dot{m}$	1.01 $\dot{m}$
Reference value ( $Q_{ref}$ )	1	0.99 $\dot{m}$	1.01 $\dot{m}$
Weighting factor ( $w$ )	3	196	196
Exponent ( $k$ )	2	2	2

## 6.3 Results and discussion

### 6.3.1 Validation of numerical model

Since the optimized geometry was planned to be manufactured and experimentally tested in LISA, the results of the single-stage, baseline geometry with unsteady inflow conditions were extensively compared and validated with previously completed measurements of the baseline geometry. The numerical predictions were compared against time-averaged data measured with 5-hole and FRAP probes.

Figure 6-5 shows the comparison between 5HP and simulation at second rotor exit, as well as some parameters of the whole second stage. Plane D is shown in Figure 6-2. For the average error quantification of the numerical results, the RMS difference was used for relative yaw angle, while the rest were calculated for each radial position and were averaged using Eq. 6-3:

$$\frac{1}{N} \sum_{i=1}^N \left| \frac{Fq_{i,EXP} - Fq_{i,CFD}}{Fq_{i,EXP}} \right| \quad \text{Eq. 6-3}$$

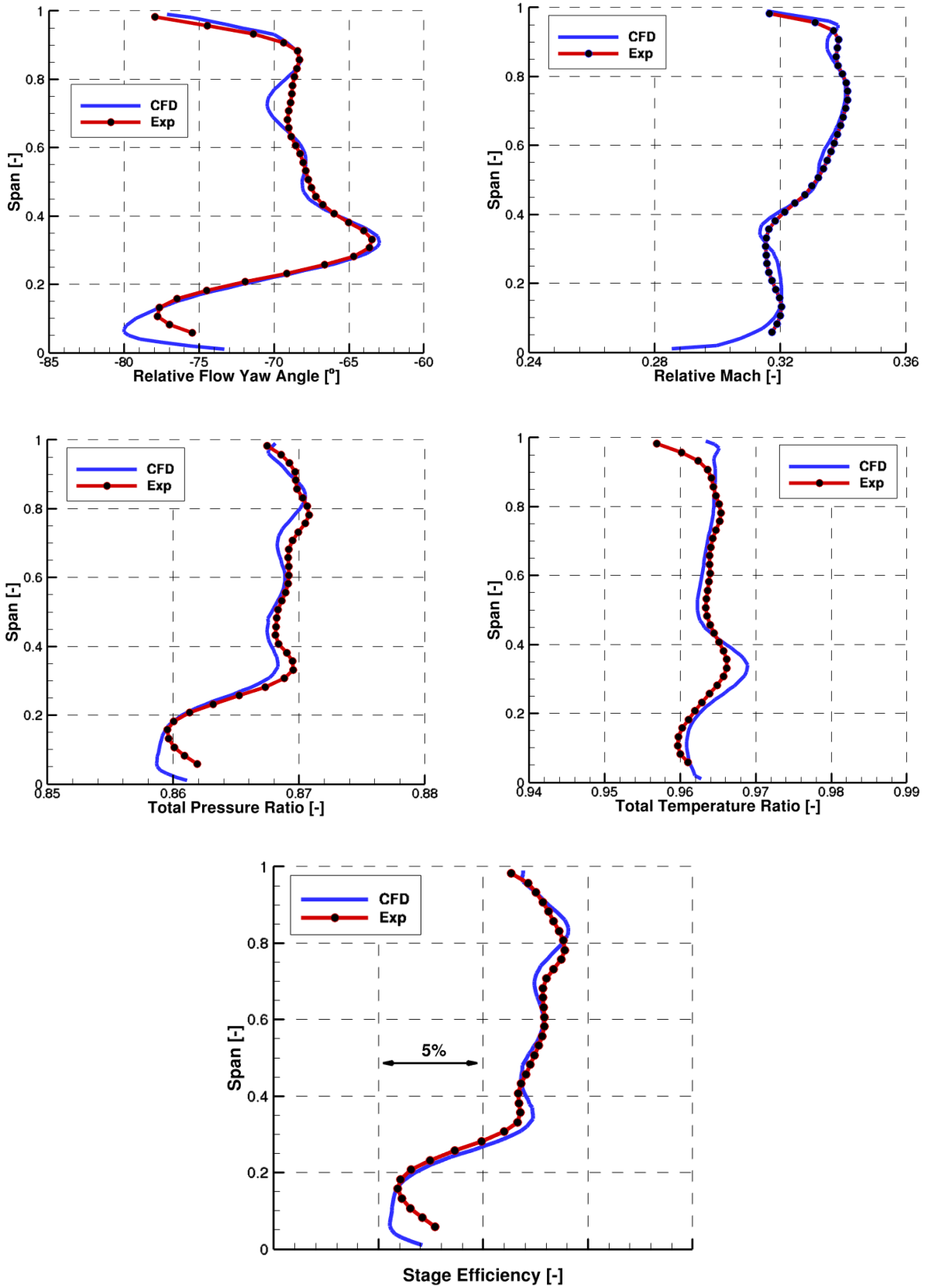


Figure 6-5: Comparison between measured (5-hole probe) and simulated values at rotor exit

As clearly seen in Figure 6-5, CFD match exceptionally well with experiments, with errors remaining below 0.5%. Additionally, the loading of 2<sup>nd</sup> stage was compared to validate the torque and mass flow predictions, given by Eq. 6-4. Detailed values of error are provided in Table 15.

$$\psi = \frac{T\omega}{\dot{m}U_{tip}^2} \tag{Eq. 6-4}$$

Table 15: Averaged errors of CFD compared to experiments

Parameter	Simulation error
<b>Rotor exit</b>	
Relative yaw angle	1.2°
Relative Mach number	0.57%
<b>Stage parameters</b>	
Stage loading	0.23%
Total pressure ratio	0.09%
Total temperature ratio	0.13%
Total-to-total torque-based stage efficiency (absolute average)	0.19%

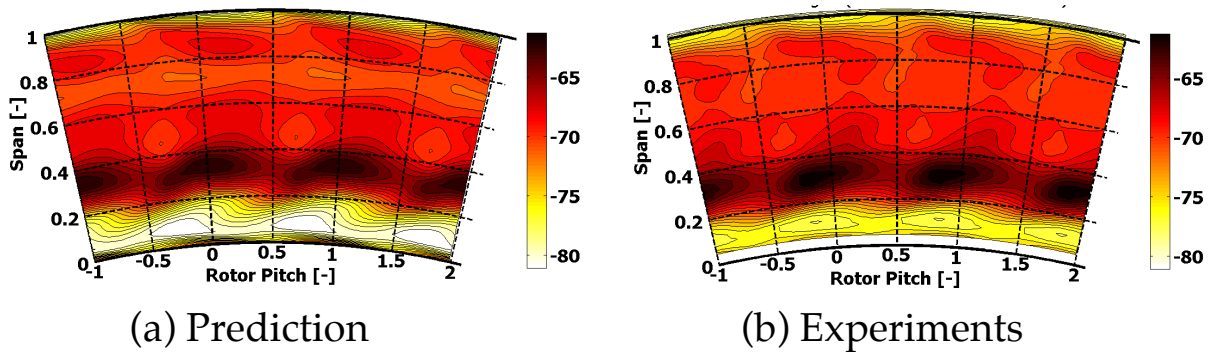


Figure 6-6: Comparison between simulated and measured (FRAP) of relative yaw angle at rotor exit, time-averaged in rotor frame of reference

Numerical results of the single-stage baseline simulation have also been compared with FRAP measurements at rotor exit, time-averaged in rotor’s frame of reference. Figure 6-6 and Figure 6-7, present the relative yaw angle and relative total pressure  $Cp_{t,rel}$ . Yaw angle matches the experiments very well, both in trends and

absolute values. Relative total pressure, on the other hand, is slightly under-predicted in terms of absolute values compared to experiments; therefore the scales of the two plots are not same. However, the area losses are captured correctly by CFD and they will be analyzed in detail in next sections. It is observed that the main flow feature of interest in rotor exit is the strong hub passage vortex that is developed, as seen from the strong flow over- and underturning in Figure 6-6 and from lower total pressure below 45% in Figure 6-7.

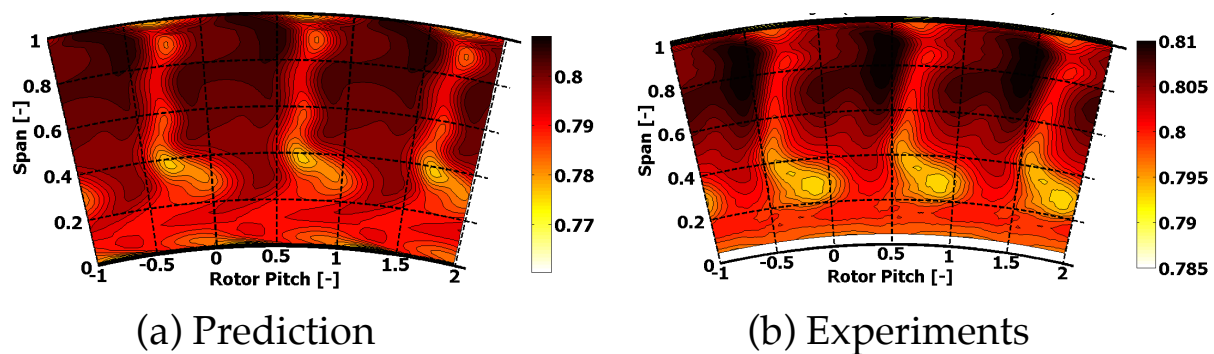


Figure 6-7: Comparison of normalised relative total pressure  $Cp_{t,rel}$  in rotor frame of reference for predictions and measurements (FRAP) at rotor exit, time-averaged in rotor relative frame of reference

The fact that CFD are able to predict the main loss regions in correct radial positions and with similar strength compared to experiments is important for the relevance and credibility of analysis presented in following sections.

### 6.3.2 Optimized end wall geometry

The optimization was performed with an objective to increase stage efficiency, while having a constraint on mass flow to ensure that the capacity of the turbine will remain the same. In order to do that, end wall contouring was applied on the rotor hub end wall, as the beneficial effects of non-axisymmetric profiles on controlling secondary flows have been shown many times in literature. In the case under investigation, a strong hub passage vortex is observed, which was attempted to be controlled by the profiled endwall.

Figure 6-8 presents the design optimization convergence of the genetic algorithm, where the predictions of the ANN and CFD are



slowly reaching to convergence over the progress of the optimization.

The best solution was found on design iteration 14 and CFD predictions show an increase in stage total-to-total torque-based efficiency by 0.27% of the profiled case compared to baseline. Mass flow remained within the imposed constraint of  $\pm 1\%$  during all design iterations. The mass flow of optimized case is reduced by -0.30% compared to baseline. The efficiency is calculated by Eq. 6-5 and the geometry is shown in the right part of Figure 6-8.

$$\eta = \frac{\left(\frac{\omega \cdot M}{\dot{m}}\right)}{c_p T_{t,in} \left(1 - \frac{p_{t,out}}{p_{t,in}}\right)^{\frac{\gamma-1}{\gamma}}} \tag{Eq. 6-5}$$

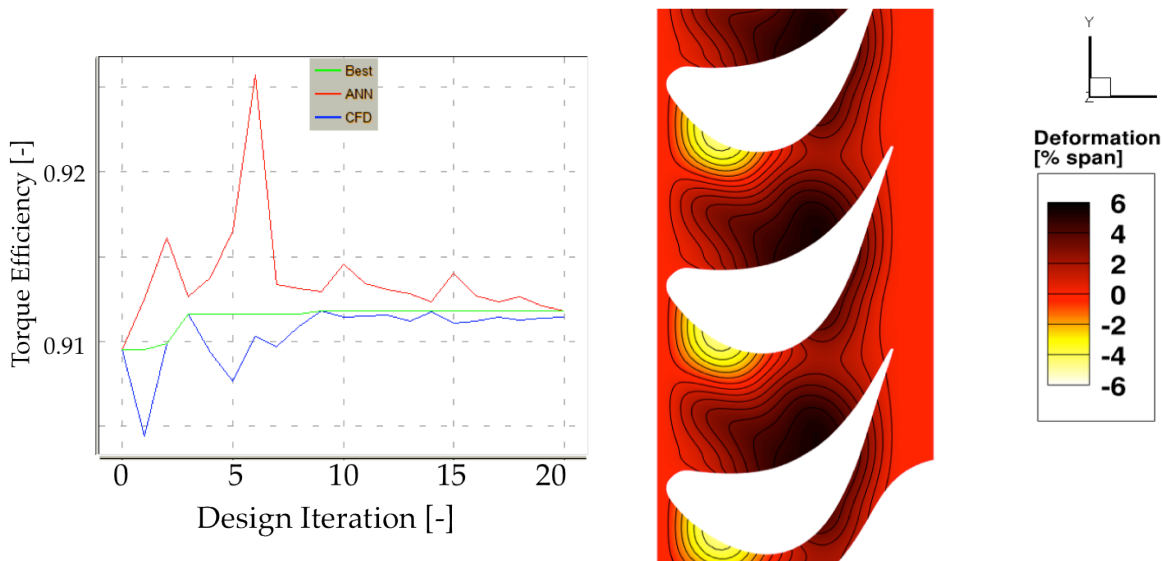


Figure 6-8: Design optimization convergence and final optimized rotor hub end wall geometry

The resulting geometry is shown as the deformation of the end wall in % of total span. Positive values denote hills or “bumps” on the end wall, while negative values imply troughs. Overall, the changes in the endwall slightly reduced the available volume compared to the baseline by -0.31%. This means more blockage is introduced in the flow, which for the same pressure ratio, leads to the mass flow reduction mentioned above.

The control points of the parameterized end wall were allowed to vary between  $\pm 7.5\%$  of the span during the optimization. Although this could potentially result in very aggressive geometries, it gives enough freedom to the optimizer to explore different solutions and areas of the design space. Eventually, the optimization converged to a solution that shows a surface deformation within  $-4.5\%$  and  $+5.5\%$  of the span.

There are three main features observed on the non-axisymmetric endwall: a hill close to the pressure, a trough close to suction side and a small elevation parallel to the trailing edge from suction side. Although the first two features are very common and found in most of the end wall designs, the third one is rather not very traditional and was a surprising result to be seen in the optimization. It is worth mentioning that in a manual attempt to remove this elevation from the geometry, the CFD results showed that there is still a  $0.2\%$  gain in efficiency but it was lower than the optimum solution of the genetic algorithm and was therefore abandoned.

In the following sections, the effect of the end wall profile on the flow field will be analyzed.

### 6.3.3 Upstream effects at S2 stator exit

As shown in Figure 6-8, the end wall is axisymmetric at the lip of the rotor disc and the contouring starts slightly downstream, closer the rotor leading edge. This is coming from a limitation of the geometry parameterization software Autoblade, where it does not allow having a non-axisymmetric profile at the lip of the rotor, but rather the non-uniformities start slightly downstream. It is worth mentioning here that this is quite restricting the available solutions, especially in cases where leakage flow from the cavity or injected purge flow in case of gas turbines enter the rotor and are involved in the secondary flow generation. Such a case with a wavy shape of rotor hub platform leading edge was demonstrated by Jenny et al [83] and it is suggested to be taken into consideration in future designs when dealing with leakage flows.

Nevertheless, due to the shape of the geometry under investigation, it is expected that the influence on the upstream flow will be small. To verify it, flow is analyzed on the stator-rotor interface of the

computational domain, plane C, as seen in Figure 6-2. The location of the interface is interesting because it includes the effect of the leakage flow coming from the stator hub cavity. Figure 6-9 shows the circumferentially and time-averaged radial distribution of static pressure and Mach number. The dashed lines show the variation of the flow in time. As expected, large variations over time are present below 20% due to the leakage flow.

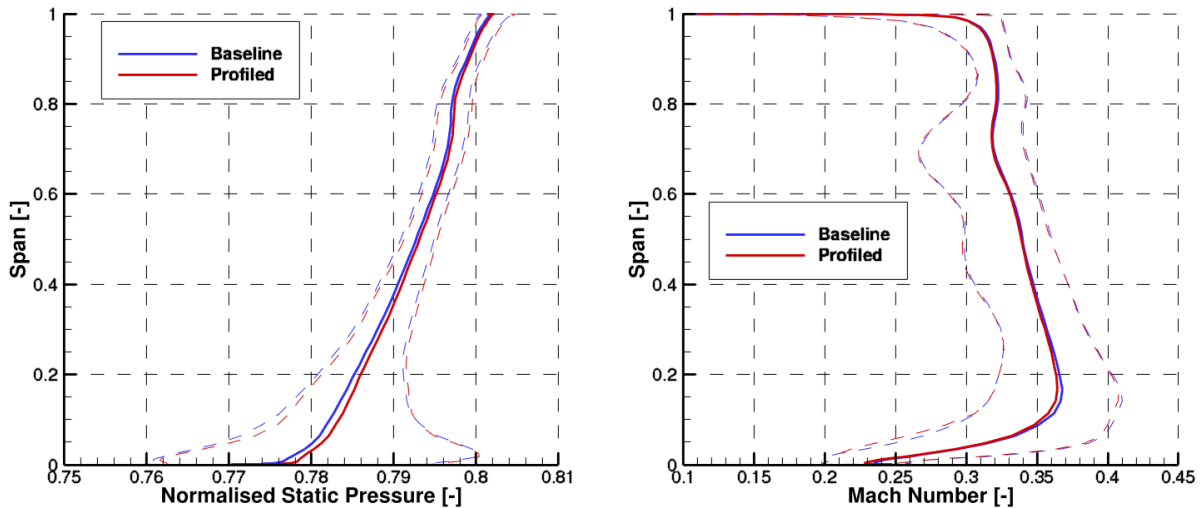


Figure 6-9: Mass- and time-averaged normalised static pressure  $Cp_s$  and Mach number at rotor inlet

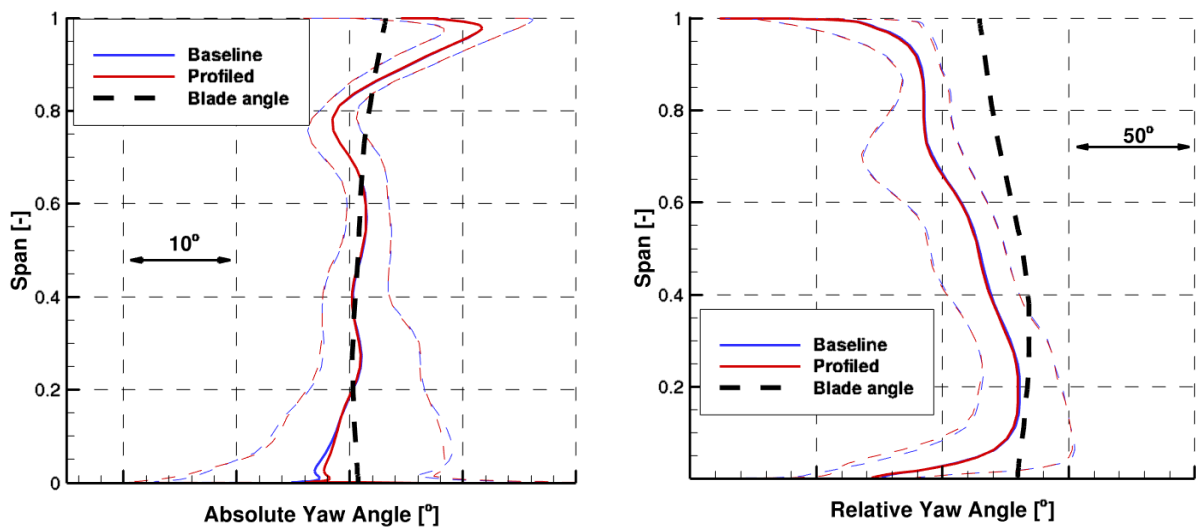


Figure 6-10: Mass- and time-averaged absolute and relative yaw angles at rotor inlet

As seen by the static pressure plot, the profiled case cause an increase in static pressure along the whole span, which is however

very low with a maximum of 0.2% at 1% span position. Similarly, absolute Mach number is slightly reduced for the profiled case by -0.5% along the span with a maximum difference of -4.5% at 1% span position.

Figure 6-10 presents the circumferentially and time-averaged absolute and relative flow yaw angles. Again, the flow remains unchanged between baseline and profiled case with small changes close to the hub due to the interaction with leakage flow. What is interesting to notice is that the flow enters the rotor with high negative incidence angle very close to the hub due to the leakage flow. Comparison with experiments showed that this effect is not captured during measurements at plane C because the location is slightly upstream from the position where cavity flow is ejected.

From figures Figure 6-9 and Figure 6-10, it is clearly seen that the flow is consistent at rotor inlet between the cases of baseline and profiled, indicating that the capacity of the turbine did not change significantly, as it was originally intended. However, the changes close to the hub are more pronounced, meaning that there are changes in the way the rotor end wall is interacting with the leakage flow coming from the rotor cavity. The effects are discussed in next section.

### 6.3.4 Influence on cavity exit flow

For the influence of the profiled rotor end wall on the exit of the cavity, the flow is examined on a cylindrical surface at 0% span, on

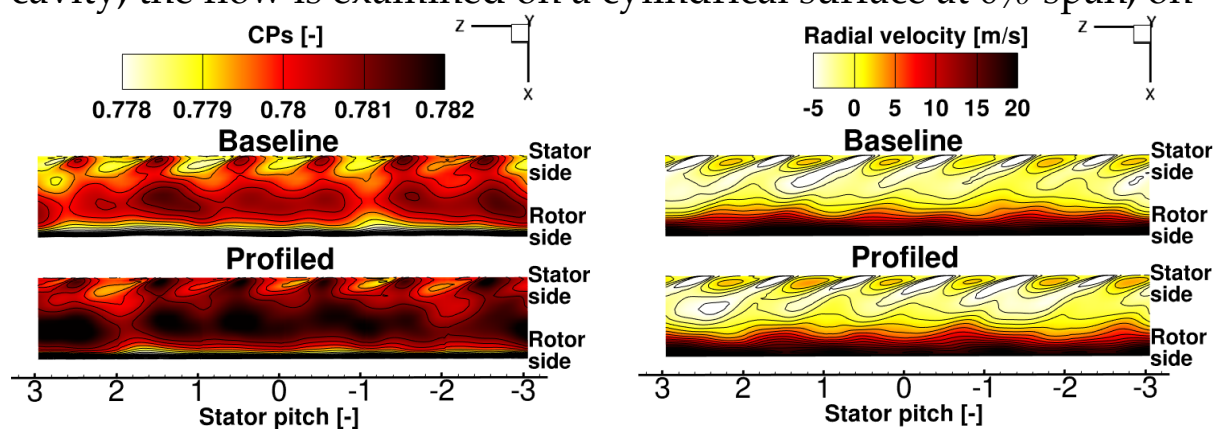


Figure 6-11: Time-averaged normalised static pressure  $C_{p_s}$  and radial velocity  $V_r$  at stator hub cavity exit (0% span)

the interface between cavity and main flow. The location of the interface is shown in Figure 6-2. First the flow is analyzed on the whole plane as seen in Figure 6-11, where normalised static pressure and radial velocity are presented, time-averaged in the stator absolute frame of reference. The plane is shown for all six passages of the computational domain. Observer looks from above and the direction of rotation is from left to right. On the top of the plane is the stator side, while the bottom is the lip of the rotor disk. Looking at normalised pressure, it is seen that there is a general increase of the static pressure for the profiled case, as it was reported in the previous section. The pressure oscillations close to the stator side are the effect of stator wakes. Looking at radial velocity, the leakage flow is clearly seen by the dark parallel contours. It is worth to mention that the areas with negative radial velocity means that flow crosses the interface into the cavity but re-enters the main flow path downstream.

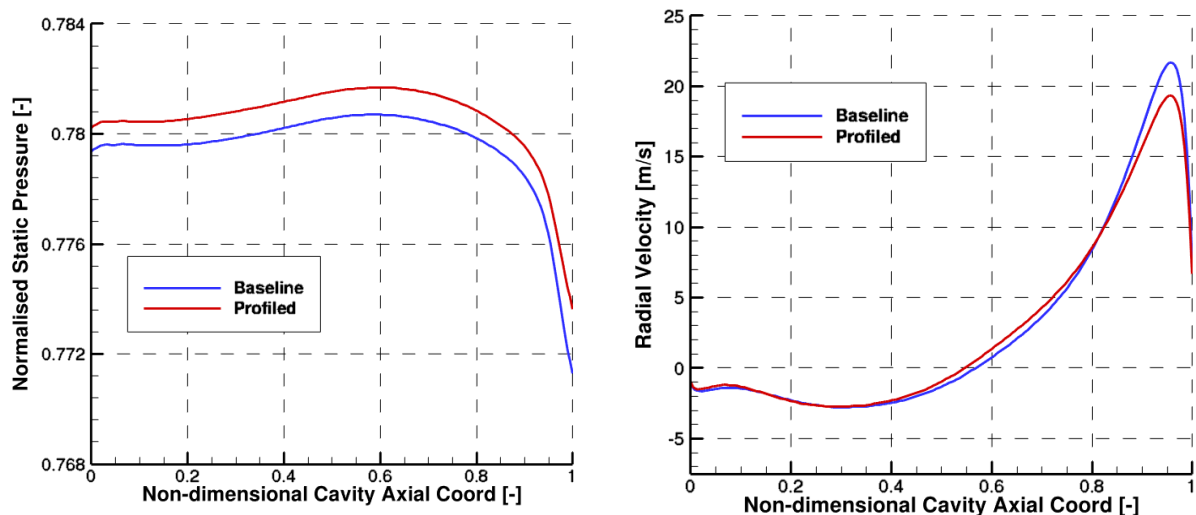


Figure 6-12: Circumferentially area- and time-averaged of  $Cp_s$  and  $V_r$  at stator hub cavity exit (0% span)

To understand the differences better, results are circumferentially area averaged and are presented in Figure 6-12. The non-dimensional cavity axial coordinate indicates the axial position along the cavity interface, where 0 is the end of the stator hub platform and 1 is the inlet to the rotor. Static pressure on the interface is slightly increased along the whole plane by 0.15% on average. Radial velocity however presents a more interesting finding. The high radial velocities close to the rotor indicate leakage

flow being injected in the rotor, with the maximum being at 95% of axial coordinate. Interestingly, the profiled case shows reduced radial velocity for the profiled case compared to baseline, by a maximum difference of 15.5% at 95% of cavity. This effect is highly desired because it keeps the radial penetration of the leakage flow to lower span positions. To understand the reason for this change, normalised static pressure and radial velocity is plot for one rotor pitch at rotor hub inlet, at 1% span, and presented in Figure 6-13.

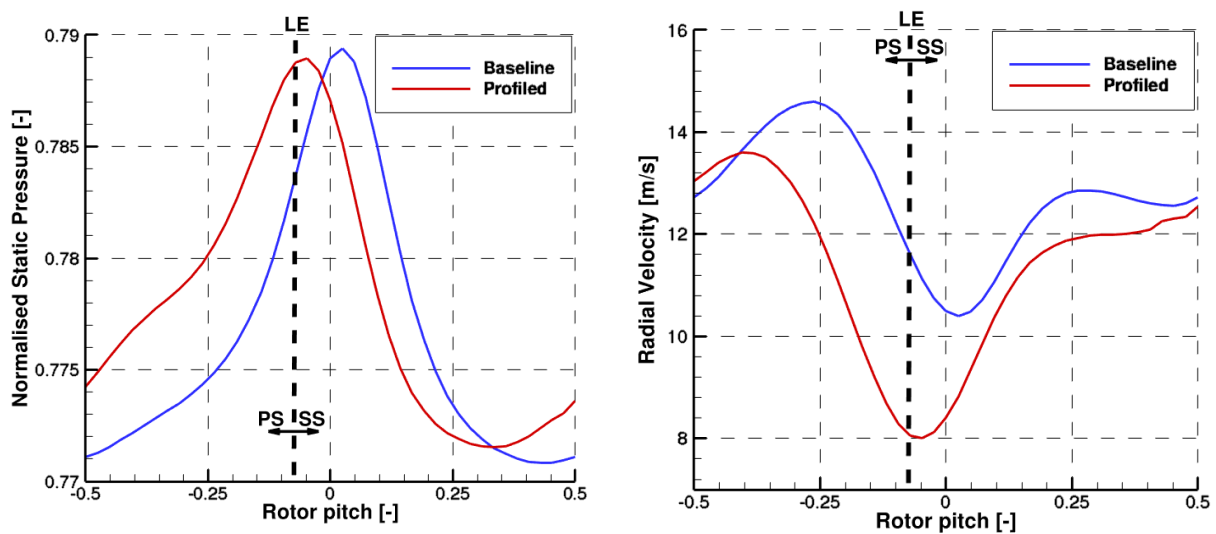


Figure 6-13: Time-averaged of  $C_{p_s}$  and  $V_r$  at rotor hub inlet, at 1% span

Looking at static pressure distribution along the pitch, a high peak of static pressure is observed with sharp drops in the sides. This peak is caused by the rotor leading edge because the location of the line is on the stator-rotor interface, which is very close to the rotor near the hub. The approximate location of the rotor leading edge is shown by the dashed line in Figure 6-13, where pressure and suction side are located at left and right respectively. The profiled end wall appears to have caused a shift of the stagnation point towards the pressure side, compared to the baseline case. While the maximum pressure peak has the same value, the minimum has increased in the profiled case and the pressure gradient from the pressure side towards the passage center is smoother, indicating a more uniform pressure field at the rotor inlet. This results in the changes of radial velocity seen in the right plot, where leakage flow seems to be entering the rotor closer to the passage center and with lower radial velocity. This acts beneficially for the passage vortex development as will be discussed in next two sections.



### 6.3.5 Profiled hub end wall effects at R2 rotor exit

In this section, the effect of end wall profiling on the flow field at rotor exit is discussed. Figure 6-14 shows the radial distributions of the circumferentially mass- and time-averaged relative yaw angle and relative circumferential velocity. Both parameters show high radial gradients from hub up to 60%, which are caused by the strong hub passage vortex, dominating the flow between these spanwise positions. The strength of the vortex seem to be successfully reduced in the case of profiled endwall as indicated by the reduced over-and underturning shown in Figure 6-14 and Figure 6-15. The profiled endwall has reduced the difference between maximum and minimum values of the circumferentially averaged relative yaw angle by  $2.5^\circ$ , from  $17^\circ$  to  $14.5^\circ$ , and the relative circumferential velocity difference by 25.2%.

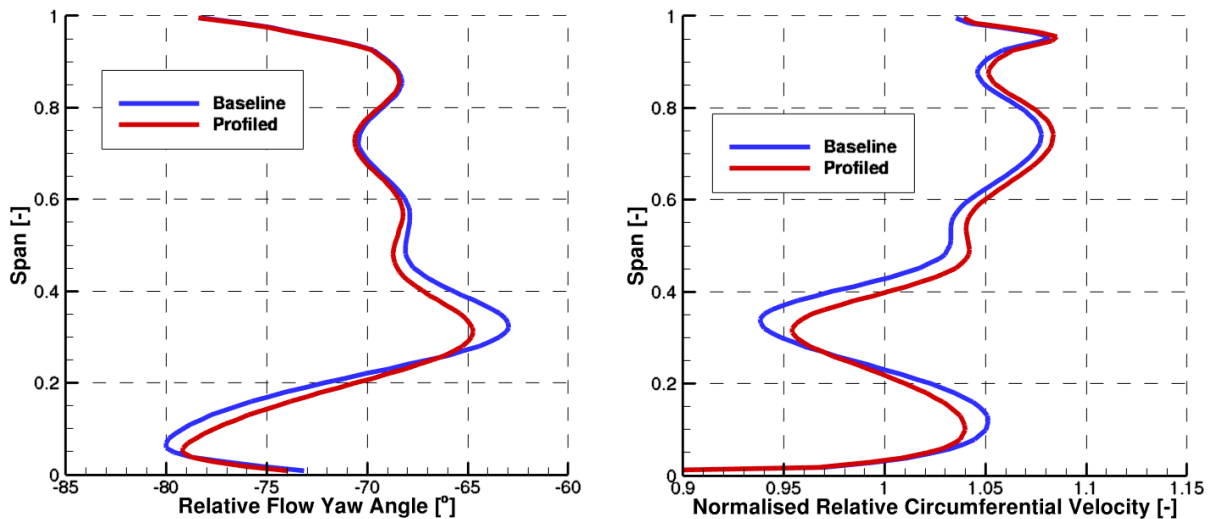


Figure 6-14: Mass- and time-averaged relative yaw angle and relative circumferential velocity  $V_{\theta,rel}$  at rotor exit

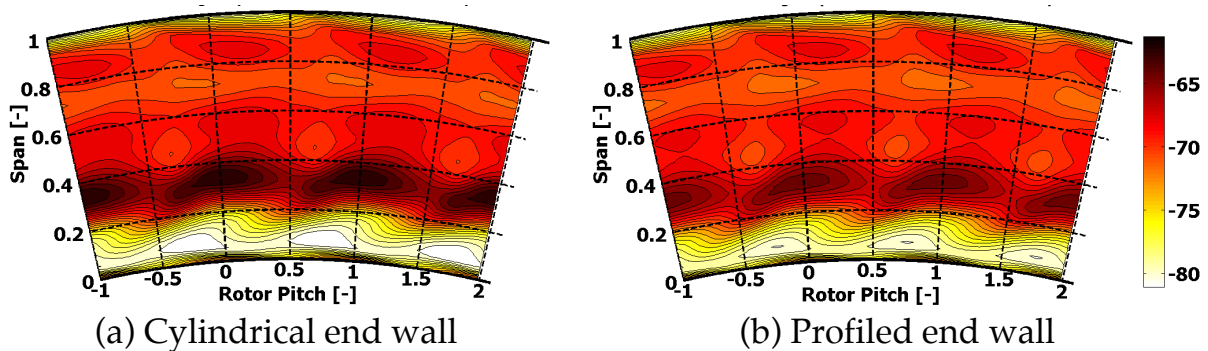


Figure 6-15: Time-averaged area plots of relative yaw angle  $[\circ]$ , in rotor relative frame of reference, at rotor exit.

The difference between baseline and profiled case is seen even more clearly in the time-averaged area plots of relative yaw angle in Figure 6-15. Another beneficial effect of the profiled endwall is it controls the radial migration of the hub passage vortex keeping it to lower spanwise positions. From Figure 6-14, it seen that it reduces the migration of the vortex by approximately 2% but the exact value will be reported below and is better extracted from the streamwise vorticity. Finally, it is worth mentioning that the profiled end wall manages to do so without leading to an increased overturning boundary layer close to hub, as it has been reported in other similar cases [18], [114], [124]. The importance of this fact is highlighted in the time averaged area plots of absolute yaw angle shown in Figure 6-16. Under the influence of the rotor end wall profile, the radial gradients have been reduced for absolute yaw angle, which would be beneficial for the downstream stage in a real configuration. However, the effect cannot be quantified for the case under investigation since there is no downstream stage.

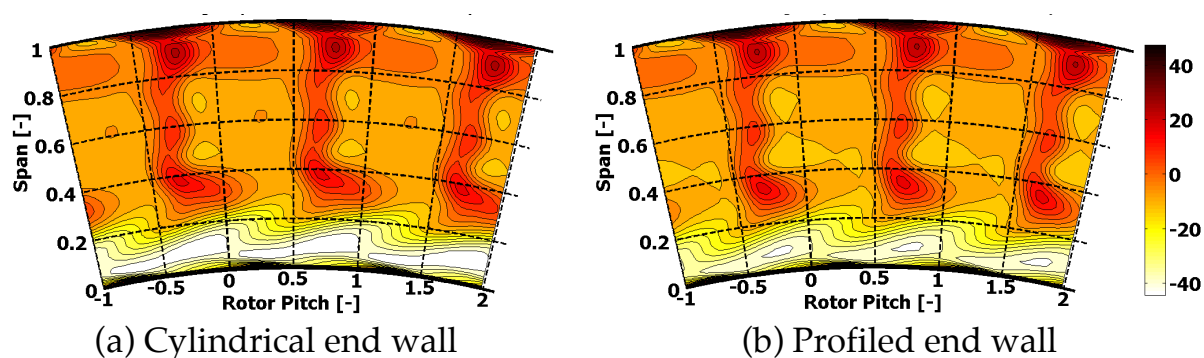


Figure 6-16: Time-averaged area plots of absolute yaw angle [°], in rotor relative frame of reference, at rotor exit.

The profiled endwall also shows an impact on the static pressure field at rotor exit. Figure 6-17 shows the comparison of the circumferentially averaged normalised static pressure and the reaction between the baseline and profiled case. Reaction  $R$  is calculated based on pressure distributions at second stage inlet, rotor inlet and rotor outlet, or planes B, C and D respectively and is given by Eq. 6-6:

$$R = \frac{P_{s,C} - P_{s,D}}{P_{s,B} - P_{s,D}} = \frac{Cp_{s,C} - Cp_{s,D}}{Cp_{s,B} - Cp_{s,D}} \quad \text{Eq. 6-6}$$



The radial distribution of rotor inlet has been shown in Figure 6-9, while of rotor outlet is presented in Figure 6-17. Results show that there is a slight increase in the reaction along the whole span, by 0.8% on average above 25% span and a maximum difference of 2.1% at 10%span. This change in reaction is mainly driven by the static pressure distribution at rotor inlet. For the profiled case, static pressure decreases above 40% span but increases below 40% at the core loss regions. However, something that cannot be seen by the radial distribution is that the pressure field at rotor exit is more uniform for the profiled case. This is presented in the time-averaged area plots of static pressure in Figure 6-18. The profiled end wall seems to be reducing the circumferential pressure gradients below 40% spanwise positions, fact which could also explain the reduced gradients of relative yaw angle and circumferential velocity.

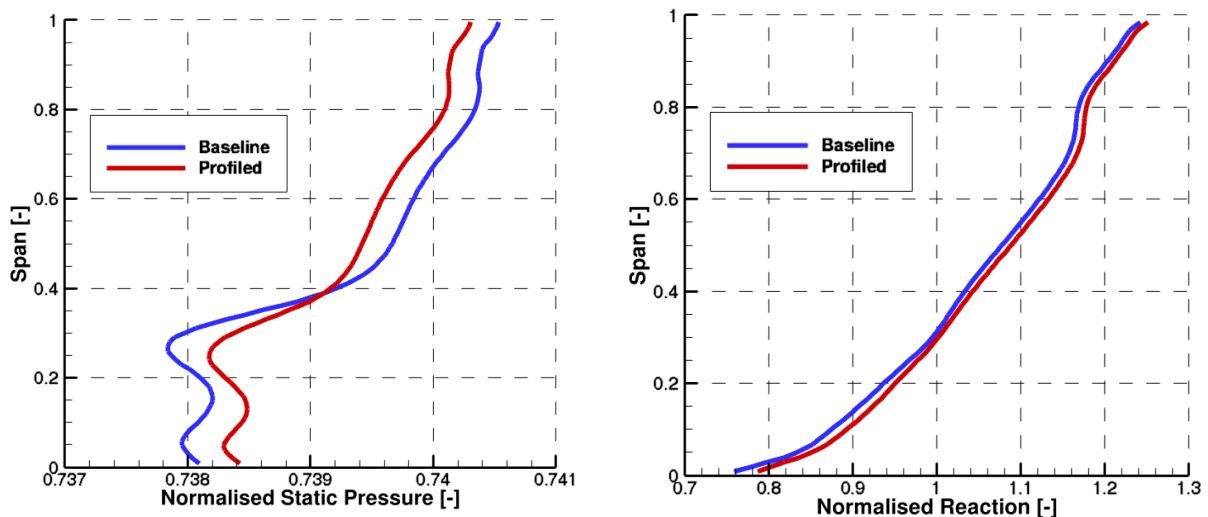


Figure 6-17: Mass- and time-averaged normalised static pressure  $Cp_s$  and reaction R at rotor exit

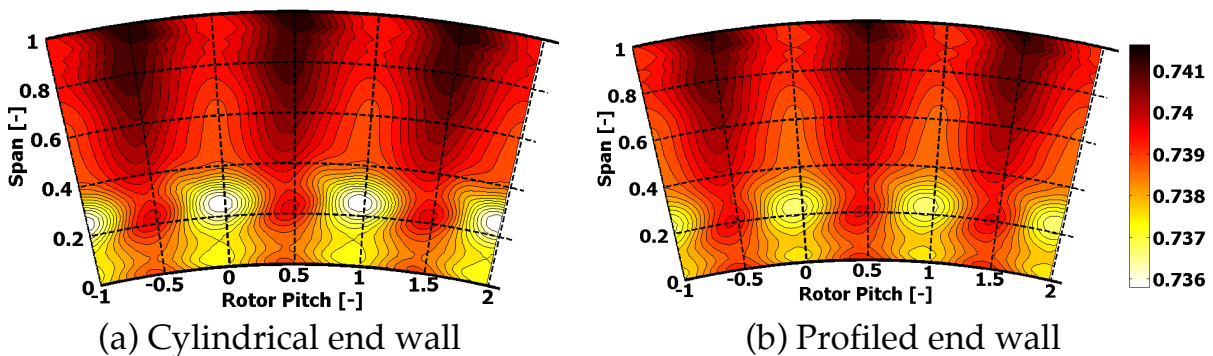


Figure 6-18: Time-averaged area plots of normalised static pressure  $Cp_s$ [-], in rotor relative frame of reference, at rotor exit

Figure 6-19 shows the time-averaged area plots of relative total pressure at rotor exit, in relative frame of reference, where certain flow features associated with loss generation are clearly visible. In the area plots, observer looks downstream towards the turbine outlet and the direction of rotation is from left to right. The projection of the rotor trailing edge is located at approximately 0.5 of each rotor passage, with the pressure side being to the left and suction side to the right.

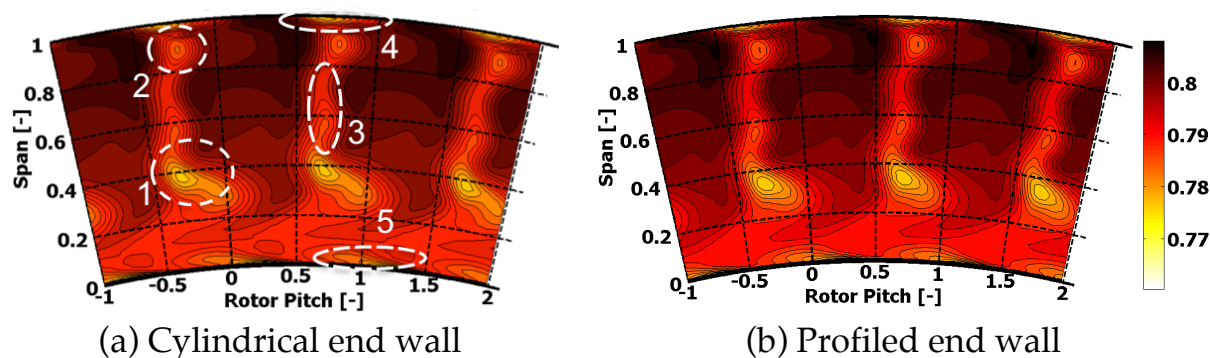


Figure 6-19: Time-averaged area plots of normalised total pressure  $Cp_{t,rel}$  [-], in rotor relative frame of reference, at rotor exit

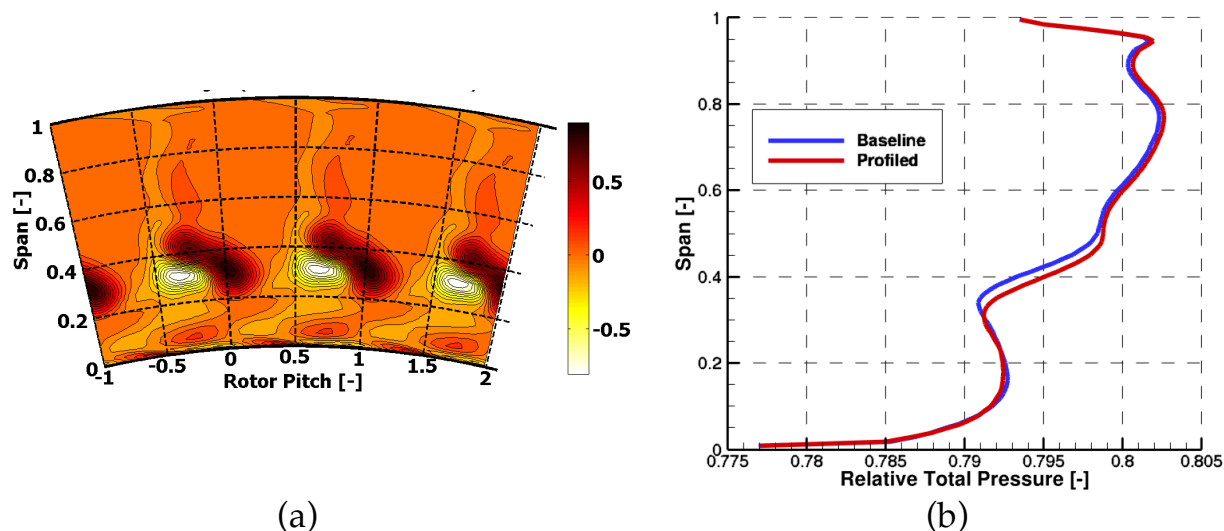


Figure 6-20: (a) Relative difference  $\Delta Cp_{t,rel}$  [%] of profiled case compared to baseline. (b) Mass- and time-averaged area plots of normalised relative total pressure  $Cp_{t,rel}$  [-] at rotor exit

There are five regions of interest, as shown by the white dashed circles. The core of the hub passage vortex is clearly seen close to 35% span by the reduced relative total pressure (zone 1). The

second zone is related to the tip passage vortex (zone 2). Between these two is the rotor wake (zone 3). Close to the tip is seen the footprint of the flow interaction from tip cavity with the main flow (zone 4). Finally, very close to the hub, the corner vortex can be identified (zone 5).

Looking at zone 1 of Figure 6-19, the loss related to hub passage vortex has indeed decreased for the profiled case and appears to be on lower span position and more concentrated in circumferential direction, compared to baseline, which appears to be spreading in both radial and circumferential direction. The differences can be seen better in the area plot of relative difference and radial distribution of  $Cp_{t,rel}$  in Figure 6-20. Between 20% and 50%, there are regions of positive relative difference next to a region of negative relative difference, which confirms the change of radial position of the hub passage vortex core to lower span, as well as the fact that it becomes more compact and concentrated in a smaller area. This is also verified by the reduction of streamwise vorticity for the case of profiled end wall, as seen in the radial distribution in Figure 6-21. The profiled end wall leads to a reduction by 9.5% of maximum streamwise vorticity and keeps the passage vortex to lower spanwise position by 3%. Finally, the radial velocity appears reduced along the whole span with maximum of -47% at the passage vortex loss core. Again, this would also be beneficial for the downstream rows.

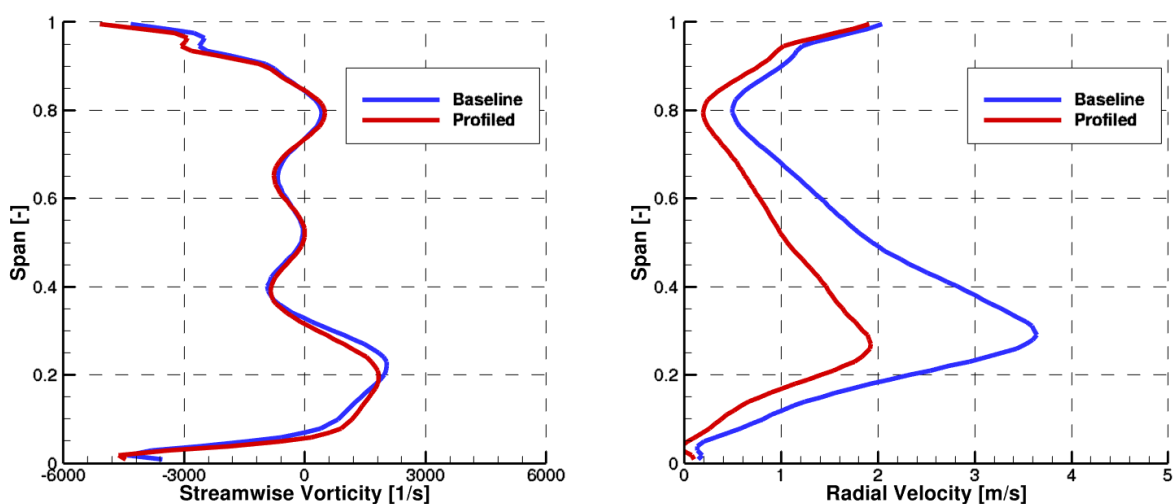


Figure 6-21: Mass- and time-averaged streamwise vorticity  $\Omega_s$  and radial velocity  $V_r$  at rotor exit

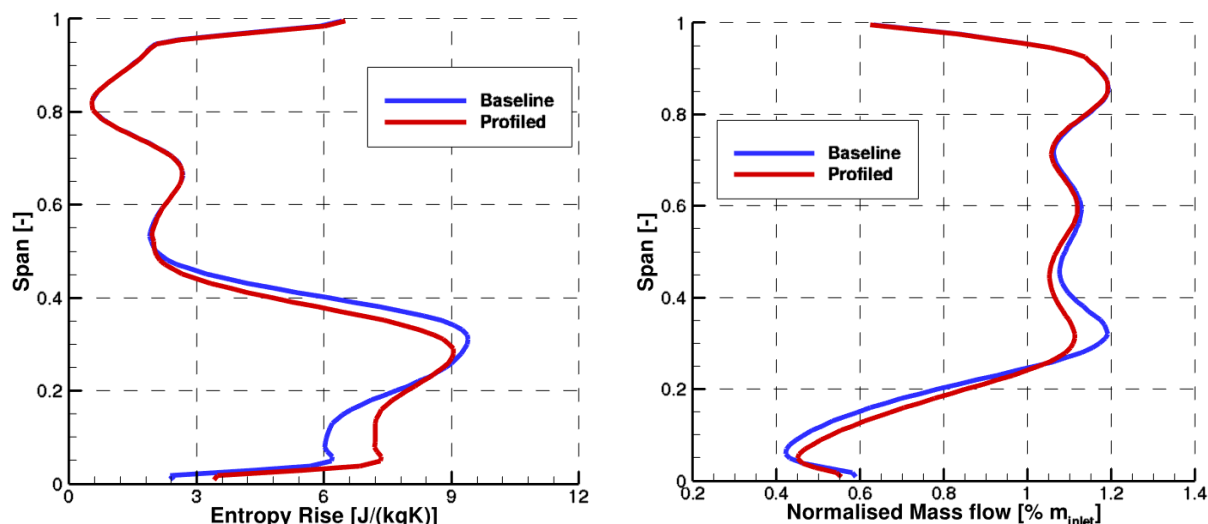


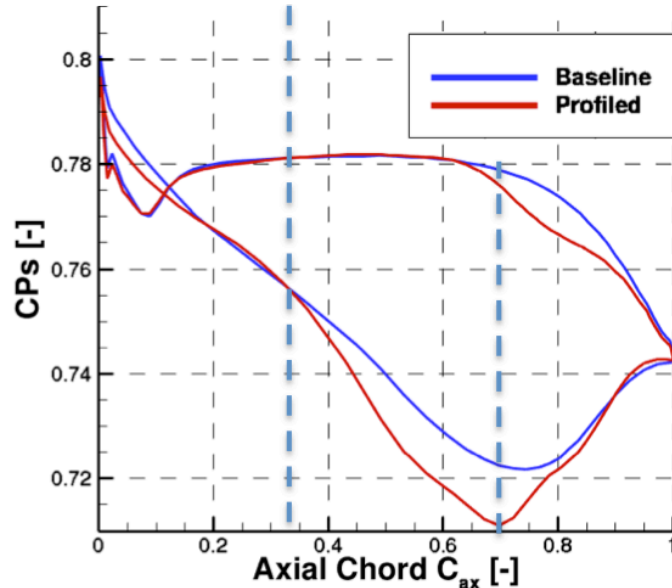
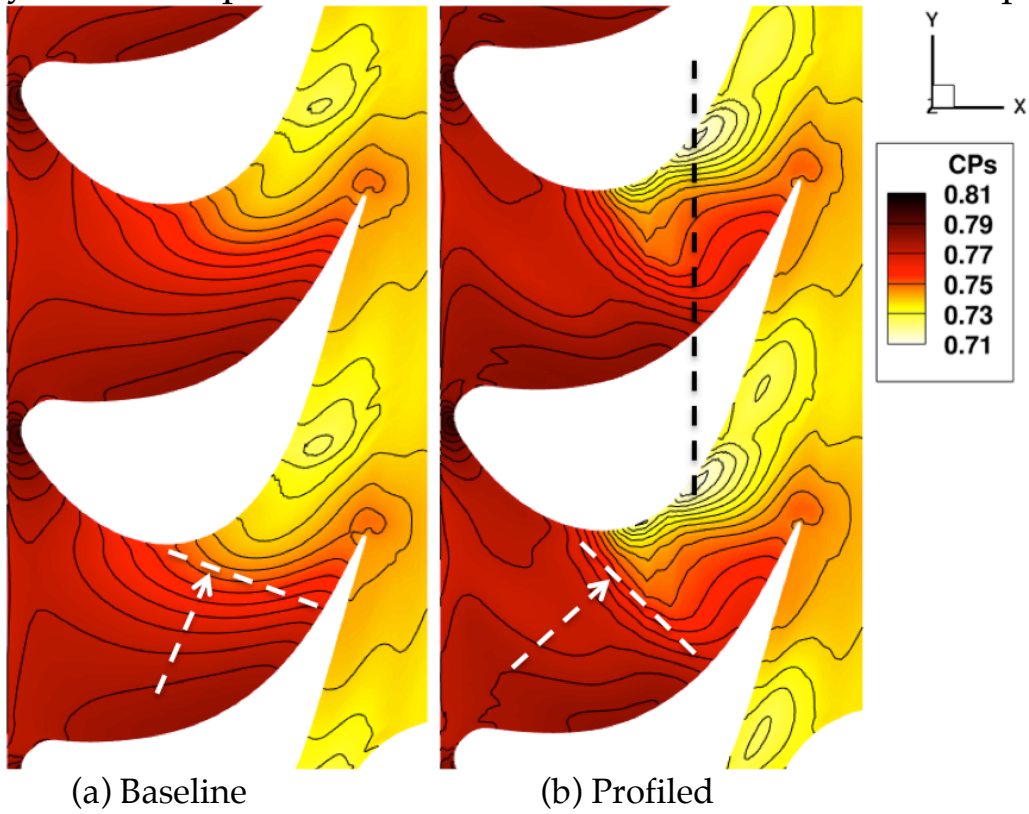
Figure 6-22: Mass- and time-averaged entropy rise and radial distribution of normalised mass flow at rotor exit

To have an estimation of the profiled end wall on loss generation, the entropy rise is calculated between stage inlet and outlet and is presented in Figure 6-22, where the results are interesting and need to be discussed. As seen on the left plot, the endwall contouring indeed decreases the losses in the core of the hub passage vortex by 4.5%, however it presents increased losses below 20% compared to baseline. This fact is very interesting and similar findings have been reported by Brennan et al [114]. The explanation lies in the fact that the high loss fluid that was swept by the passage vortex now remains on the end wall showing higher losses and that the reason for this is that the flow on the end walls are more in-line with the primary flow, which has been shown also for this case by the yaw angle distributions in Figure 6-14. Finally, this is confirmed if one looks on the mass flow distribution along the span in Figure 6-22. It is clearly seen that less mass flow is entrained in the core of the passage vortex and remains closer to the endwalls, increasing the mass flow below 20% span. Nevertheless, the radially mass-averaged entropy rise is still lower for the profiled case compared to baseline by 2.15%.

This concludes the comparison of baseline and profiled case and the effect of end wall in the evolution of secondary flows is discussed in the next section.

### 6.3.6 Rotor hub end wall effect on secondary flow evolution, blade loading and stage efficiency

To discuss the effect of profiled end wall on the evolution of secondary flows, the pressure distribution on the end wall is compared



(c) Blade loading at 6% span

Figure 6-23: Comparison of normalised static pressure  $Cp_s$  [-] distribution between (a) cylindrical and (b) profiled rotor hub end wall and its effect on (c) blade loading at 6% span

in Figure 6-23a and b. There are two areas of interest to discuss, related to the main geometrical features of the profiled end wall, as they were described in Figure 6-8. The hill on the pressure side and the trough on the suction side have as a result a more uniform pressure field in the middle of the passage as shown by the white dashed lines on Figure 6-23. This leads to a delay in the formation of the passage vortex and is beneficial for controlling the strength of the vortex and keeping it to lower span. However, the more interesting phenomenon is observed close to the throat, where the elevated end wall on the suction side of the blade causes a pressure drop and an increase in the pressure gradient in the throat area. Admittedly, this is counter-intuitive with the whole principle of end wall contouring but nevertheless it was not rejected by the genetic algorithm and the CFD simulations confirm the prediction, from the artificial neural network and the optimization, of increased efficiency. In order to analyze it further the pressure distribution along the blade close to hub is shown in Figure 6-23c, at 6% span. The blade loading shows that it is highly aft-loaded, which is considered to be beneficial for reducing the secondary flows.

There are three main areas of interest here: between the leading edge and ~10% of the axial chord, between 33% and 70% and from 70% until the trailing edge. First of all, it is observed that the loading is inverted up to 10% of axial chord and the reason is the highly negative incidence angle of the stator hub cavity leakage flow. In the presence of end wall contouring, the pressure difference has slightly reduced but it has not completely vanished. In the middle of the blade, the hill close to the suction side causes a pressure drop, which increases the loading. Although increased loading means more work, it is again counter-intuitive to the principle of end wall contouring, since increased loading means stronger secondary flows. However, there was no such evidence as seen by the analysis presented in section 6.3.5, in fact the strength is significantly reduced. The answer seems to lie in the effect of profiled end wall on loading close to trailing edge, where the loading has decreased in locations downstream of 75% of axial chord. Basically, the profiled end wall seems to increase the total loading, while unloading the trailing edge and loading more the core of the blade. This, combined with the delay in passage vortex by the first two features, leads to increased work but reduced vortex strength.



Another interesting thing to discuss is that the decreased pressure on the suction side increases the loading but also increases the isentropic Mach number, leading to increased diffusion and a potential boundary layer separation. To investigate this, the wall-limited streamlines are drawn on the blade suction side and are presented in Figure 6-24. The pressure contours on the suction side of the blade for the baseline case (black dashed circle) show high radial pressure gradients, which enhance the radial migration of the passage vortex to higher span positions. This drop is static pressure for the profiled case, not only does not cause a boundary layer separation at any point in time, but also improves the pressure gradient by making the lines less inclined compared to the end wall surface.

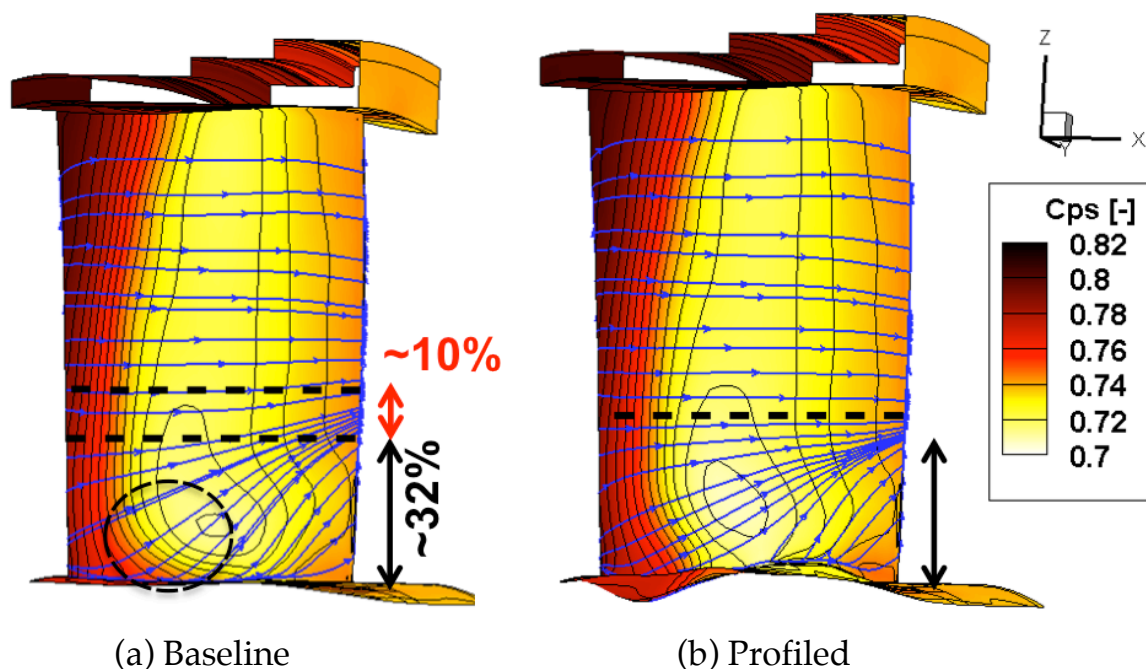
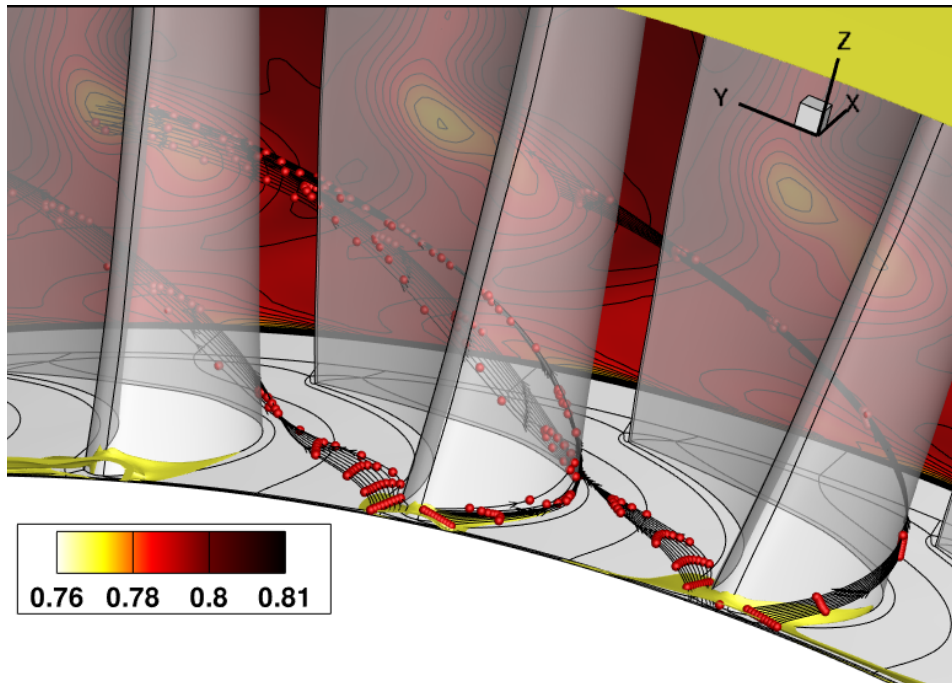


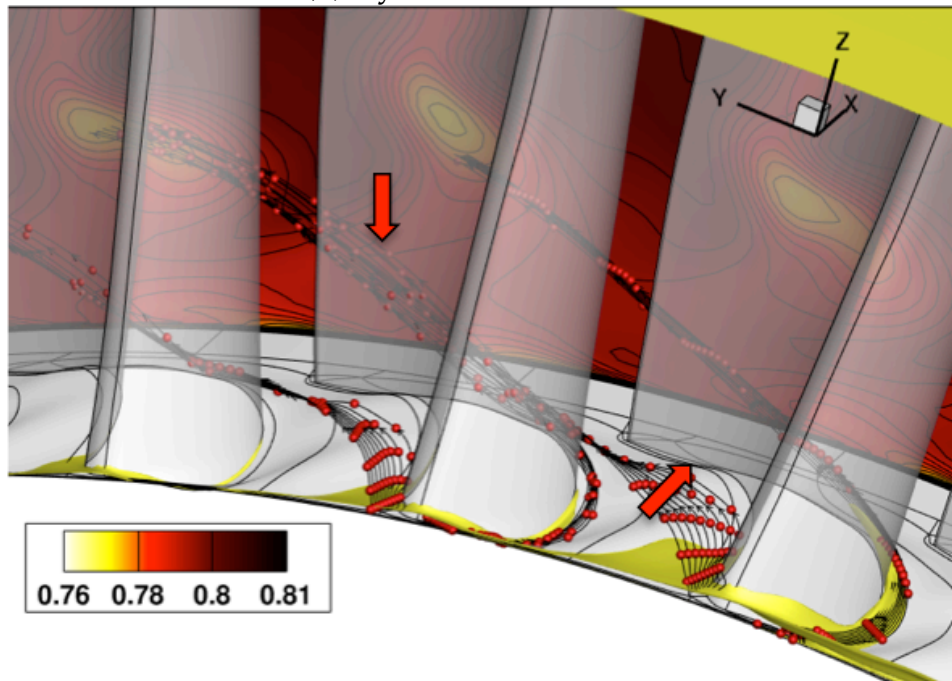
Figure 6-24: Comparison of time-averaged normalised static pressure  $Cp_s$  [-] distribution between (a) baseline and (b) profiled case on rotor suction side and wall-limited streamlines, tracing the hub passage vortex ascending on blade's suction side

Another beneficial effect is that the passage vortex impinges on the suction side much later compared to the baseline and also disturbs less the suction side boundary layer. As the suction side limb of the horseshoe vortex start rising very early close to the leading edge and is combined with the passage vortex, it causes a boundary layer motion. For the case of the profiled endwall, this interaction is lim-

ited to  $\sim 32\%$  of the span and the passage vortex impinges on the suction side at  $\sim 83\%$  of the axial chord. For the baseline case on the other hand, the passage vortex impinges at  $\sim 64\%$  of the axial chord and causes a boundary layer motion up to  $\sim 42\%$  of blade span.



(a) Cylindrical end wall



(b) Profiled end wall

Figure 6-25: Particle tracks of stator hub cavity leakage flow comparison for the two cases with (a) cylindrical and (b) profiled rotor hub end wall, in time-averaged flow field and relative frame of reference



Figure 6-25 visualizes clearly the delay in the hub passage vortex evolution, the downstream location on which it impinges on the suction side and the more controlled rising to lower span positions.

To conclude this analysis on the profiled end wall effects, area plots of efficiency are presented in Figure 6-26, while Figure 6-27 shows the difference in efficiency of profiled case compared to baseline. The torque-based efficiency is calculated by Eq. 6-5 and is increased by +0.27% on average thanks to the effects of profiled end wall, without taking into account the improved flow field that would enter the downstream stage in a real configuration.

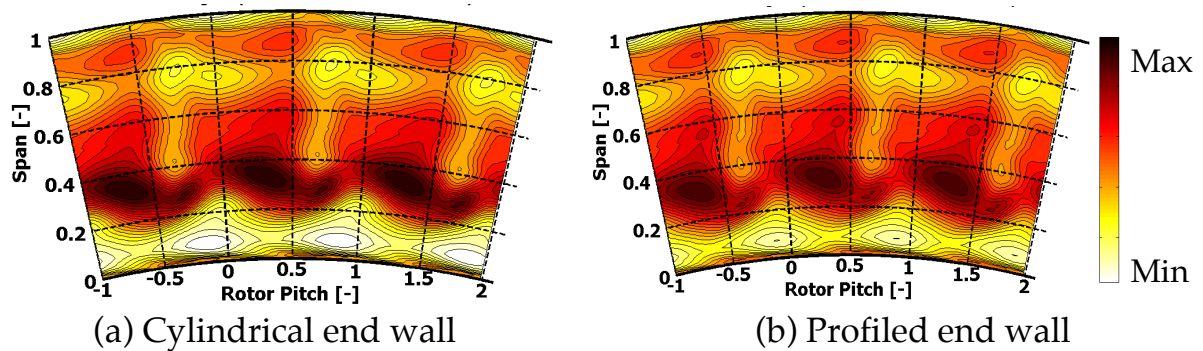


Figure 6-26: Time-averaged area plots of second stage total-to-total torque-based efficiency  $\eta_{t-t}$  [-], at rotor exit

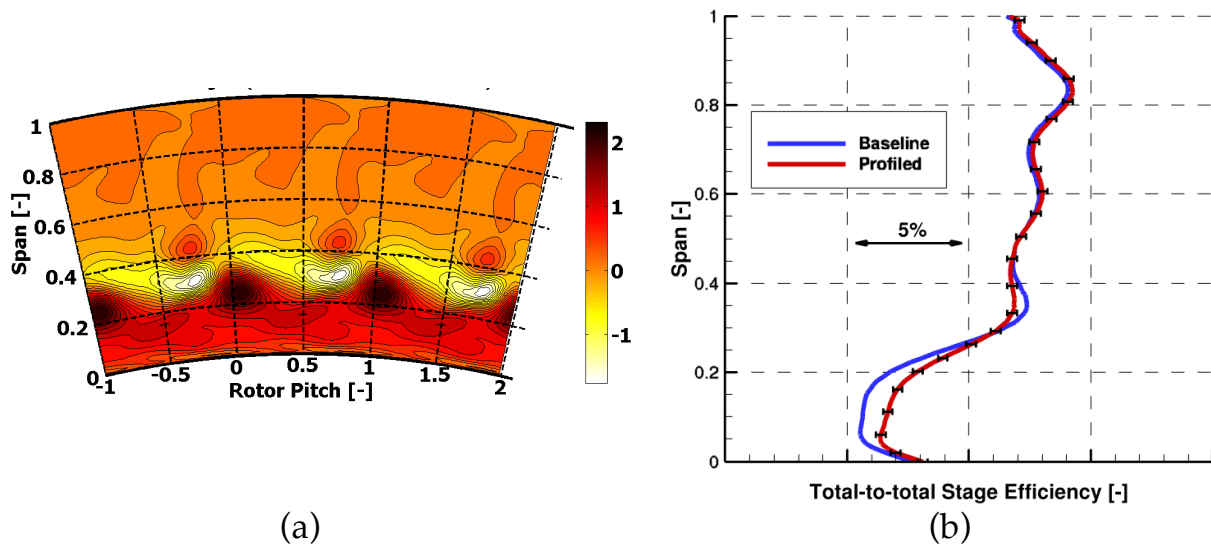


Figure 6-27: (a) Efficiency difference  $\Delta\eta_{t-t}$  [%] of profiled case compared to baseline. (b) Radial distribution of circumferentially mass- and time-averaged second stage total-to-total torque-based efficiency  $\eta_{t-t}$  at rotor exit for the baseline and profiled geometries

One of the concerns during the design and analysis of the results was that the gain in efficiency is relatively small and could be difficult to be measured by the probe when the case is tested. The probe uncertainty for efficiency was calculated to be +0.2% for coverage of one standard deviation ( $k=1$ ). While it is true that the average value of efficiency increase is close to measurement uncertainty, it is important to clarify that local changes are far bigger as seen in area and radial plots in Figure 6-27. In fact, the probe uncertainty is added on the radial distribution of the profiled case as error bars of  $\pm 0.2\%$  and it is indeed confirmed that local changes are larger than uncertainty, with maximum difference of +1.12% at 18.2% span location.

### **6.3.7 Justification of choice for presence of cavities and unsteady simulations**

As it was presented in previous sections, a stage improvement was achieved with the unsteady optimization by applying end wall contouring on the rotor hub end wall. However, this came with a very high computational cost, due to the presence of hub and tip cavities in the computational domain and the performance of time-accurate simulations. This is completely opposite to common practice used in industry during the design phases, where problems are solved in a steady state manner and cavity paths are excluded from the computational model. So the following questions arise; can the presence of the cavity paths in the computational model and its solution in a time-accurate manner be justified in a quantified way and, in the end, is it really necessary to perform an unsteady optimization? In order to be able to answer these questions, three additional cases were investigated.

The first case was created to assess the importance of cavity paths. For this, a two-stage configuration without hub and tip cavities was created. The 7-7-6-6 (S1-R1-S2-R2) blade configuration was kept the same as it was described in 6.2.1. The mesh size without cavity paths was reduced to almost half of the original, to 17.1 millions mesh nodes for the total 26 blades. The domain was split in 6 GPUs and an unsteady simulation was performed using MULTI3. The flow conditions in turbine inlet of LISA were applied as inlet boundary conditions of the simulation.

The other two cases were used to quantify the differences of the solution when the problem is solved in steady state, which is typical in industrial practices. For this, only a single pitch of the second rotor, including tip cavity path, was simulated in steady state, both for baseline and profiled geometry. The mesh size is only 1.65 million nodes and was fit in a single GPU. As inlet boundary conditions, the time averaged flow field at plane C was imposed at inlet as circumferentially averaged, radial profiles. Plane C can be seen in Figure 6-2 and the flow field was analyzed in section 6.3.3.

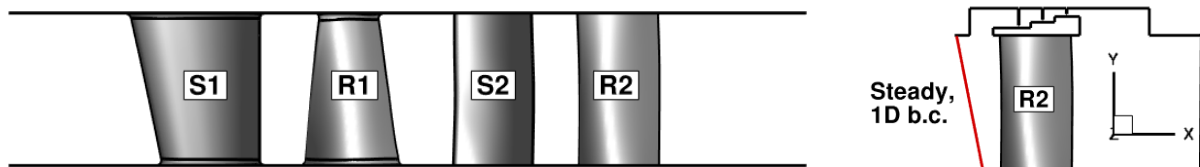


Figure 6-28: Computational domain of LISA-H2 turbine case for two-stage without cavities (left) and single-row, steady case of second rotor (right)

The solid surfaces of the above cases are shown in Figure 6-28 and the results are presented in the following sections. The results of the single-stage, unsteady simulation with unsteady boundary conditions for the baseline geometry have been analyzed in previous sections and have been validated with experimental data in section 6.3.1. Therefore, they will be used as a reference case for the comparison with the case without cavities and the steady simulations.

### 6.3.7.1 Impact of cavity paths

Figure 6-29 presents the comparison of relative yaw angle and normalised mass flow rate at the exit of the second rotor for the baseline and no cavities case. Looking at relative yaw angle, some small differences are observed above 50% span. Flow features appear to be predicted in same spanwise locations for both cases. However, the differences are much more pronounced below 50%. As it was described in Figure 6-14, this strong over- and under-turning is occurring due to the presence of a strong hub passage vortex in the rotor and its location has been confirmed by the experimental data. Although the case without cavities predicts a passage vortex of similar strength at the rotor exit, the location is

completely miscalculated and appears almost 5.5% of span lower. This is confirmed by the mass flow distribution along the span, where a mass redistribution is visible towards lower spanwise positions.

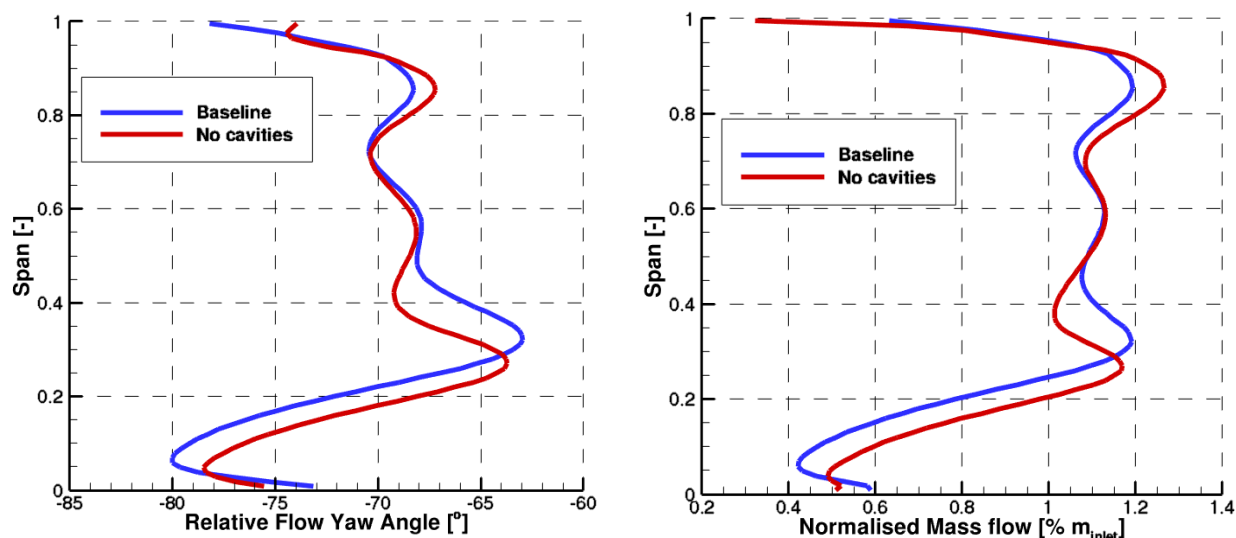


Figure 6-29: Mass- and time-averaged relative yaw angle and radial distribution of normalised mass flow at second rotor exit

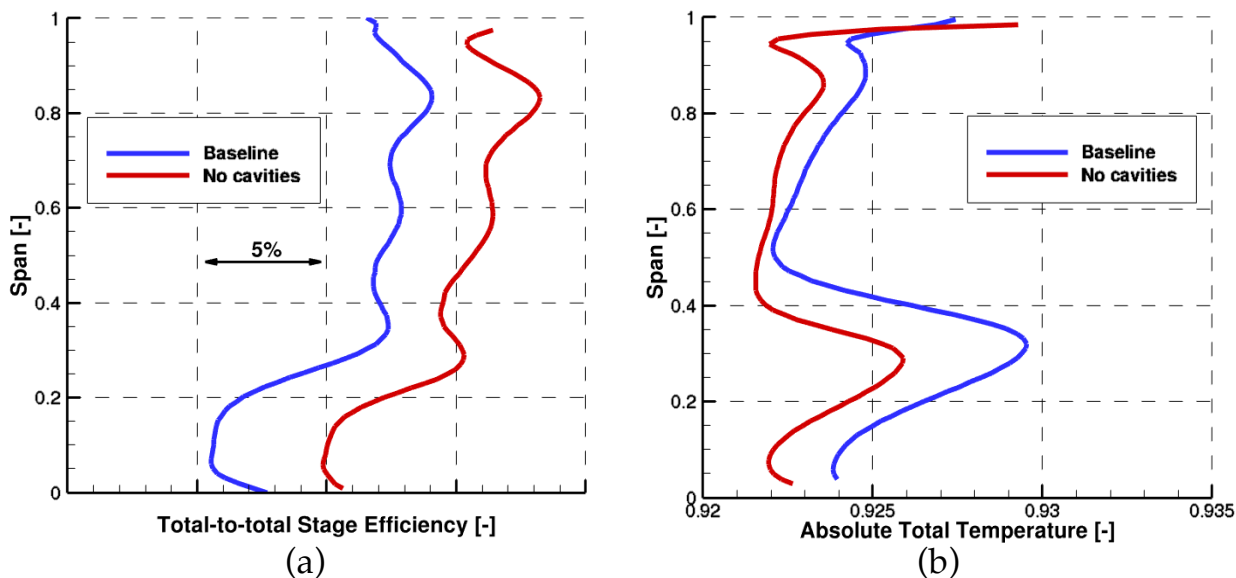


Figure 6-30: (a) Radial distribution of circumferentially mass- and time-averaged second stage total-to-total torque-based efficiency  $\eta_{t-t}$  at second rotor exit for the baseline and no cavities case. (b) Mass- and time-averaged of normalised absolute total temperature at second rotor exit

Figure 6-30 shows the radial distribution of second stage efficiency and absolute total temperature at rotor exit. Total temperature appears to be lower for the case with no cavities, implying larger work extraction from the rotor, which can be seen in the gross over-prediction of torque-based efficiency by 3.9% on average. The differences in total temperature are more clearly visible in the area plots of Figure 6-31. Locations with high total temperature are the main areas of loss generation such as the hub and tip passage vortex close to 30% and 90% spanwise locations, respectively.

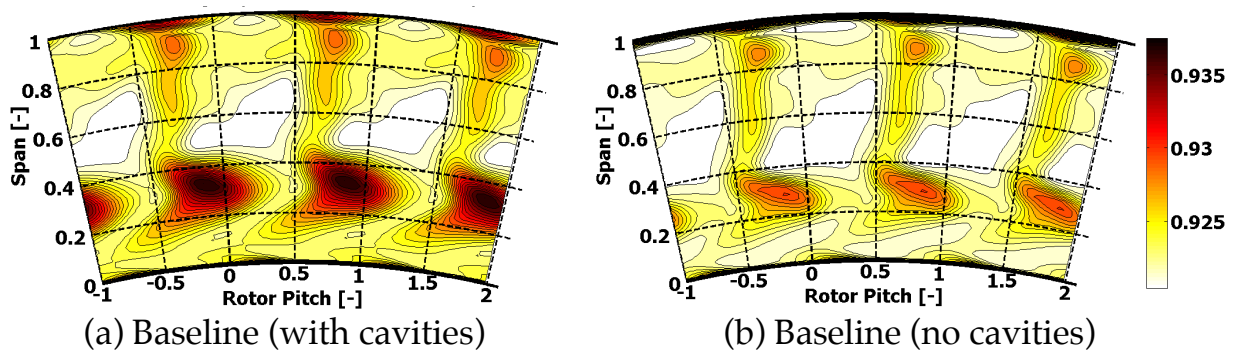


Figure 6-31: Time-averaged area plots of normalised absolute total temperature  $CT_{t,abs}$  [-], in relative frame of reference at rotor exit

The reason of these observed differences between the cases with and without cavities is fairly simple and is related to the cavity leakage flow and their interaction with the main flow. As flow is ingested in the cavity inlet, it does not expand and keeps the high temperature content, which then re-enters the main flow path at the cavity exit. Additionally, leakage flow at cavity exit has high radial velocity, as it was shown in Figure 6-12, which has a profound effect on the formation and interaction of the secondary flows inside the passage and their radial migration to higher spanwise positions. Consequently, the mechanism of the high temperature leakage flow that would enter the main flow path and push the secondary flows to higher spanwise locations and raise the temperature field at rotor exit is completely absent for the case without cavities and therefore changes considerably the nature of the problem. On the other hand, this effect appears to be more significant close to the hub than the tip.

Steam turbines require large cavity paths due to the significant thermal axial expansion of the turbine from cold state to operation state. As an example, the gap at inlet and outlet of the second stator

hub cavity path is approximately 39% and 41% of the stator axial chord. Due to the differences observed in the above analysis, it is concluded that in steam turbines or any other case with large cavity paths, leakage flows play a crucial role in the accurate prediction of loss generation and stage performance. Therefore, when the goal is to achieve a performance improvement by managing secondary flows, such as in end wall contouring optimizations, cavity paths can simply not be excluded from the computational model.

### 6.3.7.2 *Impact of unsteadiness*

Modern optimization procedures rely on steady state solutions due to their lower computational cost compared to unsteady. However, leakage flows from cavity paths and their interaction with the main flow is inherently unsteady. Neglecting unsteadiness can affect the evolution of the optimization. In order to address this, the following thought process was followed: Let it be assumed that the profiled geometry was the optimum result of a steady optimization. If the effect of unsteadiness is negligible, validation of the steady with the unsteady results should theoretically show negligible differences. It would be expected that comparison of steady-unsteady for baseline and steady-unsteady for profiled geometry should show similar trends and magnitude of changes, thus confirming the validity of the steady optimization approach.

To investigate this, results of the steady simulations are compared to unsteady solutions, for both the baseline and the optimized profiled geometry. The comparison is done in a stepwise approach, where first the baseline case is compared and then the predicted improvements of the profiled case.

Figure 6-32 shows the relative yaw angle at rotor exit. Comparison for the baseline geometry between steady and unsteady shows that the steady simulation captures the flow physics much more successfully than previously presented when cavities are not included. The hub passage vortex is not only captured in the correct radial position but with also very similar strength. Results appear to be smoother above 50% span, but a certain loss of information is to be expected since circumferentially uniform boundary conditions are applied in the inlet of the rotor for the steady state solution. However, this changes when relative yaw angle is compared for the

profiled cases. Steady solution under-predicts the weakening of the hub passage vortex compared to unsteady.

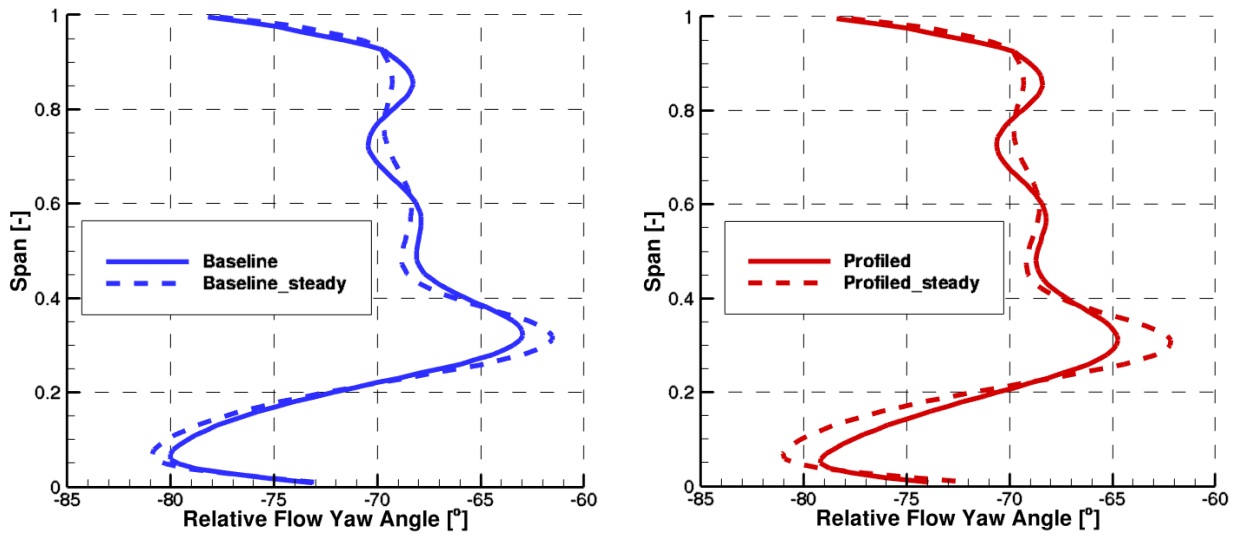


Figure 6-32: Mass- and time-averaged relative yaw angle at rotor exit

Similar observations can be made when looking at streamwise vorticity at rotor exit in Figure 6-33. Steady solution manages to capture the strength of the secondary flow features relatively well compared to the unsteady solution. However, the gain of profiled end wall is under-predicted by the steady solution compared to the unsteady.

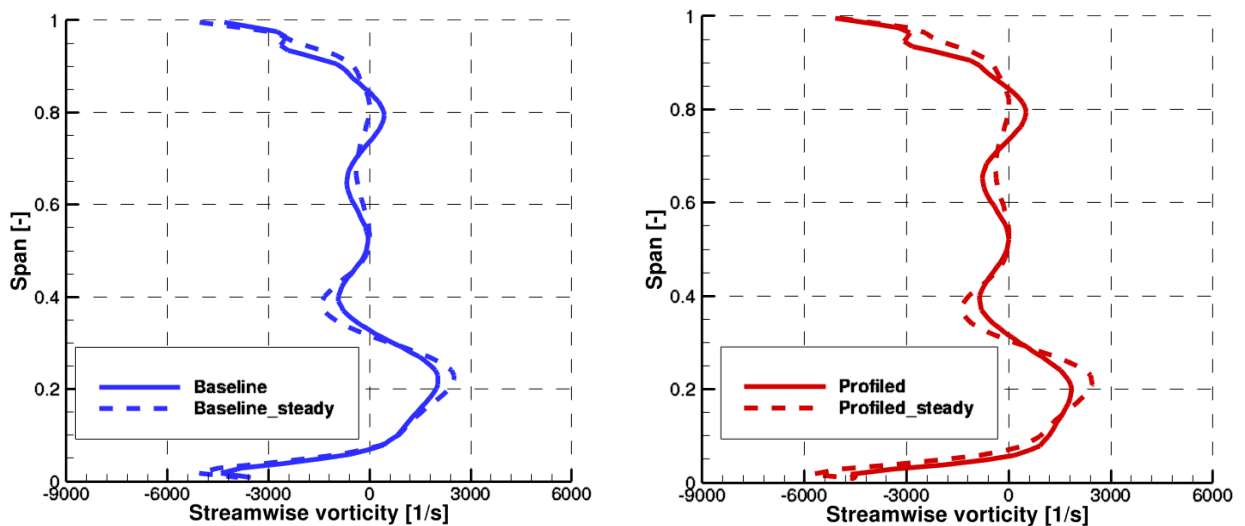


Figure 6-33: Mass- and time-averaged streamwise vorticity  $\Omega_s$  [1/s] at rotor exit



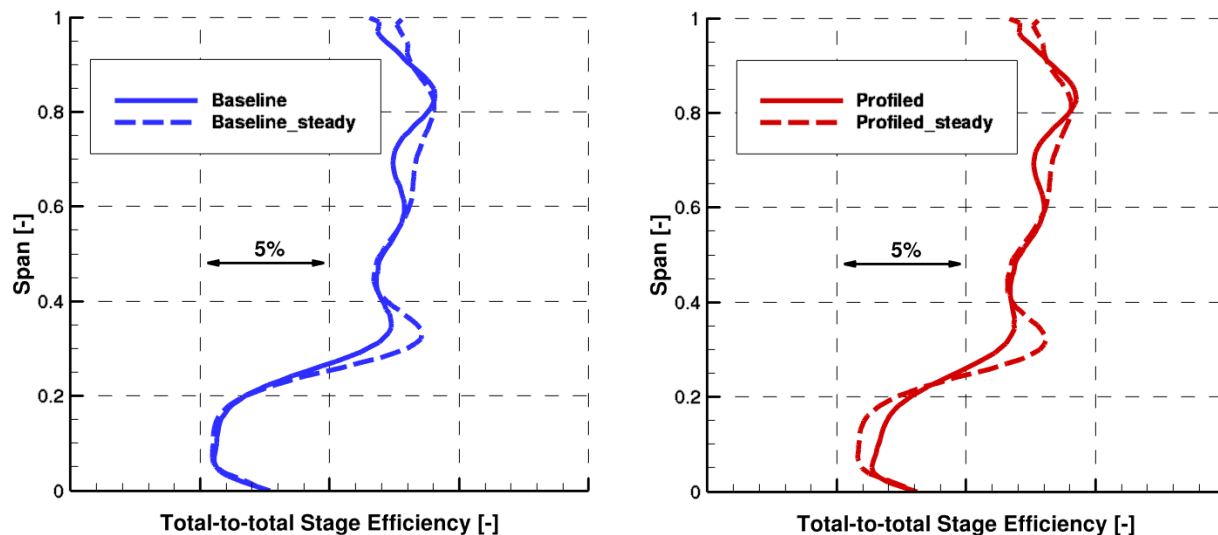


Figure 6-34: Radial distribution of circumferentially mass- and time-averaged second stage total-to-total torque-based efficiency  $\eta_{t-t}$  at rotor exit for the baseline and profiled geometries.

The same pattern is observed in the radial distribution of efficiency in Figure 6-34. Steady solution of the baseline matches relatively well the unsteady, with a difference of 0.35% in the average value of efficiency. It is important to mention here that efficiency is calculated by Eq. 6-5 for both cases and, since the steady solution is a single-row simulation, the inlet conditions are assumed to be the same for both cases. Therefore, any differences can be attributed only in changes of predicted torque, mass flow and total pressure at rotor exit. Efficiency changes for the profiled geometry are more pronounced in the unsteady solution compared to the steady solution. To analyze it further, a similar approach to section 6.3.6 is followed.

Figure 6-35 shows the area plots of the second stage efficiency for baseline and profiled geometry of the steady state solutions, but the differences are practically indistinguishable. For consistency, the contour levels are identical to those used in Figure 6-26. To make the differences more clear and pronounced, the baseline efficiency is subtracted from the profiled case and is presented in Figure 6-36, along with the circumferentially averaged, radial distribution of efficiency. Again, for the sake of consistency, the contour levels of the area plot in Figure 6-36 are identical to those in Figure 6-27. Comparing Figure 6-36 and Figure 6-27, certain observations can be made.



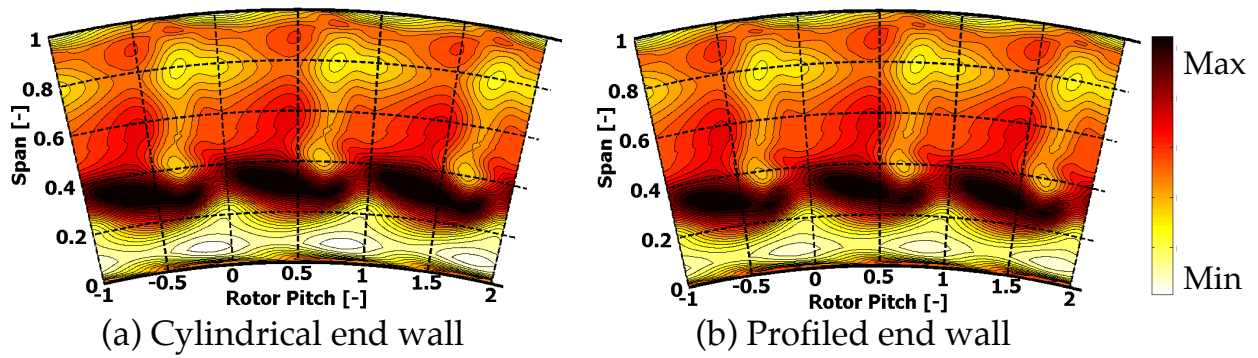


Figure 6-35: Area plots of second stage Total-to-Total torque-based efficiency  $\eta_{t-t}$  [-], at rotor exit of steady solution

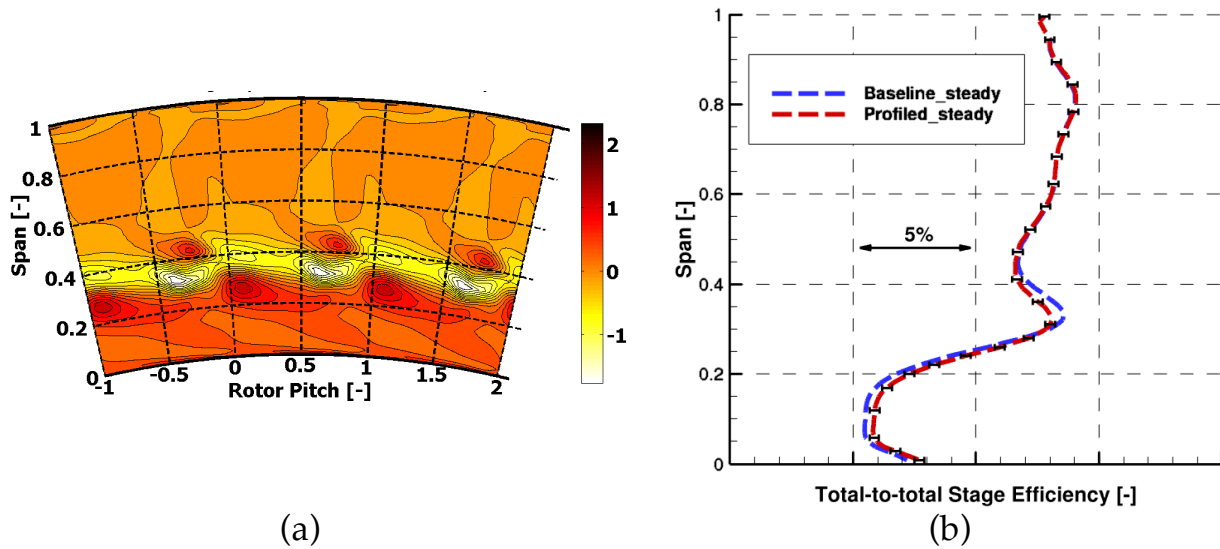


Figure 6-36: (a) Efficiency difference  $\Delta\eta_{t-t}$  [%] of profiled case compared to baseline, based on steady solutions. (b) Radial distribution of circumferentially mass- and time-averaged second stage total-to-total torque-based efficiency  $\eta_{t-t}$  at rotor exit of the steady solutions for the baseline and profiled geometries

On one hand, there is a good qualitative agreement in the area plots of efficiency difference predicted by the steady solution compared to the unsteady, as the same patterns are visible in both cases. On the other hand, however, the magnitude of the changes is lower for the steady state, which can also be observed in the radial distribution of efficiency. It can be seen that the local changes in efficiency for the profiled case, although they are still larger than the measurement uncertainty, they appear to be much closer to the error bars, increasing the difficulty to capture during probe

measurements. According to steady results, the average gain in efficiency is only marginal with the profiled end wall by 0.06%, which is 4.5 times lower than the 0.27% that was previously reported and predicted by the unsteady optimization.

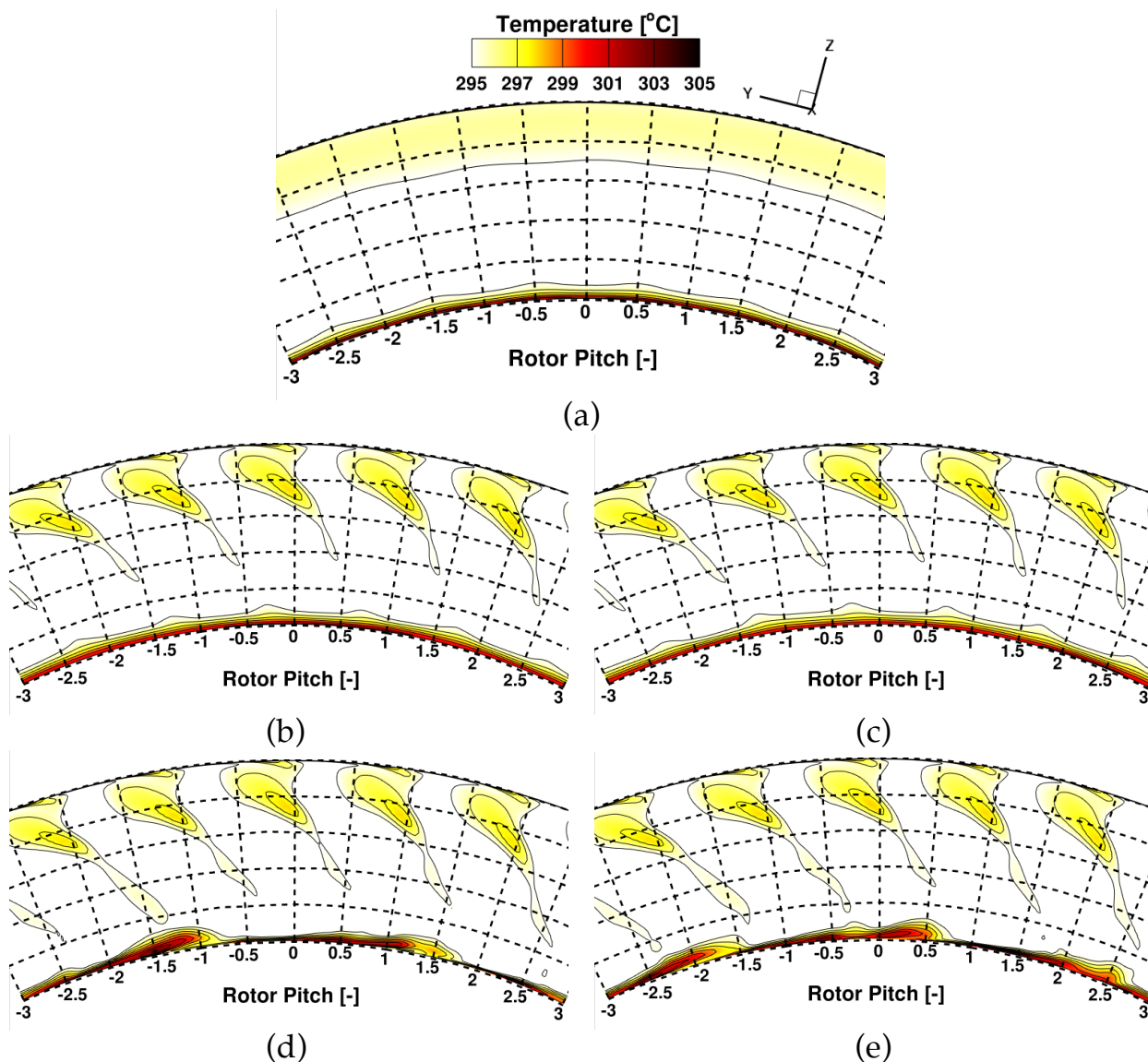


Figure 6-37: Static temperature [°C] distribution at rotor inlet at interface C:  
 (a) Radial profile of 1D inlet boundary conditions  
 (b) Time-averaged results of baseline case  
 (c) Time-averaged results of profiled case  
 (d) Instantaneous results at  $t/T=0$  for baseline case  
 (e) Instantaneous results at  $t/T=0$  for profiled case

So far, it is seen that steady state solutions are in good agreement with the unsteady solutions for the baseline case but their differences are more pronounced when looking at the profiled case. The reasons for this are attributed to inflow to the rotor on one

hand, and on flow unsteadiness on the other hand. To explain this in detail, area plots of static temperature distribution at plane C is presented in Figure 6-37.

For the steady state simulation, circumferentially averaged, radial distributions of relative total pressure, relative total temperature, relative yaw angle and pitch angle are imposed as boundary conditions at the rotor inlet. As mentioned earlier, the leakage flow coming from stator hub cavity has high static temperature since flow has not expanded in the stator. Figure 6-37a shows the static temperature distribution of the inlet boundary conditions, where regions of increased temperature are spotted below 10% span and above 70% span. Since the steady state simulations consists of a single rotor pitch, flow field has been replicated and rotated to form six pitches for a consistent comparison with the other plots. Figure 6-37b and c show the time-averaged results of the unsteady simulations that were performed during the optimization for the baseline and profiled geometry. The results are time-averaged in stator absolute frame of reference, therefore any flow features that appear in constant location relative to the stator pitch are coming from the upstream stator, while any features that are appear as circumferential lines are affected by the rotation of the rotor. For example, the large high temperature spots above 70% span are due to the strong tip passage vortex of the stator blade. This information is completely lost in the 1D boundary conditions and can explain the small differences observed in the radial plots of Figure 6-32 to Figure 6-34.

On the other hand, below 10% span, the leakage flow appears as fairly uniform contour lines in the circumferential direction. It can be easily seen that the time-averaged results do not differ considerably from the 1D boundary conditions that were imposed for the steady state problem. This is also the reason why the steady simulation of the baseline shows a good agreement with the unsteady. However, the question still remains, why the baseline simulations match so well but the profiled geometry simulations do not. Additionally, the differences between baseline and profiled are not that pronounced to justify that.

The reason for this phenomenon can only be attributed to flow unsteadiness and can be easily seen looking at Figure 6-37d and e,

which present the flow field at one snapshot of the unsteady simulation. When looking above 70% span, almost no differences can be observed compared to the time-averaged results, confirming the expectation of low flow unsteadiness coming from the stator. However, leakage flow shows distinct patterns of high temperature at certain pitch locations and, more importantly, these patterns and their locations are not the same for the baseline and profiled geometry, implying that the profiled end wall changes the unsteady interaction of the leakage flow with the rotor blade row and consequently the evolution of the secondary flows. This can be seen in the differences observed when comparing the steady and unsteady results of the profiled end wall at the exit of the rotor.

A final comment to complete the argument regarding the unsteadiness can be made by looking at the flow field in S2 stator exit, which was analyzed in section 6.3.3. As can be seen by the dashed lines in Figure 6-9, there is high flow unsteadiness close to the hub due to the leakage mass flow. More specifically, the peak-to-peak fluctuations of static pressure are  $\pm 4.8\%$  at 2% span position, compared to  $\pm 0.5\%$  at mid-span, which is 9.3 times higher unsteadiness. Similarly, the relative yaw angle fluctuations at 2% span are a staggering  $\pm 37^\circ$ , which is 2.5 times higher compared to mid-span, where the fluctuations are  $\pm 14.8^\circ$ . Even more importantly, although the time-averaged incidence angle is negative along the whole span, due to the fluctuations below 30% span, there are moments in time where incidence is changing to positive, as can be seen by the maximum dashed lines in Figure 6-10. All this unsteady information is lost in the 1D boundary conditions and subsequently in the steady solution, leading to the differences observed between steady and unsteady solutions.

With the arguments presented above, it is concluded that the assumption formulated in the beginning of section 6.3.7.1 does not stand true. The impact of unsteadiness is not negligible, it affects the results and neglecting it can lead to incorrect conclusions regarding the success of the optimization and have a strong influence on the decision making phase. Therefore, when a goal of an optimization is to achieve performance improvements by managing secondary flows, in the presence of large cavity paths, unsteadiness is important to be accounted for during the whole optimization process.

## 6.4 Summary and conclusions

This chapter presented the results of an unsteady optimization that was performed for the LISA-H2 case to apply endwall contouring on the rotor hub end wall. The reason for the unsteady optimization was the presence of hub and tip cavities in the computational domain, which has been previously shown to cause an unsteady interaction of the leakage flow with the blade rows and secondary flows and that steady state results show large differences compared to time-averaged or unsteady calculations. Therefore, the goal was to achieve an increase in stage efficiency, while taking into account for the performance assessment all the unsteady interactions present in the flow field during the whole optimization process.

The optimization was performed using a genetic algorithm method, which utilizes the predictions of an approximate model during each generation. The approximate model was an artificial neural network that was trained by a database of completed fully three-dimensional unsteady simulations with the in-house solver MULTI3.

In order to reduce the computational cost, while still maintaining high accuracy in the calculations, a new approach was suggested to apply unsteady inflow boundary conditions at the inlet of the second stage. According to this approach, the full unsteady flow field is extracted from a two-stage simulation and is applied in the inlet of a single-stage configuration of the second stage. This reduces effectively the computational domain by more than half, while still keeping the full unsteady information and therefore the final results are taking into account unsteady blade row interactions, clocking effects etc. The results of the single-stage simulation of the baseline case have been extensively compared and validated with 5-hole probe and FRAP data that were available from a completed previous measurement campaign in LISA. Comparison has shown exceptionally good matching of CFD predictions with experiments, with errors being lower than 0.5% for most relevant parameters, thus confirming the validity of using unsteady inflow boundary conditions. Therefore, all simulations of database and optimization design cycles were performed using single-stage configurations with unsteady inlet boundary conditions.

The optimization was concluded after 20 design iterations. In total, 92 unsteady simulations were performed with a mesh size of more than 18 million mesh nodes, 72 of which were used for building the initial database for the artificial neural network training. The whole optimization process, including database generation was completed in less than 25 days.

The optimization eventually resulted in a geometry that is predicted to give a +0.27% increase in torque-based stage efficiency. The optimized end wall geometry was presented and its effects on the stage were discussed in detail. Due to the slight increase in blockage introduced by the end wall contouring, the mass flow is slightly reduced by 0.3% and static pressure is increased in rotor inlet. However, the flow field in rotor inlet was found to be consistent between the baseline and profiled cases, confirming that the capacity of the turbine did not change significantly.

Although the total net mass flow of the cavity leakage flow remained the same in both cases, the radial velocity was significantly reduced by 15.5% for the profiled case compared to baseline, reducing the radial migration of the leakage flow in the rotor passage.

Comparison of the flow field at rotor exit has shown that the profile end wall has kept the passage vortex to a lower spanwise position by 3%. Additionally, the passage vortex was delayed on impinging the suction side by 19% of axial chord compared to baseline.

Although the profiled end wall has proven to weaken the strength of the hub passage vortex, beneficially impacting downstream stages in a real configuration, the reduction in the losses was relatively small with an average of 2.15%. Therefore, the increase in efficiency is also attributed to changes in the loading. The profiled end wall is seemingly increasing the specific power by producing more work with less mass flow, contributing positively for the efficiency.

Finally, the choices to perform time-accurate solutions during the whole optimization process and include hub and tip cavities were justified by performing an unsteady simulation of the baseline

geometry without cavities and two steady simulations of the rotor, for the baseline and profiled geometry.

Excluding the cavities from the computational model changes considerably the nature of the problem. With the absence of the high temperature leakage flow entering the main flow with high radial velocity and affecting the radial migration of the secondary flows, the passage vortex at the rotor exit remains at lower span position by 5.5% and total temperature is lower than should be. As a result, the main loss cores are under-predicted, leading to an inaccurately high stage efficiency, which is 3.74% higher compared to the experimentally measured.

The high peak-to-peak fluctuations close to the hub due to the leakage flow and its circumferentially non-uniform entrance in the main flow does not allow for unsteadiness to be neglected. According to steady state results, the gain in efficiency with the profiled end wall is only 0.06%, which is 4.5 times smaller compared to the reported results of the unsteady optimization.

In order to verify the optimization method, the resulting profiled geometry has been manufactured and will be experimentally tested in LEC's axial turbine facility LISA, for validation of numerical predictions.

## 7 Summary and conclusions

### 7.1 Summary

This thesis presents a set of numerical investigations with the objective to improve performance of modern steam turbines employing high fidelity unsteady simulations. Two different steam turbines were investigated: a transonic low-pressure steam turbine with supersonic airfoils near the tip of the last stage's rotor of MHPS and a two-stage shrouded model axial turbine at the Laboratory for Energy Conversion, with geometry and non-dimensional parameters matching those of high pressure steam turbines. All numerical simulations were performed using in-house developed solver MULTI3. Numerical results were extensively compared and validated with available data from past measurement campaigns.

#### **Unsteady flow mechanisms in a transonic low-pressure steam turbine**

An unsteady numerical simulation was performed for the last two stages of a real transonic low-pressure steam turbine with supersonic airfoils near the tip of the last stage rotor blade. The simulation was performed to complement unsteady measurements in wet steam flow conditions that were previously reported for the first time by the Laboratory for Energy Conversion in the steam turbine facility of MHPS in Japan. The unsteady simulations provided valuable insight in the flow physics present in the flow field and in understanding the complex interaction of the bow shock wave with the upstream stator and tip cavity. This is first time that the flow physics have been described in a time-accurate manner in the open literature and contributed in proposing ways to mitigate this interaction.

#### **Preparation for an unsteady optimization for turbomachinery applications**

Optimization processes can be very expensive, both in computational cost and real time requirements. Performing unsteady simulations during the optimization increases the complexity of the problem considerably and sufficient time needs to



be invested in preparation of that, to ensure that the allocated computational and human resources are not wasted. Certain guidelines were provided that could reduce the efforts and the required simulation time. Automation of process such as mesh generation and post-processing not only reduce the efforts considerably but also minimize human involvement and decrease the chance of mistakes happening during the process. Taking advantage of the understanding in numerical methods and flow physics involved in a problem can help in employing the correct numerical model for faster results. In this case, the presence of cavities in the computational model and the low Mach number flows in them, as well as the relatively low Mach numbers inside the main flow, made the case ideal for applying a multi-stage time integration coupled with a preconditioning method to achieve a great speed-up for a converged solution.

### **Unsteady optimization for end wall contouring in a model high-pressure steam turbine**

To the author's best knowledge, an unsteady optimization is performed for the first time in a real three-dimensional case, including hub and tip cavities. The motivation behind was that steady state solutions are known to differ considerably to time-averaged results of unsteady solutions when leakage flows or purge injection flows are involved. For this reason, an optimization was performed using unsteady simulations during the whole design optimization process, while taking into account the unsteady interactions present in the flow field. The selected optimization method that was applied was a Genetic Algorithm coupled with an Artificial Neural Network. In-house solver MULTI3 was used for all simulations, while a commercial software was used for the optimization algorithm. To reduce the domain of the real two-stage configuration, unsteady inlet boundary conditions were successfully applied to the inlet of the second stage, reducing the computational size by half, while still maintaining multi-stage effects and high accuracy in predictions. Results were compared to measurements for the baseline for validation of the suggested approach. Eventually, the optimization predicts a geometry that will offer 0.27% increase in stage efficiency. Steady state solutions have failed to capture accurately the findings of the unsteady optimization, predicting only a marginal gain in efficiency of 0.06%

with the profiled end wall. Finally, excluding hub cavity from the computational model does not capture the secondary flows in the correct radial position. The optimized rotor has already been manufactured and will be experimentally tested in the near future in LEC's axial turbine facility LISA to validate the numerical predictions.

The main findings of the current work can be summarized in the following points:

- The bow shock wave attached to the last stage rotor leading edge of a transonic low-pressure steam turbine interacts with the upstream stator and causes high unsteady fluctuations in static pressure by  $\pm 34.4\%$  and  $\pm 10.4\%$  in axial velocity.
- Due to the impingement of the bow shock wave on the suction side of the upstream stator, there are moments in time where static pressure on suction side is greater than on pressure side, causing a periodically appearing, local counter-loading close to the trailing edge. Despite that, there is no evidence of boundary layer separation at any point in time.
- The static pressure increase on the stator suction side at 85% of the axial chord is 15% lower compared to 97.5%, close to trailing edge and the maximum values on these locations appear with difference in phase equal to  $T/6$  of the rotor blade passing period.
- The bow shock wave is also interacting with the leakage mass flow ingested in the tip cavity of L-0 stage causing a suppression of the separation bubble in the lip of the rotor blade shroud, which leads to increased unsteadiness around each rotor pitch.
- The total mass flow through the tip cavity path was calculated to be 5% of the total mass flow, passing through 1.98% of the total available area in that axial location and appears to be fairly steady in time. Although the estimation is based on a "cold state" of the machine without taking into account the expansion due to rotational speed and thermal loads, the leakage mass flow is a considerable amount and should be considered during early stages of the design.
- Tip cavities and leakage flows have an important impact on the loss quantification. Traces of L-1 rotor tip leakage flow

have been identified to have radially migrated to lower span positions at L-0 stator exit, contributing with the bow shock wave to entropy generation with a maximum increase of 22.3% compared to mid-span. In the L-0 rotor on the other hand, tip leakage flow dominates the top 4% of the span with increased entropy generation by 42.3% compared to mid-span.

- State-of-art stacking techniques, such as forward curve sweeping, need to be employed on L-0 stator blade to reduce or eliminate the unsteady interaction with the rotating bow shock wave.
- Comparison of numerical predictions with time-accurate FRAP measurements show that equilibrium steam modeling can predict the underlying unsteady flow physics with high accuracy.
- Signal processing techniques have been successfully applied to assess the convergence of unsteady simulations and minimize the required simulation time until convergence.
- Using structured meshes allow the usage of a converged solution to new modified geometry, leading to case-dependent reduction in simulation time, which for the LISA-H1 and H2 cases were more than 66%.
- Coupling of a 4<sup>th</sup> order Runge-Kutta time integration scheme with a preconditioning scheme have decreased the necessary number of iterations by 85%, leading to a speed-up of unsteady simulations for LISA-H1 and H2 cases by a factor of 3.5, despite the increased computational cost by almost a factor of 2.
- Unsteady inlet boundary conditions are an effective way to decrease computational mesh size, while still keeping high accuracy in numerical predictions. Comparison with experiments have shown an exceptional agreement with errors lower than 0.5% for the relevant parameters.
- An unsteady optimization has been successfully performed for applying profiled end wall contouring on the rotor hub end wall. The whole optimization process involved more than 90 unsteady simulations and was completed within 25 days.
- In total approximately 13.000 node hours were required for the successful completion of the whole optimization process. Simulations were performed in CSCS using a parallelized, GPU-accelerated solver. Although it is now possible to

perform an unsteady optimization for a case with hundreds of simulations, 18 million mesh nodes and including real cavity paths within a reasonable time frame, the associated computational cost is still very high and the availability of computational resources may be a proven an issue.

- End wall contouring was successfully applied on the rotor hub end wall for controlling the strong passage vortex, reducing its strength and giving an increase in stage efficiency by +0.27%.
- End wall contouring has effectively decreased the radial velocity of the leakage flow by 15.5%, reducing its radial migration in the rotor passage.
- The passage vortex is kept in lower span positions by 3% and its impingement on the suction side is delayed by 19% of the rotor axial chord.
- Although the strength of the hub passage vortex, the loss reduction was not as high as expected, showing increased losses close to the hub but still having a total reduction by 2.15% on average. Apart from reduced loss generation, the gain in efficiency was associated to be related also to the increase of the specific power of the stage. However, the flow field shows improvement that could beneficially affect a downstream stage in a real configuration, but cannot be quantified in the current configuration.
- The average gain in efficiency is quite close to the probe measurement uncertainty, nevertheless the local changes are by far larger than the uncertainty and predicted changes should be possible to be captured during measurements.
- Although the gain in efficiency could be considered relatively small compared to previous studies, it implies on one hand that improved solutions could be possible achieved only with more aggressive geometry, allowing the non-axisymmetric end wall to extend up to the rotor lip. On the other hand it shows how difficult it can be to achieve large increases in efficiency of modern turbomachinery, even when high fidelity time-accurate models are employed.

## 7.2 Concluding remarks

In an attempt to address the research objectives that were posed in the beginning of the doctoral thesis, results of the presented numerical work have lead to the following conclusions:

- Axial distance between stator and rotor need to be increased or, when this is not possible due to limitations coming from bearing locations, state-of-art stacking techniques, such as forward curve sweeping, need to be employed on L-0 stator blade to reduce or eliminate the unsteady interaction with the rotating bow shock wave.
- In cases that have large cavity paths (HP steam turbines with gaps  $\sim 40\%$  of the blade axial chord) and the goal is performance improvement by managing secondary flows, cavities are not allowed to be excluded from the computational model, if an accurate representation of the problem is to be expected. Leakage flows interact with the formation of secondary flows and facilitate their radial migration to higher spanwise locations, a mechanism that is missing if cavities are excluded.
- When cavity paths are included in the computational model, even steady state solutions can accurately capture the correct position of the secondary flow features but with a penalty on their intensity prediction.
- The resulting profiled end wall geometry of the unsteady optimization leads to an increased efficiency by  $0.27\%$ . Although steady state results still predict an improvement, it is limited to only  $0.06\%$ , which is 4.5 times smaller compared to unsteady prediction.
- The average change of efficiency according to steady state solutions are below probe measurement uncertainty. Local changes are still out of the uncertainty range but much closer compared to unsteady predictions. This does not only affect the description of the optimization as “successful” or “unsuccessful” but can also have a huge impact on the decision-making. It is quite fair to assume that no industry would allocate resources for the manufacturing of this geometry if decision was based on steady state solution,

missing a potentially good opportunity since the unsteady optimization predict much higher gain.

- As turbomachinery are getting more and more difficult to improve, flow unsteadiness is an important link that is missing from current optimization practices in industry and need to be taken into account during the whole design phase and optimization process. Trying to improve a strongly unsteady problem with a steady approach is rather pointless and a misuse of valuable resources and allocations.

### 7.3 Suggestions for future work

From all the topics discussed in this work, the application of unsteady optimization in turbomachinery has an incredibly high potential for further research. Optimizations have been successfully used in turbomachinery for many decades and the objective were always more or less the same: reduction of pressure losses, reduction of secondary kinetic energy, increase of efficiency etc. However, unsteady optimizations can be applied to cases where time-accuracy is important and steady state solutions fail to capture. There are dozens of fields to be explored, new optimization functions to apply and better improvement to achieve for the whole range of turbomachinery. Indicatively, the following applications are mentioned:

- **Transonic compressors and transonic steam turbines:** Great examples are cases where shock patterns are present in the flow field and travel upstream interacting with multiple blade rows. Steady state solutions filter the interaction of the shock patterns, making it impossible to consider during an optimization. Such cases are the Darmstadt Transonic Compressor [125] or the last stage of the transonic steam turbine that was investigated in the present work. In a continuation of the work presented in Chapter 4, different stator stacking techniques were investigated and confirmed that forward sweep and change in the throat-to-pitch ratio can improve the performance of the turbine [109]. However, the suggested changes were based on past experience and a good understanding of the flow field mechanisms. With the proposed methodology, it is possible now to optimize the stator blade in a unsteady manner, taking into account the unsteady interactions. Domain could also be reduced to only the last stage by applying unsteady inlet boundary conditions extracted from the outlet of L-1 stage. Coupling with the wet steam model could ensure high accuracy in predictions and would be very interesting to further investigate. It is worth to mention however the expected computational cost will be much higher. The supersonic absolute velocities close to the hub and relative supersonic flow close to the tip, render the preconditioning scheme practically useless. Runge-Kutta has

also shown in internal investigations that it offers no significant gain to justify the doubled computational cost.

- **Cavity optimization:** Just this topic by itself has many different aspects that could be investigated. Cavity flows are well known that have a complex unsteady interaction with the main flow and the secondary flows, as well as high sensitivity of the efficiency to the amount of injected mass flow [83]. The cavity shape can also have an impact on the interaction [29]. There is an interesting attempt reported by Lott et al [81], where the objective of the optimization was to maximize the rim seal purge flow effectiveness for gas turbines using end wall contouring. However it is reported that the unsteady simulations show large differences compared to the steady state that was used in the optimization. This would be an ideal case for an unsteady optimization. Similarly, the objective could also change and the minimum required purge flow temperature and injection ratio could be optimized to have effective cooling needed without decimating the efficiency. This could additionally be coupled with complex geometrical features inside cavities for increased stage efficiency [126].
- **Low cavity modes:** There are several cases reported where non-synchronous low frequency cavity modes appear in the cavities and have severe changes in the non-uniform changes in flow field and performance [127]. Geometrical modifications in cavities could be explored to reduce or eliminate the presence of low-cavity modes.
- **Stall margin of axial and radial compressors:** This could also be investigated and taken into account during optimization, if stall and its effects are considered with time-accurate simulations.

The last two points, although very interesting, may still be too far to accomplish. The reason is that in such cases, full-annular simulations are probably required and the idea of running unsteady full-annular simulations in an optimization seems rather extreme at this point but definitely manageable in a few years.

Nevertheless, applying the unsteady optimization can be prohibitively expensive. Apart from the ever-growing advances in hardware that allow simulations to finish faster, more effort can be put on the numerical methods to accelerate unsteady simulations even



further. For example, the application of phase-lagged boundary conditions is an effective way of reducing computational size. Additionally, the nonlinear harmonic method can considerably reduce the time required for an unsteady simulation, while also reducing the computational size, since it needs only one interblade channel per blade row like a steady flow simulation.

Apart from these, a novel approach for speeding up unsteady simulations is suggested and is based on coupling the Lax-Wendroff with the Runge-Kutta scheme. As it was discussed in the thesis, Lax-Wendroff is more suitable for compressible flows (main flow path), while Runge-Kutta coupled with preconditioning is more suitable for cavity flows, which are characterized by low Mach numbers. However, Runge-Kutta scheme is almost two-times more expensive computationally. Therefore, the idea is to split the computational domain, for example in main flow path and cavities, and apply the most suitable numerical scheme for each domain, allowing to apply the expensive numerical scheme only in the locations that it is needed. Finally and most importantly, splitting of the domain in two different sub-domains, will allow the application of the so-called “fork-join model”. The fork-join model can be considered a parallel design pattern and, in a nutshell, will allow the computation of both the domains simultaneously and independently, speeding up the whole process. In the author’s opinion, issues are to be expected on the interface of the two domains, where the two different numerical schemes are used. However, the issues could be overcome in a similar way that RANS-LES models have been coupled in hybrid solvers.

# Appendix

## References

- [1] BP, "BP Statistical Review of World Energy 2017," Technical report, 2017.
- [2] Y. A. Çengel and M. A. Boles, *Thermodynamics: An Engineering Approach*. McGraw-Hill Higher Education, 2006.
- [3] "<https://www.youtube.com/LearnEngineering>." .
- [4] S. Senoo *et al.*, "Development of Titanium 3600rpm-50inch and 3000rpm-60inch Last Stage Blades for Steam Turbines," *Int. J. Gas Turbine, Propuls. Power Syst.*, vol. 6, no. 2, pp. 9–16, 2014.
- [5] S. Senoo, "Development of Design Method for Supersonic Turbine Aerofoils Near the Tip of Long Blades in Steam Turbines: Part 1—Overall Configuration," in *ASME Paper No. GT2012-68218, Volume 6: Oil and Gas Applications; Concentrating Solar Power Plants; Steam Turbines; Wind Energy*, 2012, pp. 355–365.
- [6] S. Senoo and H. Ono, "Development of Design Method for Supersonic Turbine Aerofoils Near the Tip of Long Blades in Steam Turbines: Part 2 — Configuration Details and Validation," in *Volume 5B: Oil and Gas Applications; Steam Turbines*, 2013, p. V05BT25A002.
- [7] D. G. Holmes, B. J. Moore, and S. D. Connell, "Unsteady vs. Steady Turbomachinery Flow Analysis: Exploiting Large-Scale Computations to Deepen our Understanding of Turbomachinery Flows," *SciDAC Conf.*, pp. 1–13, 2011.
- [8] S. Havakechian and J. D. Denton, "Three-Dimensional Blade-Stacking Strategies and Understanding of Flow Physics in Low-Pressure Steam Turbines—Part I: Three-Dimensional Stacking Mechanisms," *J. Eng. Gas Turbines Power*, vol. 138, no. 5, p. 52603, 2015.
- [9] H. Stüer, F. Truckenmüller, D. Borthwick, and J. D. Denton, "Aerodynamic Concept for Very Large Steam Turbine Last Stages," *ASME Conf. Proc.*, vol. 2005, no. 47306, pp. 673–687, 2005.
- [10] H. F. Vogt and M. Zippel, "Sekundärströmungen in Turbinengittern mit geraden und gekrümmten Schaufeln; Visualisierung im ebenen Wasserkanal," *Forsch. im Ingenieurwesen/Engineering Res.*, vol. 62, no. 9, pp. 247–253, 1996.
- [11] L. S. Langston, "Crossflows in a Turbine Cascade Passage," *J. Eng. Power*, vol. 102, no. 4, p. 866, 1980.
- [12] O. P. Sharma and T. L. Butler, "Predictions of Endwall Losses and Secondary Flows in Axial Flow Turbine Cascades," *J. Turbomach.*, vol. 109, no. 2, p. 229, 1987.

- [13] R. J. Goldstein and R. A. Spores, "Turbulent Transport on the Endwall in the Region Between Adjacent Turbine Blades," *J. Heat Transfer*, vol. 110, no. 4a, p. 862, 1988.
- [14] H. P. Wang, S. J. Olson, R. J. Goldstein, and E. R. G. Eckert, "Flow Visualization in a Linear Turbine Cascade of High Performance Turbine Blades," *J. Turbomach.*, vol. 119, no. 1, p. 1, 1997.
- [15] P. Schuepbach, "Influence of Rim Seal Purge Flow on the Performance of an End Wall Profiled Axial Turbine," PhD Thesis, Diss. ETH No. 18458, 2009.
- [16] P. Jenny, "Interaction Mechanisms Between Rim Seal Purge Flow and Profiled End Walls in a Low Pressure Turbine," PhD Thesis, Diss. ETH No. 20429, 2012.
- [17] K. Regina, "High-Pressure Turbines with Novel Airfoils and End Walls Operating under Engine Representative Aero-Thermodynamic Effects," PhD Thesis, Diss. ETH No. 22633, 2015.
- [18] D. Torre, R. Vázquez, E. de la Rosa Blanco, and H. P. Hodson, "A New Alternative for Reduction in Secondary Flows in Low Pressure Turbines," *J. Turbomach.*, vol. 133, no. 1, p. 11029, 2011.
- [19] N. W. Harvey, M. G. Rose, M. D. Taylor, S. Shahpar, J. Hartland, and D. G. Gregory-Smith, "Nonaxisymmetric Turbine End Wall Design: Part I— Three-Dimensional Linear Design System," *J. Turbomach.*, vol. 122, no. 2, p. 278, 2000.
- [20] J. C. Hartland, D. G. Gregory-Smith, N. W. Harvey, and M. G. Rose, "Nonaxisymmetric Turbine End Wall Design: Part II—Experimental Validation," *J. Turbomach.*, vol. 122, no. 2, p. 286, 2000.
- [21] G. Ingram, D. Gregory-Smith, and N. Harvey, "Investigation of a Novel Secondary Flow Feature in a Turbine Cascade With End Wall Profiling," *Vol. 5 Turbo Expo 2004, Parts A B*, vol. 127, no. January 2005, pp. 1199–1209, 2004.
- [22] M. G. Nagel and R.-D. Baier, "Experimentally Verified Numerical Optimization of a Three-Dimensional Parametrized Turbine Vane With Nonaxisymmetric End Walls," *J. Turbomach.*, vol. 127, no. 2, p. 380, 2005.
- [23] A. Hergt, C. Dorfner, W. Steinert, E. Nicke, and H.-A. Schreiber, "Advanced Non-Axisymmetric Endwall Contouring for Axial Compressors by Generating an Aerodynamic Separator—Part II: Experimental and Numerical Cascade Investigation," *Vol. 7 Turbomachinery, Parts A B*, vol. 133, no. April 2011, pp. 121–131, 2009.
- [24] C. Dorfner, A. Hergt, E. Nicke, and R. Moenig, "Advanced Non-Axisymmetric Endwall Contouring for Axial Compressors by Generating an Aerodynamic Separator—Part I: Principal Cascade Design and Compressor Application," *Vol. 7 Turbomachinery, Parts A B*, vol. 133, no. April 2011, pp. 113–120, 2009.
- [25] M. Eric Lyall, P. I. King, J. P. Clark, and R. Sondergaard, "Endwall Loss Reduction of High Lift Low Pressure Turbine Airfoils Using Profile Contouring—Part I: Airfoil Design," *J. Turbomach.*, vol. 136, no. 8, p. 81005, 2014.

- [26] K. Sangston, J. Little, M. E. Lyall, and R. Sondergaard, "End Wall Loss Reduction of High Lift Low Pressure Turbine Airfoils Using Profile Contouring—Part II: Validation," *J. Turbomach.*, vol. 136, no. 8, p. 81006, 2014.
- [27] T. Poehler, J. Niewoehner, P. Jeschke, and Y. Guendogdu, "Investigation of Nonaxisymmetric Endwall Contouring and Three-Dimensional Airfoil Design in a 1.5-Stage Axial Turbine—Part I: Design and Novel Numerical Analysis Method," *J. Turbomach.*, vol. 137, no. 8, p. 81009, 2015.
- [28] J. Niewoehner, T. Poehler, P. Jeschke, and Y. Guendogdu, "Investigation of Nonaxisymmetric Endwall Contouring and Three-Dimensional Airfoil Design in a 1.5 Stage Axial Turbine—Part II: Experimental Validation," *J. Turbomach.*, vol. 137, no. 8, p. 81010, 2015.
- [29] K. Barmpalias, "Steam Turbine Aerodynamics and Geometry Optimization for Effective Reduction of Leakage Flow Interactions," PhD Thesis, Diss. ETH No. 19904, 2011.
- [30] A. Egli, "The Leakage of Steam Through Labyrinth Seals," *Trans. ASME*, vol. Vol. 57, pp. 115–122, 1935.
- [31] W. Traupel, "Thermische Turbomaschinen, Erster Band," *Springer, Berlin*, 2. Aufl., 1966.
- [32] S. S. Rao, *Engineering Optimization: Theory and Practice*. Wiley, 2009.
- [33] A. Demeulenaere and R. Van den Braembussche, "Three-dimensional Inverse Method for Turbomachinery Blading Design," *ASME 1996 Int. Gas Turbine Aeroengine Congr. Exhib.*, vol. 120, no. April 1998, pp. 1–11, 1996.
- [34] W. T. Tiow and M. Zangeneh, "A Viscous Transonic Inverse Design Method for Turbomachinery Blades: Part I — 2D Cascades," in *Volume 1: Turbomachinery*, 1998, p. V001T01A037.
- [35] L. de Vito, R. A. Van den Braembussche, and H. Deconinck, "A Novel Two Dimensional Viscous Inverse Design Method for Turbomachinery Blading," *Vol. 5 Turbo Expo 2002, Parts A B*, vol. 125, no. April 2003, pp. 1071–1080, 2002.
- [36] D. Bonaiuti and M. Zangeneh, "On the Coupling of Inverse Design and Optimization Techniques for the Multiobjective, Multipoint Design of Turbomachinery Blades," *J. Turbomach.*, vol. 131, no. 2, p. 21014, 2009.
- [37] L. He and P. Shan, "Three-Dimensional Aerodynamic Optimization for Axial-Flow Compressors Based on the Inverse Design and the Aerodynamic Parameters," *J. Turbomach.*, vol. 134, no. 3, p. 31004, 2012.
- [38] N. Chen, H. Zhang, Y. Xu, and W. Huang, "Blade Parameterization and Aerodynamic Design Optimization for a 3D Transonic Compressor Rotor," *J. Therm. Sci.*, vol. 16, no. 2, pp. 105–114, 2007.

- [39] D. X. Wang, L. He, Y. S. Li, R. G. Wells, and T. Chen, "Adjoint Aerodynamic Design Optimization for Blades in Multi-Stage Turbomachines: Part II—Validation and Application," *Vol. 6 Turbomachinery, Parts A, B, C*, vol. 132, no. April 2010, pp. 2157–2169, 2008.
- [40] D. X. Wang and L. He, "Adjoint Aerodynamic Design Optimization for Blades in Multistage Turbomachines—Part I: Methodology and Verification," *J. Turbomach.*, vol. 132, no. 2, p. 21011, 2010.
- [41] M. Pini, G. Persico, D. Pasquale, and S. Rebay, "Adjoint Method for Shape Optimization in Real-Gas Flow Applications," *J. Eng. Gas Turbines Power*, vol. 137, no. 3, p. 32604, 2014.
- [42] B. Walther and S. Nadarajah, "Optimum Shape Design for Multirow Turbomachinery Configurations Using a Discrete Adjoint Approach and an Efficient Radial Basis Function Deformation Scheme for Complex Multiblock Grids," *J. Turbomach.*, vol. 137, no. 8, p. 81006, 2015.
- [43] L. Fang and X. Li, "Design Optimization of Unsteady Airfoils with Continuous Adjoint Method," *Appl. Math. Mech. (English Ed.)*, vol. 36, no. 10, pp. 1329–1336, 2015.
- [44] C. Ma, X. Su, and X. Yuan, "An Efficient Unsteady Adjoint Optimization System for Multistage Turbomachinery," *J. Turbomach.*, vol. 139, no. 1, p. 11003, 2016.
- [45] J. Yi and L. Capone, "Adjoint-Based Sensitivity Analysis for Unsteady Bladerow Interaction Using Space–Time Gradient Method," *J. Turbomach.*, vol. 139, no. 11, p. 111008, 2017.
- [46] G. Ntanakas, M. Meyer, and K. C. Giannakoglou, "Employing the Time-Domain Unsteady Discrete Adjoint Method for Shape Optimization of Three-Dimensional Multirow Turbomachinery Configurations," *J. Turbomach.*, vol. 140, no. 8, p. 81006, 2018.
- [47] A. Rubino *et al.*, "Adjoint-based Fluid Dynamic Design Optimization in Quasi-periodic Unsteady Flow Problems using a Harmonic Balance Method," *J. Comput. Phys.*, vol. 372, pp. 220–235, 2018.
- [48] A. Rubino, S. Vitale, M. Pini, and P. Colonna, "Assessment of Fully-Turbulent Steady and Unsteady Adjoint Sensitivities for Stator-Rotor Interaction in Turbomachinery," in *Proceedings of Montreal 2018 Global Power and Propulsion Forum*, 2018, p. GPPS-NA-2018-130.
- [49] S. Pierret and R. A. Van den Braembussche, "Turbomachinery Blade Design Using a Navier–Stokes Solver and Artificial Neural Network," *J. Turbomach.*, vol. 121, no. 2, p. 326, 1999.
- [50] S. Pierret, A. Demeulenaere, B. Gouverneur, C. Hirsch, and R. A. Van Den Braembussche, "Designing Turbomachinery Blades with the Function Approximation Concept and the Navier-Stokes Equations," *AIAA J.*, no. c, 2000.

- [51] A. Demeulenaere, A. Ligout, and C. Hirsch, "Application of Multipoint Optimization to the Design of Turbomachinery Blades," in *Volume 5: Turbo Expo 2004, Parts A and B*, 2004, pp. 1481–1489.
- [52] M. L. Kuzmenko, I. N. Egorov, Y. N. Shmotin, and K. S. Fedechkin, "Optimization of the Gas Turbine Engine Parts Using Methods of Numerical Simulation," *Vol. 6 Turbo Expo 2007, Parts A B*, pp. 425–431, 2007.
- [53] S. F. A. Hashmi, Q. W. Yang, and C. P. Ping, "Numerical Investigation on Effect of Rotor Blade Lean Angle Variation on Single Stage Fan Stability," *Proc. 2013 10th Int. Bhurban Conf. Appl. Sci. Technol. IBCAST 2013*, pp. 275–285, 2013.
- [54] S. Reising and H.-P. Schiffer, "Non-Axisymmetric End Wall Profiling in Transonic Compressors—Part I: Improving the Static Pressure Recovery at Off-Design Conditions by Sequential Hub and Shroud End Wall Profiling," in *Volume 7: Turbomachinery, Parts A and B*, 2009, pp. 11–24.
- [55] S. Reising and H.-P. Schiffer, "Non-Axisymmetric End Wall Profiling in Transonic Compressors—Part II: Design Study of a Transonic Compressor Rotor Using Non-Axisymmetric End Walls—Optimization Strategies and Performance," in *Volume 7: Turbomachinery, Parts A and B*, 2009, pp. 25–37.
- [56] B. Jiang, S. Wang, G. Feng, and Z. Wang, "Numerical Study on End-Wall Flow in Highly Loaded Supercritical Compressor Cascades," in *Volume 7: Turbomachinery, Parts A and B*, 2009, pp. 203–214.
- [57] J. Lu, W. Chu, and Y. Wu, "Effects of Endwall Profiling on Axial Flow Compressor Stage," in *Volume 7: Turbomachinery, Parts A and B, GT2009-59418*, 2009, pp. 145–154.
- [58] X. Li, W. Chu, and Y. Wu, "Numerical Investigation of Inlet Boundary Layer Skew in Axial-flow Compressor Cascade and the Corresponding Non-axisymmetric End Wall Profiling," *Proc. Inst. Mech. Eng. Part A J. Power Energy*, vol. 228, no. 6, pp. 638–656, 2014.
- [59] Z. Na and B. Liu, "Numerical Investigation of Non-Axisymmetric Endwalls in a High Pressure Axial Flow Turbine," in *ASME. Turbo Expo: Power for Land, Sea, and Air*, 2015, vol. 2A, pp. 1–11.
- [60] J. M. Franco-Nava, E. Rosado-Tamariz, J. M. Fernández-Dávila, and R. Rangel-Espinosa, "CFD-based Energy Improvement of a Parametric Blade Model for a Francis Turbine Runner," in *American Society of Mechanical Engineers, Power Division (Publication) PWR*, 2008, pp. 641–647.
- [61] M. Qi, C. Ma, and C. Yang, "Numerical Optimization on a Centrifugal Turbocharger Compressor," *SAE Int. J. Fuels Lubr.*, 2008.
- [62] H. Safikhani, A. Khalkhali, and M. Farajpoor, "Pareto-based Multi-Objective Optimization of Centrifugal Pumps Using CFD, Neural Networks and Genetic Algorithms," *Eng. Appl. Comput. Fluid Mech.*, vol. 5, no. 1, pp. 37–48, 2011.

- [63] A. Khalkhali, M. Farajpoor, and H. Safikhani, "Modeling and Multi-Objective Optimization of Forward-Curved Blade Centrifugal Fans Using CFD and Neural Networks," *Trans. Can. Soc. Mech. Eng.*, vol. 35, no. 1, pp. 63–79, 2011.
- [64] S. Derakhshan and N. Kasaeian, "Optimal Design of Axial Hydro Turbine for Micro Hydropower Plants," in *IOP Conference Series: Earth and Environmental Science*, 2012, vol. 15, no. PART 4.
- [65] D. Barsi and C. C. Carlo Costa Gianluca Ricci, "Aerodynamic Design of a Centrifugal Compressor Stage Using an Automatic Optimization Strategy," *Proc. ASME Turbo Expo 2014 Turbine Tech. Conf. Expo.*, 2014.
- [66] D. Dieu, Y. Deletrain, R. Van Lieffering, and C. Hirsch, "A Strategy for Parameterization and Optimization of Turbine Cooling Channels," in *Proceedings of ASME Turbo Expo 2015: Turbine Technical Conference and Exposition*, 2015, pp. 1–12.
- [67] A. Demeulenaere, J.-C. Bonaccorsi, D. Gutzwiller, L. Hu, and H. Sun, "Multi-Disciplinary Multi-Point Optimization of a Turbocharger Compressor Wheel," in *Proceedings of ASME Turbo Expo 2015: Turbine Technical Conference and Exposition*, 2015, pp. 1–9.
- [68] A. Perrone, L. Ratto, G. Ricci, F. Satta, and P. Zunino, "Multi-Disciplinary Optimization of a Centrifugal Compressor for Micro-Turbine Applications," in *Proceedings of ASME Turbo 2016: Turbomachinery Technical Conference and Exposition*, 2016, pp. 1–12.
- [69] S. Hu, F. X. Zhang, M. Benner, P. Gostelow, and E. Vlasic, "Geometric Optimization of Aggressive Inter-Turbine Ducts," in *Proceedings of the ASME 2010 International Mechanical Engineering Congress & Exposition*, 2016, pp. 1–10.
- [70] . Numeca International, "User Manual FINE/Turbo v.11.2." 2017.
- [71] S. C. Wang, *Interdisciplinary Computing in Java Programming*. Springer US, 2003.
- [72] Z. Yin, B. Jia, S. Wu, J. Dai, and D. Tang, "Comprehensive Forecast of Urban Water-Energy Demand Based on a Neural Network Model," *Water (Switzerland)*, vol. 10, no. 4, pp. 1–16, 2018.
- [73] M. Melanie, "An Introduction to Genetic Algorithms," *Comput. Math. with Appl.*, vol. 32, no. 6, p. 133, 1996.
- [74] S. Reising, "Steady and Unsteady Performance of a Transonic Compressor Stage with Non-Axisymmetric End Walls," Technische Universität Darmstadt, 2010.
- [75] J. Li, B. Li, L. Song, and Z. Feng, "Multidisciplinary optimization design of long blade turbine stage based on parallel self-Adaptive multi-objective differential evolution algorithm," in *Proceedings of the ASME Turbo Expo*, 2016, vol. 8.



- [76] M. Yin *et al.*, "Aerodynamic Optimization Design of Last Stage Long Blade for Steam Turbine using Self-adaptive Differential Evolutionary Algorithms and RANS Solutions," in *Proceedings of the ASME Turbo Expo*, 2017, vol. 8.
- [77] L. Song, C. Luo, J. Li, and Z. Feng, "Automated Multi-Objective and Multidisciplinary Design Optimization of a Transonic Turbine Stage," in *Proceedings of the Institution of Mechanical Engineers, Part A: Journal of Power and Energy*, 2012, vol. 226, no. 2, pp. 262–276.
- [78] M. Haraguchi, T. Nakamura, H. Yoda, T. Kudo, and S. Senoo, "Nuclear Steam Turbine with 60 inch Last Stage Blade," in *Volume 1: Plant Operations, Maintenance, Engineering, Modifications, Life Cycle and Balance of Plant; Nuclear Fuel and Materials; Radiation Protection and Nuclear Technology Applications*, 2013.
- [79] S. Hu and H. Luo, "Endwall Contouring Optimization in a High Pressure Turbine Vane With Consideration of Rim Seal Flow," in *Volume 2C: Turbomachinery*, 2014, p. V02CT38A039.
- [80] H. Tang, S. Liu, and H. Luo, "Design Optimization of Profiled Endwall With Consideration of Cooling and Rim Seal Flow Effects," in *Proceedings of ASME Turbo Expo 2016: Turbomachinery Technical Conference and Exposition GT2016-57219*, 2016, pp. 1–11.
- [81] P. T. Lott, N. J. Hills, J. W. Chew, T. Scanlon, and S. Shahpar, "High Pressure Turbine Stage Endwall Profile Optimisation for Performance and Rim Seal Effectiveness," *Vol. 7 Turbomachinery, Parts A B*, pp. 1075–1087, 2009.
- [82] S. Shahpar, S. Caloni, and L. de Prieëlle, "Automatic Design Optimization of Profiled Endwalls Including Real Geometrical Effects to Minimize Turbine Secondary Flows," *J. Turbomach.*, vol. 139, no. 7, p. 71010, 2017.
- [83] P. Jenny, R. S. Abhari, M. G. Rose, M. Brettschneider, and J. Gier, "A Low Pressure Turbine With Profiled Endwalls and Purge Flow Operating With a Pressure Side Bubble," *J. Turbomach.*, vol. 134, no. 6, p. 61038, 2012.
- [84] S. Hu and H. Luo, "Endwall Contouring Optimization in a High Pressure Turbine Vane With Consideration of Rim Seal Flow," *Volume 2C: Turbomachinery*. p. V02CT38A039, 2014.
- [85] R.-H. Ni, "A Multiple-Grid Scheme for Solving the Euler Equations," *AIAA J.*, vol. 20, no. 11, pp. 1565–1571, 1982.
- [86] A. Jameson, W. Schmidt, and E. Turkel, "Numerical Solution of the Euler Equations by Finite Volume Methods Schemes," *Convergence*, vol. M, no. AIAA 81-1259, pp. 1–19, 1981.
- [87] A. M. Basol, "Turbine Design Optimizations Using High Fidelity CFD," PhD Thesis, Diss. ETH No. 21559.
- [88] D. C. Wilcox, "Reassessment of the Scale-Determining Equation for Advanced Turbulence Models," *AIAA J.*, vol. 26, no. 11, pp. 1299–1310, 1988.

- [89] M. Kato and B. Launder, "The Modelling of Turbulent Flow Around Stationary and Vibrating Square Cylinders," in *9th Symposium on Turbulent Shear Flows*, 1993, p. 10.4.1-10.4.6.
- [90] P. K. Sweby, "High Resolution Schemes Using Flux Limiters for Hyperbolic Conservation Laws," *SIAM J. Numer. Anal.*, vol. 21, no. 5, pp. 995–1011, 1984.
- [91] A. Jameson, "Time-dependent Calculations using Multigrid, with Applications to Unsteady Flows past Airfoils and Wings," in *10th Computational Fluid Dynamics Conference*, 1991.
- [92] M. Kleinheinz, "Convergence Acceleration of Unsteady CFD Simulations for Turbomachinery Applications," LEC - ETH Zurich, 2017.
- [93] J. M. Weiss and W. A. Smith, "Preconditioning Applied to Variable and Constant Density Flows," *AIAA J.*, vol. 33, no. 11, pp. 2050–2057, 1995.
- [94] S. Venkateswaran, J. M. Weiss, C. L. Merkle, and Y.-H. Choi, "Propulsion-Related Flowfields using the Preconditioned Navier-Stokes Equations," in *AIAA, SAE, ASME, and ASEE, Joint Propulsion Conference and Exhibit*, 1992, p. 16p.
- [95] C. Liu, X. Zheng, and C. H. Sung, "Preconditioned Multigrid Methods for Unsteady Incompressible Flows," *J. Comput. Phys.*, vol. 139, no. 1, pp. 35–57, 1998.
- [96] S. Jafari, "Efficient Simulation of Wind and Wake Flows in Wind Farms Using a Preconditioned Multistage Solver," PhD Thesis, Diss. ETH No. 21837.
- [97] M. Holmgren, "X Steam, Thermodynamic Properties of Water and Steam." 2008.
- [98] S. Senoo, K. Segawa, H. Hamatake, T. Kudo, T. Nakamura, and N. Shibashita, "Computations for Unsteady Compressible Flows in a Multistage Steam Turbine With Steam Properties at Low Load Operations," *J. Eng. Gas Turbines Power*, vol. 133, no. 10, p. 103001, 2011.
- [99] M. Giles, "Non-reflecting Boundary Conditions for Euler Equation Calculations," in *9th Computational Fluid Dynamics Conference*, 1989.
- [100] J. P. Clark and E. A. Grover, "Assessing Convergence in Predictions of Periodic-Unsteady Flowfields," in *Volume 6: Turbomachinery, Parts A and B*, 2006, vol. 2006, pp. 1831–1841.
- [101] M. H. Ahmed and T. J. Barber, "Fast Fourier Transform Convergence Criterion for Numerical Simulations of Periodic Fluid Flows," *AIAA J.*, vol. 43, no. 5, pp. 1042–1052, May 2005.
- [102] P. Amtsfeld, D. Bestle, and M. Meyer, "Direct 3D Aerodynamic Optimization of Turbine Blades with GPU-accelerated CFD," in *Computational Methods in Applied Sciences*, 2015, vol. 36, pp. 197–207.

- [103] T. Mengistu and W. Ghaly, "Aerodynamic Optimization of Turbomachinery Blades using Evolutionary Methods and ANN-based Surrogate Models," *Optim. Eng.*, vol. 9, no. 3, pp. 239–255, 2008.
- [104] R. Dornberger, P. Stoll, D. Bueche, and A. Neu, "Multidisciplinary Turbomachinery Blade Design Optimization," *38th Aerosp. Sci. Meet. Exhib.*, 2000.
- [105] M. Kleinheinz, "Minimum Convergence Level of Unsteady CFD Simulations for Design Optimization Cycle," LEC - ETH Zurich, 2017.
- [106] M. Wolfe, "The PGI Accelerator Programming Model on NVIDIA GPUs." PGI, 2009.
- [107] M. Huber, "GPU Acceleration of a Fluid Flow Solver for Turbomachinery Applications," LEC - ETH Zurich, 2011.
- [108] "<https://www.nvidia.com/en-us/data-center/tesla-p100/>."
- [109] A. Raheem, "Improvement of Transonic Low Pressure Steam Turbine using High Performance Computations," PhD Thesis, Diss. ETH No. 25646, 2019.
- [110] M. G. Rose, "Non-Axisymmetric Endwall Profiling in the HP NGV's of an Axial Flow Gas Turbine," *Vol. 1 Turbomach.*, vol. ASME GT199, 1994.
- [111] J. C. Hartland, D. G. Gregory-Smith, and M. G. Rose, "Non-Axisymmetric Endwall Profiling in a Turbine Rotor Blade," no. ASME GT1998-525. 1998.
- [112] D. G. Gregory-Smith, G. Ingram, P. Jayaraman, N. W. Harvey, and M. G. Rose, "Non-axisymmetric Turbine End Wall Profiling," *Proc. Inst. Mech. Eng. Part A J. Power Energy*, vol. 215, no. 6, pp. 721–734, 2001.
- [113] G. Ingram, D. G. Gregory-Smith, M. G. Rose, N. W. Harvey, and G. Brennan, "The Effect of End-Wall Profiling on Secondary Flow and Loss Development in a Turbine Cascade," in *Volume 5: Turbo Expo 2002, Parts A and B*, 2002, pp. 135–145.
- [114] G. Brennan, N. Harvey, M. G. Rose, N. Fomison, and M. D. Taylor, "Improving the Efficiency of the Trent 500-HP Turbine Using Nonaxisymmetric End Walls—Part I: Turbine Design," *J. Turbomach.*, vol. 125, no. 3, pp. 497–504, Aug. 2003.
- [115] Z. Li and X. Zheng, "Review of design optimization methods for turbomachinery aerodynamics," *Prog. Aerosp. Sci.*, vol. 93, no. May, pp. 1–23, 2017.
- [116] I. Bosdas, M. Mansour, A. I. Kalfas, R. S. Abhari, and S. Senoo, "Unsteady Flow Field and Coarse Droplet Measurements in the Last Stage of a Low-Pressure Steam Turbine With Supersonic Airfoils Near the Blade Tip," *J. Eng. Gas Turbines Power*, vol. 139, no. 9, p. 91601, 2017.
- [117] L. Porreca, "Aerothermal Optimization of Partially Shrouded Axial Turbines," PhD Thesis, Diss. ETH No. 17138.

- [118] M. Treiber, P. Kupferschmied, and G. Gyarmathy, "Analysis of the Error Propagation Arising from Measurements with a Miniature Pneumatic 5-Hole Probe," 1998.
- [119] P. Kupferschmied, P. Köppel, W. Gizzi, C. Roduner, and G. Gyarmathy, "Time-resolved Flow Measurements with Fast-Response Aerodynamic Probes in Turbomachines," *Meas. Sci. Technol.*, vol. 11, no. 7, pp. 1036–1054, 2000.
- [120] A. Pfau, M. Treiber, M. Sell, and G. Gyarmathy, "Flow Interaction from the Exit Cavity of an Axial Turbine Blade Row Labyrinth Seal," *J. Turbomach.*, vol. 123, no. 2, p. 342, 2001.
- [121] J. Schlienger, "Evolution of Unsteady Secondary Flows Turbine in a Multistage Shrouded Axial Turbine," PhD Thesis, Diss. ETH No. 17138.
- [122] P. K. Kundu, I. M. Cohen, D. R. Dowling, and G. Tryggvason, *Fluid Mechanics*, 6th ed. Amsterdam: Elsevier, 2016.
- [123] M. G. Turner, S. E. Gorrell, and D. Car, "Radial Migration of Shed Vortices in a Transonic Rotor Following a Wake Generator: A Comparison Between Time Accurate and Average Passage Approaches," *J. Turbomach.*, vol. 133, no. 3, p. 31018, 2011.
- [124] T. Germain, M. Nagel, I. Raab, P. Schuepbach, R. S. Abhari, and M. G. Rose, "Improving Efficiency of a High Work Turbine Using Non-Axisymmetric Endwalls: Part I—Endwall Design and Performance," *Vol. 6 Turbomachinery, Parts A, B, C*, pp. 1109–1119, 2008.
- [125] F. Eulitz, "Unsteady Flow Simulations," in *VKI Lecture Series, Numerical Investigation in Turbomachinery: The State of the Art*, 2009.
- [126] R. Schädler, A. I. Kalfas, R. S. Abhari, G. Schmid, T. auf dem Kampe, and S. B. Prabhu, "Novel High-Pressure Turbine Purge Control Features for Increased Stage Efficiency," *J. Glob. Power Propuls. Soc.*, vol. 1, p. 68MK5V, 2017.
- [127] R. Schädler, A. I. Kalfas, R. S. Abhari, G. Schmid, and S. Voelker, "Modulation and Radial Migration of Turbine Hub Cavity Modes by the Rim Seal Purge Flow," *J. Turbomach.*, vol. 139, no. 1, p. 11011, 2016.

## Nomenclature

### Symbols

$c$	Speed of sound	[m/s]
$c_p$	Heat capacity at constant pressure	[J/(kg*K)]
$c_v$	Heat capacity at constant volume	[J/(kg*K)]
$C_{ax}$	Normalized axial velocity	[%]
$C_{ps}$	Static pressure coefficient	[-]
$C_{pt}$	Total pressure coefficient	[-]
$CTt$	Total temperature coefficient	[-]
$E$	Energy per unit mass	[J/kg]
$f$	Frequency	[1/s]
$F_{inv}$	Inviscid flux vector	
$F_{vis}$	Viscous flux vector	
$h$	Enthalpy	[J/kg]
$i$	Spatial index	[-]
$j$	Spatial index	[-]
$k$	Spatial/temporal index	[-]
$M$	Torque	[Nm]
$\dot{m}_f$	Mass flow	[kg/s]
$Ma$	Mach number	[-]
$P$	Pressure	[Pa]
$q$	Entropy loss coefficient	[-]
$R$	Individual gas constant for water vapour = 461.5	[J/(kg*K)]
$Re$	Reynolds number	[-]
$S$	Entropy	[J/(kg*K)]
$SKE$	Secondary kinetic energy	[J/kg]
$T$	Temperature	[°C]/[K]
$T_t$	Total temperature	[°C]/[K]
$T$	Time period	[s]
$TKE$	Turbulent kinetic energy	[J/kg]
$u_x$	Velocity in x-direction	[m/s]
$u_y$	Velocity in y-direction	[m/s]
$u_z$	Velocity in z-direction	[m/s]
$V_r$	Radial velocity	[m/s]
$V_\theta$	Circumferential velocity	[m/s]

**Greek symbols**

$a$	<i>Limit value</i>	<i>[-]</i>
$\beta$	<i>Limit value for preconditioning</i>	<i>[-]</i>
$\gamma$	<i>Isentropic coefficient</i>	<i>[-]</i>
$\Gamma$	<i>Preconditioning matrix</i>	<i>[-]</i>
$\eta_{tt}$	<i>Efficiency (total-to-total)</i>	<i>[-]</i>
$\lambda$	<i>Eigenvalue</i>	<i>[-]</i>
$\Psi$	<i>Loading coefficient</i>	<i>[-]</i>
$\rho$	<i>Density</i>	<i>[kg/m<sup>3</sup>]</i>
$\tau$	<i>Viscous stresses</i>	<i>[N/m<sup>2</sup>]</i>
$\tau$	<i>Pseudo-time</i>	<i>[s]</i>
$\Omega_s$	<i>Streamwise vorticity</i>	<i>[1/s]</i>
$\omega$	<i>Angular frequency</i>	<i>[rad/s]</i>

**Subscripts**

<i>abs</i>	<i>Absolute</i>
<i>EXP</i>	<i>Experimental Data</i>
<i>in</i>	<i>Blade inlet</i>
<i>out</i>	<i>Blade outlet</i>
<i>ref</i>	<i>Reference</i>
<i>rel</i>	<i>Relative</i>
<i>stat</i>	<i>Static</i>
<i>tot</i>	<i>Total</i>
<i>t-t</i>	<i>Total-to-total</i>

**Superscripts**

$\sim$	<i>Time resolved data</i>
$-$	<i>Time averaged data</i>

**Abbreviations**

5HP	<i>Pneumatic 5-hole probe (Cobra shape)</i>
ANN	<i>Artificial Neural Networks</i>
BPF	<i>Blade Passing Frequency</i>
CFD	<i>Computational Fluid Dynamics</i>
CFL	<i>Courant–Friedrichs–Lewy condition</i>
CSCS	<i>Swiss National Supercomputing Centre</i>
DFT	<i>Discrete Fourier Transform</i>
DoE	<i>Design of Experiments</i>
$F_q$	<i>Flow field quantity (pressure, yaw, etc.)</i>
FRAP-HTH	<i>Fast response aerodynamic probe</i>
FRAP-HTH	<i>High temperature, fast response aerodynamic heated probe</i>
GA	<i>Genetic algorithm</i>
GPU	<i>Graphic Processing Unit</i>
GP-GPU	<i>General Purpose - Graphic Processing Unit</i>
HP	<i>High pressure</i>
IAPWS-IF97	<i>The International Association for the Properties of Water and Steam - Industrial Formulation 1997</i>
LEC	<i>Laboratory for Energy Conversion</i>
LP	<i>Low pressure</i>
LW	<i>Lax-Wendroff</i>
MHPS	<i>Mitsubishi Hitachi Power Systems, Ltd.</i>
MPI	<i>Message Passing Interface</i>
PC	<i>Preconditioning</i>
PS	<i>Pressure side</i>
PSC	<i>Part-span connector</i>
RMS	<i>Root Mean Square</i>
RANS	<i>Reynolds-averaged Navier-Stokes equations</i>
RK4	<i>4<sup>th</sup> order Runge-Kutta scheme</i>
RPM	<i>Revolutions per minute</i>
SS	<i>Suction side</i>
TE	<i>L-0 stator trailing edge</i>
URANS	<i>Unsteady Reynolds Averaged Navier-Stokes</i>

## List of Figures

Figure 1–1: Energy by Fuel [1] .....	1
Figure 1–2: Energy by Region [1] .....	1
Figure 1–3: Schematic of Rankine cycle (left) with the respective temperature (T)-entropy (s) diagram of a steam turbine (right) [2] .....	2
Figure 1–4: Different stages of a steam turbine [3] .....	3
Figure 1–5: Sketch of Mach number and static pressure radial distribution in the last stage of a low-pressure steam turbine [9].....	6
Figure 1–6: Losses associated to shock waves at the tip region of a supersonic rotor blade profile [6] ..	7
Figure 1–7: Side view of a forward swept stator blade at tip region from the last stage simulated by Stüer et al. [9] .....	8
Figure 1–8: Secondary flow model described in [10].....	9
Figure 1-9: (a) Shrouded and (b) unshrouded turbine blade [29].....	13
Figure 1-10: Examples of labyrinth seal configurations; look through (a), stepped labyrinth (b), and gas turbine (c) [29].....	14
Figure 1-11: Classification of design methods .....	16
Figure 1-12: Penalty types [70].....	18
Figure 1-13: Architecture of an ANN [72] .....	19
Figure 2-1: High clustering of the cavities is propagated inside main flow path and lead to numerical errors .....	29
Figure 2-2: Mesh relaxation removes the numerical error and leads to a reasonable solution.....	29
Figure 2-3: Comparison of stability regions: Explicit Euler method (black curve) vs. explicit fourth order Runge Kutta method (red curve) .....	32
Figure 2-4: Improved stiffness at wider Mach number range due to preconditioning.....	34
Figure 2-5: Steam table range in terms of pressure and internal energy generated table for pressure $P=f(q,e)$ derived from IAPWS-IF97.....	44
Figure 2-6: Temperature for wet steam and ideal, dry steam .....	46
Figure 2-7: Partial derivatives of enthalpy with respect to pressure at constant density for wet-steam and ideal, dry steam conditions. ....	46
Figure 2-8: Single stage turbine schematic visualizing the selected interface numbering for the calculation of design variables .....	53
Figure 2-9: Multi-GPU parallelization architecture. A CPU-GPU pair is responsible for sub-domain computations independently, except sub-domain boundaries are computed at “GPU 0” master node .....	58
Figure 2-10: Flow chart of the optimization process [70].....	60
Figure 2-11: “Across method” of endwall parametrization [70].....	62
Figure 2-12: “Along method” of endwall parametrization [70].....	62
Figure 2-13: Optimization procedure [70] .....	64
Figure 2-14: Example of sigmoidal function with two nodes [71].....	67
Figure 3-1: MHPS’ low-pressure steam turbine test facility where FRAP-HTH and FRAP-OB measurements were conducted (a). Schematic of test facility, the measurement plane of the probe is marked in red (b). [116] .....	69



Figure 3-2: FRAP-HTH probe tip schematic. A: Probe tip ( $D_p=2.5\text{mm}$ ), B: Heating elements ( $D_{\text{Heating-spot}}=4.7\text{mm}$ ), C: Tip temperature monitoring ( $T_{\text{tip}}$ ), D: 8mm shaft. [116].....	70
Figure 3-3: Schematic of LISA turbine test facility.....	71
Figure 3-4: Schematic of LISA-H1 (a) and LISA-H2 (b) turbine cases .....	72
Figure 3-5: 5HP pneumatic probe on the left, FRAP probe on the right (with match for scale comparison) .....	73
Figure 4-1: Solid surfaces of L-1 and L-0 domains plus diffuser .....	76
Figure 4-2: Shroud geometry of L-1 and L-0 rotor blades .....	76
Figure 4-3: Convergence according to mass flow rate in the last 2 periods.....	80
Figure 4-4: Static pressure variation over time at monitoring points 50 and 51 .....	80
Figure 4-5: Schematic of steam turbine test facility with respective probe measurement locations.....	82
Figure 4-6: Comparison of CFD and 5HP for absolute yaw angle (a) and total temperature (b) at rotor exit of L-1 stage.....	83
Figure 4-7: Comparison of CFD and time-averaged FRAP-HTH for delta flow yaw angle from the mean blade metal angle (a) and relative Mach number (b) at L-0 stator exit .....	84
Figure 4-8: Comparison of CFD and time-resolved FRAP-HTH of $C_{ps}$ [-] at L-0 stator exit, 90% span – Unsteady comparison in four time steps of one rotor blade passing period .....	86
Figure 4-9: Static pressure coefficient $C_{ps}$ [-] at 90% span - Bow shock formation and interaction with upstream stator for one rotor blade passing period .....	87
Figure 4-10: Circumferential distribution of $C_{ps}$ [-] at 92.5% axial chord of L-0 stator blade .....	89
Figure 4-11: Circumferential distribution of normalized axial velocity $C_{ax}$ [%] at 92.5% axial chord of L-0 stator blade .....	89
Figure 4-12: Circumferential distribution of deviation flow angle [ $^{\circ}$ ] at 107.5% axial chord of L-0 stator blade, 90% span .....	91
Figure 4-13: Circumferential distribution of $C_{ps}$ [-] at 107.5% axial chord of L-0 stator blade, 90% span .....	91
Figure 4-14: $C_{ps}$ [-] distribution along stator suction side between 76% and 105% of stator axial chord, at 90% span .....	92
Figure 4-15: Time resolved $C_{ps}$ [-] distribution at 85% and 97.5% of stator axial chord, at 90% span.....	92
Figure 4-16: Extracted planes of cavity flow analysis - Contours of $C_{ps}$ [-] .....	94
Figure 4-17: Plane BB' - Circumferential distribution of $C_{ps}$ [-] (a-b), normalised axial velocity $C_{ax}$ [-], (c-d), and incidence angle [ $^{\circ}$ ] (e-f) at time steps of maximum (left) and minimum (right) mass flow.....	95
Figure 4-18: Plane CC' – Meridional view of $C_{ps}$ [-] at time steps of maximum (a) and minimum (b) mass flow.....	97
Figure 4-19: Formation of bow shock in time steps of max (a) and min (b) mass flow through plane BB' .....	97
Figure 4-20: Meridional view and entropy levels in L-0 stage inlet.....	99
Figure 4-21: Entropy loss coefficient [-] for L-0 stator for top 50% of blade span.....	99
Figure 4-22: Entropy loss coefficient [-] for L-0 rotor for top 50% of blade span.....	99
Figure 5-1: Solid surfaces of LISA-H1 turbine case .....	106
Figure 5-2: Stationary (grey), rotating (purple) and counter-rotating (blue) defined walls relative to the respective frame of reference.....	109

Figure 5-3: Static pressure distribution of the initial guess .....	109
Figure 5-4: History of the root-mean-square of the numerical residuals [105].....	112
Figure 5-5: Convergence history of the root-mean-square of the numerical residuals [105] .....	112
Figure 5-6: History of the mass flow at row interfaces [105].....	113
Figure 5-7: Convergence history of the mass flow at domain outlet .....	113
Figure 5-8: History of mass averaged total enthalpy at stages outlet [105] .....	113
Figure 5-9: History of mass averaged, non-dimensionalized entropy generation at stages outlet [105] .....	113
Figure 5-10: Convergence history of all investigated variables for the first stage [105].....	114
Figure 5-11: Convergence history of all investigated variables for the second stage [105] .....	114
Figure 5-12: History of mass averaged total pressure loss values across rotor row in a relative frame of reference at stage outlets [105] .....	114
Figure 5-13: History of mass averaged total-to-total isentropic efficiency at stage outlets [105].....	115
Figure 5-14: History of mass averaged secondary kinetic energy values at stage outlets [105] .....	115
Figure 5-15: History of local pressure signals at specific locations inside the flow field [105] .....	117
Figure 5-16: Convergence history of local pressure signals at specific locations inside the flow field [105].....	117
Figure 5-17: History of local temperature signals at specific locations inside the flow field [105].....	117
Figure 5-18: Convergence history of local temperature signals at specific locations inside the flow field .....	117
Figure 5-19: History of local TKE signals at specific locations inside the flow field [105].....	118
Figure 5-20: Convergence history of local TKE signals at specific locations inside the flow field [105] .....	118
Figure 5-21: History of local turbulent dissipation signals at specific locations inside the flow field [105].....	118
Figure 5-22: Convergence history of local turbulent dissipation signals inside the flow field [105] ...	118
Figure 5-23: Measurement planes in LISA .....	119
Figure 5-24: Plane B, Evolution of Mach number distribution along the span over time and comparison with experimental data.....	120
Figure 5-25: Plane B, Evolution of absolute yaw angle distribution along the span over time and comparison with experimental data.....	120
Figure 5-26: Plane B, Evolution of total pressure coefficient along the span over time and comparison with experimental data.....	121
Figure 5-27: Plane D, Evolution of Mach number distribution along the span over time and comparison with experimental data.....	122
Figure 5-28: Plane D, Evolution of absolute yaw angle distribution along the span over time and comparison with experimental data.....	122
Figure 5-29: Plane D, Evolution of total pressure coefficient along the span over time and comparison with experimental data.....	123
Figure 5-30: Mach number distribution along the domain .....	124
Figure 5-31: Time-averaged relative yaw angle [°] at plane D [104] .....	126
Figure 6-1: Approach to reduce computational cost of optimization, while maintaining high accuracy – Unsteady inflow .....	131

Figure 6-2: Computational domain of LISA-H2 turbine case for two-stage (left) and single-stage (right)	132
Figure 6-3: Boundary conditions at single-stage inlet at $t/T=0$	135
Figure 6-4: Geometry parameterization with Autoblade	137
Figure 6-5: Comparison between measured (5-hole probe) and simulated values at rotor exit	142
Figure 6-6: Comparison between simulated and measured (FRAP) of relative yaw angle at rotor exit, time-averaged in rotor frame of reference	143
Figure 6-7: Comparison of normalised relative total pressure $Cp_{t,rel}$ in rotor frame of reference for predictions and measurements (FRAP) at rotor exit, time-averaged in rotor relative frame of reference	144
Figure 6-8: Design optimization convergence and final optimized rotor hub end wall geometry	145
Figure 6-9: Mass- and time-averaged normalised static pressure $Cp_s$ and Mach number at rotor inlet	147
Figure 6-10: Mass- and time-averaged absolute and relative yaw angles at rotor inlet	147
Figure 6-11: Time-averaged normalised static pressure $Cp_s$ and radial velocity $V_r$ at stator hub cavity exit (0% span)	148
Figure 6-12: Circumferentially area- and time-averaged of $Cp_s$ and $V_r$ at stator hub cavity exit (0% span)	149
Figure 6-13: Time-averaged of $Cp_s$ and $V_r$ at rotor hub inlet, at 1% span	150
Figure 6-14: Mass- and time-averaged relative yaw angle and relative circumferential velocity $V_{\theta,rel}$ at rotor exit	151
Figure 6-15: Time-averaged area plots of relative yaw angle [°], in rotor relative frame of reference, at rotor exit	151
Figure 6-16: Time-averaged area plots of absolute yaw angle [°], in rotor relative frame of reference, at rotor exit	152
Figure 6-17: Mass- and time-averaged normalised static pressure $Cp_s$ and reaction R at rotor exit	153
Figure 6-18: Time-averaged area plots of normalised static pressure $Cp_s[-]$ , in rotor relative frame of reference, at rotor exit	153
Figure 6-19: Time-averaged area plots of normalised total pressure $Cp_{t,rel} [-]$ , in rotor relative frame of reference, at rotor exit	154
Figure 6-20: (a) Relative difference $\Delta Cp_{t,rel} [\%]$ of profiled case compared to baseline. (b) Mass- and time-averaged area plots of normalised relative total pressure $Cp_{t,rel} [-]$ at rotor exit	154
Figure 6-21: Mass- and time-averaged streamwise vorticity $\Omega_s$ and radial velocity $V_r$ at rotor exit	155
Figure 6-22: Mass- and time-averaged entropy rise and radial distribution of normalised mass flow at rotor exit	156
Figure 6-23: Comparison of normalised static pressure $Cp_s [-]$ distribution between (a) cylindrical and (b) profiled rotor hub end wall and its effect on (c) blade loading at 6% span	157
Figure 6-24: Comparison of time-averaged normalised static pressure $Cp_s [-]$ distribution between (a) baseline and (b) profiled case on rotor suction side and wall- limited streamlines, tracing the hub passage vortex ascending on blade's suction side	159
Figure 6-25: Particle tracks of stator hub cavity leakage flow comparison for the two cases with (a) cylindrical and (b) profiled rotor hub end wall, in time-averaged flow field and relative frame of reference	160

Figure 6-26: Time-averaged area plots of second stage total-to-total torque-based efficiency $\eta_{t-t}$ [-], at rotor exit .....	161
Figure 6-27: (a) Efficiency difference $\Delta\eta_{t-t}$ [%] of profiled case compared to baseline. (b) Radial distribution of circumferentially mass- and time-averaged second stage total-to-total torque-based efficiency $\eta_{t-t}$ at rotor exit for the baseline and profiled geometries .....	161
Figure 6-28: Computational domain of LISA-H2 turbine case for two-stage without cavities (left) and single-row, steady case of second rotor (right).....	163
Figure 6-29: Mass- and time-averaged relative yaw angle and radial distribution of normalised mass flow at second rotor exit.....	164
Figure 6-30: (a) Radial distribution of circumferentially mass- and time-averaged second stage total-to-total torque-based efficiency $\eta_{t-t}$ at second rotor exit for the baseline and no cavities case. (b) Mass- and time-averaged of normalised absolute total temperature at second rotor exit .....	164
Figure 6-31: Time-averaged area plots of normalised absolute total temperature $CT_{t,abs}$ [-], in relative frame of reference at rotor exit .....	165
Figure 6-32: Mass- and time-averaged relative yaw angle at rotor exit .....	167
Figure 6-33: Mass- and time-averaged streamwise vorticity $\Omega_s$ [1/s] at rotor exit.....	167
Figure 6-34: Radial distribution of circumferentially mass- and time-averaged second stage total-to-total torque-based efficiency $\eta_{t-t}$ at rotor exit for the baseline and profiled geometries... ..	168
Figure 6-35: Area plots of second stage Total-to-Total torque-based efficiency $\eta_{t-t}$ [-], at rotor exit of steady solution.....	169
Figure 6-36: (a) Efficiency difference $\Delta\eta_{t-t}$ [%] of profiled case compared to baseline, based on steady solutions. (b) Radial distribution of circumferentially mass- and time-averaged second stage total-to-total torque-based efficiency $\eta_{t-t}$ at rotor exit of the steady solutions for the baseline and profiled geometries .....	169
Figure 6-37: Static temperature [°C] distribution at rotor inlet at interface C:.....	170

## List of Tables

Table 1: List of all quantities that are calculated or assessed at row interfaces distributed along the span, as well as mass averaged over the whole interface .....	54
Table 2: Operating conditions of the turbine.....	74
Table 3: Mesh size of the different flow domains .....	77
Table 4: Mesh quality report of whole domain .....	78
Table 5: Mesh size per GPU of the different flow domains, in millions.....	107
Table 6: Mesh quality report of whole domain .....	107
Table 7: Inlet boundary conditions .....	108
Table 8: Mesh size of the different flow domains per pitch, in millions .....	133
Table 9: Mesh quality report of whole domain .....	133
Table 10: Inlet boundary conditions .....	135
Table 11: End wall parameterization setup in Autoblade .....	138
Table 12: Artificial neural network learning setup.....	139
Table 13: Genetic algorithm optimization setup .....	140
Table 14: Summary of objective function .....	141
Table 15: Averaged errors of CFD compared to experiments.....	143



## List of Publications

Parts of the author's following publications are included in this doctoral thesis.

Papagiannis I., Raheem A., Basol A., Kalfas A., Abhari R., Fukushima H., Senoo S. (2017). Unsteady flow mechanisms in the last stage of a transonic low pressure steam turbine—multistage effects and tip leakage flows. Proceedings of the 1<sup>st</sup> Global Power and Propulsion Forum, GPPF-2017-89, Zurich, Switzerland.

Papagiannis I., Raheem A., Basol A., Kalfas A., Abhari R., Fukushima H., Senoo S. (2017). Unsteady flow mechanisms in the last stage of a transonic low pressure steam turbine—multistage effects and tip leakage flows. Journal of the Global Power and Propulsion Society. 1: 95–112. <https://doi.org/10.22261/F4IW8S>

Papagiannis I., Kalfas A., Abhari R., Senoo S. Unsteady optimization of profiled rotor hub end wall. *Under preparation* (2018).





## Curriculum Vitae

### Ilias Papagiannis

Born on August 1, 1989 in Thessaloniki, Greece.

#### Education

- 2001 – 2007 Secondary Education, 1<sup>st</sup> Lyceum of Sykies, Thessaloniki, Greece
- 2007-2012 Dipl.-Ing in Mechanical Engineering, Aristotle University of Thessaloniki, Greece
- 2014-2018 Swiss Federal Institute of Technology, Zurich (ETHZ), Laboratory for Energy Conversion (LEC)  
Doctoral candidate

#### Experience

- 2012-2013 Military service in Hellenic Army
- 2014-2018 Research assistant, Laboratory for Energy Conversion-ETH Zurich

#### Distinctions/Awards

- 2007-2009 National Scholarship Fellow (Two times, for excellent performance during the academic years 2007-2008, 2009-2010)
- 2012 First among all the graduate students of November of 2012

